



Universitat de Lleida

Energy efficient active cooling in advanced microelectronic systems

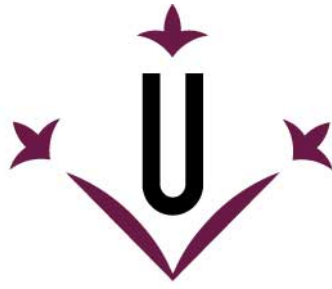
Montse Vilarrubí Porta

<http://hdl.handle.net/10803/668020>

ADVERTIMENT. L'accés als continguts d'aquesta tesi doctoral i la seva utilització ha de respectar els drets de la persona autora. Pot ser utilitzada per a consulta o estudi personal, així com en activitats o materials d'investigació i docència en els termes establerts a l'art. 32 del Text Refós de la Llei de Propietat Intel·lectual (RDL 1/1996). Per altres utilitzacions es requereix l'autorització prèvia i expressa de la persona autora. En qualsevol cas, en la utilització dels seus continguts caldrà indicar de forma clara el nom i cognoms de la persona autora i el títol de la tesi doctoral. No s'autoritza la seva reproducció o altres formes d'explotació efectuades amb finalitats de lucre ni la seva comunicació pública des d'un lloc aliè al servei TDX. Tampoc s'autoritza la presentació del seu contingut en una finestra o marc aliè a TDX (framing). Aquesta reserva de drets afecta tant als continguts de la tesi com als seus resums i índexs.

ADVERTENCIA. El acceso a los contenidos de esta tesis doctoral y su utilización debe respetar los derechos de la persona autora. Puede ser utilizada para consulta o estudio personal, así como en actividades o materiales de investigación y docencia en los términos establecidos en el art. 32 del Texto Refundido de la Ley de Propiedad Intelectual (RDL 1/1996). Para otros usos se requiere la autorización previa y expresa de la persona autora. En cualquier caso, en la utilización de sus contenidos se deberá indicar de forma clara el nombre y apellidos de la persona autora y el título de la tesis doctoral. No se autoriza su reproducción u otras formas de explotación efectuadas con fines lucrativos ni su comunicación pública desde un sitio ajeno al servicio TDR. Tampoco se autoriza la presentación de su contenido en una ventana o marco ajeno a TDR (framing). Esta reserva de derechos afecta tanto al contenido de la tesis como a sus resúmenes e índices.

WARNING. Access to the contents of this doctoral thesis and its use must respect the rights of the author. It can be used for reference or private study, as well as research and learning activities or materials in the terms established by the 32nd article of the Spanish Consolidated Copyright Act (RDL 1/1996). Express and previous authorization of the author is required for any other uses. In any case, when using its content, full name of the author and title of the thesis must be clearly indicated. Reproduction or other forms of for profit use or public communication from outside TDX service is not allowed. Presentation of its content in a window or frame external to TDX (framing) is not authorized either. These rights affect both the content of the thesis and its abstracts and indexes.



Universitat de Lleida

DOCTORAL THESIS

**Energy efficient active cooling in advanced
microelectronic systems**

Montse Vilarrubí Porta

Thesis presented for the degree of Doctor by Universitat de Lleida
Doctorate Programme in Engineering and Information Technologies

Directors

Jérôme Barrau, Joan Ignasi Rosell Urrutia

Tutor

Jérôme Barrau

2019

*"Don't let anyone rob of your imagination,
your creativity or your curiosity"*

- Mae Jemison

Acknowledgements

First of all, I would like to sincerely thank my supervisors, Jérôme, Joan Ignasi and Manel for their confidence, constant support and advices. This work would not be possible without their help.

Thanks also to prof. Luc G. Fréchette and the rest of the team from Université de Sherbrooke, who give me the opportunity to discover the world of microfabrication and also for their inspiration and assistance.

To the rest of the STREAMS team, everything I have learned being involved with this project has been very meaningful to me.

To Laia, Gerard and the rest of work colleagues who have made this travel much easier.

To my family, who always believed in me and give me all their support throughout all the stages of my life. Without them I would not be here today.

And last but not least, to my partner in life, Felip, for the patience, support and unconditional love.

Abstract

Actual cooling solutions of 3D integrated circuits (3D-IC) do not provide systems able to adapt their behavior to changing boundary conditions in time and space, what leads to overcooling when refrigerating demands are low. That implies additional pressure drops in the fluid channel and so, oversized pumping powers for changing conditions. Also, in the existing works, the surface temperature uniformity of the chip is only optimized for a given heat load distribution and cannot be adapted to variable heat load scenarios in time and space.

To overcome these problems, this thesis proposes a system based on self-adaptive fins acting as passive thermal actuators. The principle of thermal expansion of the materials is the responsible for the smart behavior of these fins, which will be activated, without any external excitation, in function of their own temperature. The demonstrated capabilities of flow disturbing elements inside microchannels are used only for high cooling demands; otherwise, the fins will remain in flat position, reducing the pressure drop inside the cooling device. With this solution, the system will be able to tailor its internal geometry to time dependent and non-uniform heat flux distributions, optimizing the local heat transfer enhancement and the pressure drop to the instantaneous cooling need and thus, reducing the needed pumping power for a more energy efficient cooling system.

Within this work, the working principle, design and validation of the self-adaptive fins to reach the desired behavior of self-adaptation by using the thermal expansion of the materials have been evaluated. The increment of the convective heat transfer due to the presence of this type of flow disturbing elements inside the fluidic channel has been assessed, defining a 10 % enhancement compared with a plain channel. Also, a more uniform surface thermal gradient has been observed, experimentally and numerically, due to the presence of self-adaptive fins when the cooling device is submitted to non-uniform heat fluxes. Finally, a reduction of 10 % in pumping power is estimated due to the self-adaptation concept, compared with a cooling system of fixed flow disturbing elements.

Resum

Les solucions actuals de refrigeració en circuits integrats en 3D (3D-IC) no proporcionen sistemes capaços d'adaptar el seu comportament a condicions variables en el temps i l'espai, fet que comporta un sobre refredament quan la demanda de fred és baixa. Això implica caigudes de pressió addicionals al canal del fluid i per tant, potències de bombeig sobredimensionades per condicions variables. A més, en els treballs existents, la uniformitat de temperatura sobre la superfície del xip només està optimitzada per una distribució de càrrega de calor determinada i no pot adaptar-se a escenaris de càrregues de calor variables en el temps i l'espai.

Per abordar aquests problemes, aquesta tesi proposa un sistema basat en aletes auto-adaptatives que actuen com a actuadors tèrmics passius. El principi d'expansió tèrmica dels materials és el responsable del comportament intel·ligent d'aquestes aletes, que s'activaran, sense cap excitació externa, en funció de la seva pròpia temperatura. Les capacitats, ja demostrades, d'elements pertorbadors del flux dins de microcanals, s'utilitzen només quan la demanda de refrigeració és alta; en cas contrari, les aletes romanen en posició plana, reduint així la caiguda de pressió dins del dispositiu de refredament. Amb aquesta solució, el sistema és capaç d'adaptar la seva geometria interna a distribucions de flux de calor temporals i no uniformes, optimitzant la millora de la transferència de calor i la caiguda de pressió a les necessitats de refrigeració instantànies. Així, és redueix la potència de bombeig necessària, fent el sistema de refrigeració més eficient energèticament.

Dins d'aquest treball, s'ha avaluat el principi de treball, el disseny i la validació de les aletes auto-adaptatives per aconseguir el comportament desitjat d'adaptabilitat utilitzant la dilatació tèrmica dels materials. S'ha avaluat l'increment de la transferència de calor convectora a causa de la presència d'aquest tipus d'elements pertorbadors del flux dins del canal fluid, definint un increment del 10 % en comparació amb un canal buit. A més, s'ha observat un gradient tèrmic superficial més uniforme, experimentalment i numèricament, a causa de la presència d'aletes auto-adaptatives quan el dispositiu de refrigeració està sotmès a fluxos de calor no uniformes. Finalment, s'estima una reducció del 10 % de la potència de bombeig degut al concepte d'auto-adaptació, comparat amb un sistema de refredament basat en elements pertorbadors del flux fixos.

Resumen

Las soluciones de refrigeración actuales en circuitos integrados 3D (3D-IC) no proporcionan sistemas capaces de adaptar su comportamiento a las cambiantes condiciones de calor en el tiempo y el espacio. Este hecho conduce a un enfriamiento excesivo cuando las demandas de refrigeración son bajas y, por lo tanto, se inducen caídas de presión adicionales en el canal de fluido y se obtienen potencias de bombeo sobredimensionadas para condiciones cambiantes. Además, en las obras existentes, la uniformidad de la temperatura de la superficie del chip solo se optimiza para una distribución de carga térmica dada y no se puede adaptar a los escenarios de carga térmica variable en el tiempo y el espacio.

Para abordar estos problemas, esta tesis propone un sistema basado en aletas auto-adaptativas que actúan como actuadores térmicos pasivos. El principio de expansión térmica de los materiales es el responsable del comportamiento inteligente de estas aletas, que se activarán, sin ninguna excitación externa, en función de su propia temperatura. Las capacidades demostradas de los elementos que perturban el flujo dentro de los microcanales se usan solo para altas demandas de enfriamiento; de lo contrario, las aletas permanecerán en posición plana, reduciendo la caída de presión dentro del dispositivo de enfriamiento. Con esta solución, el sistema podrá adaptar su geometría interna a distribuciones de flujo de calor dependientes y no uniformes de tiempo, optimizando la mejora de la transferencia de calor local y la caída de presión a la necesidad de enfriamiento instantáneo y, por lo tanto, reduciendo la potencia de bombeo necesaria para una Sistema de refrigeración más eficiente energéticamente.

Dentro de este trabajo, se ha evaluado el principio de trabajo, diseño y validación de las aletas auto-adaptativas para alcanzar el comportamiento deseado de auto-adaptación mediante el uso de la expansión térmica de los materiales.

Se ha evaluado el incremento de la transferencia de calor por convección debido a la presencia de este tipo de elementos perturbadores del flujo dentro del canal, que definen una mejora del 10 % en comparación con un canal plano. Además, se ha observado un gradiente térmico superficial más uniforme, experimental y numéricamente, debido a la presencia de aletas auto-adaptativas cuando el dispositivo de enfriamiento se somete a flujos de calor no uniformes. Finalmente, se estima una reducción del 10 % en la potencia de bombeo debido al concepto de auto-adaptación, en comparación con un sistema de enfriamiento de elementos perturbadores de flujo fijo.

Table of contents

Abstract	VII
Resum.....	IX
Resumen.....	XI
List of figures	XVII
List of tables	XXV
Nomenclature	XXVII

1. INTRODUCTION

1.1. The importance of cooling in microelectronics.....	3
1.2. Current thresholds in microelectronics cooling.....	4
1.3. Background (STREAMS H2020 Project).....	7
1.3.1. Functionality 1: Versatile microfluidic actuation	10
1.3.2. Functionality 2: Anticipation of the thermal map.....	16
1.3.3. Functionality 3: Thermal energy harvesting.....	16
1.4. Objectives of this thesis	16
1.5. Parameters for performance assessment.....	18
1.5.1. Flow characterization	18
1.5.2. Heat transfer	19
1.5.3. Figures of merit	19

2. STATE-OF-THE-ART: CURRENT COOLING METHODS FOR MICROELECTRONICS

2.1. 3D-IC microfluidic cooling	25
2.1.1. Introduction to 3D-IC architectures	25
2.1.2. State-of-the-art on 3D-IC cooling.....	26
2.2. Non-uniform heat loads and hotspot mitigation	31
2.3. Heat transfer enhancement techniques	36
2.3.1. Passive techniques for heat transfer enhancement within microchannels.....	37
2.3.2. Active techniques for heat transfer enhancement within microchannels	46
2.4. Conclusions about the state-of-the-art.....	47

3. SELF-ADAPTIVE FINS ACTING AS VORTEX GENERATORS

3.1. Background: Shape memory alloys used as self-adaptive cooling device within miniscale.....	51
3.1.1. Analytic study.....	52
3.1.2. Experimental validation of TWSME.....	54
3.1.3. Experimental validation of the self-adaptive concept	58
3.2. Definition of self-adaptive fins requirements for microscopic scale	60
3.2.1. Numerical model.....	61
3.2.2. Governing equations	62
3.2.3. Grid independence test.....	63
3.2.4. Thermal performance assessment for different fin inclination	64
3.3. Bimetallic structures	66
3.3.1. Working principle	66
3.3.2. Minimum thickness for self-adaptive bimetallic fins inside a microchannel.....	68
3.3.3. Proposed geometries of the fins.....	73
3.3.4. Microfabrication of the fins.....	80
3.3.5. Conclusions and perspectives on bimetallic self-adaptive fins.....	88
3.4. Doubly clamped structures	89
3.4.1. Motivation.....	89
3.4.2. Working principle	90
3.4.3. Geometric study and numerical analysis of the doubly clamped fins	95
3.4.4. Possible thresholds of this technology.....	98

4. IMPACT ASSESSMENT OF THE SELF-ADAPTIVE FINS INSIDE A MICROCHANNEL

4.1. Model definition.....	101
4.2. Numerical assessment of self-adaptive fins impact.....	105
4.2.1. Boundary conditions	106
4.2.2. Grid independence test.....	107
4.2.3. Numerical results	108
4.3. Experimental validation of the impact of the self-adaptive fins inside a microchannel	118
4.3.1. Experimental test bench and experimental device.....	118
4.3.2. Error analysis.....	120
4.3.3. Results and discussion.....	122
4.4. General overview of the impact of self-adaptive fins inside a microchannel cooling device	137

5. IMPACT ASSESSMENT OF THE SELF-ADAPTIVE FINS INSIDE A MICROFLUIDIC CELL SYSTEM

5.1. Geometry of the microfluidic cell.....	141
5.2. Numerical assessment of self-adaptive fins performance.....	144
5.2.1. Boundary conditions	144
5.2.2. Induced error on the simulation of solid fins.....	145
5.2.3. Grid independence test.....	146
5.2.4. Numerical results	148
5.3. General overview of the impact of self-adaptive fins inside a microfluidic cooling cell.	163

6. GENERAL CONCLUSIONS

7. FUTURE WORK

8. PUBLICATIONS

8.1. Journals	177
8.2. Conferences.....	178
8.3. Patent	179
Literature.....	181
Annex I.....	193

List of figures

Figure 1.1. Breakdown of energy usage by systems for 94 data centers [11].	4
Figure 1.2. A schematic representation of a 3D-IC chip cooled with a coolant layer [24].	5
Figure 1.3. STREAMS cooling platform (Source: www.project-streams.eu).	8
Figure 1.4. STREAMS strategy and positioning versus actual state-of-the-art cooling technologies low points.	10
Figure 1.5. (a) Matrix of microfluidic cells. (b) Schematic of one single microfluidic cell.	13
Figure 1.6. a) Thermal dice of the STREAMS test vehicle. b) STREAMS test vehicle composed of four thermal dice and the ASIC.	13
Figure 1.7. Schematic of the coolant flow distributor (a) with the cover that contains the inlet and outlet slots for the flow and (b) without the slots cover.	14
Figure 1.8. Microvalve placement within a single microfluidic cell.	15
Figure 1.9. Schematic of the self-adaptive concept of nonlinear microvalves. At low temperatures, the beam remains at a low position (b), while at high temperatures, the beam buckles and opens the air gap that allows to pass the flow rate (c) [40].	15
Figure 1.10. Self-adaptive fins working principle.	17
Figure 2.1. 3D thermal management using a conventional air cooling heat sink [52].	26
Figure 2.2. Schematic of a 3D circuit with a microchannel cooling system [53].	27
Figure 2.3. Schematic of a 3D-IC stack cooled with microchannels with electrical and fluidic TSV interconnects [24].	28
Figure 2.4. Schematic of the four-layer chip stack with microchannel cooling [57].	28
Figure 2.5. Overall view of the pin fin heat sink [51].	29
Figure 2.6. Scheme of the integrated liquid cooling system [60].	30
Figure 2.7. Temperature difference between the maximum and the minimum temperatures of the heated wall for a heat flux of 36 kW/m^2 , when using water (○) or dielectric fluid (●) [62].	31
Figure 2.8. Schematic of the stepwise varying width microchannel cooling device [66].	32
Figure 2.9. Temperature uniformity along the flow path of: a) a conventional cooling scheme; b) a cooling scheme with decreasing thermal resistance along the flow path [66].	33
Figure 2.10. Chip temperature profile in presence of two hotspots dissipating 200 W/cm^2 while the rest of the substrate dissipates 100 W/cm^2 [29].	34
Figure 2.11. Schematic of the heat sink presented by Green et al [70].	35

Figure 2.12. Oblique finned microchannel heat sink presented by Lee et al. [30].	35
Figure 2.13. Passive and active heat transfer enhancement techniques within microchannels [75].	37
Figure 2.14. Common flow disturbing elements and their geometrical definitions [78].	38
Figure 2.15. Schematic diagram of a microchannel with divergent RWP. (a) Top view and (b) side view [80].	39
Figure 2.16. Schematic of (a) half microchannel heat sink with ribs and grooves and (b) half of the test system studied by Wang et al. [82].	40
Figure 2.17. Different configurations of the herringbone microstructures studied by Marschewski et al. [47].	41
Figure 2.18. Different configurations of microchannel with cylindrical vortex generators [45].	42
Figure 2.19. (a) Cross-section of the 3D-IC with interlayer liquid cooling. (b) Cross-section of the different microchannel structures [86].	44
Figure 2.20. Schematic view of a heat sink with (a) triangular cavities and rectangular ribs and (b) rectangular cavities [87].	44
Figure 2.21. Schematic view of the microchannel with ridges at the bottom. The red and green lines represent trajectories in the flow [88].	45
Figure 2.22. Piezoelectric enhanced microchannel [75].	47
Figure 3.1. Ideal working cycle of the SMA wing [100].	52
Figure 3.2. Test module setup.	54
Figure 3.3. 3D view of the cooling test module (exploded view).	55
Figure 3.4. Photography of the cooling device test module with bottom side view of the channel.	56
Figure 3.5. Raised position (austenitic phase) of the SMA wing above T_{Af} (photography from Sample 2) and flat position (martensitic phase) below T_{Mf} .	57
Figure 3.6. Temperature evolution of the junction temperature under varying heat flux (Sample 2, $T_{in} = 3^{\circ}C$, $Q = 320$ ml/min) [100].	59
Figure 3.7. Schematic of (a) half plain microchannel and (b) half microchannel with fins inside assessed on numerical CFD simulations.	61
Figure 3.8. Grid independence test for the pressure drop within the microchannel.	64
Figure 3.9. Vortex generation within the fluid inside the microchannel due to the variation of the fin inclination. The streamlines in red show the velocity field of the fluid and the color bar the velocity magnitude in m/s.	65
Figure 3.10. Heat transfer and pressure drop increment for different fin inclinations within the channel.	66

Figure 3.11. Behavior of a bimetallic strip while uniformly heated. (b) Assuming the materials are not joined and (c) assuming the materials are bonded together.	67
Figure 3.12. Working principle of the bimetallic self-adaptive fins, where F_1 and F_2 are the forces at which each material is subjected due to the behavior of the other material.	67
Figure 3.13. Schematic of a bimetallic fin inside the microchannel.	68
Figure 3.14. Displacement of a bimetallic fin due to a temperature increase of 50 K when $Q = 0$ ml/min. The color legend represents the total displacement of the solid. The initial position of the fin is represented without color.	69
Figure 3.15. Maximum Von Mises stress at a bimetallic fin for different flow rates. The considered thickness of the fin in this case is $t_{fin} = 4 \mu\text{m}$	72
Figure 3.16. Maximum Von Mises stress at the fin when $\Delta T = 50$ K and $Q = 0$ ml/min assessed for different fin thicknesses and compared with the yield strength of the silver.	72
Figure 3.17. Maximum vertical rise of the bimetallic fin due to a temperature increase of 50 K for different fin thicknesses and flow rates.	73
Figure 3.18. Schematic of the model 1 of bimetallic fins. (a) Frontal view. (b) Lateral view.	75
Figure 3.19. Schematic of the Model 2 of the bimetallic fins. (a) Frontal view. (b) Lateral view.	76
Figure 3.20. Schematic of the model 3 of the bimetallic fins. (a) Frontal view. (b) Lateral view.	77
Figure 3.21. Schematic of the bimetallic fin corresponding to model 4. (a) Frontal view. (b) Lateral view.	78
Figure 3.22. Schematic of the model 5 of the bimetallic fins. (a) Frontal view. (b) Lateral view.	79
Figure 3.23. Vertical displacement (in % of the length of the fins) of each model of bimetallic fins.	80
Figure 3.24. Microfabrication process flow for the fabrication of bimetallic self-adaptive fins (left side of the Si wafer, blue and green colors) and self-adaptive microvalve (right side of the Si wafer, in blue).	82
Figure 3.25. Scanning electron microscope (SEM) image of Ag fins fabricated for feasibility study.	83
Figure 3.26. SEM images of fabricated Ag-Au bimetallic fins (Model 3) after releasing step.	85
Figure 3.27. Experimental setup for deflection visualization of the self-adaptive fins.	86
Figure 3.28. (a) Microscopic image of the plastic deformation of the Ag-Au fins when submitted to high temperatures. (b), (c) SEM image of plastic deformations at the Ag-Au fins.	87

Figure 3.29. Completely released bimetallic fins at room temperature and at high temperature.	88
Figure 3.30. Clamped-clamped beams with small eccentricities [39].	91
Figure 3.31. Non-dimensional design curves for central deflection at various eccentricities as a function of the temperature rise (θ) [39].....	92
Figure 3.32. Vertical displacement of the 1733 μm valve in function of the hot plate temperature [106].	93
Figure 3.33. Behavior of the self-adaptive fins for different heat flux distributions: a) Uniform high heat flux. b) Uniform medium heat flux. c) Non-uniform heat flux. d) Constant low heat flux.....	94
Figure 3.34. Schematic of the microvalve geometry with the main design parameters [106]...	95
Figure 3.35. Relation between maximum deflection and temperature rise of doubly clamped fins of different lengths.....	96
Figure 3.36. Doubly clamped fin with triangle cut in the middle.....	97
Figure 3.37. Comparison of the rise of some bimetallic fins with the doubly clamped fins.....	98
Figure 4.1. (a) Cooling device based on an array of microchannels with the self-adaptive fins inside. (b) Zoom on the fin distribution inside one microchannel. (c) Geometry of one self- adaptive fin. (All units in mm).	102
Figure 4.2. a) Schematic of the self-adaptive doubly clamped fin. (b) Simplification of the self- adaptive fins into a semielliptical object.....	103
Figure 4.3. Microfluidic cell with (a) fine fins inside and (b) solid fins inside.	104
Figure 4.4. Microchannel geometry (units in mm).	106
Figure 4.5. Grid independence test assessed on a) the average chip temperature and b) the pressure drop within the channel.	108
Figure 4.6. Heat transfer enhancement and pressure drop increment in a microchannel due to self-adaptive fins for different Re numbers.	109
Figure 4.7. Nusselt number enhancement and apparent friction factor increment inside the microchannel for the different configurations of fins, compared with a plain microchannel.	110
Figure 4.8. Schematic of the fin placement at the cold wall within a single microchannel.....	111
Figure 4.9. Heat transfer enhancement and apparent friction factor increment for different Reynolds numbers when the fins are placed at the cold side of the microchannel.....	112
Figure 4.10. Comparison of the heat transfer enhancement and apparent friction factor increment between fins placed at hot or cold wall of the microchannel.	112
Figure 4.11. Average temperature at the chip surface, cooled down by the microchannels...	113

Figure 4.12. Streamline representation of the flow velocity inside the microchannel for $Re=600$ and the fins placed at the cold side wall.	113
Figure 4.13. Non-uniform and time dependent heat load scenario applied.	114
Figure 4.14. Comparison of the pressure drop within the microchannel for the assessed systems.	115
Figure 4.15. Average pumping power of both studied systems.	116
Figure 4.16. Comparison of chip temperature between a plain microchannel, a microchannel with fixed fins and a microchannel with self-adaptive fins.....	117
Figure 4.17. Chip temperature difference between the plain microchannel and the microchannels with fixed fins and self-adaptive fins respectively.....	118
Figure 4.18. Fluidic test module setup.....	119
Figure 4.19. Initial microfluidic device based on microchannels to evaluate the impact of self-adaptive fins on its thermo-hydraulic performance.	120
Figure 4.20. Schematic of the assessed device based on a configuration of plain microchannels.	122
Figure 4.21. (a) Experimental setup with the heater placed above the cooling device. (b) Thermocouples located between the heater and the cooling device following a channel path.	123
Figure 4.22. Comparison between numerical and experimental values for (a) average surface temperature and (b) pressure drop along the device.....	124
Figure 4.23. Correlation between experimental and numerical data for (a) Average temperature surface and (b) Pressure drop.	125
Figure 4.24. Schematic of experimental cooling device based on microchannels with self-adaptive fins inside.....	127
Figure 4.25. (a) Reverse part of the microfluidic device with microchannels and self-adaptive fins, partly disassembled to have direct access to the wall where the fins are etched. (b) Infrared camera vision of the Si microchannels with self-adaptive fins (seen through the Si wall where the fins are etched).	128
Figure 4.26. IR camera assessment of the temperature along one microchannel when only two of them are active. The Si surface of one channel is painted in black for a correct reading of the temperature ("Line 1").	129
Figure 4.27. Comparison between numerical and experimental values for (a) average surface temperature and (b) pressure drop along the device.....	131
Figure 4.28. Schematic of the non-uniform configuration applied at (a) 2 microchannels with self-adaptive fins; and (b) 7 microchannels without fins.....	132

Figure 4.29. Non-uniform heating of (a) Self-adaptive fins: $q'=3,07$ W and (b) Plain microchannels: $q'=10,75$ W.....	134
Figure 4.30. Comparison of the temperature evolution along one microchannel in both assessed devices for different flow rates.....	134
Figure 4.31. Temperature evolution along the microchannel for different positions of "Line 1": (a) Outside the self-adaptive fins, (b) Above the anchors and (c) Above the self-adaptive fins.....	136
Figure 5.1. (a) 3D view of half empty microfluidic cell with the outlet microvalve. (b) Top view, (c) front view and (d) side view of half microfluidic cell.....	142
Figure 5.2. 3D view (a) and lateral view (b) of half microfluidic cell with fins inside.....	144
Figure 5.3. Grid independence test performed on a) the average chip temperature of the microfluidic cell and b) the pressure drop within the cell.....	147
Figure 5.4. Nusselt number and Fanning friction factor of the microfluidic cell with self-adaptive fins.....	148
Figure 5.5. Heat transfer enhancement and pressure drop increment in a microfluidic cell with fins inside compared with a plain cell for different Reynolds.....	149
Figure 5.6. (a) Configuration based in 4 pairs of fins. (b) Configuration based in long transversal fins inside the microfluidic cell.....	150
Figure 5.7. Heat transfer enhancement inside a microfluidic cell performed by both configurations of fins.....	151
Figure 5.8. Apparent friction factor for both configurations within a microfluidic cell.....	152
Figure 5.9. Schematic vision of half microfluidic cell with (a) fins placed at the hot wall of the cell, and (b) fins placed at the cold wall of the cell.....	153
Figure 5.10. Heat transfer enhancement within a microfluidic cell when the fins are placed in its hot or cold wall.....	154
Figure 5.11. Outlet microvalve placed in the microfluidic cell.....	155
Figure 5.12. Schematic of the microfluidic cell where the effect of the microvalve is assessed.....	155
Figure 5.13. Pressure drop at the cell with and without outlet valve and pressure drop at the valve with its regression line represented.....	156
Figure 5.14. Pressure drop within a microfluidic cell of different channel height with and without outlet microvalve and pressure drop induced by the microvalve in each case.....	158
Figure 5.15. Thermal resistance of the microfluidic cell with and without outlet valve assessed for two different channel heights.....	158
Figure 5.16. Heat load scenario defined.....	159

Figure 5.17. Pressure drop assessed within the microfluidic cell for the different configurations for the given heat load scenario.	160
Figure 5.18. Average pumping power required for the fix system and the system with self-adaptive fins.	161
Figure 5.19. Chip temperature along the cell length for an empty cell and a cell with fins (Re = 200).	162
Figure 5.20. Temperature gradient at the base of the cell for different Re.	162
Figure A.1. (a) General overview of Mask B (low CTE material mask). (b) Detail of Model 3 designed for the photomask. Each color corresponds to one mask. (c) Detail of Model 4 designed to print at the photomask.	196
Figure A.2. Microscopic image of the bimetallic Ag-Nb fins (Model 3) after the double lift-off (before releasing).	197
Figure A.3. Microscopic image of the Ni-Nb bimetallic fins (Model 3) after the double lift-off (before releasing).	198
Figure A.4. Microscopic image of the Ni-Cr fabricated bimetallic fins (Model 4) after the double lift-off (before releasing).	199
Figure A.5. (a) Microscopic image of the Ag-Mo fins (Model 4) fabricated after the double lift-off, before releasing. (b) SEM image of the same bimetallic fins after releasing.	200
Figure A.6. (a) Microscopic image of the Au-Cr fins (Model 3) before releasing. (b) SEM image of the Au-Cr bimetallic fins (Model 2) after the releasing process.	202
Figure A.7. Microscopic image of the Ti-Cr fins (Model 4) before releasing.	203

List of tables

Table 3.1. Properties of the tested SMA wing fabricated with two different samples of Nitinol.	56
Table 3.2. Verification of the necessary conditions for sample 2. $T_4 = T(x=14\text{mm})$	58
Table 3.3. Main geometric dimensions of the microchannel and the fins.	62
Table 3.4. Thin film Ag and Cr mechanical properties [102].	69
Table 3.5. Different structures proposed for the bimetallic self-adaptive fins. The low CTE material is represented in blue while yellow represents the high CTE material. The anchors that fix the fins to its restraint are remarked in black.	74
Table 3.6. Material combinations tried within the microfabrication of the bimetallic fins.....	84
Table 3.7. Geometric dimensions and material values of the doubly clamped fin.	95
Table 3.8. Critical load and temperature for both studied lengths of the fin.	96
Table 3.9. Vertical displacement of the central part of doubly clamped fins (as % of its length).	97
Table 4.1. Geometrical parameters of the microfluidic cell.....	104
Table 4.2. Computed relative error on the CFD results between solid valve and fine valve simulation.....	105
Table 4.3. Description of the different configurations of self-adaptive fins inside a microchannel.	110
Table 4.4. T-test evaluation of the results.	126
Table 4.5. T-test evaluation of the results.	131
Table 4.6. Proportional flow rate and heat flux applies to both assessed devices.....	133
Table 4.7. Assessment of the results for heat transfer enhancement and power efficiency of both devices for two different flow rates.....	135
Table 5.1. Main dimensions of the microfluidic cell.	143
Table 5.2. Relative error on the CFD simulation results between solid valve and fine valve simulation.....	146
Table 5.3. Dimensions of the microfluidic valve placed at the outlet of the cell.....	155
Table 5.4. Relative error on the numerical calculation of pressure drop compared with the values obtained from simulations.	157

Nomenclature

A	Surface (m^2)
C	Right Cauchy-Green deformation tensor (-)
COP	Coefficient of performance (-)
C_p	Specific heat ($J/kg \cdot K$)
df	Degrees of freedom (-)
D_h	Hydraulic diameter (m)
e	Eccentricity (m)
E	Young Modulus (Pa)
Er	Error
f	Apparent friction factor (-)
F	Force (N)
FS	Full-scale (-)
Fv	Volume force per unit deformed volume vector (N)
G	Deformation gradient tensor (-)
h	Local heat transfer coefficient ($W/m^2 \cdot K$)
H	Height (m)
I	Modulus of inertia ($kg \cdot m^2$)
I	Identity tensor (-)
J	Invariant of the deviatoric stress tensor ($Kg^2/m^2 \cdot s^4$)
L	Length (m)
M	Moment of force (N/m)
n	Unitary vector (-)

XXVIII

Nu	Nusselt number (-)
p	Perimeter (m)
P	Power (W)
ΔP	Pressure drop (Pa)
P_{chip}	Total power dissipated by the chip or heaters (W)
P_{cr}	Critical axial force of a doubly clamped beam without eccentricity (N)
P_{pump}	Pumping power (W)
q''	Heat flux (W/m^2)
Q	Flow rate (m^3/s)
R_{th}	Thermal resistance ($\text{m}^2\cdot\text{K}/\text{W}$)
Re	Reynolds number (-)
S	Second Piola-Kirchoff stress (N/m^2)
t	Thickness (m)
T	Temperature (K)
ΔT	Temperature difference (K)
T_{cr}	Critical temperature of a doubly clamped beam without eccentricity (K)
TPF	Thermal performance factor (-)
\mathbf{u}	Velocity vector (m/s)
v	Velocity (m/s)
W	Width (m)
z	Vertical displacement (m)

Greek symbols

α	Secant coefficient of thermal displacement (K^{-1})
----------	--

$\Delta\alpha$	Difference in thermal expansion coefficient between two materials (K^{-1})
β	Angle of attack of the fins ($^{\circ}$)
γ	Heat transfer enhancement (-)
δ	Non-dimensional maximum central deflection (-)
ε	Relation between thickness and eccentricity of a beam (-)
ϵ	Green-Lagrange strain tensor (-)
η	Efficiency (-)
Θ	Inclination angle respect a flat position ($^{\circ}$)
θ	Non-dimensional temperature rise (-)
κ	Thermal conductivity ($W/m\cdot K$)
μ	Dynamic viscosity ($Pa\cdot s$)
ν	Poisson ratio (-)
ξ	Pressure drop increment (-)
ρ	Density (kg/m^3)
σ	Stress (Pa)
$\sigma_1, \sigma_2, \sigma_3$	Principal stresses of the Cauchy tensor (Pa)
φ	Power efficiency (-)
Φ	Recovery rate (-)

Subscript

A	Austenitic phase
Af	Austenitic phase finish point
As	Austenitic phase starting point
Ag	Silver

XXX

ad	Additional
av	Average
base	Solid region between the chip (heat flux) and the fluidic channel
bg	Background
cell	Microfluidic cell
ch	Channel
chip	Base of the microchannel or microfluidic cell
const	Constrained
el	Elastic
entr	Entrance
f	Fluid
fin	Fin inside the microchannel or microfluidic cell
hp	Hotspot
in	Inlet
inel	Inelastic
init	Initial
M	Martensitic phase
Mf	Martensitic phase finish point
Ms	Martensitic phase starting point
max	Maximum
min	Minimum
out	Outlet
rev	Reverse chamber
s	Solid

Si	Silicon
TIM	Thermal Interface Material
valve	Outlet valve of the microfluidic cell
VM	Von Mises
w	Wing
y	Yield

INTRODUCTION

1. INTRODUCTION

1.1. The importance of cooling in microelectronics

In 1965, Gordon E. Moore expressed that the number of transistors in a dense integrated circuit doubles every year and projected this rate of growth to continue at least another decade. In 1975 he revised his own work, as the integration pace slowed, and predicted that the integration capacity would not be duplicated every 12 months but approximately every 24 months, looking forward to the next decade. This observation was named Moore's law, and the continue increasing in circuit density has largely kept pace with it during the past few decades [1]. Concurrently, in 1974, Robert H. Dennard coauthored a paper where they presented a scaling law, known as Dennard scaling (or also MOSFET scaling) [2]. This law states that the power density of transistors remains constant as they get smaller, so both voltage and current scale downward proportionally with area. However, since around 2005-2007, Dennard scaling seems to have broken down because, while the number of transistors per circuit is still growing nowadays, its performance improvements are much slower [3], [4].

During the last decades, the continuous increasing power density of integrated circuits (IC) coupled with advanced fabrication and packaging technologies in micro- and nanoelectronic systems improved significantly the performance of the chips. Nevertheless, the inability to follow the Dennard scaling law resulted in an exponential increase on heat dissipation, settling thermal management as one of the major concerns for the information and communication technologies (ICT) community [5].

Nowadays, one of the biggest thermal management challenges is found in data centers. The increasing demand for data processing, networking and data storage systems, coupled with the performance improvement on electronics, resulted in a huge growth rate of the data center industry, which became a worldwide energetic problem. Many data centers include servers with power densities higher than 100 W/cm^2 and even up to as high as 200 W/cm^2 , meaning that a rack with $0,65 \text{ m}^2$ footprint can dissipate up to 30 kW, 30 times higher than the power dissipated by a same-size rack in 1980 [6]. Statistics from 2012 showed that the datacenter industry was responsible for 1,30 % of the worldwide electricity consumption [7]. An important part of this consumption, up to 40 % in average, can be attributed to the thermal management, as they are

commonly cooled by global air conditioning systems [8] (Figure 1.1). For this reason, energy efficient liquid cooling of microelectronics can significantly reduce the energy bill [9], [10].

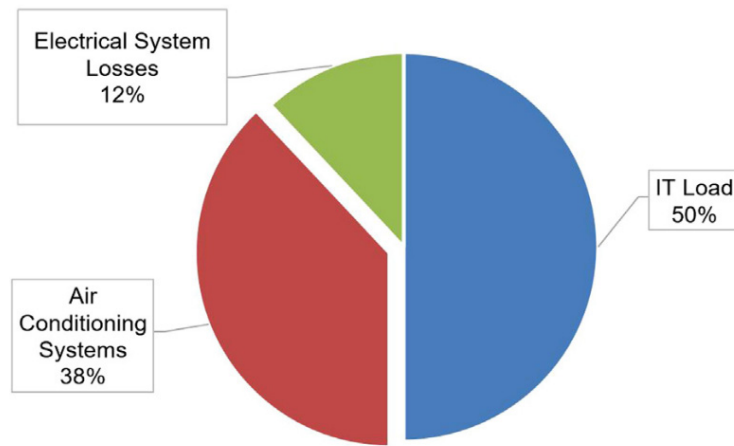


Figure 1.1. Breakdown of energy usage by systems for 94 data centers [11].

1.2. Current thresholds in microelectronics cooling

Continuous air-cooling solutions such as passive approaches by natural convection or active cooling with fans or heat sinks have been widely used on thermal management until last years. However, the continuous miniaturization of power electronics and the ever-increasing power density of chips are pushing this technology to the limit of heat extraction, making it virtually obsolete. Alternatives like single-phase and two-phase liquid cooling are becoming of great interest at this moment [12].

In 1981, Tuckerman and Pease [13] demonstrated for the first time the feasibility of liquid cooling through microchannels for electronic chips, as the heat transfer coefficient scales inversely with the characteristic channel dimension for a fully developed laminar flow. They stated a maximum power density dissipation of 790 W/cm^2 with a thermal resistance of $0,10 \text{ }^\circ\text{C}\cdot\text{cm}^2/\text{W}$, but with a pressure drop of 200 kPa. Since then, liquid cooling solutions for chips have been extensively studied to improve the performance of microchannels, including investigations on traditional microchannel heat sinks [14], manifold microchannel heat sinks

[15], [16] and spray and jet cooling [17]. Most of the research on liquid cooling has been focused on the goal of keeping the junction temperature at or below the maximum allowable limit (commonly around 85 °C) under uniform heat load conditions. However, large temperature gradients at the package level, inherent to microchannels technology, increase thermal stresses in the heat sink interface, reduce the electronic reliability in high temperature regions and create circuit imbalances in CMOS devices [18]. Additionally, large pressure drops within the microchannels are another important drawback to overcome.

Due to power and memory limitations of single-core processors [19], the IC industry is increasing its interest to multicore processors, where each core contains the main executing units, inducing them to dissipate multiple times the heat flux dissipated on the rest of the chip [20]. This fact results on the appearance of hotspot regions and highly non-uniform power map distributions [21], [22]. In a similar way, three dimensional integrated circuits (3D-IC) are being persuaded by researchers and chip manufacturers in an effort to increase processor speeds. 3D-IC architectures incorporate multiple device layer that are interconnected through vertical interconnectors to extend the performance of a 2D chip (Figure 1.2). In 3D-IC chips the thermal management becomes highly important as the heat generating layers are aligned in adjacent films creating localized hotspots, and any dissimilarity between power maps of individual chips constituting the stack would add another geometrical dimension to the thermal non-uniformity [23], [24].

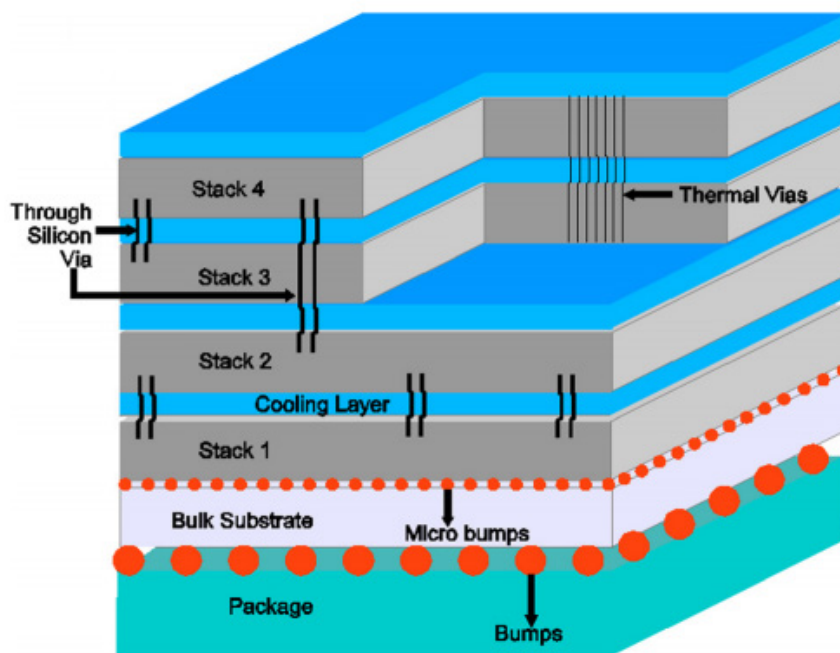


Figure 1.2. A schematic representation of a 3D-IC chip cooled with a coolant layer [24].

In high performance chips like the ones described above, the goal of isothermal junction temperature becomes more challenging, due to the presence of hotspot and background regions. Dang et al. [25] and Kandlikar et al. [26] noted that thermal resistance can be reduced by circulating the coolant through embedded or direct chip backside microchannel cooling. Attempts using single phase liquid cooling have also been reported with different degree of success [27]–[30].

Furthermore, high flow rates are needed to cool down hotspot regions with high power densities, implying large pressure drops and high pumping power. However, as hotspots are usually localized, high constant flows through all the cooling device turn on overcooled systems. For an efficient and optimum thermal management approach, the coolant should therefore be targeted to the hotspot zones to achieve an isothermal condition while minimizing the overall flow rate and pressure drop to reduce the pumping power of the system. Some works focused on this topic, for example, Barrau et al. [31] and Riera et al. [32] presented an hybrid jet impingement/microchannel cooling scheme with variable microchannel width along the coolant flow path, and demonstrated their capacity to provide low thermal resistances, good temperature uniformities and lower pressure drops than conventional microchannels for specific heat flux distributions. Also, Vilarrubí et al. [33] demonstrated numerically and experimentally the potential of variable pin-fin density heat sinks as an effective alternative to microchannel heat sinks for the dissipation of high heat fluxes from small areas. Low thermal resistance coefficient and reduced surface temperature non-uniformities were achieved while presenting low pressure drops. Besides, Sharma et al [21], [22] showed a novel, hotspot-targeted and highly efficient cooling system by optimizing the microchannel geometry and flow rate distribution through passively throttling the flow in regions of low heat flux in order to direct more flow towards the regions of high heat flux. Also, localized microchannels were presented by Collin et al. [34] to cool down high local heat fluxes of 1185 W/cm^2 with a pressure drop below 20 kPa. The main drawback of the previously listed systems is that they do not tailor their behavior to time dependent heat load scenarios, so they are only feasible for specific heat flux distributions previously defined. Consequently, their constant flow rate distributions are too conservatives and lead to oversized pumping powers for varying operation conditions.

Another research topic to increase the performance of microchannel technology is focused on further enhancing locally the cooling capacity of the microchannels. Indeed, several works focused on disturbing the thermal boundary layer through flow disruption techniques, such as reentrant cavities, porous medium, ribs and grooves structures, fins or rough surfaces [35]. The

main drawback of these systems is the increase on pressure drop due to the addition of elements within the channel and so, the increment of pumping power in a permanent way.

Within the actual solutions to improve the performance of the microelectronics cooling devices, it is observed that any proposal is focused on developing a system able to adapt to changing boundary conditions in time and space in an efficient way. Thus, turns into heat transfer enhancements on the cooling system even when not needed, for example when the heat loads are low. Consequently, additional pressure drops are induced in the fluid channel, what causes oversized pumping powers for changing conditions. Moreover, the chip temperature uniformity is usually optimized for a given heat load scenario, without considering time dependent distributions. By the self-adaptation concept, this thesis assesses how to overcome these issues: the disturbing elements inside the flow will be able to adapt its shape, in function of its own temperature, to time dependent and non-uniform heat load scenarios. In this case, for high cooling demands of the device, the self-adaptive elements will act as flow disturbing elements to enhance the heat transfer between the chip and the fluid; otherwise, the self-adaptive fins will remain in a flat position, to reduce the pressure drop inside the cooling device.

1.3. Background (STREAMS H2020 Project)

The current thesis is integrated within the Horizon 2020 Project STREAMS (Smart Technologies for eneRgy Efficient Active cooling in advanced Microelectronic Systems). The consortium of the project includes one major European industrial in electronics field (STMicroelectronics), three research and technology organizations (Commissariat à l'Énergie Atomique et aux Énergies Alternatives - CEA, Centre National de la Recherche Scientifique - CNRS-LN2 and Hahn-Schickard-Gesellschaft - HSG) and two universities (University of Lleida – UdL and Albert-Ludwig University of Freiburg – UFR-IMTEK).

The main goal of the project is to develop a generic, smart, adaptable and embedded active cooling thermal management solution, to keep nano-electronic devices and systems performances at their best. Starting from low technological readiness level (TRL) [36], STREAMS will endeavor to reach TRL4 (technology validated in laboratory) on the co-integration of three advanced functionalities to be developed in a Si-based interposer (Figure 1.3):

1. Introduction

1. **Versatile microfluidic actuation**, in which this thesis is focused, to manage liquid cooling of varying thermal scenarios in an energy efficient way.
2. **Anticipation of the thermal map**, to enable the real-time spatial control of the thermal state of dies in complex packages.
3. **Thermal energy harvesting**, to provide sufficient energy to power the developed active cooling thermal management solutions.

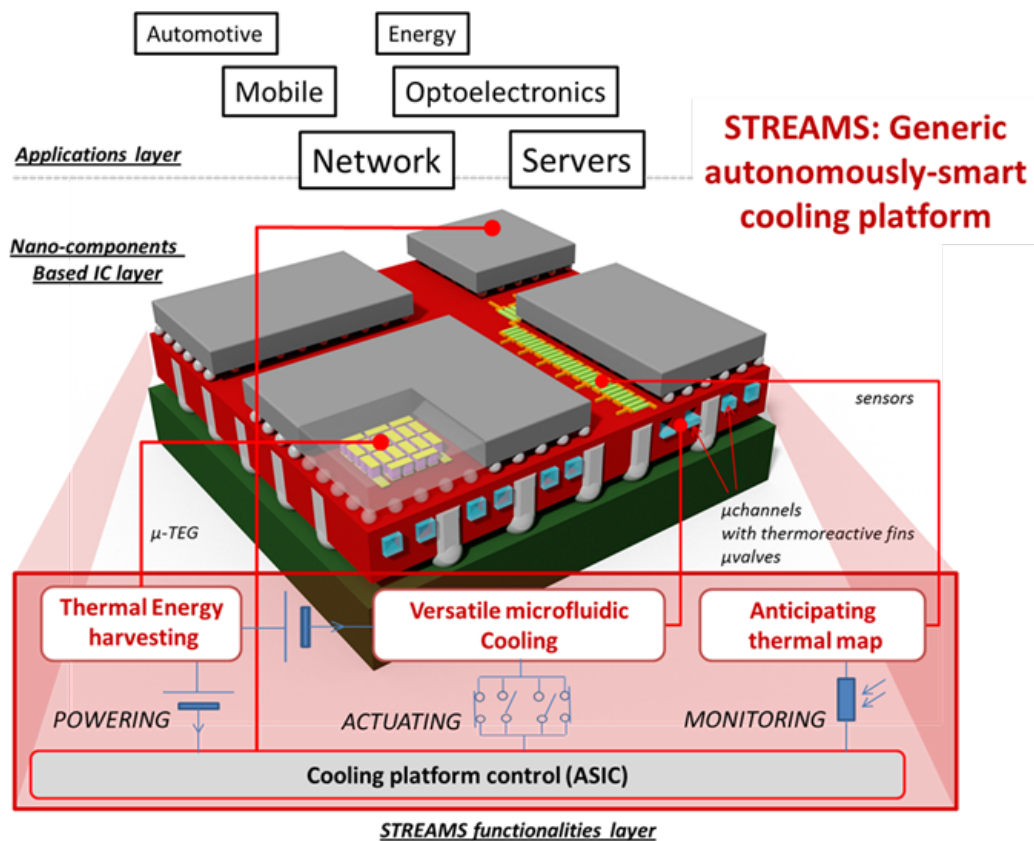


Figure 1.3. STREAMS cooling platform (Source: www.project-streams.eu).

Some specific objectives have been defined to successfully integrate these functionalities in a system in package.

- **Objective 1.** Lay-out advanced functionalities for the power efficient cooling control of application use-cases with critical heat load spatial distributions, including hotspot areas (150 to 300 W/cm^2) and background areas (20 W/cm^2), and temporal heat load variations in typical sub-second time microelectronic scale.

- **Objective 2.** Develop self-adaptive and controlled micro-fluidic actuators to decrease by 25 % both the pressure drop and the fluid flow rate, while controlling the temperature distribution within 15 % below the acceptable limits of each component for spatial and temporal heat flux variation scenarios.
- **Objective 3.** Integrate IC compatible passive heat flux sensors, with sensitivity up to $S = 100 \text{ mV/K}$, at the interposer level to anticipate the thermal map variation.
- **Objective 4.** Take advantage of existing thermal gradients to embed high performance nanostructured thermoelectric generators (with harvested power up to 10 mW) to power local functionalities.
- **Objective 5.** Integrate the developed functionalities into a Si-based interposer to demonstrate a smart, adaptable and embedded active cooling thermal management solution with reduced footprint (70 % of thickness reduction) and reduced consumption (50 % reduction).
- **Objective 6.** Assess the reliability and performance of STREAMS thermal management solution in real future high performance applications in micro-servers ($P = 50 \text{ W}$) and network use cases ($P = 200 \text{ W}$).

The performance of the thermal management solution is determined by three main physical indicators (Figure 1.4).

- **Cooling efficiency.** The existing liquid cooling solutions are able to prevent from temperature overshoots, as they increase up to three orders of magnitude the heat transfer coefficient compared to air cooling solutions. Nevertheless, they are not able to avoid overcooling, which implies additional power consumption from the cooling systems. STREAMS targets similar cooling efficiency with adaptable configurations to widely varying spatial and temporal heat load scenarios.
- **Compactness.** By developing an embedded liquid cooling solution within the package, STREAMS intends to strongly reduce the footprint of active cooling in terms of package thickness (70 % reduction) compared to the state-of-the-art.
- **Consumption.** By a smart control and appropriate activation of the cooling system in due time and only when necessary, STREAMS will strongly reduce the energy

consumption associated with water cooling thermal management solutions (50 % reduction).

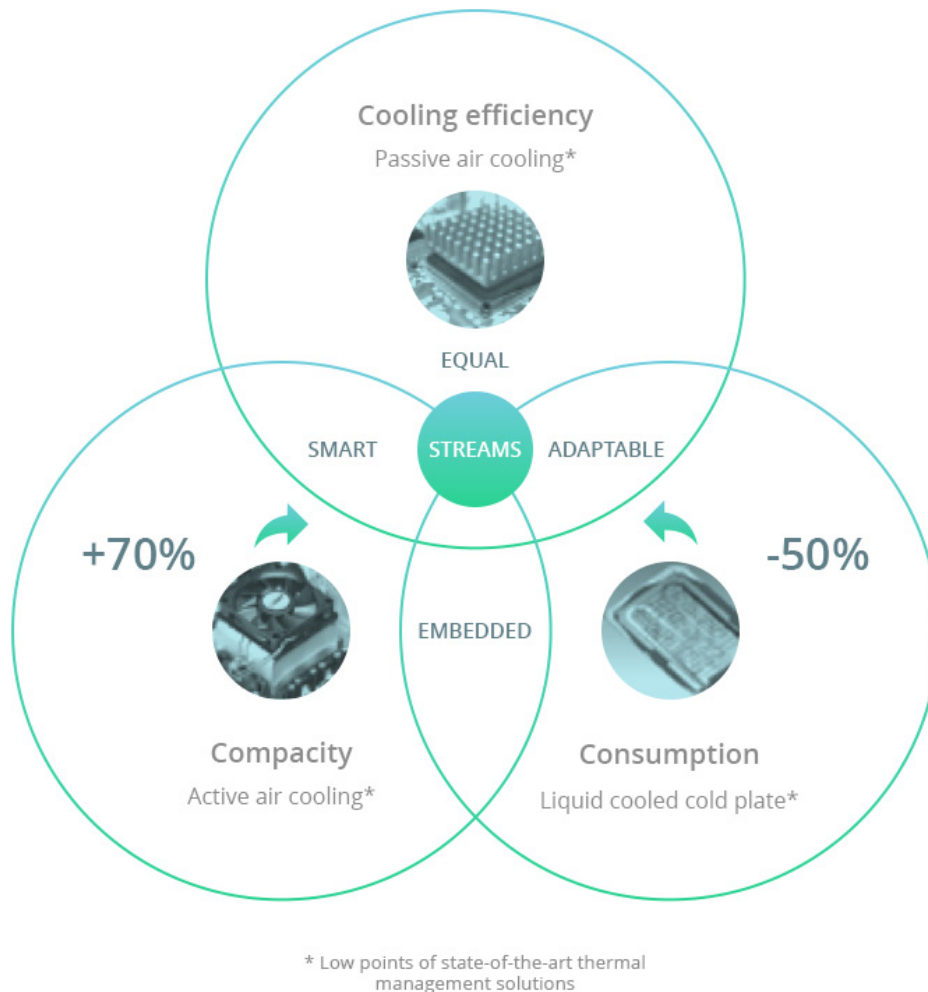


Figure 1.4. STREAMS strategy and positioning versus actual state-of-the-art cooling technologies low points.

1.3.1. Functionality 1: Versatile microfluidic actuation

STREAMS project is looking forward to improving the energy efficiency of microchannel cooling technology by reducing the pressure losses in 25 % while keeping the operating temperature and its uniformity within the appropriate ranges (Objective 2).

The first proposed action to reach this objective, in which this thesis is focused, is the addition of self-adaptive fins within the microchannels to enhance the heat transfer performance acting as vortex generators. These structures are able to tailor their geometry in function of their own

temperature, what leads to reach the main requirements listed above under different steady state and time dependent heat flux distributions. The pressure drop, and therefore the pumping power, will be self-optimized for each heat flux distribution.

Nevertheless, a foreseen risk is the long-term reliability of the self-adaptive fins. For this reason, a more conservative solution has been proposed. This is based on the implementation of a matrix of microfluidic cells (Figure 1.5), explained in detail below, instead of conventional microchannels, which will permit to adjust both the flow distribution and the heat extraction capacity to values that fit the cooling requirements throughout the microelectronics package and, therefore, provide good temperature uniformity with low pumping power. Additionally, to further reduce the pumping power, the flow would be directed only to the warmest zones by the use of self-adaptive microfluidic valves, which will tailor the flow to the various zones of the microelectronic assembly.

Compared to conventional microchannel cooling systems, the microfluidic cell array combined with the thermoregulated valves will provide the following advantages:

- Local control: The valve opening, that depends on its own temperature, will allow to tailor the mass flow rate of each microfluidic cell to the local cooling needs. As a consequence, the overall cooling will be managed easily with low pumping power cost.
- Low pressure drop. As the length of each cell is going to be shorter than the length of the microchannel, even if high flow rates are required, the corresponding pressure drop will be lower than in a microchannel.
- Versatile microfluidic actuation. In microchannels or other cooling schemes, the designs are usually optimized for a given heat load scenario or adapted to the worst scenario. In this case, the self-adaptive local coolant flow rate will provide versatility in order to adapt its behavior to varying spatial and temporal heat load scenarios.

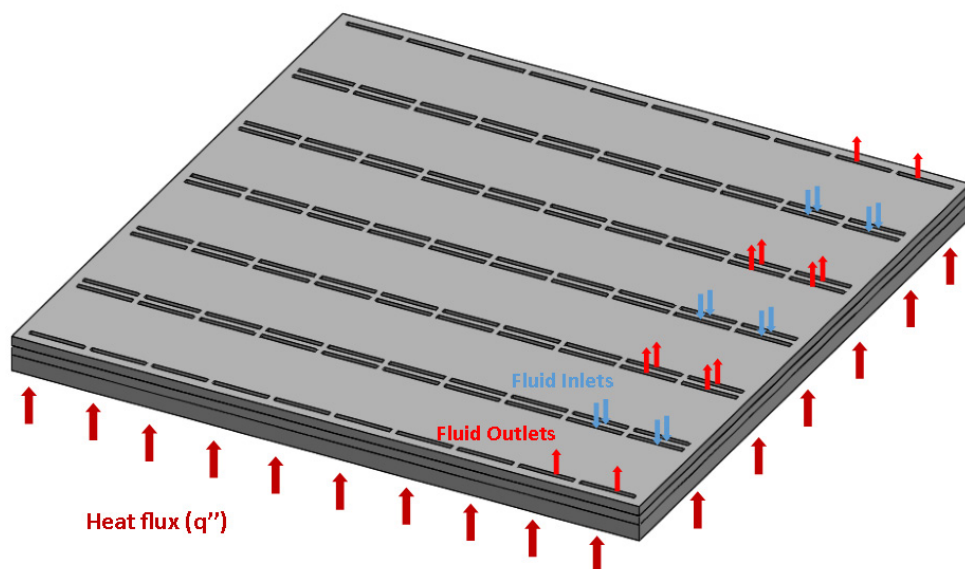
1.3.1.1. Matrix of microfluidic cells

As a conservative solution to the project, to bypass the possible long term reliability problems of the self-adaptive fins, an array of microfluidic cells was presented, each one responsible for removing the local heat flux (Figure 1.5a) [37]. The main goal of this new configuration is to

overcome the main drawbacks of conventional microchannel cooling technology, such as poor temperature uniformity at the chip surface and large pressure drops due to its flow path length, which become more significant under non-uniform and time dependent power map distributions.

In the STREAMS Project, the microfluidic cell array is formed by a matrix of 6 x 10 microfluidic cells (Figure 1.5), with an external size of 2,00 x 2,00 cm². The dimensions of the cell matrix have been adjusted to the requirements of the STREAMS test vehicle, designed by the industrial partner of the STREAMS Project.

The STREAMS test vehicle, used in the project instead of a commercial dice, is designed to allow thermal studies with a strategy of versatile heaters to mimic hotspots in real dice, and a plurality of sensors to perform thermal mapping. The test vehicle is based on four thermal dice placed on the interposed with the additional ASIC (Figure 1.6b). Its dimensions are 2,00 x 2,00 cm² and the configuration is considered to mimic a micro-server application. Each thermal dice is heated with a typical power of 2 to 10 W, representing a maximal total power on the test vehicle of 40 W. The power is distributed on each dice with one peripheral heater ($q''_{\text{max}} = 60 \text{ W/cm}^2$), one central heater ($q''_{\text{max}} = 80 \text{ W/cm}^2$) and two hotspot heaters ($q''_{\text{max}} = 300 \text{ W/cm}^2$) (Figure 1.6a).



(a)

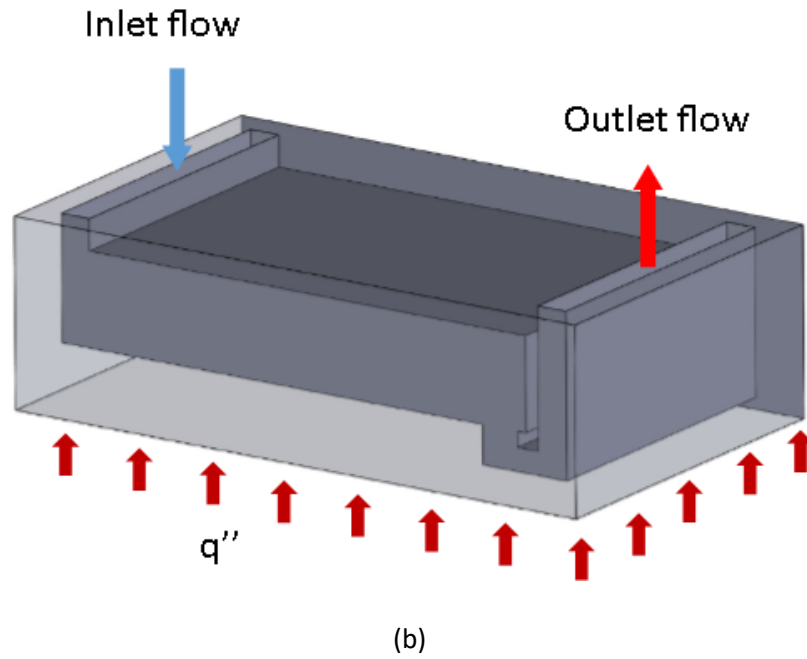


Figure 1.5. (a) Matrix of microfluidic cells. (b) Schematic of one single microfluidic cell.

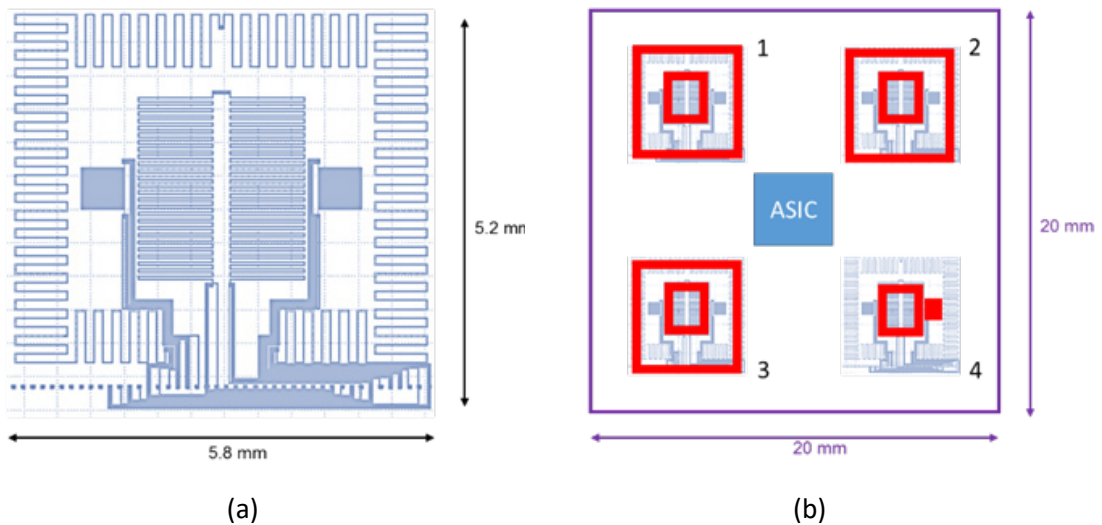


Figure 1.6. a) Thermal dice of the STREAMS test vehicle. b) STREAMS test vehicle composed of four thermal dice and the ASIC.

The coolant flow is distributed to the cells by a microfluidic distributor that has two main channels, one for the inlet and one for the outlet. The main channels are branched into smaller ones that distribute the flow to each microfluidic cell (Figure 1.7). The heat is removed by the

1. Introduction

flow through each cell and, due to its length, the pressure drop is minimized compared to traditional microchannels that would span the entire chip.

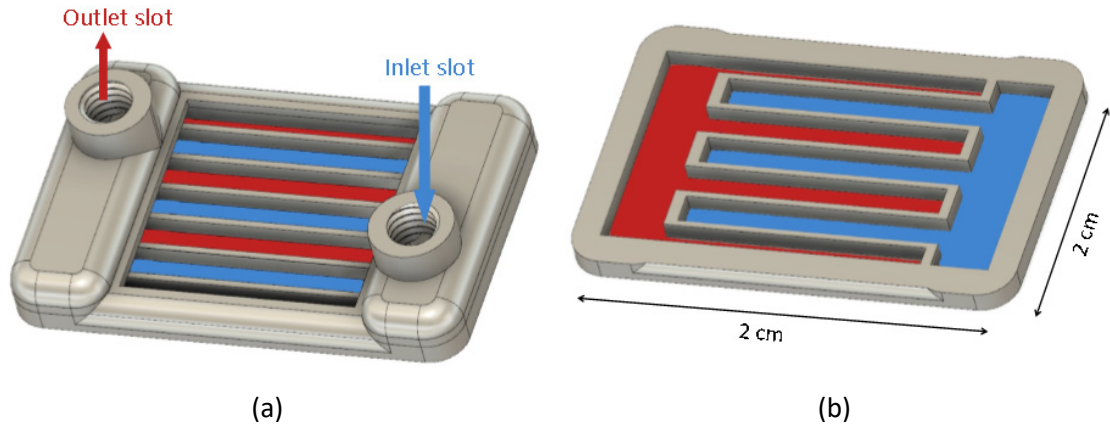


Figure 1.7. Schematic of the coolant flow distributor (a) with the cover that contains the inlet and outlet slots for the flow and (b) without the slots cover.

1.3.1.2. Self-adaptive nonlinear microfluidic valves

Additionally, self-adaptive microfluidic valves will be integrated into the microfluidic cell matrix to locally control the flow rate in each cell (Figure 1.8) as the aperture of the valves is tailored to the local temperature (Figure 1.9). This local control will tailor the flow rate to the momentary heat load distribution and cooling needs of the microelectronic assembly to further reduce the pumping power and avoid overcooling.

The behavior of the self-adaptive microfluidic valves is based on previous investigations done by McCarthy et al. [38], [39], where the mechanism of nonlinear thermal buckling of doubly clamped beams with small eccentricities was studied.

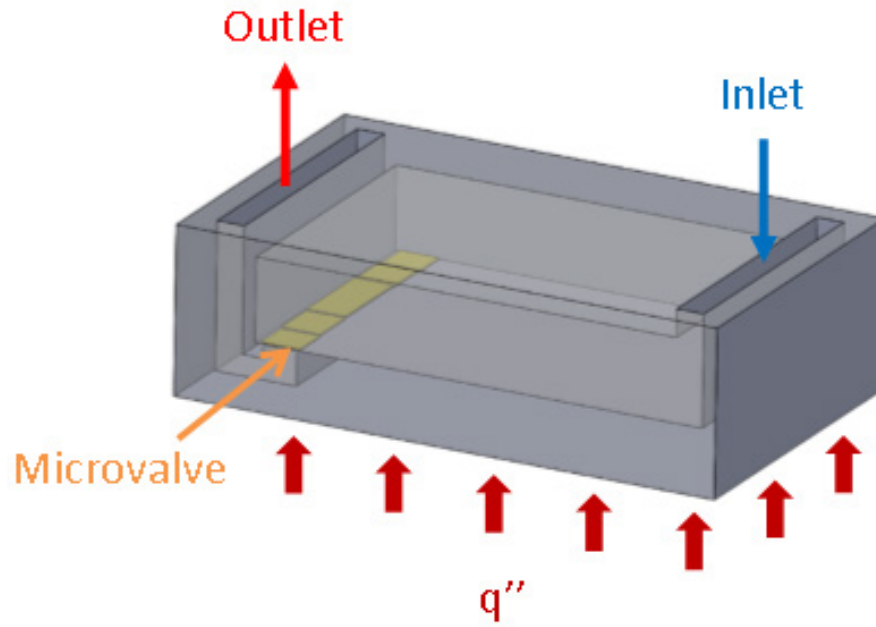


Figure 1.8. Microvalve placement within a single microfluidic cell.

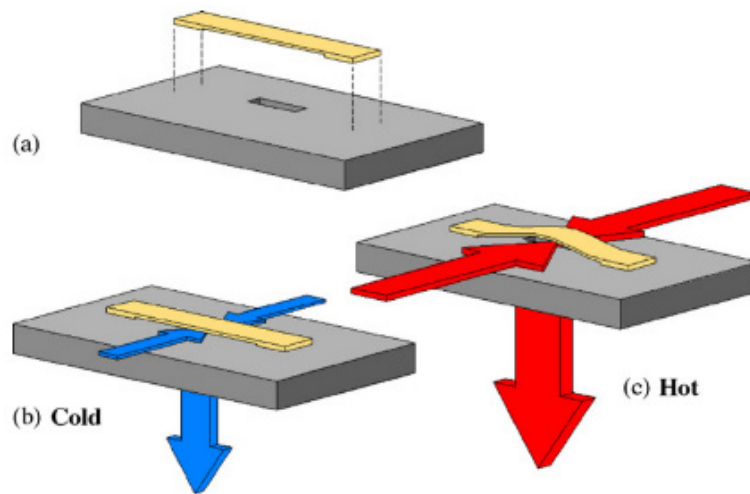


Figure 1.9. Schematic of the self-adaptive concept of nonlinear microvalves. At low temperatures, the beam remains at a low position (b), while at high temperatures, the beam buckles and opens the air gap that allows to pass the flow rate (c) [40].

1. Introduction

1.3.1.3. *Tailored flow rate by external pump control*

Additionally, to further reduce the pumping power in accordance to the heat load scenarios and the varying cooling configurations, a miniaturized-pump module will adapt the pump flow rate to the heat extraction needs [41].

1.3.2. Functionality 2: Anticipation of the thermal map

This functionality is planned to be achieved through the development of planar thermoelectric sensor arrays between dies of the package and its associated read-out electronics to increase the thermal monitoring sensitivity up to 100 mV/K, the time response down to 200 ms, as well as suppress the sensor consumption.

1.3.3. Functionality 3: Thermal energy harvesting

The achievement of this functionality will be based on the integration of nanostructured active thermoelectric layers based on silicide Quantum Dots SuperLattices in SiGe into advanced thermoelectric generator microarchitectures with optimized thermal environment, associated with a high yield step-up converter (functionality based on a thermoelectric energy harvesting patented by CEA/LITEN [42]).

1.4. Objectives of this thesis

The main objective of this thesis, related to the versatile microfluidic actuation (Functionality 1) of the STREAMS project, is to develop and validate an energy efficient active cooling system based on self-adaptive fins placed inside a liquid cooling device. The self-adaptive fins will be used as passive thermal actuators, as they will be activated in function of their own temperature, without external excitation, using the principle of thermal expansion of the materials (Figure

1.10). Within this solution, the system will be able to tailor its internal geometry to time dependent and non-uniform heat flux distributions, optimizing the local heat transfer enhancement and the pressure drop for each heat flux distribution. Also, the chip temperature will be kept within the operating range (less than 85 °C) to avoid electronic reliability issues.

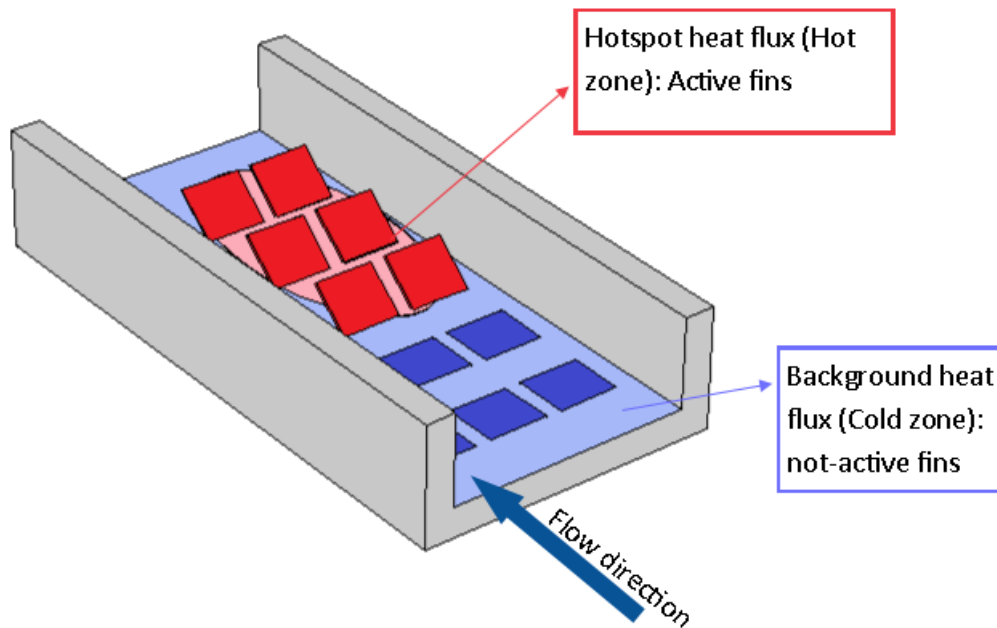


Figure 1.10. Self-adaptive fins working principle.

Some specific objectives have been defined to successfully achieve the above defined goal:

- **Objective 1:** Design, fabrication and validation of the self-adaptive fins to reach the desired behavior of self-adaptation by using the thermal expansion of the materials.
- **Objective 2:** Increase the convective heat transfer of a microchannel or a microfluidic cell cooling device due to the use of the fins, that will rise up for high heat fluxes. The goal is to enhance the heat transfer by more than 10 % compared with a cooling system without flow disturbing elements, what will allow to keep the maximum junction temperature below its limits with less flow rate demand.

- **Objective 3:** Achieve more temperature uniformity at the chip surface when non-uniform heat loads are applied, as the heat transfer will only be enhanced at the highest cooling-demand zones due to self-adaptation of the fins.
- **Objective 4:** Reduce the pumping power by 25 % compared with a system of fixed disturbing elements inside, as the pressure drop will be reduced when the cooling demand decrease because the self-adaptive fins will remain in a flat position.

1.5. Parameters for performance assessment

The selected parameters in this thesis for the evaluation of the thermo-hydraulic performance of the different cooling systems are widely used in the literature. The main parameters to perform this evaluation are: The Nusselt number (Nu), which computes the ratio of convective to conductive heat transfer across a boundary in a fluid. The average apparent friction factor, or Fanning friction factor, which is defined as the ratio between the wall shear stress to the flow kinetic energy per unit volume but also can be expressed in terms of pressure drop and mass flux [43]. In both parameters, the hydraulic diameter of microchannels or microfluidic cells is calculated at the region without flow promoters. Finally, the hydraulic pumping power is considered a key parameter for performance assessment.

Below, the main equations used for the evaluation of the different cooling systems are listed.

1.5.1. Flow characterization

- Reynolds number (-)

$$Re = \frac{\rho_f \cdot v_f \cdot D_h}{\mu_f} \quad (1)$$

- Hydraulic diameter for non-circular cross section (m)

$$D_h = \frac{4 \cdot A}{p} = \frac{2 \cdot W_{ch} \cdot H_{ch}}{W_{ch} + H_{ch}} \quad (2)$$

- Fanning friction factor (-)

$$f = \frac{2 \cdot \Delta P \cdot D_h}{\rho_f \cdot L_{ch} \cdot v_f^2} \quad (3)$$

- Hydraulic pumping power (W)

$$P_{pump} = Q \cdot \Delta P \quad (4)$$

1.5.2. Heat transfer

- Convection heat transfer coefficient (W/m²·K)

$$h = \frac{q''}{T_{chip,av} - T_{in}} \quad (5)$$

- Thermal resistance (m²·K/W)

$$R_{th} = \frac{1}{h} \quad (6)$$

- Nusselt number (-)

$$Nu = \frac{h \cdot D_h}{\kappa} \quad (7)$$

1.5.3. Figures of merit

- Heat transfer enhancement (-)

The heat transfer enhancement due to the improvement of a cooling system is computed as the relation between the Nusselt number of the improved system and the Nusselt number of the same cooling system without the addition of improvements (Nu_0).

$$\gamma = \frac{Nu}{Nu_0} \quad (8)$$

- Pressure drop increment (-)

The pressure drop increment within a cooling system due to the addition of disturbing elements inside the channel flow is computed as the relation between the apparent friction factor of the improved cooling system (f) and the apparent friction factor of the same system without improvements (f_0).

$$\xi = \frac{f}{f_0} \quad (9)$$

- Thermal performance factor (-)

The thermal performance factor computes the relation between heat transfer enhancement and pressure drop increment within an improved cooling system compared with the same system without improvements, for equal pumping power [44]. The evaluation of the TPF can be highly significant for fixed geometries, especially when flow disturbing elements are added within a fluidic channel and its commonly used within the literature [45]–[48]. Nevertheless, in the case of self-adaptive fins, the TPF does not provide a significant result as the pumping power is not constant.

$$TPF = \frac{Nu}{Nu_0} \frac{1}{\left(\frac{f}{f_0}\right)^{\frac{1}{3}}} \quad (10)$$

- Power efficiency (-)

With the aim of achieving the cooling with the minimum energy input in form of pumping power is defined the quotient between the pumping power and the total power dissipated by the chip [21].

$$\varphi = \frac{P_{pump}}{P_{chip}} \quad (11)$$

STATE-OF-THE-ART

2. STATE-OF-THE-ART: CURRENT COOLING METHODS FOR MICROELECTRONICS

In this chapter, a review over the present liquid cooling solutions for microelectronics has been developed. The state-of-the-art of microfluidic cooling for three dimensional integrated circuits (3D-IC) is first evaluated. Also, some works focused on the reduction of temperature non-uniformities at the chip surface when submitted to non-uniform heat load scenarios and different existing heat transfer enhancement techniques within microchannels are presented.

2.1. 3D-IC microfluidic cooling

2.1.1. Introduction to 3D-IC architectures

3D-IC are based on multiple device layers interconnected through vertical connections to extend the performance of two-dimensional circuits (2D). High performance, short global interconnect lengths, high circuit functionality and small footprint of the chip are some of the benefits that 3D architectures offers over 2D chips [49].

Although the advantages, thermal management of 3D-IC becomes more complex as the heat flux increases proportionally to the number of active layers in the stack. For example, if stacking two microprocessors with a power density of 100 W/cm^2 each, the total net power density of the 3D-IC becomes 200 W/cm^2 , beyond the heat removal capacity of today's air cooled solution [50]. Additionally, complex electrical connections among different layers, large temperature gradients, localized hotspots and difficult fluidic connections make the implementation of 3D-IC a significant challenge.

Through-silicon-vias (TSV) technology is one of the technical options available for intra-layer communications, for example between stacked processors and memory chips. Thinner and shorter TSVs results in fast interconnects and low power consumption. However, an agreement between the optimum heat sink size (large microchannels induce less pressure drops) and short

2. State-of-the-art

TSV should be found. Additionally, the impact of the microfluidic heat sink on the performance of electrical TSVs has to be taken into account [51].

2.1.2. State-of-the-art on 3D-IC cooling

Firsts works on 3D-IC cooling focused on conventional air cooling using heat sinks (Figure 2.1), however air is not able to reach the high heat extraction requirements of high performance 3D stacks. Up to now, several works focused on liquid cooling of 3D architectures, due to the higher thermal conductivity and higher specific heat of water compared to air [52]. Some of the recent studies in the literature are reported below.

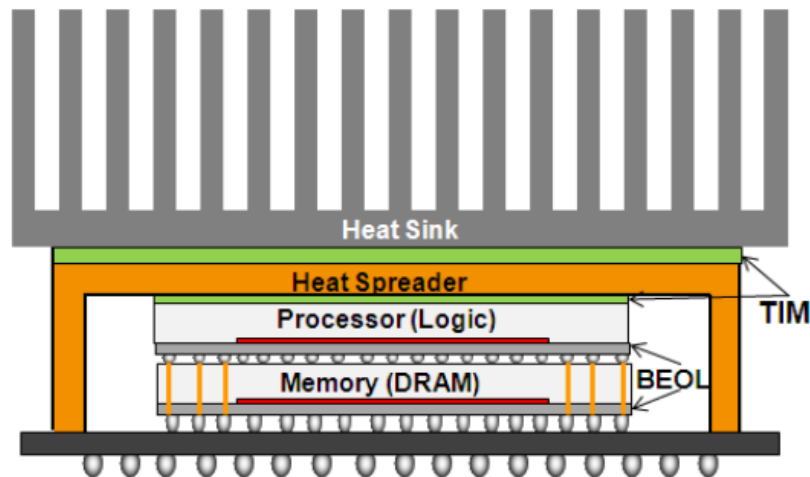


Figure 2.1. 3D thermal management using a conventional air cooling heat sink [52].

Koo et al. [53] presented a 3D circuit cooling architecture based on flow boiling convection within microchannel network (Figure 2.2), where the effect of hotspot locations on chip temperature uniformity and maximum temperature was studied. The higher heat generating devices were placed near the channel outlet to reduce the two-phase pressure drop, and their theoretical calculations predicted a pressure drop of 26,30 kPa and a maximum chip temperature gradient in a device layer of 55 K/cm with a maximum temperature difference of 13 K. These results were compared with a conventional air-cooling heat sink, where the temperature gradient was 300 K/cm with a maximum junction temperature difference of 45 K.

Nevertheless, they pointed out issues on two-phase liquid cooling, such as flow maldistribution and instabilities, according to the previous work presented by Kandlikar [54].

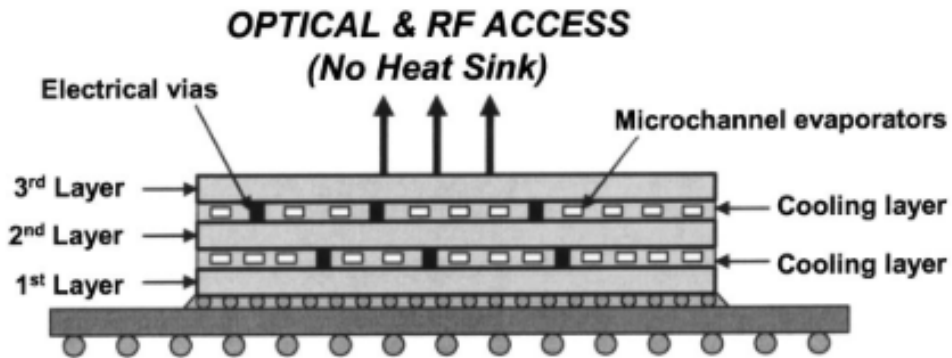


Figure 2.2. Schematic of a 3D circuit with a microchannel cooling system [53].

Sekar et al. [55] addressed the challenging thermal interconnect problem of 3D-IC by developing integrated microchannels within a 3D stack while employing fluidic TSVs to deliver liquid to the microchannels. A significant reduction in chip-to-chip interconnect lengths on microchannel cooled 3D-IC as well as an improvement on the thermal resistance compared with air cooled 2D servers was stated. Measurements for single chip prior to 3D stacking revealed that each die in a two-chip 3D stack may potentially exhibit a junction-to-ambient thermal resistance of 0,40 K/W.

Dang et al. [56] presented a report on fabrication, assembly and testing of an integrated microchannel heat sink and cooper TSVs. The fluid was transferred across the chip to the next microchannel through polymer micropipes. A chip temperature increment of 18,10 K and a thermal resistance of 0,40 K/W were obtained with a flow rate of 65 mL/min. Additionally, a conceptual design with the electrical and fluidic TSV in a 3D architecture (Figure 2.3), which can dissipate over 100 W/cm², was introduced.

Alfieri et al. [57] developed a multiscale conjugate heat transfer model for integrated water cooling of chip layers and validated it experimentally on a four-layer chip stack (Figure 2.4). The cooling structure consisted on microchannels with cylindrical pin fins inside. The total power dissipated in the stack was 390 W at a temperature gradient budget of 60 K, which corresponds

to a volumetric cooling of $1,30 \text{ kW/cm}^3$. This work demonstrated the feasibility of single-phase liquid cooling for 3D-IC cooling demands, although a high-pressure drop was achieved (110 kPa for 10 mm of flow length).

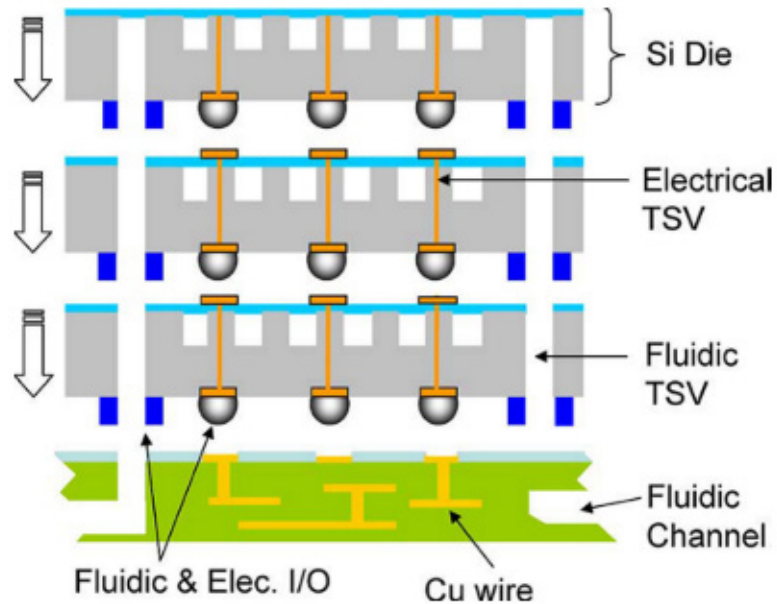


Figure 2.3. Schematic of a 3D-IC stack cooled with microchannels with electrical and fluidic TSV interconnects [24].

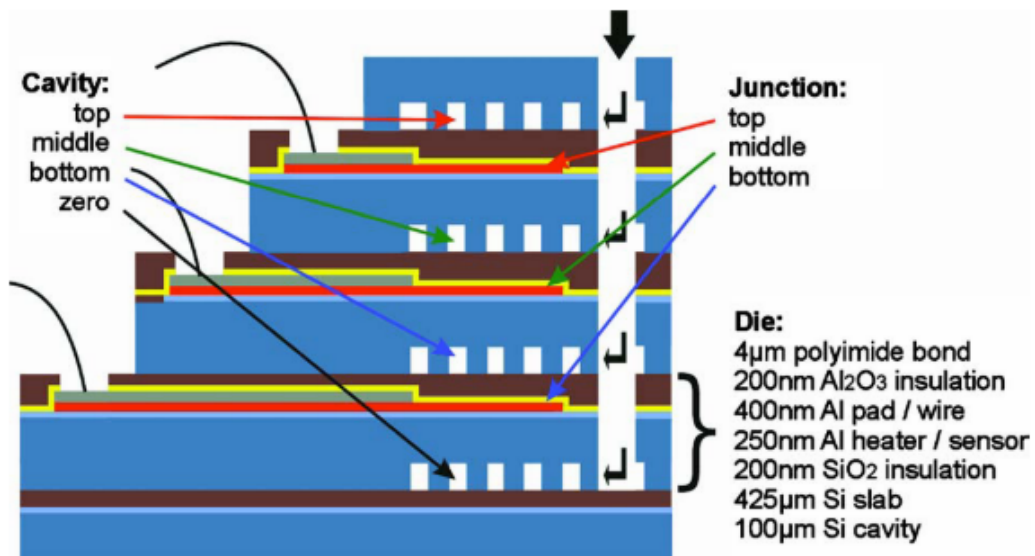


Figure 2.4. Schematic of the four-layer chip stack with microchannel cooling [57].

Zhang et al. [51] studied the performance of pin fins heat sink on 3D-IC while being TSV compatible (Figure 2.5). A comparison between microfluidic and air-cooling systems was also performed, demonstrating that microfluidic cooling provides lower junction temperature with much smaller heat sink volume. Also, the impact of the heat sink geometry on TSV capacitance was analyzed and novel ideas to decrease it were presented.

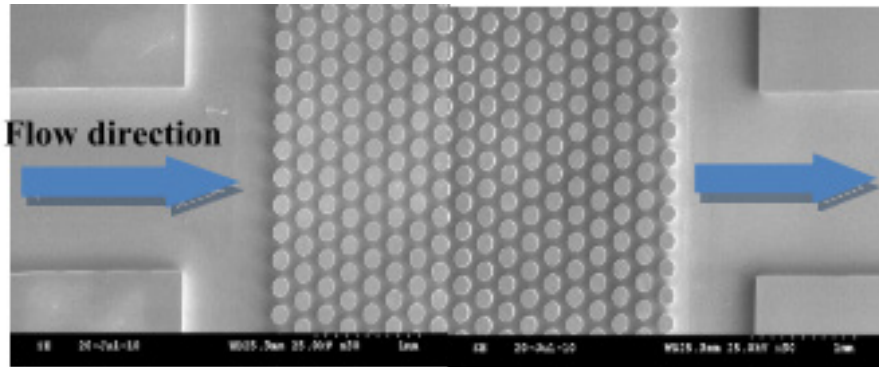


Figure 2.5. Overall view of the pin fin heat sink [51].

Zhang and Bakir [58] analyzed the impact of independent microfluidic cooling of the different layers of 3D-IC within microchannels. They reduced the junction temperature difference between layers of different power dissipation from 12 K to 7 K. Also, the maximum junction temperature was decreased compared to conventional air-cooling technology.

Shi et al. [59] presented a hybrid microchannel/TSV module and studied the power savings by using TSVs to assist on transferring heat to the microchannels. Their experiments showed that the hybrid cooling scheme could provide higher cooling capabilities while consuming 55 % less cooling power compared with single microchannel cooling.

Khan et al. [60] reported an integrated liquid cooling solution for thermal management on a two-layer stack with integrated cooling components (heat exchanger, pump and electrical and fluidic connectivity) (Figure 2.6). A chip carrier with embedded microchannels and fluidic manifolds was developed, reporting an overall heat dissipation of 100 W per chip and a thermal resistance of 0,58 K/W per chip. A junction temperature difference lower than 10 K with a heat

flux of 100 W/cm^2 and a reduced pressure drop thanks to a dual-port fluidic design of the microchannels architecture were achieved.

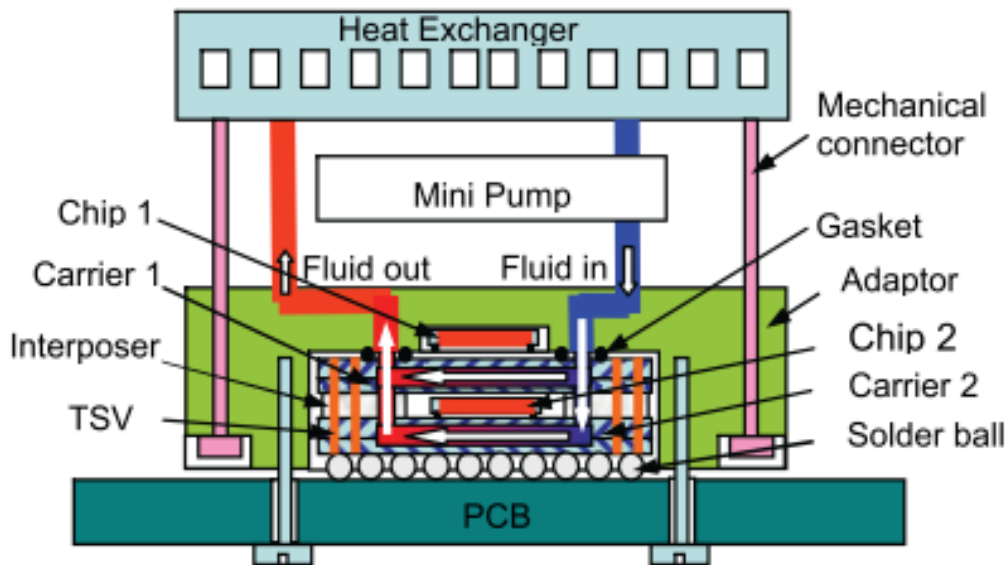


Figure 2.6. Scheme of the integrated liquid cooling system [60].

In the last work presented in this section, Collin et al. [61] numerically assessed the impact of microchannel cooling in a single chip and a 3D-IC based on two stacked chips with localized heat sources. The study reported that increasing the total number of channels was more beneficial than increasing the flow rate. Indeed, when the flow rate was increased, the total thermal resistance was reduced, however its impact reached an asymptote and the value increased. On the other hand, the number of microchannels increased linearly the maximum chip power allowable within the system. Additionally, the importance of the interdie underfill layer on 3D architectures was pointed out, as it increases the total thermal resistance of these configurations. This effect could be alleviated by the addition of copper micropillars which increased the interdie thermal conductivity.

2.2. Non-uniform heat loads and hotspot mitigation

Large temperature non-uniformities on the chip surface have a negative impact on the performance and the reliability of the chip, as explained before. In order to mitigate this issue, several works in the literature focused on the reduction of these temperature gradients. Some examples of these works are presented below.

Hetsroni et al. [62] studied the effect of dielectric flow boiling at low temperature to achieve an isothermal condition at the chip surface. Using flow boiling with dielectric fluid Vertex XF, a maximum temperature difference of 5 K at the chip heated wall was reported, while the temperature difference when using single-phase water as coolant was of 20 K (Figure 2.7).

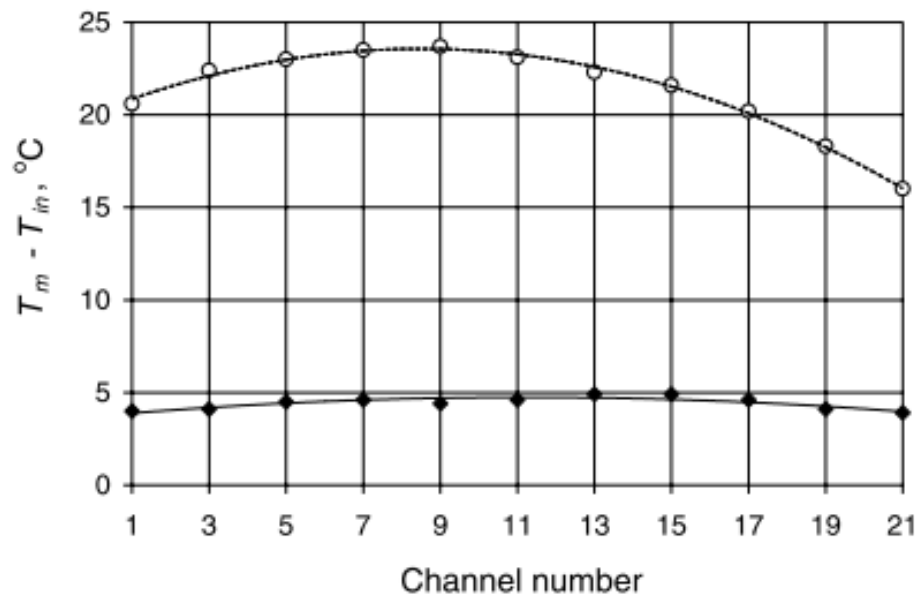


Figure 2.7. Temperature difference between the maximum and the minimum temperatures of the heated wall for a heat flux of 36 kW/m^2 , when using water (\circ) or dielectric fluid (\bullet) [62].

Rubio-Jimenez et al. [63] presented a novel pin fin heat sink with variable fin density in order to decrease the thermal gradient in the IC chip junctions. An overall temperature gradient lower than 2 K/mm was achieved. In a similar way, Xie et al. [64] developed multistage bifurcated plates in a microchannel heat sink and demonstrated its utility to reduce both the thermal

resistance and the junction thermal gradients. Additionally, Lin et al. [65] presented a silicon based double layer microchannel heat sink to optimize the flow and the heat transfer in a water-cooled device. A minimum global thermal resistance of 0,089 K/W was found by simultaneously optimize six design variables: channel number, bottom channel height, vertical rib width, thickness of two horizontal ribs and coolant velocity.

With the same goal of isothermal junction temperature, Barrau et al. [31] and Riera et al. [32] presented a cooling device base on hybrid jet/impingement microchannel able to provide high temperature uniformities with reduced pressure drop. A stepwise varying width microchannel cooling device was studied, where the fluid entered through the slot jet located in the symmetry plane of the heat sink and went along the channels to leave the heat sink at its extremities (Figure 2.8). With the aim of counteracting the temperature increment of the fluid along the flow path, the fluid flowed through a series of microchannels with variable width and, as the fluid heats up, the channel diameter decreases to consequently decrease the convective thermal resistance (Figure 2.9). Also, Riera et al. [66] studied the effect of the thermal interface material (TIM) layer on the performance of the stepwise varying width microchannel cooling device, showing that the TIM layer has a smoothing effect on the temperature distribution generated by these microchannels. Finally, Vilarrubí et al. [33] demonstrated numerically and experimentally the potential of micro pin fin heat sinks as an alternative for microchannel devices when dissipating high heat fluxes from small areas. Their results showed that for a constant heat flux of 500 W/cm², a thermal resistance coefficient of 0,26 cm²K/W and a temperature uniformity along 5 cm of 2 K were achieved.

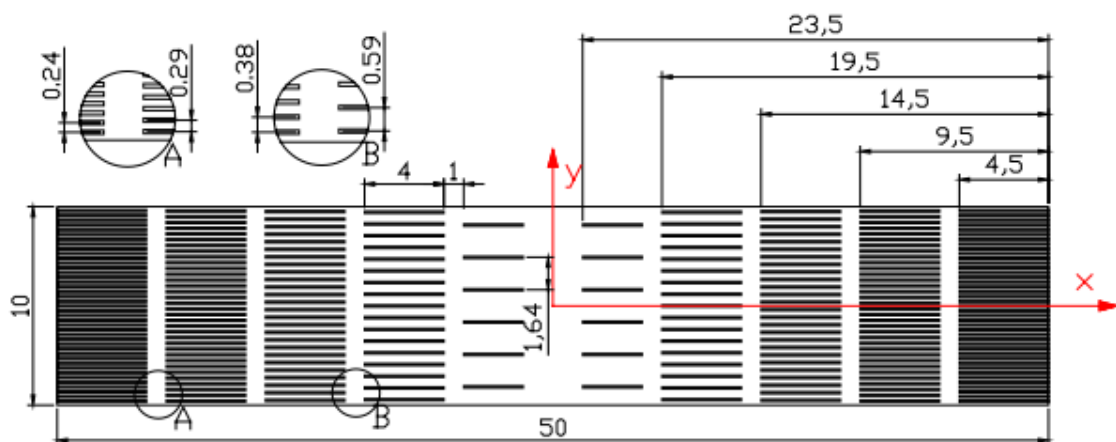


Figure 2.8. Schematic of the stepwise varying width microchannel cooling device [66].

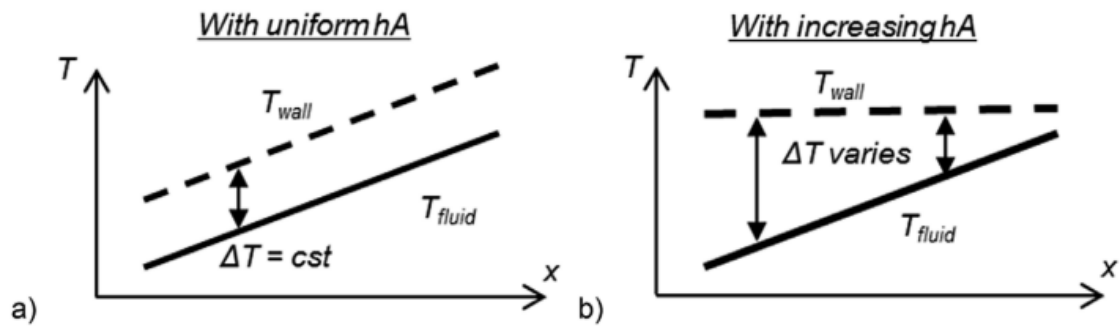


Figure 2.9. Temperature uniformity along the flow path of: a) a conventional cooling scheme; b) a cooling scheme with decreasing thermal resistance along the flow path [66].

All the literature reported above was focused on the cooling of uniform heat fluxes and did not take into consideration non-uniform and time dependent heating of chips, although the increasing interest of the IC industry on high performance chips and multicore processors for chip performance improvements. In multicore processors, each core contains the main execution units and so, most of the processing power is concentrated in these specific regions. Subsequently, the cores dissipate most of the heat flux compared with the rest of the chip, inducing the appearance of hotspot (in the cores) and background regions (in the rest of the chip) [67]. Also, the activity of System-On-Chips based on multiple cores varies over time depending on the requirements, what leads to time dependent heat load profiles. Due to this non-uniform heating, to goal of low thermal gradients at the chip becomes more challenging [68], [69].

In an attempt to overcome this issue, Lee et al. [29] used the recess created in the lid of a microchannel heat sink to modulate the flow for heat transfer enhancement at the hotspot regions. The recess induced more flow into the system due to lower flow resistance and thus, enhanced the heat transfer. For a chip with 2 hotspots of 200 W/cm^2 and a background heat flux of 100 W/cm^2 , a reduction in temperature gradient of $6,20 \text{ K}$ while enhancing the heat transfer by 150% was reported (Figure 2.10).

Brunschwiler et al. [27] developed a tailored flow cold plate where the fluid flows through a layered mesh network, where the number of mesh layers was modulated. A reduction of the thermal gradient was achieved, however, the peak temperatures were maintained compared with a conventional microchannel heat sink. A reduction of flow rate by 28% and pumping power by 43% were reported.

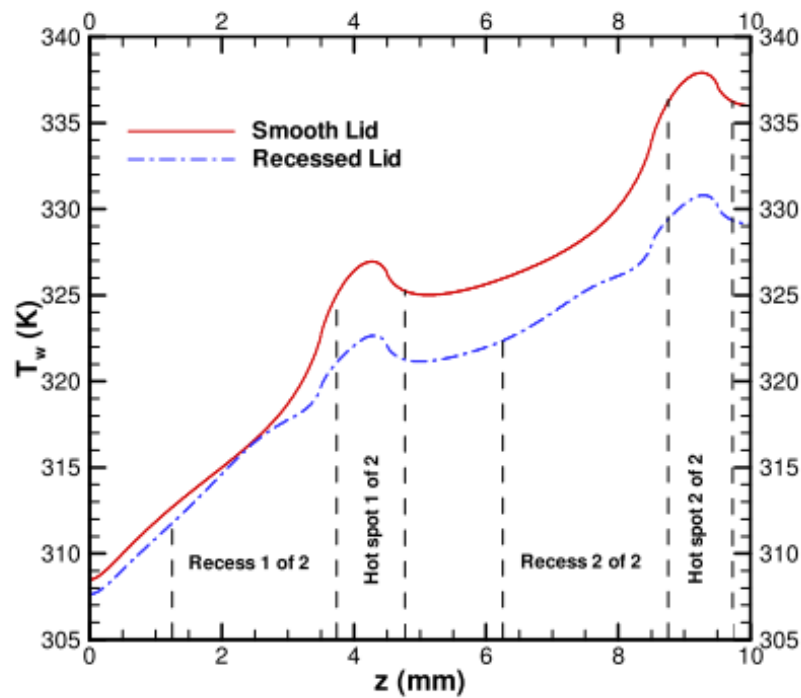


Figure 2.10. Chip temperature profile in presence of two hotspots dissipating 200 W/cm^2 while the rest of the substrate dissipates 100 W/cm^2 [29].

Green et al. [70] presented a heat sink that uses two separate unmixed fluids to meet the cooling requirements of high-performance chips. One chip was used uniquely to cool the hotspot zones whereas the other to cool the background zones and as an on-chip regenerator for the hotspot fluid, avoiding external chilling (Figure 2.11). Their experimental results shown that the hybrid system could dissipate up to 400 W/cm^2 at the hotspot with low pumping power requirements.

Lee et al. [30] reported the performance of an oblique finned microchannel that breaks the fluid boundary layer and generates secondary flows in order to enhance the heat transfer. Also, the flow rate was tailored to the cooling needs by varying the fin pitch (Figure 2.12). An experimental validation using a Silicon chip with 2 hotspots was reported, achieving a reduction in the temperature gradient and the pressure drop.

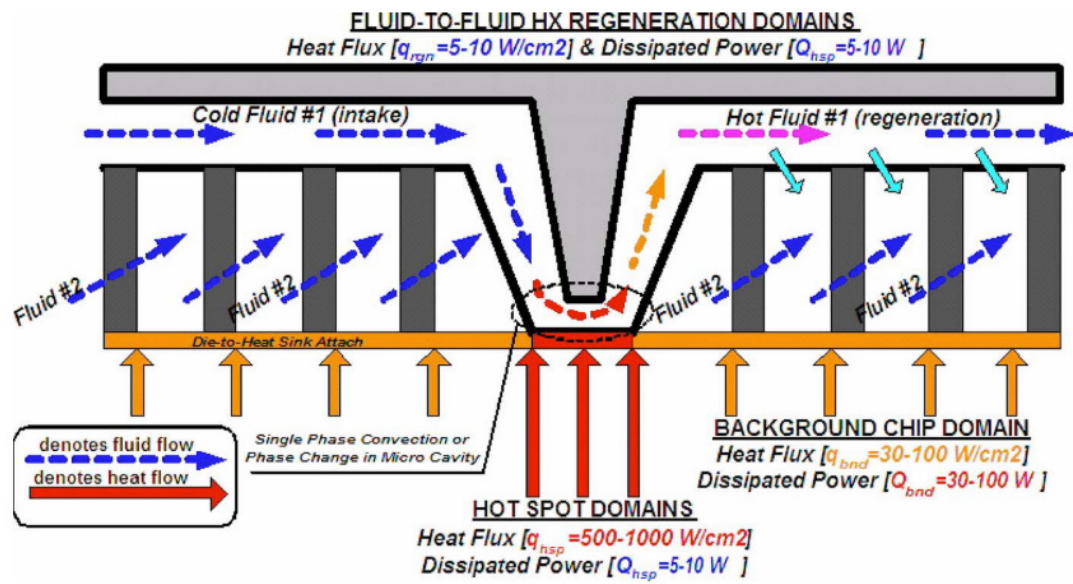


Figure 2.11. Schematic of the heat sink presented by Green et al [70].

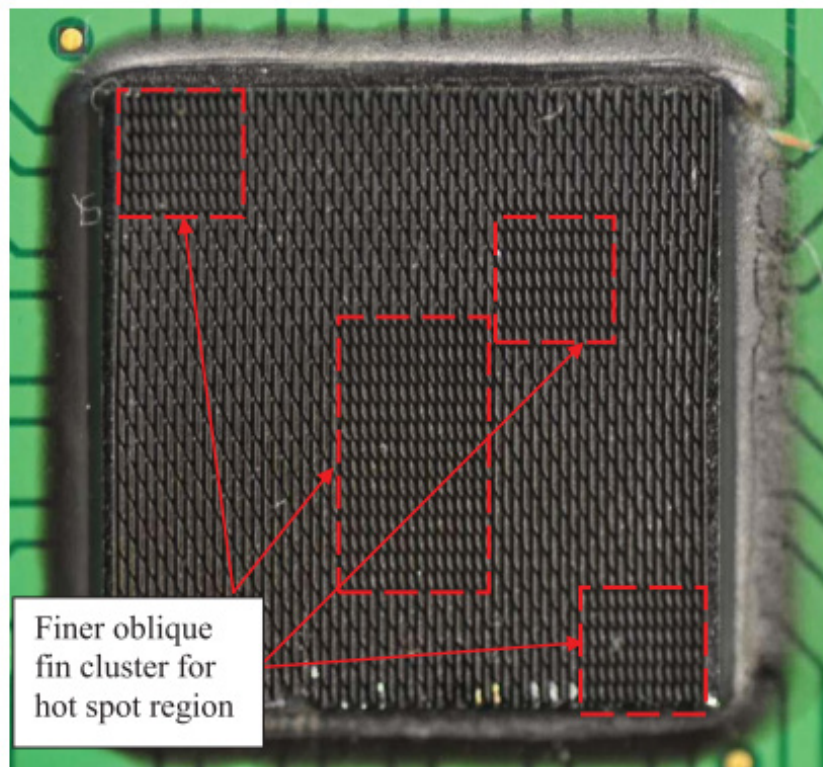


Figure 2.12. Oblique finned microchannel heat sink presented by Lee et al. [30].

Sharma et al. [21], [22] presented a hotspot targeted manifold microchannels heat sink with multiple inlets and outlets, able to distribute the coolant through the chip without any external flow control device. The coolant fluid used was water. Narrow channels were defined at the hotspot locations while wider channels were used to cool the background zones. For a hotspot heat flux of 150 W/cm^2 and a background of 20 W/cm^2 , a reduction of the chip temperature gradient by 61 % was reported, and for a hotspot heat flux of 300 W/cm^2 the temperature gradient reduction was reported to be of 54 %.

Collin et al. [34] experimentally studied the performance of a non-invasive and hotspot aware microchannel die that was in direct fluidic contact with the backside of a highly thinned chip. With a high heat flux of 1185 W/cm^2 , a thermal resistance of $2,80 \text{ K/W}$ and a maximum temperature rise of 55 K were achieved. Also, a low pressure drop of $19,20 \text{ kPa}$ was obtained with the described conditions.

Additionally, some works have been focused on developing thermal models to predict the thermal behavior of the chip and thus, the hotspots locations, to optimize the cooling device at a design stage [67], [71], [72]. However, the research presented above fixes its geometry at the design stages and is not able to tailor their behavior to time-dependent heat load scenarios. Consequently, their constant flow rate distributions are overly conservatives and lead to oversized pumping powers for varying operation conditions.

2.3. Heat transfer enhancement techniques

Microchannel technology presents several benefits over conventional heat sinks, such as larger surface area to volume ratio and higher heat transfer coefficients. Nevertheless, they are not able to provide good temperature uniformities, which, as explained in previous sections, implies electronic reliability issues. Additionally, the flow in traditional plain and rectangular microchannels is always laminar and, due to the continuous increase of heat loads on the chips, turbulent flows are at the point of interest due to its higher thermal performance. For these reasons, several works focused on developing techniques to increase the heat transfer within microchannels. Bergles et al. [73] reviewed the earlier literature on convective heat transfer

enhancement and classified the augmentation techniques in two categories, passive, without the requirement of external energy, and active, which require external excitation. Passive mechanisms are considered more reliable in the current literature, due to the absence of moving parts.

Based on another review, Tao et al. [74] defined three mechanisms to enhance the heat transfer: the decrease of the thermal boundary layer, the increase of flow interruptions and the increase of the velocity gradient near the heated surface. These mechanisms can be used within passive and active enhancement techniques (Figure 2.13).

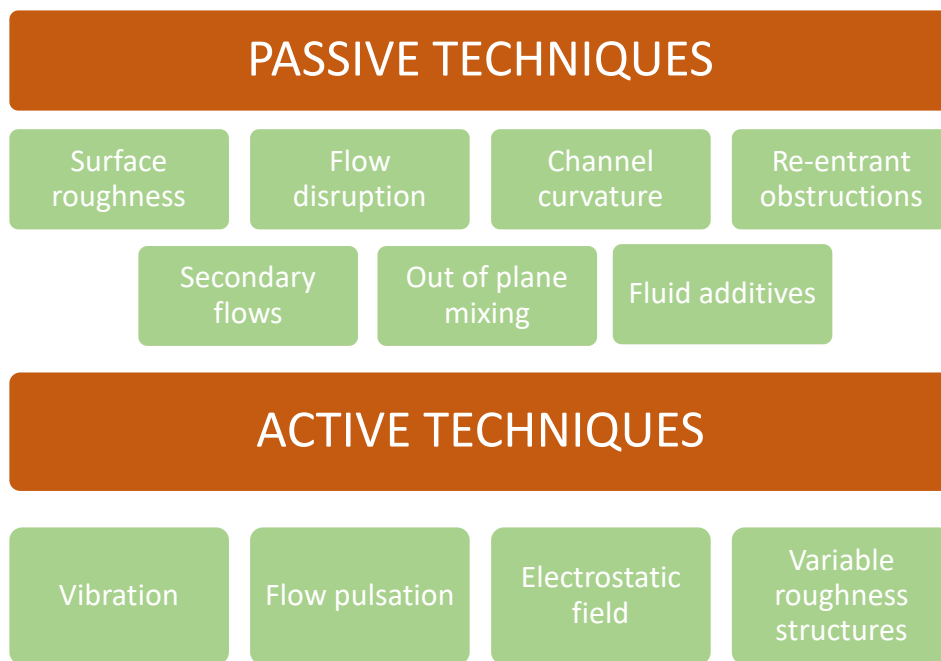


Figure 2.13. Passive and active heat transfer enhancement techniques within microchannels [75].

2.3.1. Passive techniques for heat transfer enhancement within microchannels

Flow disturbing elements are the most common passive elements in the literature used for heat transfer enhancement. This enhancement is achieved by the breakage of the boundary layer, that leads to better mixing and redevelopment of this layer, resulting in lower thermal resistances. These disturbing elements can be ribs, wings, winglets or vortex generators able to create vortices and secondary flows to improve the mixing and heat transfer (Figure 2.14). Fiebig

et al. [76], [77] analyzed the overall performance of vortex generators within air flow and reported that for heat transfer enhancement, longitudinal vortex generators (LVG), which create vortices along the channel direction, were more effective than transverse vortex generators (TVG), that create vortices transversally to the channel. Also, for identical parameters of study, they reported that delta wings provide more effective cooling than rectangular wings and winglets.

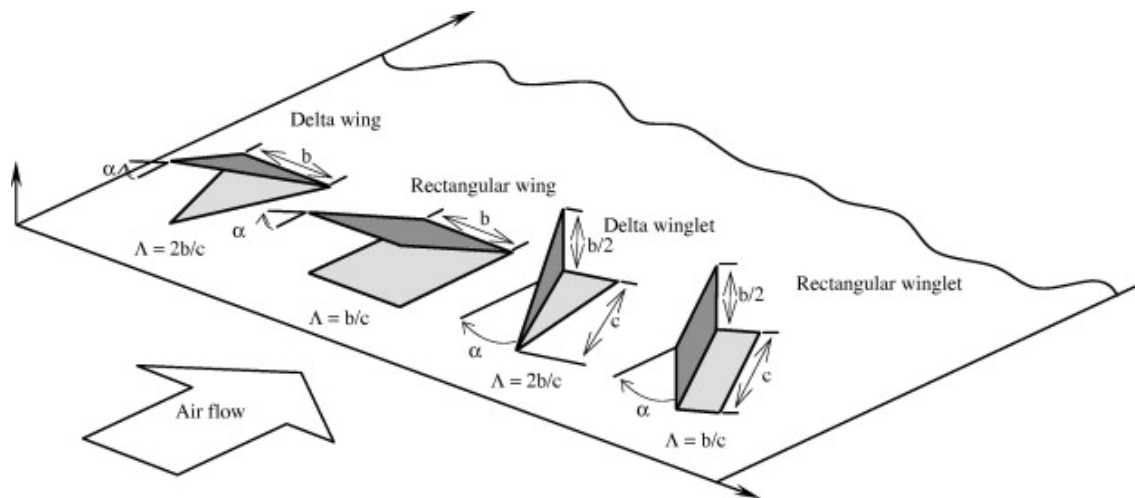


Figure 2.14. Common flow disturbing elements and their geometrical definitions [78].

Liu et al. [79] performed an experimental study to determine the overall performance of LVGs within a rectangular microchannel for Reynolds numbers between 170 and 1200. They used 6 different configurations of LVG pairs, with the same height as the microchannel ($H = 100 \mu\text{m}$) and reported an early transition to turbulent flow at low Reynolds (between 600 and 730). A heat transfer enhancement of 20 % under laminar flow was reported, however large pressure drop increments (83 %) made the overall heat transfer performance lower than one.

Hsiao et. al [80] studied micromixers based on T-shaped channel with rectangular winglet pairs (RWP) mounted on the bottom of the main channel, which generate longitudinal vortices (Figure 2.15). They investigated, by numerical simulations, the effects of the geometrical parameters on the mixing performance within LVGs and compared the results with the experimental ones. The study was performed at low Reynolds numbers, from 0,03 to 64. The results obtained showed that the degree of mixing increased with the Reynolds number, and the mixing efficiency of the

micromixer with RWP was greater than that of the micromixer without RWP. The relative influence of the geometric parameters was ranked as asymmetry index (d) > angle of attack (θ) > winglet height (h) > winglet spacing (D) and, based on these results, they defined an optimal parameter group.

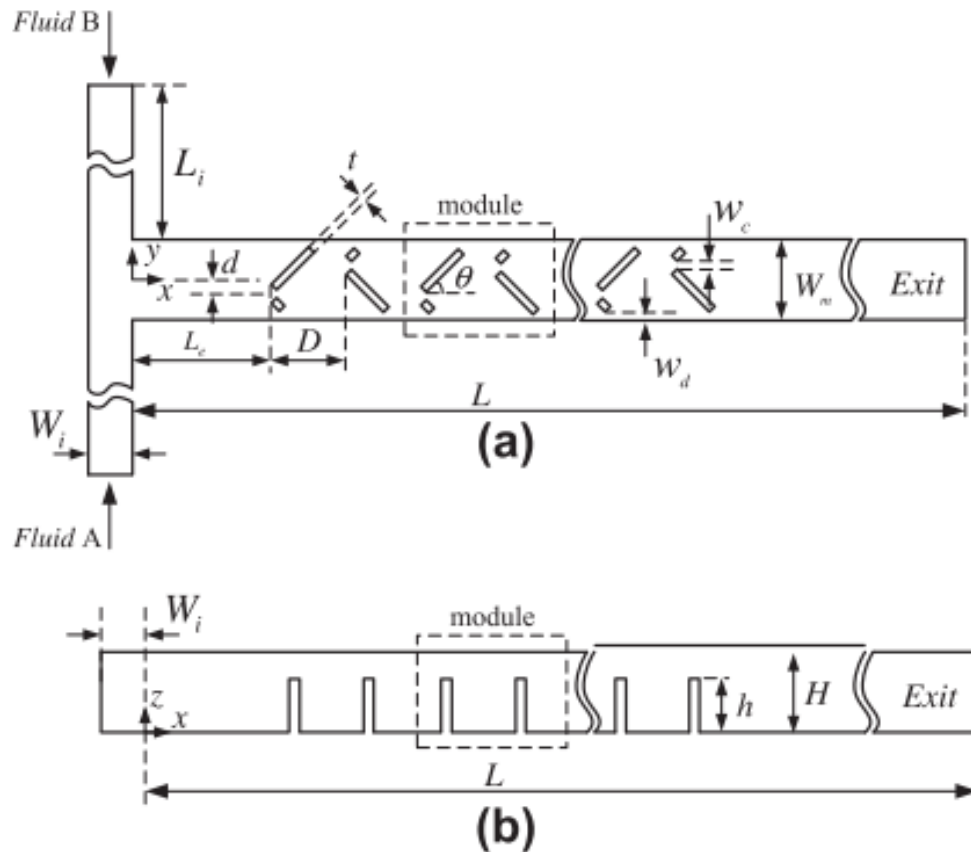


Figure 2.15. Schematic diagram of a microchannel with divergent RWP. (a) Top view and (b) side view [80].

Chen et al. [81] conducted an experimental study to explore the overall thermal performance of de-ionized water flowing through rectangular microchannels with rectangular LVGs when applying a constant wall temperature of 323,15 K at the bottom of the chip. The aspect ratio of the channel, the height of the LVG and the number of LVG pairs was changed for the different studied configurations, while the angle of attack was set constant at 45 °. The Reynolds number varied from 300 to 1500. From the obtained results, they reported that microchannel with aspect ratio of 0,25 had better overall heat transfer performance than those with aspect ratio

of 0,067. They also stated an early transition to turbulent flow regime, at Reynolds number lower than 1000.

Wang et al. [82] presented a microchannel heat sink with micro-scale ribs and grooves for chip cooling (Figure 2.16). Experimental and numerical simulations were performed with a constant heat flux of 100 W/cm^2 and Reynolds numbers from 100 to 1000. The height of the ribs was varied for different study cases. A maximum chip temperature decrease of 8 K was reported for the microchannel with ribs and grooves compared with a plain microchannel. Also, the Nusselt number increased with the rise of the relative rib height, achieving a heat transfer enhancement of 55 % for a relative rib height of 0,85. Nevertheless, high induced pressure drops, up to 700 % compared with a smooth microchannel, lead to a thermal performance factor lower than 1 for all the studied cases.

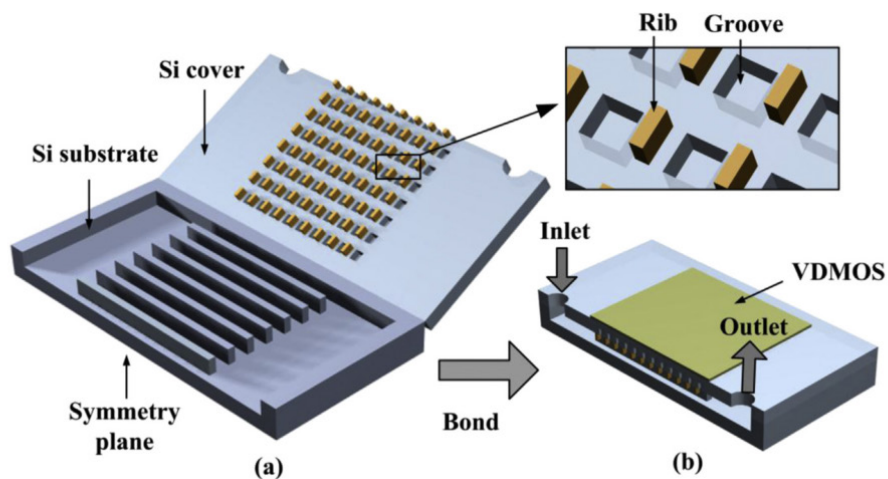


Figure 2.16. Schematic of (a) half microchannel heat sink with ribs and grooves and (b) half of the test system studied by Wang et al. [82].

Ebrahimi et al. [46] performed a numerical study on the heat transfer performance of single phase laminar flow in rectangular microchannels with LVGs when applying a constant chip temperature of 323,15 K. They studied 5 different configurations of rectangular microchannels with different angles of attack of the LVGs and different Reynolds numbers, from 100 to 1000. The height of the winglets was the same as the channel height. They suggested that the use of LVGs in microchannels led to an increase in overall thermal efficiency that increases with

Reynolds number. The Nusselt number was increased by 25 % and the friction factor by 30 % compared with a plain microchannel. The thermal performance factor reported was higher than 1 for all the cases except one at $Re = 100$.

Marschewski et al. [47] studied the cooling performance of microchannels with herringbone microstructures. Four different configurations were studied, varying the heating power between 6,40 W and 16,40 W and the flow rate between 2 ml/min and 6 ml/min (Figure 2.17). They reported an overall thermal performance factor higher than one for all the studied cases, concluding that herringbone microstructures could be an attractive flow promoter for enhanced heat transfer in microchannels.

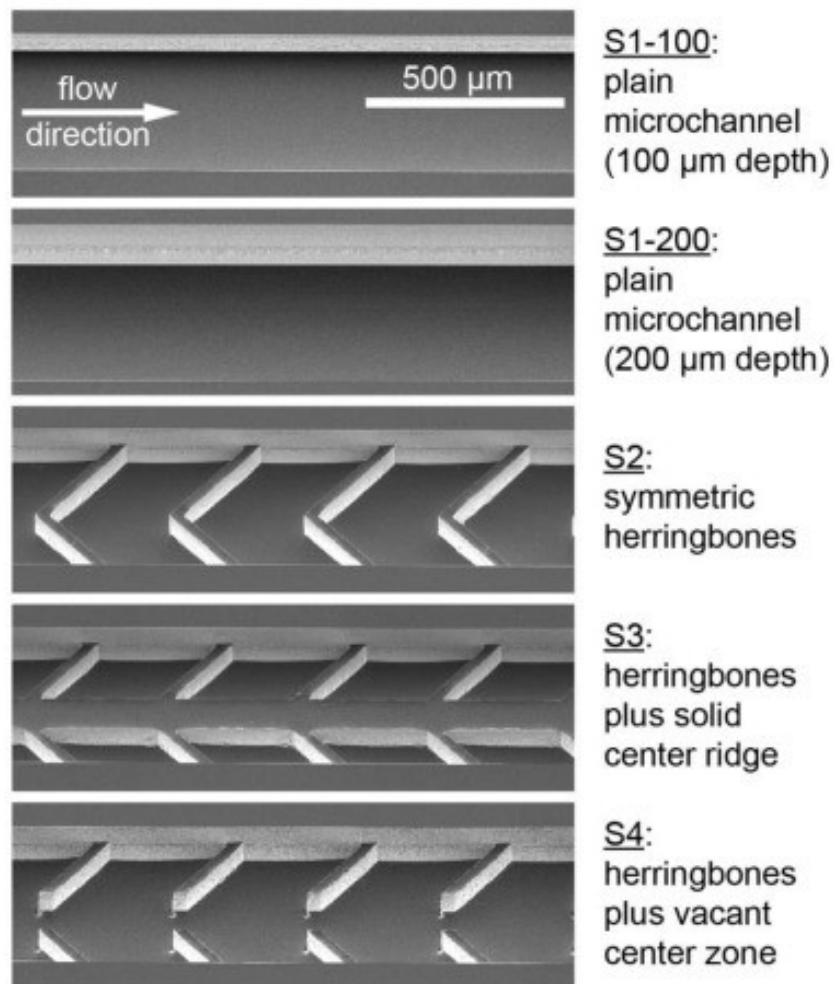


Figure 2.17. Different configurations of the herringbone microstructures studied by Marschewski et al. [47].

Yadav et al. [45] carried out a study using extended surface microchannels with micro-fins inside acting as cylindrical vortex generators. Three different configurations were studied, changing the placement of the fins inside the channel (Figure 2.18). Constant heat fluxes of 100 W/cm^2 and 200 W/cm^2 were applied. The best thermal performance factor was achieved with the upstream finned microchannel case, concluding that higher heat transfer coefficients are achieved with the vortex generators placed at the beginning of the channel.

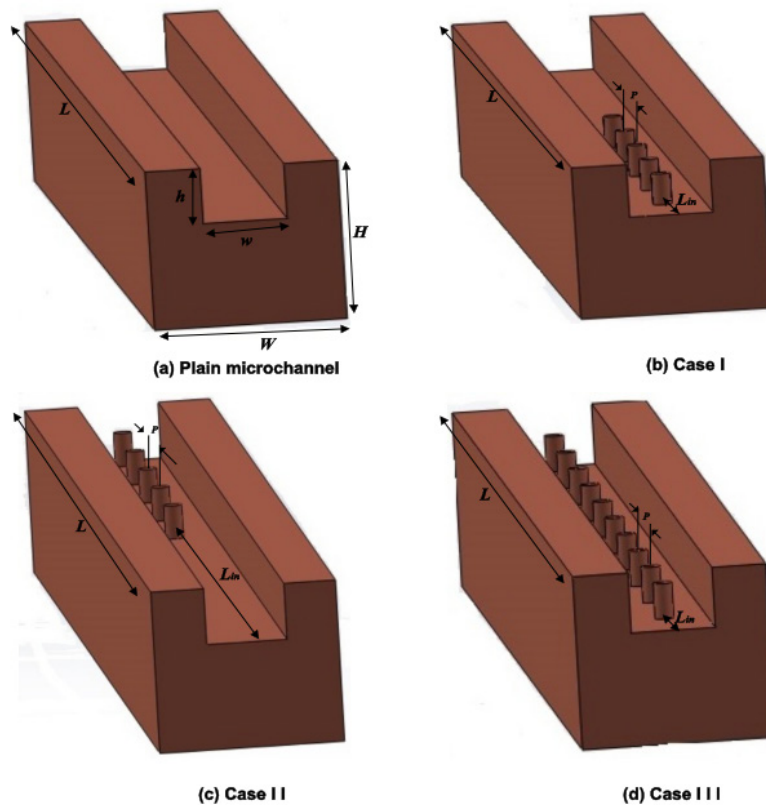


Figure 2.18. Different configurations of microchannel with cylindrical vortex generators [45].

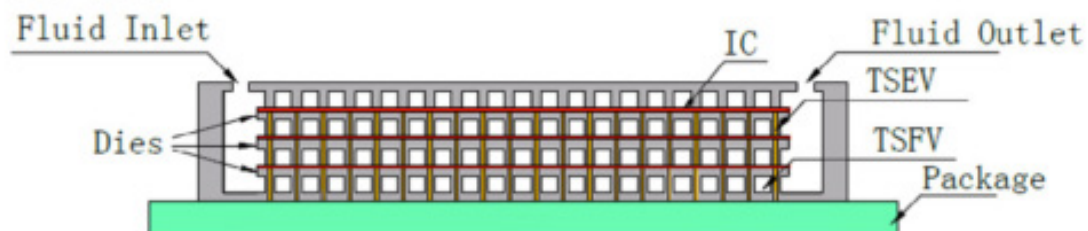
Datta et al. [83] assessed the performance of 2 pair of LVGs on a short microchannel, of 1,50 mm length. The main purpose of this study was to find out the best inclination, position and distance between LVGs and the effect of wall thickness on the overall thermal performance. They reported that for Reynolds numbers higher than 600, an angle of attack of 30° offers the best performance, while higher angles work better at low Reynolds. Also, they concluded that larger length downstream of the 2nd LVG pair is more effective for heat transfer enhancement.

Al-Asadi et al. [84] explored the thermal performance of cylindrical vortex generators with quarter-circle and half-circle cross sections of different dimensions. The study was conducted with Reynolds numbers from 100 to 2300 and a constant heat flux varying between 100 W/cm^2 and 300 W/cm^2 . With quarter-circle cross sections no overall heat transfer enhancement was founded. Contrarily, half-circle cross sections showed good thermal performance factors, especially with small radius at low Reynolds numbers.

Renfer et al. [85] studied the generation of vortices with single-phase liquid cooling systems on 3D-IC by taking advantage of the TSVs. A heat transfer enhancement of 230 % and a reduction of the chip temperature gradient by a factor of 3 were reported when comparing the system with plain microchannels. Although the increments on pressure drop and pumping power, a thermal performance factor enhancement of 190 % was achieved.

Xia et al. [86] performed a numerical study on interlayer microchannel structures within 3D-IC. A study on the effects of geometric parameters on fluid flow and heat transfer characteristics with triangular re-entrant cavities (TRC) and fan-shaped re-entrant cavities (FRC) was performed (Figure 2.19). The length of the microchannels varied between 5 mm and 10 mm, the pitch between 0,10 mm and 0,20 mm and the flow rate between 0,10 L/min and 1,80 L/min. For $Re < 300$, the best configuration was found on rectangular microchannels while for higher Reynolds, fan-shaped re-entrant cavities were founded as the best option by the researchers.

In a similar way, Li et al. [87] presented a numerical study on the fluid flow and heat transfer characteristics of a microchannel heat sink with triangular cavities and rectangular ribs, for Reynolds numbers between 173 and 635 (Figure 2.20). The influence of relative rib width and relative cavity width on the hydraulic and thermal performances were also studied. Results showed that the proposed microchannels had more uniform and lower chip temperatures while achieving better heat transfer performance compared with plain microchannels.



(a)

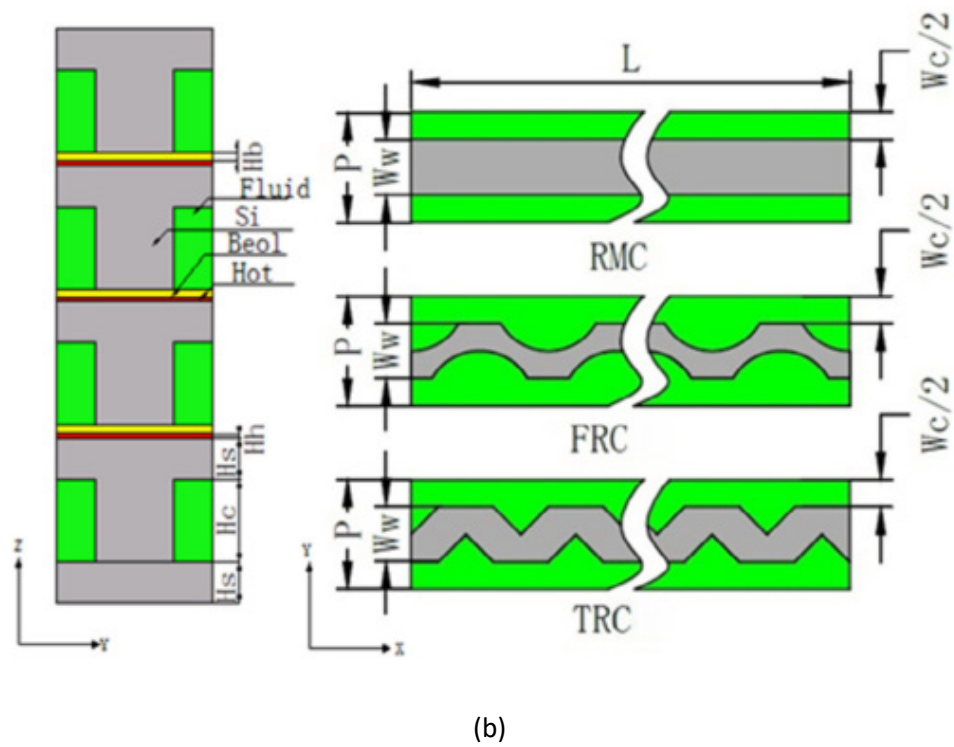


Figure 2.19. (a) Cross-section of the 3D-IC with interlayer liquid cooling. (b) Cross-section of the different microchannel structures [86].

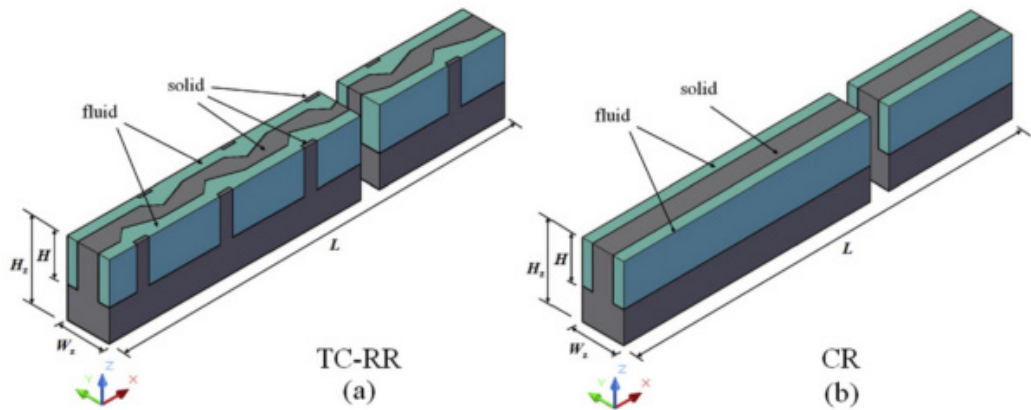


Figure 2.20. Schematic view of a heat sink with (a) triangular cavities and rectangular ribs and (b) rectangular cavities [87].

A different passive technique to enhance heat transfer is the use of fluids with solid nanoparticles inside, known as nanofluids. Sabaghan et al. [48] reported a numerical study of

the thermo-hydraulic performance of a rectangular microchannel with six different geometries of LVGs. Different nanofluids, such as ethylene-glycol, water mixture and transformer oil were considered. The normalized efficiency of the system was improved up to 14 % with the LVGs, while the efficiency improvement due to the use of nanofluids was computed at 27 %.

Bas-relief structures on the base of the channel to enhance mixing within microchannels at low Reynolds numbers were presented by Strook et al. [88] (Figure 2.21). In a similar way, Hong et al. [89] performed a numerical study about mixing in microchannels when using periodic patterned zeta potential surfaces to induce chaotic fluid flow in electro-osmotically driven microfluidic devices. They discussed the generation of vortices with different patterns such as periodic zeta potential patterns, straight striped zeta potential patterns and herringbone patterns to create an efficient micromixer.

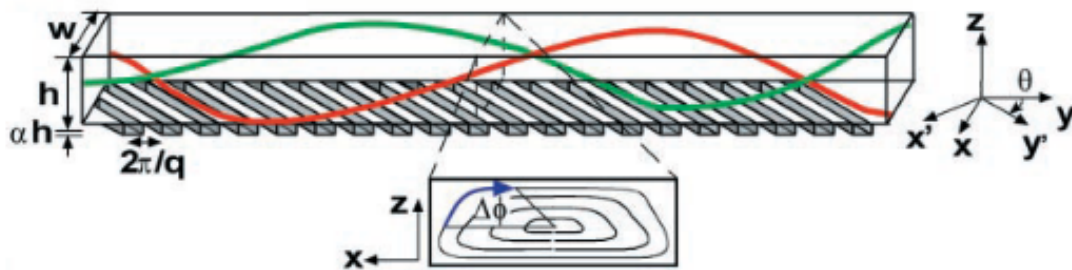


Figure 2.21. Schematic view of the microchannel with ridges at the bottom. The red and green lines represent trajectories in the flow [88].

The effect of roughness on heat transfer was also reported in the literature as a passive thermal enhancement mechanism. Wu and Cheng [90] experimentally studied the effect of geometric parameters and surface roughness on the pressure drop and heat transfer in microchannels under laminar regime. They reported an increase on Nusselt number when the surface roughness increases, especially at larger Reynolds numbers. Even though, they stated that the geometric parameters have a higher significant effect on the microchannel performance than the surface roughness.

Gamrat et al. [91], [92] reported an interesting summary of experimental and numerical works on rough microchannels in the literature. They modelled roughness as a pattern of

parallelepiped elements distributed periodically within microchannels and studied the influence of roughness on heat transfer in laminar flows. Numerical simulations and rough-layer models agreed to show that both the Poiseuille number (Po) and the Nusselt number increased with relative roughness. They defined a relative roughness value normalized with the half channel height (k^*) and stated that for $k^* > 0,46$, roughness increases more the heat transfer than the pressure drop, achieving a thermal performance criterion higher than one.

Finally, Brackbill and Kandlikar [93] experimentally examined the effect of different roughness structures in high aspect ratio rectangular microchannels and used a model based on lubrication theory to compare with the obtained results. The experiments studied the effect of uniform roughness, saw tooth roughness and varying pitch saw tooth roughness in laminar and turbulent flow, with Reynolds numbers from 30 to 15000. They conclude that roughness structures of less than 5 % of relative roughness had appreciable effects on laminar flow and led to earlier transition to turbulent regime.

2.3.2. Active techniques for heat transfer enhancement within microchannels

Active thermal management usually requires an external input into the system, such as power, electricity, RF signals or external pumps, which adds an extra power cost to the system. Also, these systems are usually considered less reliable than passive systems due to the presence of moving parts. However, most of them can adapt their behavior to time dependent and non-uniform power map scenarios, avoiding overcooling and extra pressure drops usually reached by passive systems [94].

Different studies in the literature developed and studied the performance of different active techniques such as vibration [95], electrostatic fields [96] and flow pulsation [97]. However, these techniques are difficult to implement within microchannels due to its large sizes. Steinke and Kandlikar [75] proposed different adaptations of the above described active techniques to made it feasible for microchannels technology. For example, they proposed the use of piezoelectric material embedded on microchannel walls to generate surface vibrations (Figure 2.22) or variable roughness structures. Fang et al. [98] developed an active heat transfer solution based on an array of synthetic jets that generates periodic disturbances when interacts with

microchannel flow. They achieved an enhancement on heat transfer of 130 % while reducing the pressure drop.

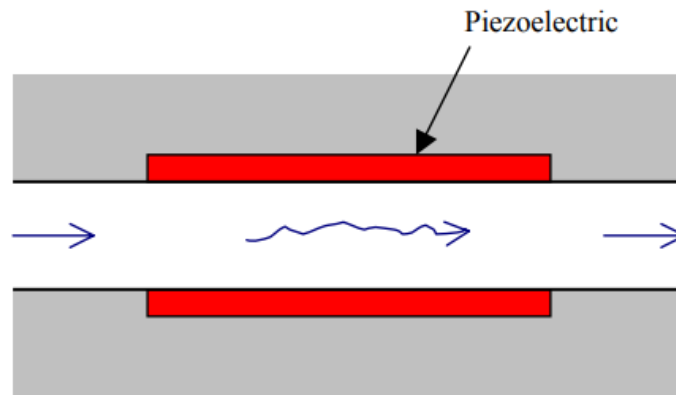


Figure 2.22. Piezoelectric enhanced microchannel [75].

In 2001, Champagne and Bergles [99] presented a novel work involving a variable roughness heat exchanger tube, consisting in shape memory alloy (SMA) wire coils. The heat transfer enhancement and pressure drop were experimentally assessed for this self-adaptive system. In a similar way, Aris et al. [78] studied later the effect of SMA delta wings acting as vortex generators for convective cooling using air as working fluid and demonstrated the effectiveness of this device on heat transfer enhancement. Although these devices demonstrated their capability to adapt to time dependent and non-uniform heat load scenarios, they were tested at miniscale due to the present difficulties to fabricate SMA systems at smaller scales.

2.4. Conclusions about the state-of-the-art

An exhaustive review of the existing literature was done in this chapter. First, different attempts on cooling 3D-IC were described, focusing on the importance of liquid cooling for removing high heat fluxes. Then, the importance of low temperature gradients on chips was assessed, especially for hotspot mitigation on multicore processors. Several works that focused on this issue were presented. Although the important advances that the listed works presented on

microelectronics thermal management, they are focused on fixed geometries, what makes the systems unable to adapt to time-dependent heat load scenarios.

Finally, a review of different passive and active techniques for heat transfer enhancement inside microchannels to further decrease the thermal resistance was done. Although several attempts achieved good thermal performance factors, these works were assessed with constant heat fluxes in time and space.

It can be seen that neither active nor passive heat transfer enhancement techniques have been developed to adapt to changing boundary conditions in time and space, what leads to heat transfer enhancements on the cooling system even when not needed, for example when the heat loads are low. Due to this fact, additional pressure drops are induced in the fluid channel, what causes oversized pumping powers for changing conditions. Additionally, the surface temperature uniformity is only optimized for a given heat load distribution and cannot be adapted to non-uniform and time dependent heat load scenarios. The solution proposed in this thesis overcomes these problems due to the self-adaptation concept, as the disturbing elements inside the flow will adapt its shape, in function of its own temperature, to time dependent and non-uniform heat load scenarios. The demonstrated capabilities on heat transfer enhancement of flow disturbing elements will be used only when the cooling demands of the device increase; otherwise, the fins will remain in a flat position, reducing the pressure drop inside the cooling device.

SELF-ADAPTIVE FINS ACTING AS VORTEX GENERATORS

3. SELF-ADAPTIVE FINS ACTING AS VORTEX GENERATORS

In this chapter, the concept, working principle and feasibility of the self-adaptive fins within microscale is detailed. First of all, a previous work based on the use of shape memory alloys as self-adaptive structures within miniscale is presented to demonstrate the feasibility of this concept. Then, the requirements that the self-adaptive fins must met in microscopic scale to perform a significant impact within the performance of cooling devices is defined. Also, different structures of self-adaptive fins are proposed and evaluated to find an optimum configuration.

3.1. Background: Shape memory alloys used as self-adaptive cooling device within miniscale

A previous work, published by Vilarrubí et al. [100], studied a self-adaptive cooling device based on the use of shape memory alloys (SMA), with the aim of providing constant and uniform temperature distributions under time dependent heat load scenarios while reducing both the pressure drop and the pumping power to the minimum required for each heat load. The working principle was based on Two Way Shape Memory Effect (TWSME) of trained SMA wings. Through this training, the wing elevates into the flow when a critical temperature is reached, both enhancing the heat transfer and generating a vortex in the fluid to disturb the flow. Contrarily, when the wing is cooled down, it returns to the initial flat shape to reduce the pressure drop in the channel and thus, the pumping power.

The conditions for proper operation of TWSME are first defined analytically. Then, the impact of the SMA wing on thermal resistance and the ability of the self-adaptive concept to maintain a uniform junction temperature when the heat flux increases were both experimentally demonstrated. The SMA material used was Nitinol, with a composition of 50 % Nickel and 50 % Titanium, and the coolant fluid used was water.

3.1.1. Analytic study

At a first stage, the sequence that must be reached to obtain the desired behavior of the device, based on the TWSME, is defined (Figure 3.1), assuming constant flow rate and inlet temperature:

1. While the SMA wing temperature is below the starting temperature of the austenite phase change (T_{As}) it remains in its martensitic phase. The wing is flat and does not perturb the flow.
2. When the temperature of the SMA wing rises from T_{As} to T_{Af} , the wing bends upwards due to the austenitic transformation, creating a vortex effect which is gradually increasing (A_f is the austenite finish point). The vortex enhances the mixing and therefore reduces the convective thermal resistance.
3. If the temperature is then reduced below T_{Ms} , the reverse martensitic transformation starts (M_s is the martensite start point).
4. As the temperature reduction continues until T_{Mf} , the SMA wing returns to its initial flat shape, as in step 1 (M_f is the martensite finish point).

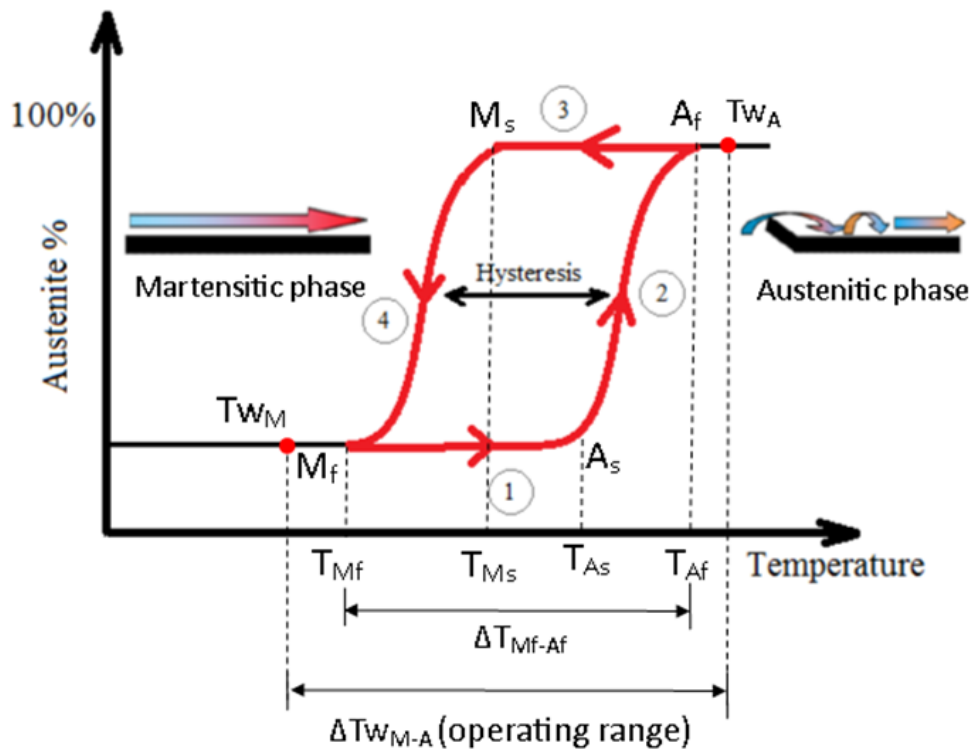


Figure 3.1. Ideal working cycle of the SMA wing [100].

This sequence requires two-way training of the SMA and phase transformation temperatures that are within the expected operating temperature range of the device, which are defined as T_{W_M} and T_{W_A} for the flat and raised wing positions respectively. More specifically, the following conditions must be met for the SMA wing to complete a whole working cycle and self-regulate the temperature distribution.

Condition 1. The temperature difference between the two positions of the SMA wing ($\Delta T_{W_{M-A}}$) needs to be higher than the required for the SMA phase transformation (hysteresis cycle, ΔT_{Mf-Af}).

$$\Delta T_{W_{M-A}} > \Delta T_{W_{Mf-Af}} \quad (12)$$

Where:

$$\Delta T_{W_{Mf-Af}} = T_{Af} - T_{Mf} \quad (13)$$

Condition 2. The temperature of the SMA wing at the deformed position (T_{W_A}) must be higher than the final austenitic temperature (T_{Af}), and the SMA temperature in the flat state (T_{W_M}) had to be lower than the final martensitic temperature (T_{Mf}) to allow the shape transformation.

$$\begin{cases} T_{W_M} < T_{Mf} \\ T_{W_A} > T_{Af} \end{cases} \quad (14)$$

The fulfilment of the previous conditions ensures the ideal situation to obtain a complete TWSME. A_f , M_f and ΔT_{Mf-Af} depends on the properties of the SMA sample, specifically on the composition of the SMA, the annealing process and the characteristics of the training procedure used to obtain the TWSME. Otherwise, the temperature of the sample in the martensitic phase (T_{W_M}) and in the austenite phase (T_{W_A}) are obtained through the following equations:

$$T_{W_M} = T_{in} + q'' \cdot R_M \quad (15)$$

$$T_{W_A} = T_{in} + q'' \cdot R_A \quad (16)$$

3. Self-adaptive fins acting as vortex generators

Where T_{in} is the inlet temperature of the coolant (fixed), and R_M and R_A are the thermal resistances provided by the SMA wing in the martensitic phase and in the austenitic phase respectively. These thermal coefficients depend on the coolant flow rate, which is fixed, and the shape of the SMA wing. For a given coolant flow rate, the elevation of the SMA wing in the austenitic phase (raised position) will provide lower thermal resistance than in the martensitic phase (flat position). The temperature difference between the two positions will be:

$$\Delta T_{W_{M-A}} = q'' \cdot (R_M - R_A) \quad (17)$$

3.1.2. Experimental validation of TWSME

In order to demonstrate the capabilities of the proposed concept, a microchannel cooling device with an embedded SMA wing will be studied experimentally (Figure 3.2).

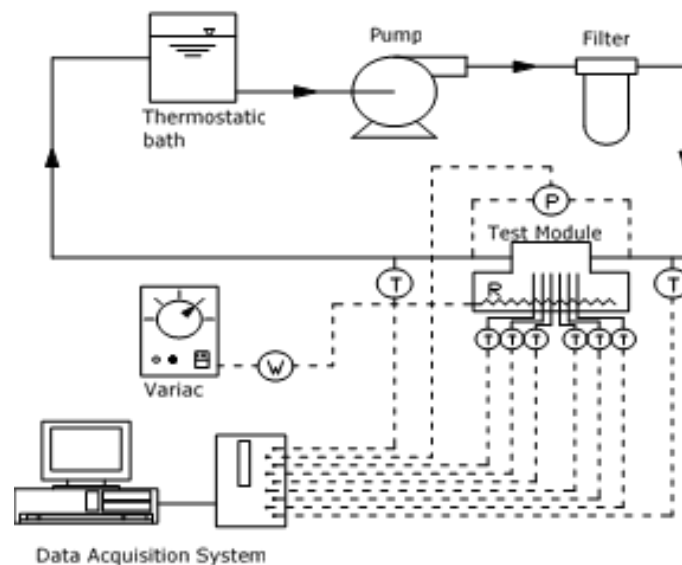


Figure 3.2. Test module setup.

The test module (Figure 3.3) is composed of a coolant distributor, a thermoplastic part that forms the cooling channel, a copper layer (with its thermoplastic housing) where the thermocouples are assembled, and finally a ceramic heater. The working fluid (water) enters to

the coolant distributor from a silicone tube and descends vertically through the coolant cover plate to the cooling channel. The heated water returns to the cooling tank through the outlet tube. Heat with a uniform heat flux is provided by a ceramic heater and conducted through a copper layer with thermocouples which acts as the bottom channel wall.

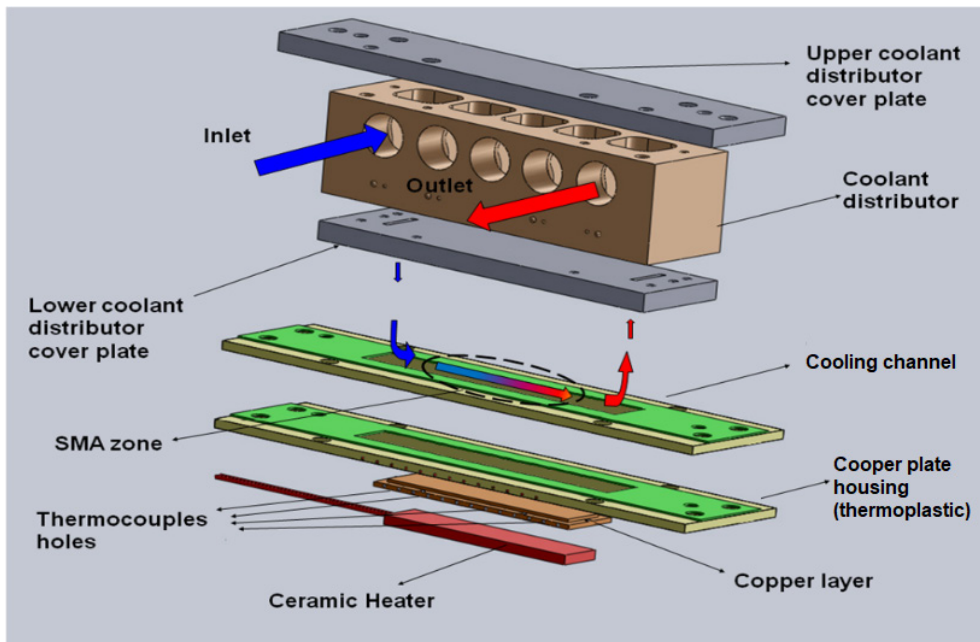


Figure 3.3. 3D view of the cooling test module (exploded view).

The trained part through TWSME (self-adaptive part) of the SMA sample is neither thermally nor mechanically connected to the copper layer. The fixed part of the SMA wing is sealed, within the cooling channel, on the top of the copper layer (Figure 3.4) through a thin layer of thermal interface material (TIM, $\kappa_{TIM} = 0,82 \text{ W/m}\cdot\text{K}$). The thickness of the TIM layer has been measured with a microscope ($50 \mu\text{m}$, $\pm 5 \mu\text{m}$). The channel side walls are defined by thermoplastic parts with a thickness of $3,50 \text{ mm}$. The deformable part of the SMA wing is located upstream ($x = 0 \text{ mm}$), so its flow disturbance can be advected downstream and affect the convective thermal resistance and the temperature distribution through the channel.

The heat flux is provided by an advanced ceramic heater (Watlow Ultramic 600), controlled by a Variac, which can give more than 100 W/cm^2 . Type-K thermocouples are used to measure the water temperature at the inlet (T_{in}) and outlet (T_{out}) of the microchannel heat exchanger and the

3. Self-adaptive fins acting as vortex generators

temperature distribution in the copper layer along the flow path (from $x = 0$ cm to $x = 5$ cm) at the centerline ($y = 0$ mm) of the coolant channel base (copper plate). These measurements are acquired by a data logger (Campbell CR23X) and sent to a computer to be stored and analyzed.

The uncertainty owing to the error of the TIM thickness measurement of $\pm 5 \mu\text{m}$ can be valued with a margin of $\pm 1,10 \text{ }^\circ\text{C}$. Added to the uncertainty due to thermocouples measurement of $\pm 0,50 \text{ }^\circ\text{C}$, the total margin of error within the test module is $\pm 1,60 \text{ }^\circ\text{C}$. Additionally, the uncertainty in electrical power levels is $\pm 10 \text{ W}$.

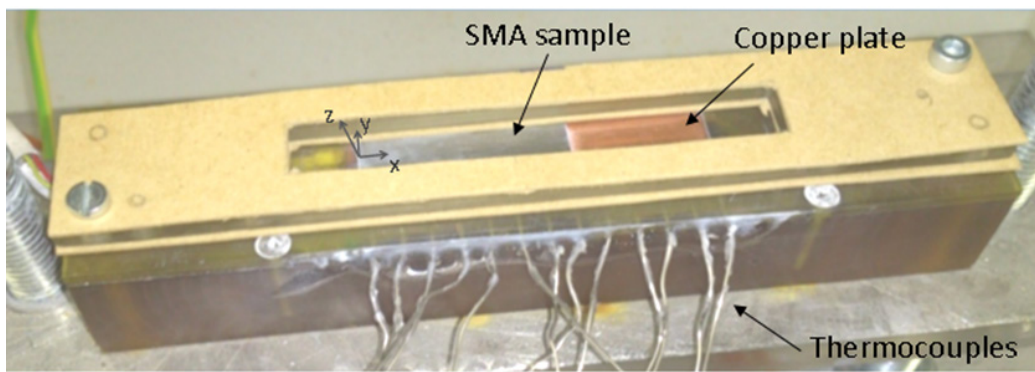


Figure 3.4. Photography of the cooling device test module with bottom side view of the channel.

The properties of the tested SMA wing fabricated with two different samples of Nitinol, after the annealing process and the TWSME training, have been experimentally defined by observing the wing deformation as a function of temperature (Table 3.1). The significant difference of temperatures between the two samples of Nitinol are due to differences in the alloy composition of both samples.

	Dimensions (mm)			Temperatures ($^\circ\text{C}$)				
	t	W	L	As	Ms	Af	Mf	$\Delta T_{\text{Af-Mf}}$
Sample 1	0,5	10	30	75	60	85	40	45
Sample 2	1,2	10	30	95	90	112	70	42

Table 3.1. Properties of the tested SMA wing fabricated with two different samples of Nitinol.

An annealing process is required to set the raised SMA wing shape while in the austenite phase. The annealing conditions have been fixed to 450 °C for 1 hour. To achieve the cyclic motion, additional training is required since the TWSME is not an inherent property of SMAs. Repeated thermo-mechanical treatments along specific loading profiles (training) are required. The selected training procedure consists of thermal cycling through the martensitic transformation under a constant stress level, achieved through a bending mechanism. In order to ensure that the extreme points M_f and A_f are achieved during the thermal cycling, 2 water baths at 5 °C and 100 °C are used. The elevated position of the SMA wing consists in bending a length of $L = 3,50$ mm from the leading edge of the sample with an angle (Θ) with respect to the flat position. The recovery rate (Φ) is assessed at several numbers of thermal cycles (18).

$$\Phi = \frac{\theta_A - \theta_M}{\theta_{const} - \theta_{init}} \cdot 100 (\%) \quad (18)$$

Where Θ_{init} is the angle after the annealing process, Θ_{const} is the angle applied during the training, Θ_M is the measured wing angle in the martensite phase and Θ_A , in austenite phase, all with respect to the flat shape.

A final recovery rate close to 18 % is obtained. Once trained, the angle of the raised wing is $\Theta = 26^\circ$ (Figure 3.5).

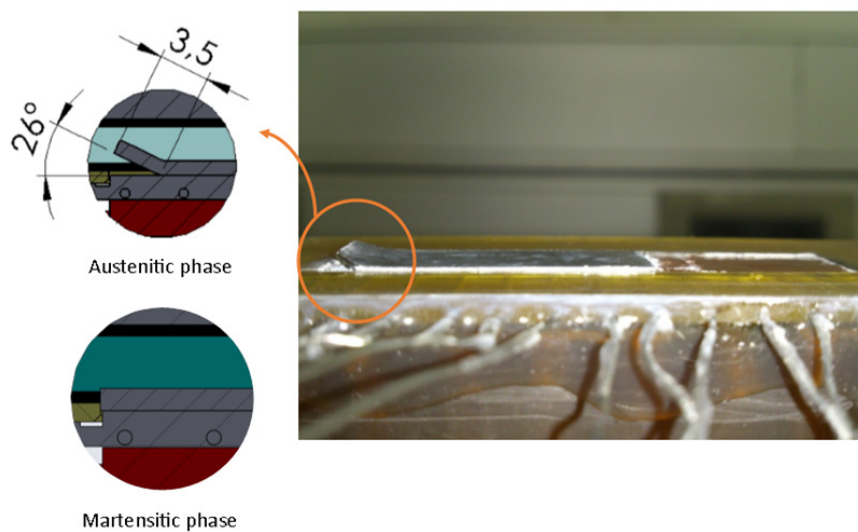


Figure 3.5. Raised position (austenitic phase) of the SMA wing above T_{Af} (photography from Sample 2) and flat position (martensitic phase) below T_{Mf} .

3. Self-adaptive fins acting as vortex generators

3.1.3. Experimental validation of the self-adaptive concept

Only one sample of the two studied verifies both conditions that ensures TWSME for a flow rate of 320 ml/min (Table 3.2). It can be seen within this way that the trained SMA wing has the capacity to self-execute the entire work sequence defined previously.

	Sample 2	
	Q = 320 ml/min	Q = 550 ml/min
T_{Af} (°C)	112	112
T_{Mf} (°C)	70	70
ΔT_{Mf-Af} (°C)	42	42
$T_{4,flat}$ (°C)	114	99,5
$T_{4,elevated}$ (°C)	60,5	49
$\Delta T_{W_{M-A}}$ (°C)	53,5	50,5
Condition #1: ($\Delta T_{W_{M-A}} > \Delta T_{Mf-Af}$)	Achieved	Achieved
Condition #2: ($T_{4,flat} > T_{Af}, T_{4,elevated} < T_{Mf}$)	Achieved	Not achieved

Table 3.2. Verification of the necessary conditions for sample 2. $T_4 = T(x=14mm)$.

Additionally, an experimental validation to ensure that this behavior can indeed be used to provide near constant temperature even though the heat rate increases is provided. To do so, for fixed inlet coolant temperature ($T_{in} = 3$ °C) and fixed flow rate ($Q = 320$ ml/min) a non-uniform heat flux was applied, firstly increased from 0 W/cm² to 67 W/cm² and then reduced back to 0 W/cm². For each heat flux value, the temperature measurements are taken once steady-state conditions are reached.

The chip temperature evolution as a function of heat flux, when the self-adaptive SMA wing was acting, was analyzed (Figure 3.6). The results are assessed for a thermocouple located at $x = 14$ mm. The cycle was repeated five times, and for a given SMA sample, the variation of the temperature measurements was lower than the uncertainty of the thermocouples.

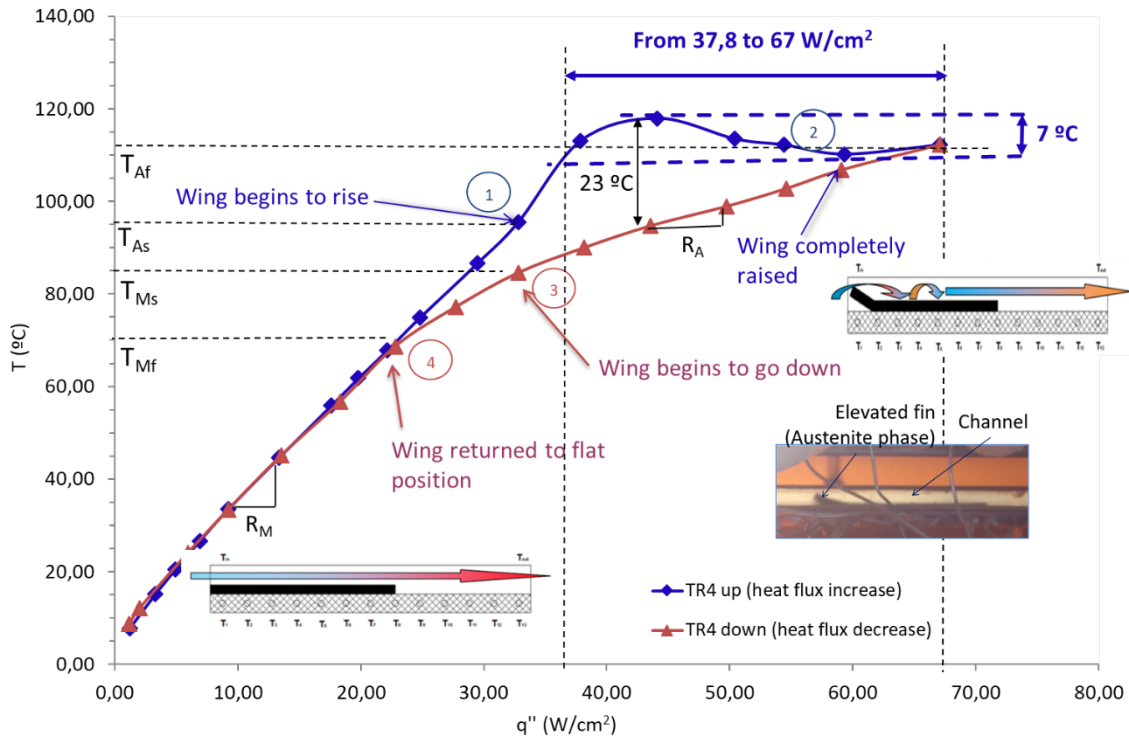


Figure 3.6. Temperature evolution of the junction temperature under varying heat flux (Sample 2, $T_{in} = 3^{\circ}\text{C}$, $Q = 320 \text{ ml/min}$) [100].

For a constant wing geometry, a relatively linear trend of $T = f(q'')$ would be expected, with the slope of this trend representing the thermal resistance. This trend is indeed observed below T_{Mf} . The impact of phase change from martensite to austenite significantly affects this trend as the heat flux goes above 37 W/cm^2 . Indeed, self-adaptation of the SMA wing shape occurs when the SMA temperature increases from T_{As} to T_{Af} , reducing the thermal resistance. This allows the local temperature to remain nearly constant over a wide range of heat flux, with only $\Delta T_{\max} = 7^{\circ}\text{C}$ between $37,80$ and 67 W/cm^2 . This effect can be attributed to the rise of the wing, acting as a flow disturbing element. A flow perturbation is induced in the fluid when the fin rises up, which breaks the flow boundary layer and enhances the heat transfer along the channel wall. Due to the self-adaptation of the wing, the induced flow perturbation increases with the heat flux, as does the angle of the wing. This reduces the thermal resistance for convective heat transfer when the heat load increases, preventing the wall temperature from increasing. A relative contact wall temperature is achieved due to the self-adaptive SMA wing.

In comparison, an increase in temperature of more than 85 °C would have been expected with no self-adaptation, assuming a linear trend for wall temperature. The self-adaptive SMA wing therefore improved the temperature uniformity by an order of magnitude.

Within this study, the working principle of a cooling device that self-adapts the distribution of the local heat extraction capacity as a function of the local temperature was validated. The obtained results opened new perspectives for developing universal cooling devices that could adapt their behavior to different heat load scenarios, with non-uniform and time dependent requirements, without the need for sensors or active control. The proposed cooling device demonstrated its ability to provide both enhanced temperature uniformities at the chip and minimized pumping powers. Nevertheless, this validation was performed within a miniscale cooling device as, up to now, the manufacture of SMA samples in smaller scales presents considerable difficulties. In the following sections, the described working principle is going to be assessed within microscopic scale by using other microfabrication technologies and working principles for the self-adaptive wings.

3.2. Definition of self-adaptive fins requirements for microscopic scale

As seen in previous chapters, the addition of flow disruption elements within a cooling channel, acting as vortex generators, enhances its heat transfer performance by creating vortices and reducing the thermal boundary layer. Nevertheless, the addition of elements inside the channel implies an increase of the pressure drop for constant flow rate and so, of the required pumping power.

The solution proposed in this thesis to reduce the requested pumping power while maintaining the flow rate is based on self-adaptive fins (Figure 1.10). These fins are able to adapt their shape to the instantaneous cooling requirements; for example, when high heat fluxes are applied, they will rise up to both maximize the heat transfer enhancement surface and disturb the flow boundary layer. On the contrary, when the cooling requirements remain low, the fins will remain in a flat position, reducing the pressure drop within the channel and so, the pumping power.

One of the key parameters for the design of the self-adaptive fin is the fin inclination or relative height of the fin to the overall channel. In this section, the optimum inclination of rectangular fins inside a microchannel is assessed. Additionally, the thickness of the fin is another important parameter to assess before defining its geometry. Thicker fins have higher section for thermal conduction and will be more resistant to the impact of the fluid, that will tend to rise them down. However, in some configurations of self-adaptive fins, thicker fins will rise up less as they are heavier.

3.2.1. Numerical model

The thermo-hydraulic performance of a Si microchannel, with an arbitrary distribution of rectangular fins inside, is numerically compared to the performance of a plain microchannel, without fins (Figure 3.7). Comsol Multiphysics software is used to perform the CFD simulation.

The defined channel has 15 rectangular fins inside, made of Ag, equi-spaced in 3 columns of 5 fins in each. The separation between columns is of $333,30\ \mu\text{m}$ and the separation between each row is $400\ \mu\text{m}$ (Figure 3.7b). The inclination of the fins is varied in order to assess the optimum impact. The main dimensions of the microchannel, designed to cool a microchip of $2,00\ \text{mm} \times 2,00\ \text{mm}$, and the fins are listed in Table 3.3. The coolant considered is water.

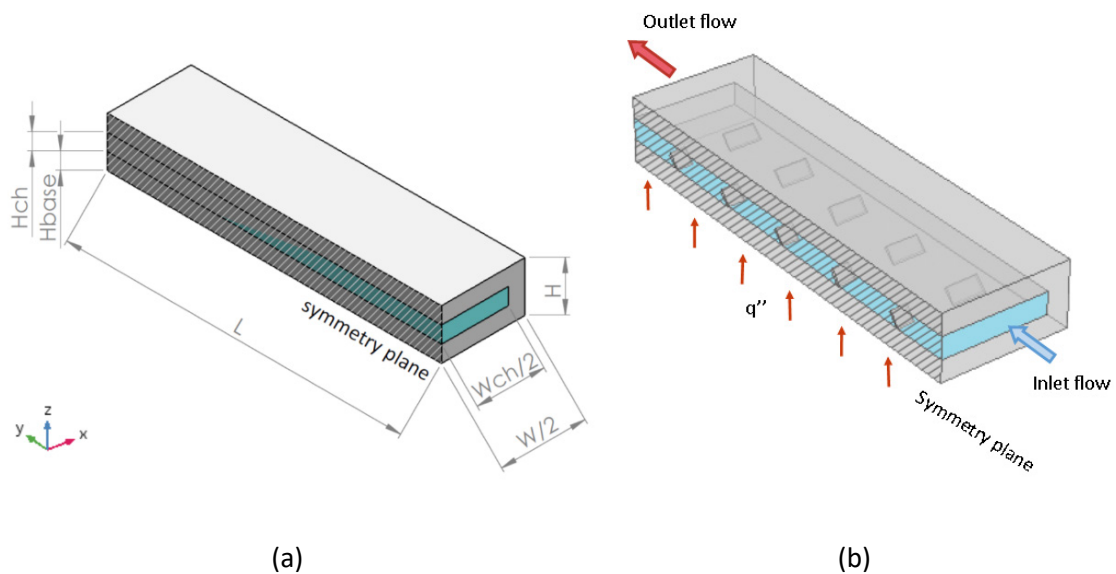


Figure 3.7. Schematic of (a) half plain microchannel and (b) half microchannel with fins inside assessed on numerical CFD simulations.

3. Self-adaptive fins acting as vortex generators

Parameter	Value	Description
L	2000 μm	Length of the microchannel
W	1000 μm	Width of the microchannel
H	300 μm	Height of the microchannel
H _{ch}	100 μm	Height of the fluid channel
W _{ch}	800 μm	Width of the fluid channel
H _{base}	100 μm	Wall thickness from the chip to the fluid
L _{fin}	75 μm	Height of the fin
W _{fin}	150 μm	Width of the fin
t _{fin}	10 μm	Thickness of the fin
Δx	333,30 μm	Distance between fins in x axis
Δy	400 μm	Distance between fins in y axis

Table 3.3. Main geometric dimensions of the microchannel and the fins.

3.2.2. Governing equations

3.2.2.1. General equations

The Reynolds number (1), calculated at the entrance of the microchannel, is 213, so the fluid flow is assumed to be laminar. Also, it is considered steady, incompressible and Newtonian, with gravitational effects neglected.

The water properties of density (ρ_f), dynamic viscosity (μ_f), specific heat ($C_{p,f}$) and thermal conductivity (κ_f) are calculated for temperature dependence, while the properties of silicon and silver are assumed constant ($\kappa_{Si} = 130 \text{ W/m}\cdot\text{K}$, $\kappa_{Ag} = 429 \text{ W/m}\cdot\text{K}$) due to low changes with temperature.

The governing equations for the flow are the continuity equation for conservation of mass and the Navier-Stokes equations for conservation of momentum (19), (20) [101].

$$\nabla \cdot (\rho_f \mathbf{u}) = 0 \quad (19)$$

$$\rho_f (\mathbf{u} \cdot \nabla) \mathbf{u} = -\nabla P + \nabla \cdot \mu_f [\nabla \mathbf{u} + (\nabla \mathbf{u})^T] \quad (20)$$

The energy equations for liquid (21) and solid (22) are also defined in function of the absolute temperature [102].

$$\nabla \cdot (\rho C_p \mathbf{u} T) = \nabla \cdot (\kappa_f \nabla T) \quad (21)$$

$$\kappa_s \nabla^2 T = 0 \quad (22)$$

3.2.2.2. Boundary conditions

At the inlet of the microchannel, the flow is considered fully developed with constant flow rate $Q = 7,02$ ml/min ($Re = 213$) and entrance length $L_{entr} = L/10$ (23). The flow rate selected is the minimum flow rate that ensures a maximum junction temperature of 85 °C. The inlet temperature (24) is settled at 20 °C and a constant heat flux, $q'' = 300$ W/cm², is applied at the bottom surface (25).

$$L_{entr} \nabla_t \cdot [-P + \mu(\nabla_t \mathbf{u} + (\nabla_t \mathbf{u})^T)] = -P_{entr} \mathbf{n} \quad (23)$$

$$T = T_{f,in} \quad (24)$$

$$-\mathbf{n} \cdot \mathbf{q} = q'' \quad (25)$$

No slip boundary condition at walls and symmetry boundary condition (symmetry plane defined in Figure 3.7) are assumed.

3.2.3. Grid independence test

To ensure the independency of the results from the grid size, a mesh sensitivity analysis is carried out (Figure 3.8). The mesh size is controlled by the physics and based on tetrahedral elements and 4 boundary layers. The relative mesh error is computed according to (26), where F_1 is the current value of any parameter and F_2 is the value of the same parameter with the finest grid size.

3. Self-adaptive fins acting as vortex generators

$$error (\%) = \frac{|F_1 - F_2|}{F_2} \cdot 100 \quad (26)$$

According to the obtained results, when the number of elements is bigger than $1 \cdot 10^6$, the relative error of pressure drop (ΔP) is lower than 1% (Figure 3.8), which is considered acceptable. The chosen grid has 1.368.586 elements and a ΔP error of 0,50 % with the finest grid.

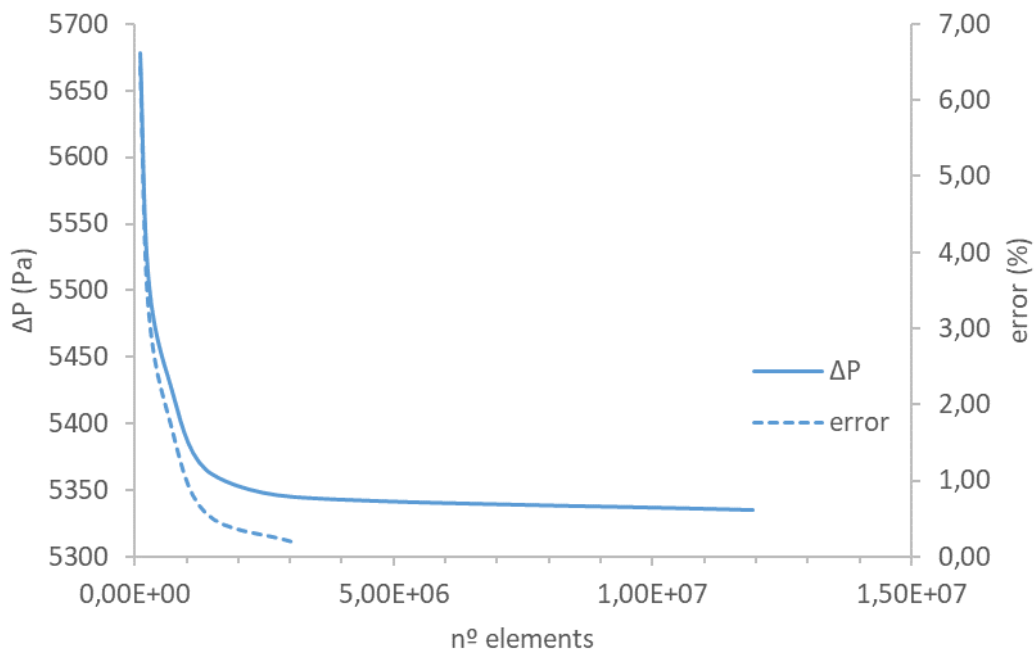


Figure 3.8. Grid independence test for the pressure drop within the microchannel.

3.2.4. Thermal performance assessment for different fin inclination

Through a numerical simulation, the inclination of the fins is changed to find the optimum position that ensures the maximum heat transfer enhancement. The inclination of the fins is varied from 10° to 80° respect the base of the channel and is expressed in function of the fin rise respect to the channel height (z/H). The heat transfer enhancement, defined in equation (8), increases with the fin rise until $z/H = 0,57$, where it reaches a maximum of $Nu/Nu_0 = 1,31$. If looking in a cut plane at the center of the channel, it is seen that the generation of vortices

behind the fin goes in the same line, as it increases until the fin inclination is around 50° respect the channel base ($z/H = 0,57$) and it stabilizes for higher inclinations (Figure 3.9). The vorticity magnitude in the figure below gives an idea of the mixing process in the flow.

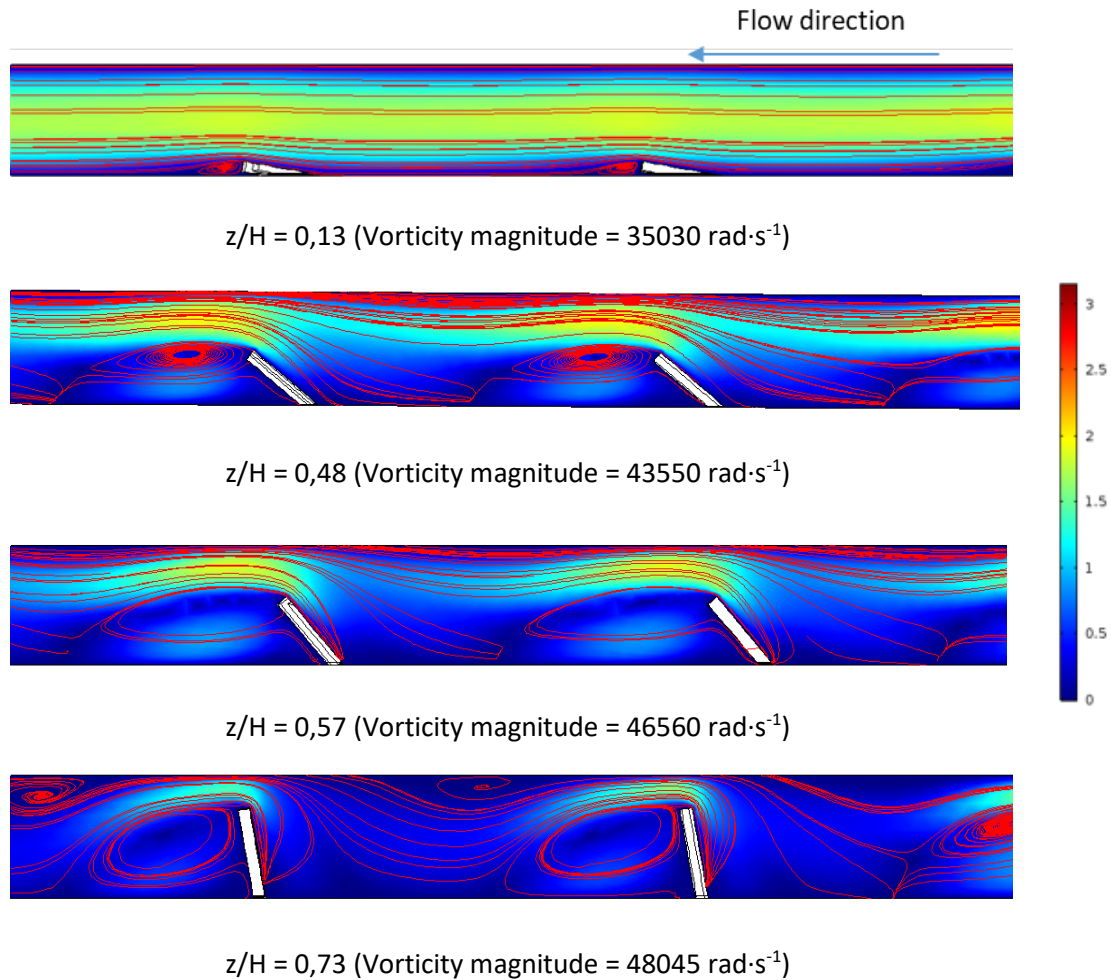


Figure 3.9. Vortex generation within the fluid inside the microchannel due to the variation of the fin inclination. The streamlines in red show the velocity field of the fluid and the color bar the velocity magnitude in m/s.

Additionally, as expected, the pressure drop, defined in equation (9), increases with the fin rise (Figure 3.10), achieving a maximum of $f/f_0 = 3,30$ when the inclination respect to the surface is 80° . For an optimum configuration, lower fin inclinations could be considered to avoid high pressure drops as, for a relative height of the fin compared to the channel of $z/H = 0,30$, the heat transfer enhancement is superior to 10 %, which was defined as the objective of this thesis, and lower pressure drops are induced.

3. Self-adaptive fins acting as vortex generators

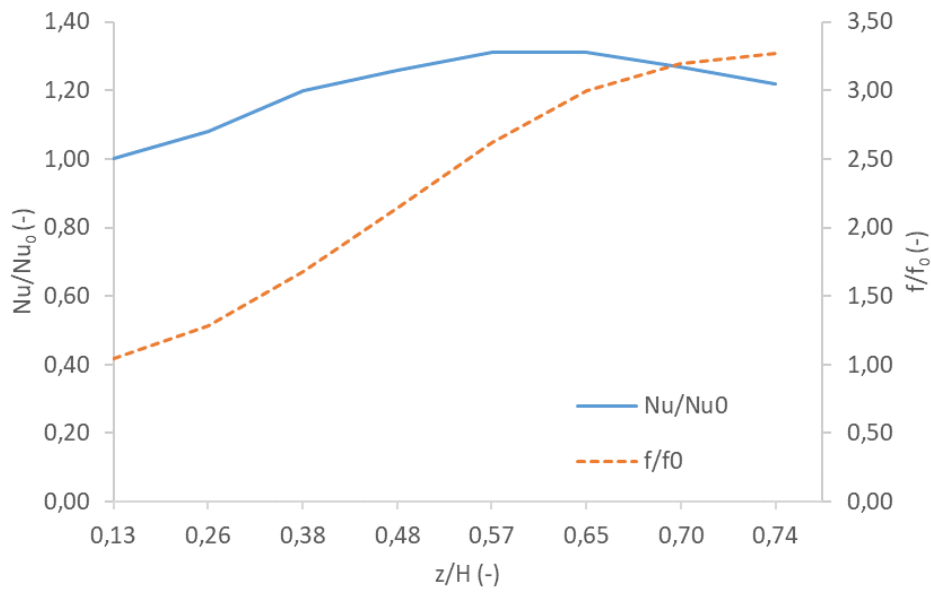


Figure 3.10. Heat transfer and pressure drop increment for different fin inclinations within the channel.

3.3. Bimetallic structures

3.3.1. Working principle

The working principle of the bimetallic self-adaptive fins is based on the bending theory of a bimetallic strip submitted to uniform heating [103]. Being α_1 and α_2 the coefficients of thermal expansion (CTE) of each material and assuming $\alpha_2 > \alpha_1$, the length of the metals will change if they are submitted to a temperature rise. If the metals are bonded together, the strip with high CTE will be subject to an axial compressive force F_2 , while the one with low CTE will be under an axial tensile force F_1 , what produces a moment that makes the strip to bend upwards (Figure 3.11).

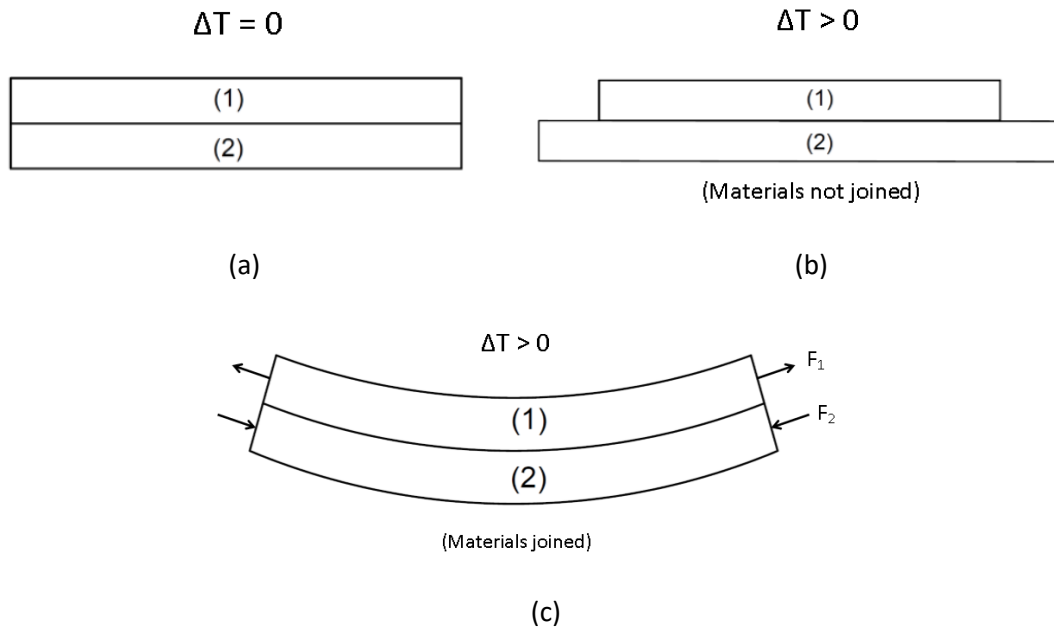


Figure 3.11. Behavior of a bimetallic strip while uniformly heated. (b) Assuming the materials are not joined and (c) assuming the materials are bonded together.

Based on the bending theory of a bimetallic strip, the self-adaptive fins are proposed to be made of two metallic materials with different CTE, creating a bimetallic structure fixed on its bottom ends (Figure 3.12). As the high CTE material is placed below, the fin will buckle upwards, achieving the effect of rising inside the microchannel. In the following section, different structures based on this working principle are assessed to find the optimum configuration.

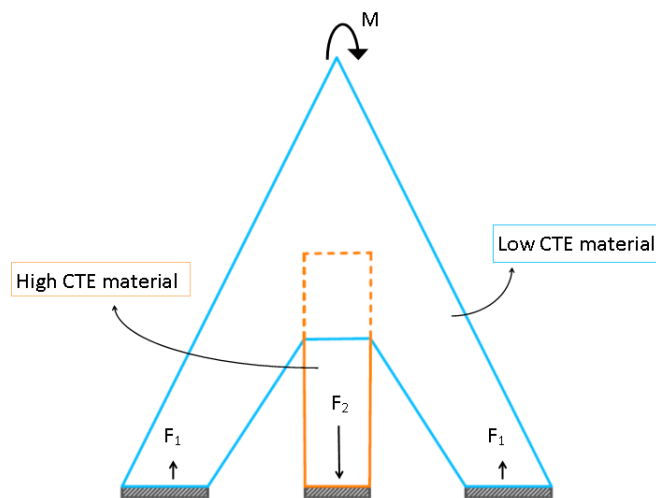


Figure 3.12. Working principle of the bimetallic self-adaptive fins, where F_1 and F_2 are the forces at which each material is subjected due to the behavior of the other material.

3. Self-adaptive fins acting as vortex generators

3.3.2. Minimum thickness for self-adaptive bimetallic fins inside a microchannel

The interaction between the fluid and the fin is numerically assessed to determine the minimum fin thickness that will resist the impact of the coolant flow without a significant backwards displacement and avoiding plastic deformations. A 2D numerical simulation is performed with Comsol Multiphysics to assess the interaction between the fluid and the fin structure.

The geometry defined consists of a bimetallic fin, able to adapt their shape in function of its own temperature, placed inside a water channel (Figure 3.13). The channel dimensions are 100 μm height, 1000 μm width and 300 μm length, with fully developed flow. The fin, which has a length of 200 μm , is made of two layers of metal joined together, with the bottom layer made of silver (Ag) and the top layer made of chromium (Cr) in this case. The two metallic materials have been selected due to their thermal properties. The same thickness is considered for both materials.

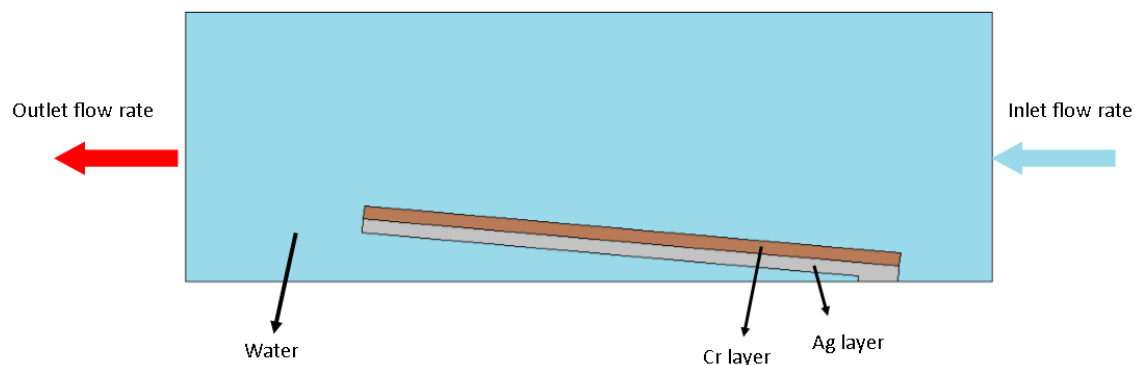


Figure 3.13. Schematic of a bimetallic fin inside the microchannel.

To assess the impact of the fluid on the bimetallic fin when is raised up, a temperature increase of 50 K is applied at the fin, which deforms upwards due to the difference in the thermal expansion coefficient (CTE) of both materials, Cr and Ag in this case (Figure 3.14). The mechanical properties of both materials are assumed constant at 50 $^{\circ}\text{C}$ (Table 3.4). The water inlet temperature considered is 20 $^{\circ}\text{C}$ and the flow rate is 7,02 ml/min, the same defined in the boundary conditions (section 3.2.2.2), which is assumed laminar, Newtonian and fully developed.

	Value		Unit
	Ag	Cr	
Yield strength (σ_y)	200	370	MPa
Young Modulus (E)	74,0	279	GPa
Poisson ratio (ν)	0,37	0,21	-
Secant thermal expansion coefficient (α)	$19,60 \cdot 10^{-6}$	$4,90 \cdot 10^{-6}$	K^{-1}

Table 3.4. Thin film Ag and Cr mechanical properties [104].

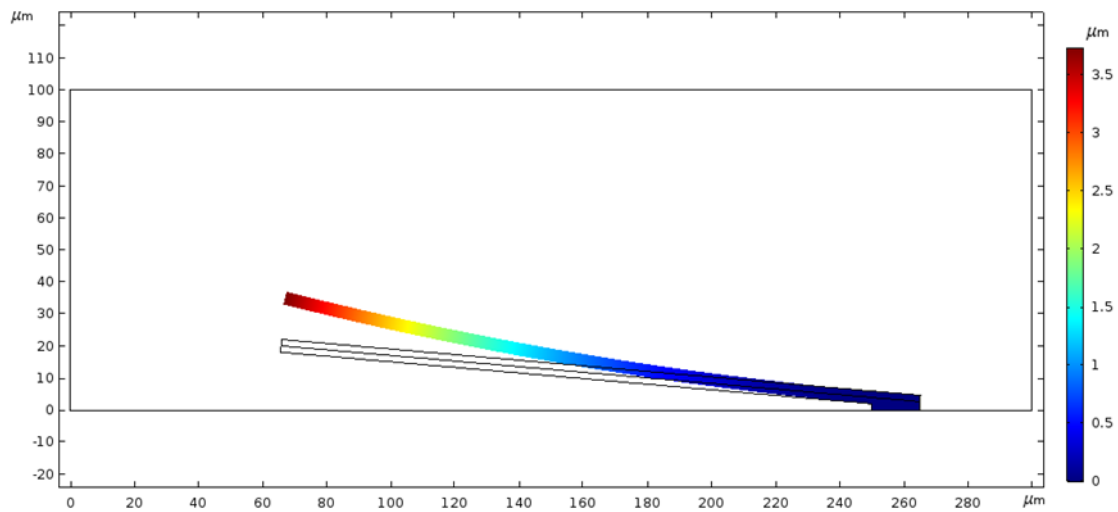


Figure 3.14. Displacement of a bimetallic fin due to a temperature increase of 50 K when $Q = 0$ ml/min. The color legend represents the total displacement of the solid. The initial position of the fin is represented without color.

The governing equations for the flow are the Navier-Stokes equation and the continuity equation (19), (20). For the mechanical analysis of this model, the governing equation are the equilibrium equation given by Newton's second law (27) and the Hooke's law (28), both expressed in terms of the deformation gradient tensor (G), the second Piola-Kirchhoff stress tensor (S) and the Green Lagrange strain tensor (ϵ) due to geometric nonlinearity [105].

$$0 = \nabla \cdot (G \cdot S)^T + \mathbf{F}_V \quad (27)$$

3. Self-adaptive fins acting as vortex generators

$$S = S_{ad} + J_i \cdot G_{inel}^{-T} \cdot (C : \epsilon_{el}) \cdot G_{inel}^{-1} \quad (28)$$

S_{ad} are additional stress contributions and J_i are the invariants of the deviatoric stress tensor. The right Cauchy-Green deformation tensor (C) is defined by (29).

$$C = G^T \cdot G \quad (29)$$

The elastic strain or elastic Green-Lagrange strain tensor (ϵ_{el}) is computed as (30).

$$\epsilon_{el} = \frac{1}{2} (G_{el}^T \cdot G_{el} - 1) \quad (30)$$

Where the elastic deformation gradient tensor is defined as (31).

$$G_{el} = G \cdot G_{inel}^{-1} \quad (31)$$

The inelastic deformation gradient tensor, derived from inelastic processes, considers the thermal expansion process (32). In this equation, I is the identity tensor [105]. The thermal gradient is computed from the thermal strain (33), which takes into account the secant coefficient of thermal expansion (α).

$$G_{inel} = G_{th} = I - \epsilon_{th} \quad (32)$$

$$\epsilon_{th} = \alpha(T - T_{ref}) \quad (33)$$

The strains are represented by the Green-Lagrange strain tensor (34).

$$\epsilon = \frac{1}{2} [(\nabla \mathbf{u})^T + \nabla \mathbf{u} + (\nabla \mathbf{u})^T \nabla \mathbf{u}] \quad (34)$$

To model the plastic behavior of the fins due to the impact of the fluid, the Von Mises yield criterion is used, computed with the Von Mises stress, a scalar value derived from the stress tensor (35), where σ_1 , σ_2 and σ_3 are the principal stresses. The Von Mises yield criterion states that a material starts to yield when the Von Mises stress is higher than the yield strength (36).

$$\sigma_{VM} = \sqrt{\frac{(\sigma_1 - \sigma_2)^2 + (\sigma_2 - \sigma_3)^2 + (\sigma_3 - \sigma_1)^2}{2}} \quad (35)$$

$$\sigma_{VM,max} \geq \sigma_y \quad (36)$$

Where $\sigma_{VM,max}$ is the maximum Von Mises stress computed at the fins.

The maximum Von Mises stress at the fin will appear when no flow rate flows through the channel and all the stress at the fin is due to the thermal displacement. As the fluid flows in the opposite direction of the fin rise, it tends to bend backwards the fin and counteracts the stress due to thermal displacement, reducing the overall Von Mises stress (Figure 3.15).

The thickness of the bimetallic fin influences the maximum Von Mises stress achieved. Hence, in order to avoid plastic deformations at the fin when the temperature rises, the maximum Von Mises stress is computed for different fin thicknesses assuming the worst boundary conditions of flow ($Q = 0$ ml/min), when no flow rate will counteract the thermal displacement and maximum deflections of the fins will be achieved, and a temperature increase of 50 K at the fin (Figure 3.16).

As the yield strength of silver is lower than the one of chromium (Table 3.4), the Ag value is considered as the stress limit to avoid plastic deformations. In this case, when the thickness of the bimetallic fin is higher than 1,20 μm (0,60 μm each layer), the maximum Von Mises stress is lower than the yield strength of the silver, so no plastic deformation will be reached due to thermal stress when $\Delta T \leq 50$ K.

3. Self-adaptive fins acting as vortex generators

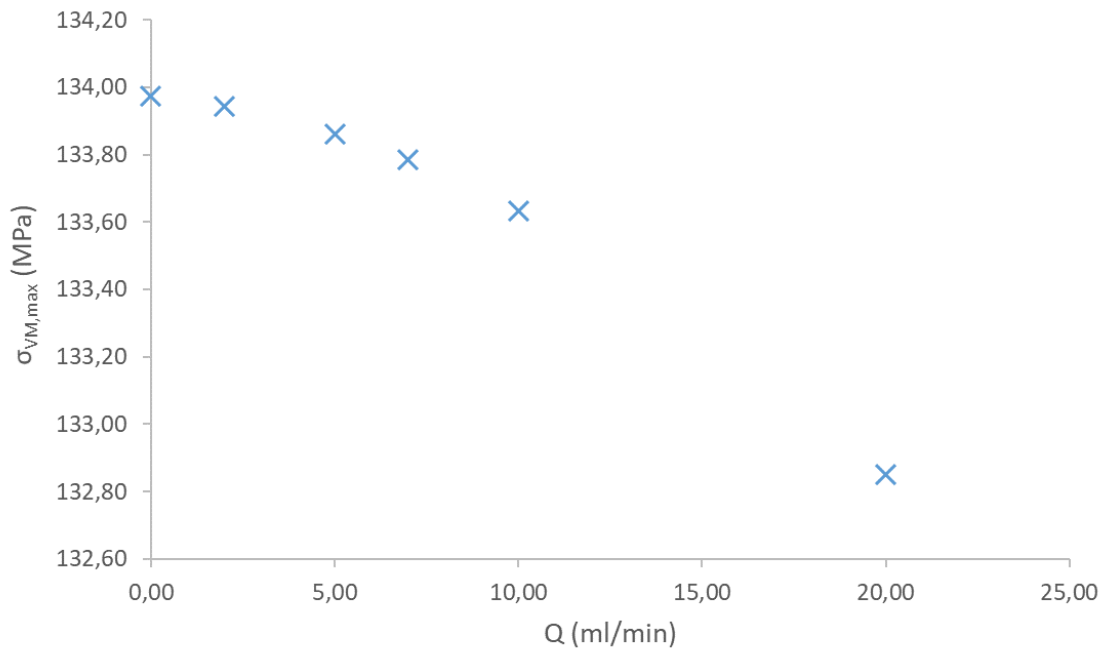


Figure 3.15. Maximum Von Mises stress at a bimetallic fin for different flow rates. The considered thickness of the fin in this case is $t_{fin} = 4 \mu\text{m}$.

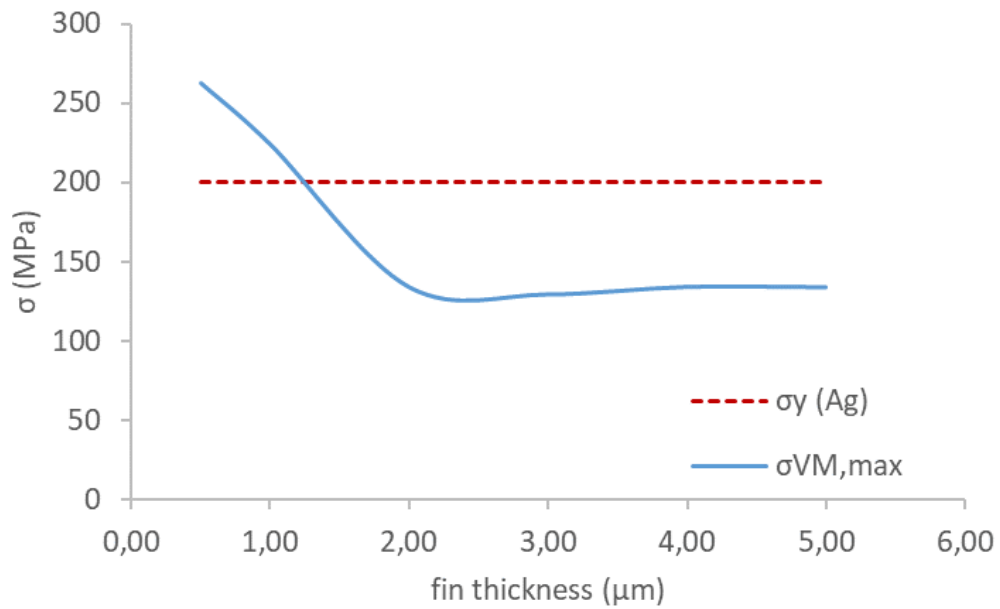


Figure 3.16. Maximum Von Mises stress at the fin when $\Delta T = 50 \text{ K}$ and $Q = 0 \text{ ml/min}$ assessed for different fin thicknesses and compared with the yield strength of the silver.

Moreover, when a flow rate is applied through the channel, the maximum vertical displacement achieved by the fin due to temperature increase, will be reduced. This reduction depends on the fin thickness and the applied flow rate (Figure 3.17). Assuming a flow rate of 7,02 ml/min, defined in the boundary conditions, we can consider acceptable a fin thickness of 2 μm (1 μm for Ag layer and 1 μm for Cr layer), where the reduction of the fin displacement due to the flow is less than 3 %. In this case, the maximum Von Mises stress achieved is 128 MPa, so no plastic deformations are reached.

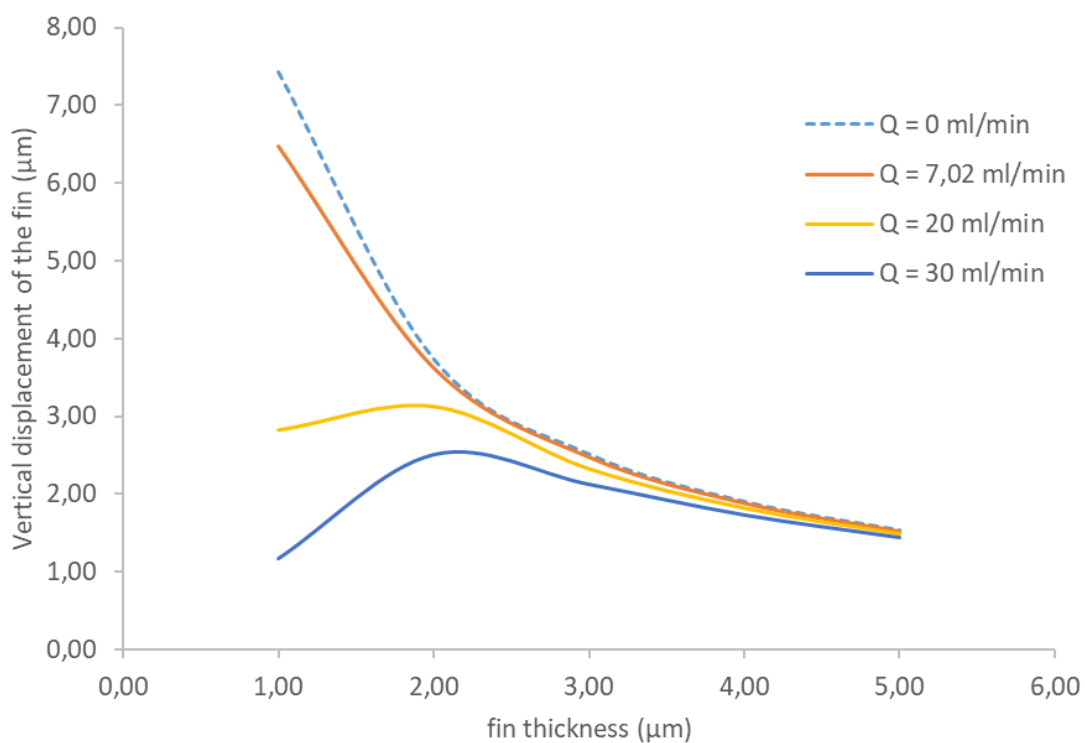


Figure 3.17. Maximum vertical rise of the bimetallic fin due to a temperature increase of 50 K for different fin thicknesses and flow rates.

3.3.3. Proposed geometries of the fins

Different fin geometries based on bimetallic structures have been proposed to find an optimum self-adaptive fin, able to provide large vertical deflections while avoiding plastic deformations when submitted to a uniform temperature increase of 50 K (Table 3.5).

3. Self-adaptive fins acting as vortex generators

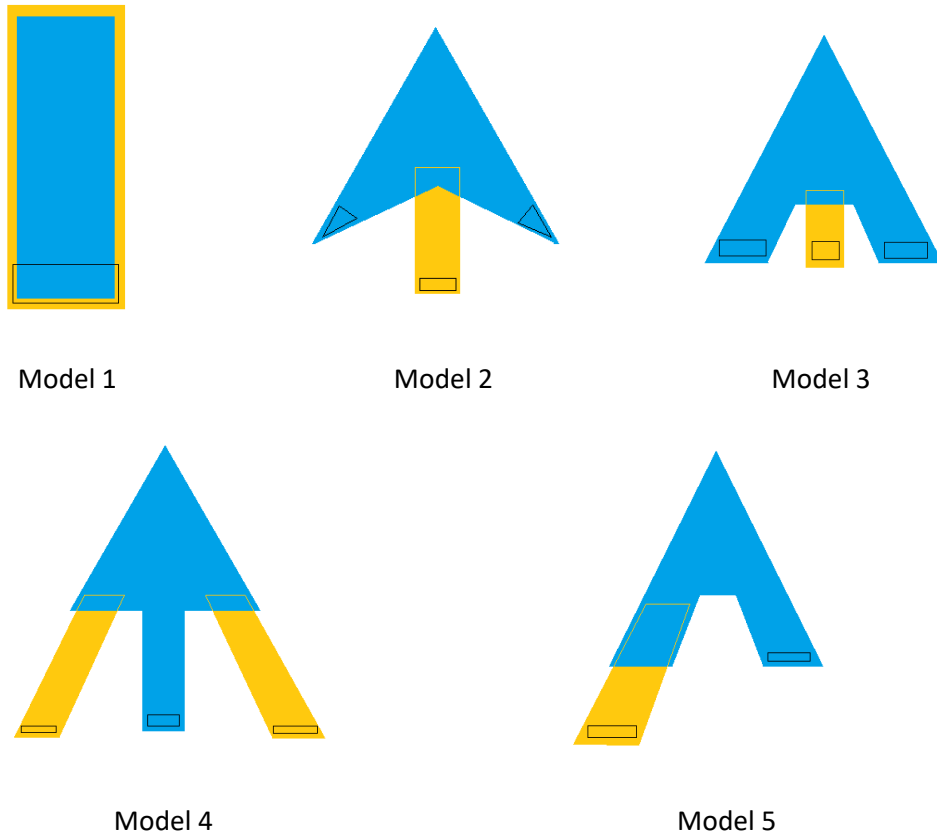


Table 3.5. Different structures proposed for the bimetallic self-adaptive fins. The low CTE material is represented in blue while yellow represents the high CTE material. The anchors that fix the fins to its restraint are remarked in black.

The numerical model of the different proposals is defined by equations (27) - (34). All the fins are considered to be fabricated with Ag as high CTE material ($\alpha_{Ag} = 19,60 \cdot 10^{-6} K^{-1}$) and Cr as low CTE material ($\alpha_{Cr} = 4,90 \cdot 10^{-6} K^{-1}$), with a total thickness of $2,50 \mu m$ ($1,50 \mu m$ for the Ag layer and $1,00 \mu m$ for the Cr layer). The different geometries proposed have been optimized through a parametric study to ensure the maximum deflection and minimum stress. A detailed explanation of each model is given below.

- **Model 1**

The first proposed model consists on a bimetallic strip fixed by an anchor at its bottom part (Figure 3.18). The high CTE material is placed below the lowest one to ensure an upwards deflection.

The length and width of this fin are $250\ \mu\text{m}$ and $100\ \mu\text{m}$ respectively. The anchor dimensions and geometry were adjusted through a parametric study to minimize the Von Mises stress while considering a minimum anchor length about 10 % of the length of the fin due to microfabrication restrictions. The final anchor is a rectangle of $30\ \mu\text{m}$ high and $90\ \mu\text{m}$ width, with the corners rounded.

When applying a temperature increment of 50 K to this model, the maximum vertical displacement achieved was $11,07\ \mu\text{m}$, 4,43 % of the length of the fin.

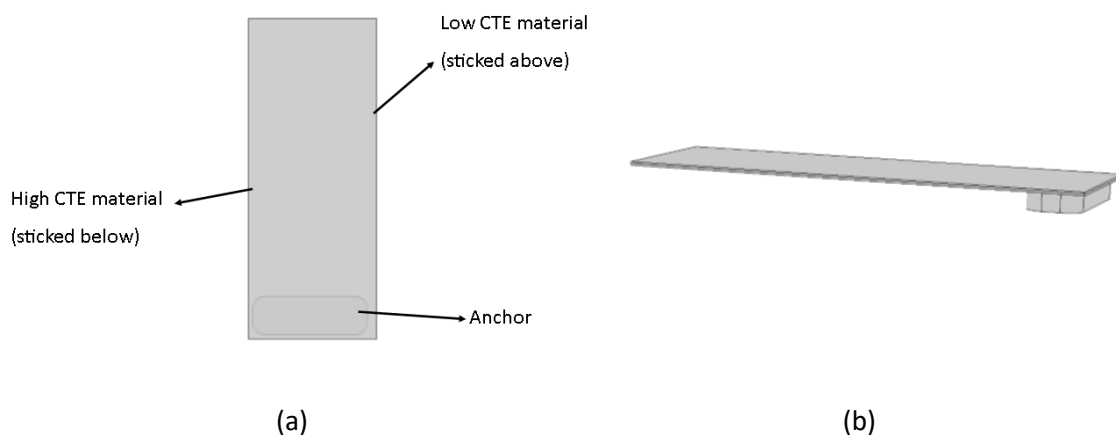


Figure 3.18. Schematic of the model 1 of bimetallic fins. (a) Frontal view. (b) Lateral view.

- **Model 2**

This proposed model consists on a strip of high CTE material centered below a triangular layer of low CTE material. Both materials are fixed by its bottom ends (Figure 3.19) and the working principle of this fin is the same as the one defined in Figure 3.12.

The length and width of the triangular layer are $350\ \mu\text{m}$ and $300\ \mu\text{m}$ respectively. Additionally, the anchors of the low CTE material have been adjusted through a parametric study to minimize the induced stresses due to deflection, creating triangular anchors with rounded base that have a length around 10 % the total length of the fin.

The length and width of the high CTE material strip have been adjusted through a parametric study to achieve maximum deflections without exceeding the elastic limit of the material. The final dimensions of the strip are $45\ \mu\text{m}$ width and $350\ \mu\text{m}$ length. Similar to model 1, the anchor

3. Self-adaptive fins acting as vortex generators

of the high CTE material is a rectangle with rounded corners, with $30\ \mu\text{m}$ width and $35\ \mu\text{m}$ height.

For the default defined thicknesses and materials ($1,50\ \mu\text{m}$ of Ag and $1,00\ \mu\text{m}$ of Cr), the maximum displacement achieved by the fin when the temperature increment was $50\ \text{K}$, was $9,83\ \mu\text{m}$ ($2,81\ \%$ of its length).

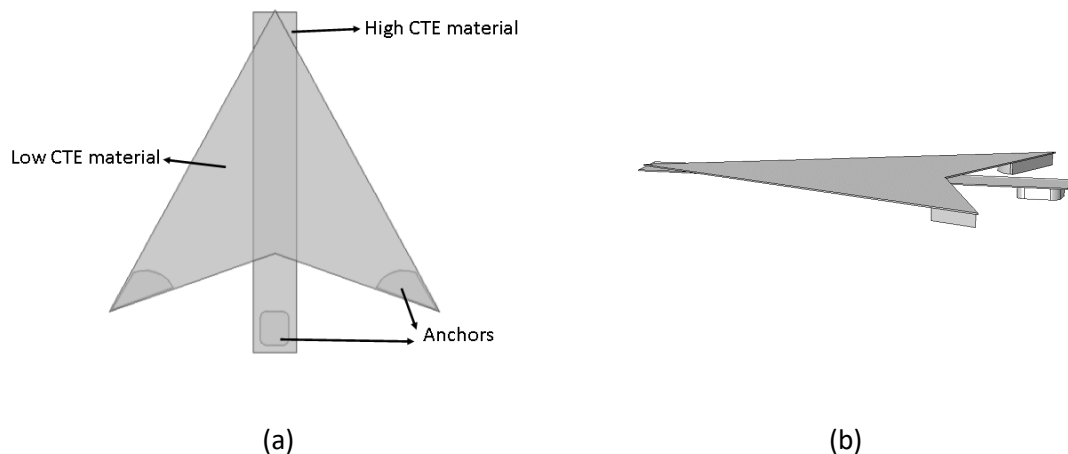


Figure 3.19. Schematic of the Model 2 of the bimetallic fins. (a) Frontal view. (b) Lateral view.

- **Model 3**

The design of this model is pretty similar to Model 2, but the central and bottom part of the triangle structure have been changed for mechanical stress reduction (Figure 3.20).

The sizes of the low CTE material are $350\ \mu\text{m}$ length and $300\ \mu\text{m}$ width, and its central dimensions and anchors have been adjusted through a parametric study. The anchors of the low CTE material are rectangular with rounded corners with $80\ \mu\text{m}$ width and $20\ \mu\text{m}$ height.

The dimensions of the high CTE material have been optimized for maximum deflection and minimum stress, having finally a strip of $40\ \mu\text{m}$ width and $350\ \mu\text{m}$ length. Its anchor is also rectangular with rounded corners, with $30\ \mu\text{m}$ width and $70\ \mu\text{m}$ length.

When applying a uniform temperature increase of $50\ \text{K}$, the maximum displacement achieved was $11,92\ \mu\text{m}$, $3,41\ \%$ of its length.

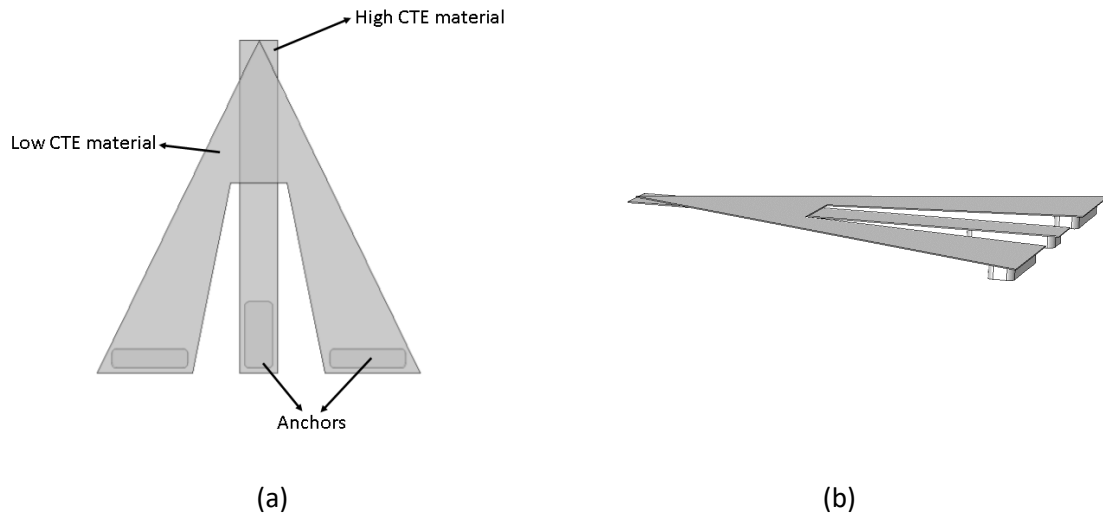


Figure 3.20. Schematic of the model 3 of the bimetallic fins. (a) Frontal view. (b) Lateral view.

- **Model 4**

In this proposed structure, the high CTE material pushes the bimetallic fin from the lateral sides while the low CTE material defines an arrow geometry. Both materials are anchored by its bottom ends (Figure 3.21).

The dimensions of the low CTE material are $85\ \mu\text{m}$ length and $160\ \mu\text{m}$ width for the triangle part and $65\ \mu\text{m}$ length and $40\ \mu\text{m}$ width for the rectangular part. The anchor is rectangular with rounded corners and size $32\ \mu\text{m} \times 10\ \mu\text{m}$. The lengths of both parts, the width of the rectangular part and the anchors have been optimized through a parametric study.

The high CTE material part consists of two parallelograms with sizes $45\ \mu\text{m} \times 96\ \mu\text{m}$ and an inclination of $68,70^\circ$. The geometry of the anchors is the same as for the low CTE part, with size of $22\ \mu\text{m} \times 24\ \mu\text{m}$. All the dimensions have been optimized through a parametric study.

Within this configuration, the maximum deflection achieved was $2,61\ \mu\text{m}$, $1,74\%$ of the total length.

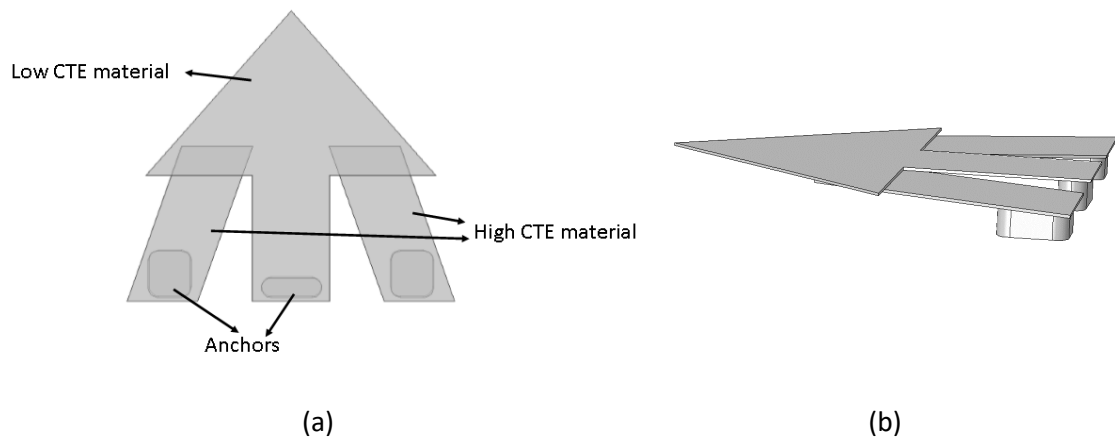


Figure 3.21. Schematic of the bimetallic fin corresponding to model 4. (a) Frontal view. (b) Lateral view.

- **Model 5**

The last designed model consists on a high CTE material strip that pushes from one side a triangular fin on low CTE material (Figure 3.22). The high CTE material is placed below the low CTE material to ensure upward deformations and both metals are fixed by its bottom ends. Within this structure, the generation of flow vortices inside the channel is expected to improve due to the non-symmetric deformations.

The low CTE material consists on a layer of Cr of 350 μm length and width. It is fixed to the substrate by a rectangular anchor with rounded corners placed at the right of the fin, with dimensions 90 μm x 20 μm .

The high CTE material is a parallelogram Ag strip that has a length of 460 μm , a width of 100 μm and an inclination of 11 $^\circ$. Similar to the low CTE material layer, this strip is anchored by its lower part to the substrate through a rectangular anchor with rounded corners and dimensions of 80 μm width and 10 μm height.

The parameters that have been optimized through a parametric numerical simulation are the dimensions of both anchors, the length, width, inclination and position of the high CTE material and the dimensions of the paths of the low CTE material.

Within these considerations, the maximum deformation of the fin was 24,27 μm , (6,93 % of the length of the fin).

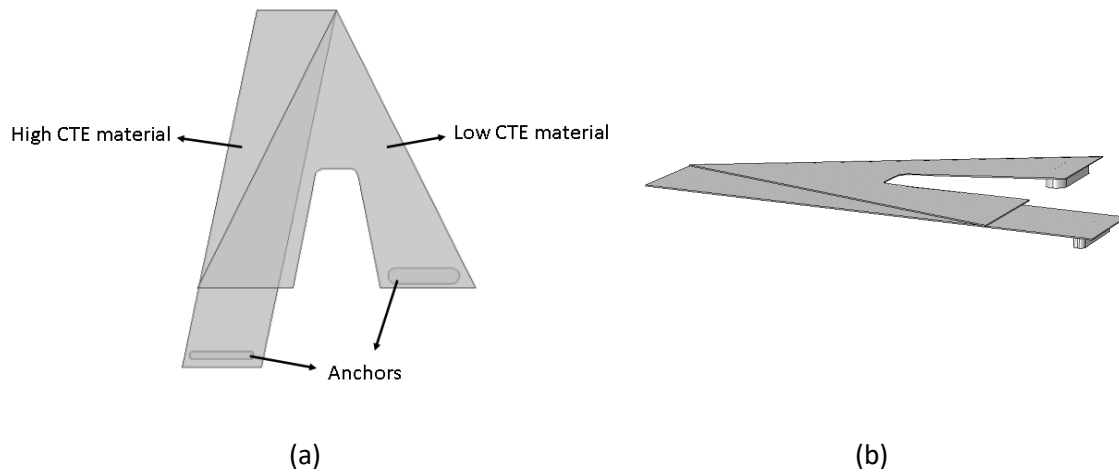


Figure 3.22. Schematic of the model 5 of the bimetallic fins. (a) Frontal view. (b) Lateral view.

Figure 3.23 summarizes the vertical displacements of all the proposed models as percentage of its total length. The highest vertical deflection is achieved by model 5, that reaches a deflection almost 7 % its length. Considering a channel height of $100\ \mu\text{m}$, the relative height of the fin within the channel is 0,24 and, according to previous assessments (Figure 3.10), this could represent a maximum heat transfer enhancement (Nu/Nu_0) of 1,10, which represents an increase of 10 % compared to plain systems, which goes in accordance with the initial objectives. Additionally, the maximum Von Mises stress at the junctions of the fins, due to the vertical displacement, is very close to the elastic limit of the silver, what can induce on plastic deformation for large temperature increments.

3. Self-adaptive fins acting as vortex generators

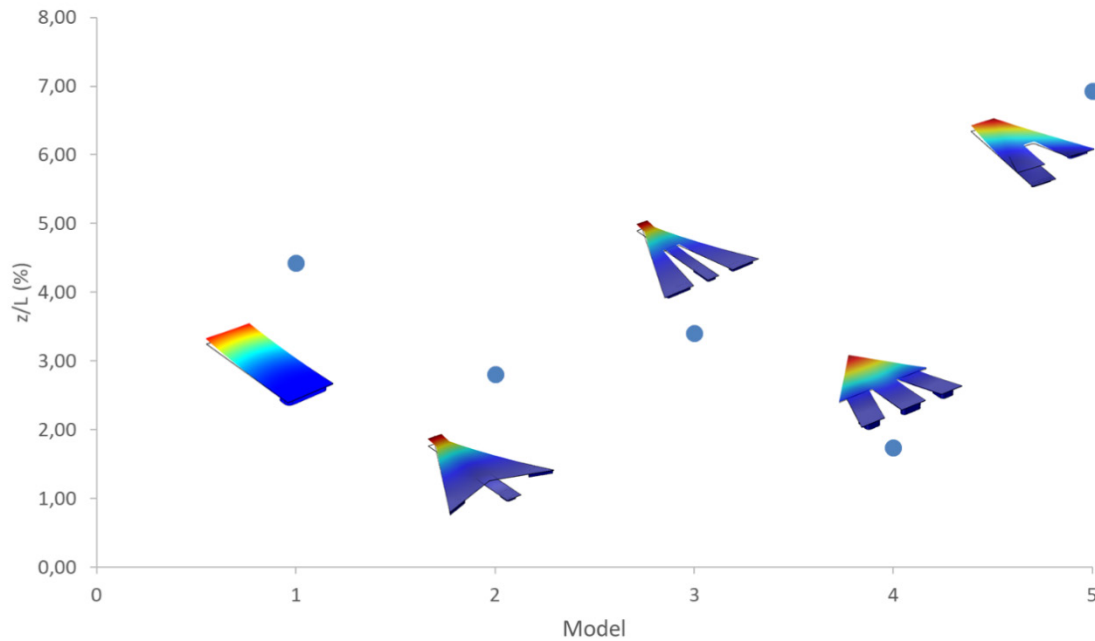


Figure 3.23. Vertical displacement (in % of the length of the fins) of each model of bimetallic fins.

3.3.4. Microfabrication of the fins

The microfabrication of the bimetallic fins was done by the author of this thesis, in collaboration with other experts, during an international research stage at the University of Sherbrooke, in Québec, Canada.

3.3.4.1. *Microfabrication process flow*

A microfabrication process flow was defined for the fabrication of the bimetallic self-adaptive fins, together with the self-adaptive microvalve (explained in section 1.3.1), (Figure 3.24), using a double lift-off method for the fabrication. First, a sacrificial layer was deposited on a silicon wafer (Figure 3.24a) and then, anchors were created in the sacrificial layer by wet etching or dry plasma etching (Figure 3.24b). For both cases photoresist was used as a mask. After photolithography using single layer negative resist or bi-layer resist (Figure 3.24c), the high CTE material was deposited by sputter, evaporation or plasma-enhanced chemical vapor deposition (PECVD) technique (Figure 3.24d). Lift-off was then accomplished by immersing the sample in acetone (Figure 3.24e). The same procedure was repeated for the low CTE material (Figure 3.24f-

h). Finally, the sacrificial layer was removed by wet etching to release the fins and the valves (Figure 3.24i).



a) Sacrificial layer deposition.



b) Photolithography (Mask 1) and Sacrificial layer etching to create the anchors.

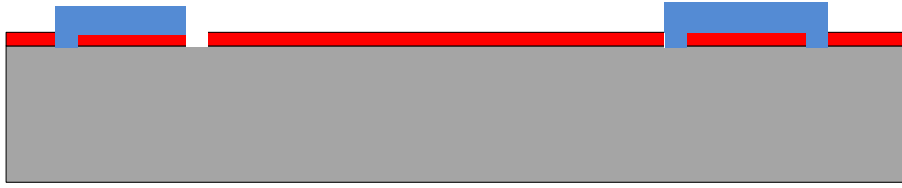


c) Photolithography (Mask 2).



d) Metal 1 deposition.

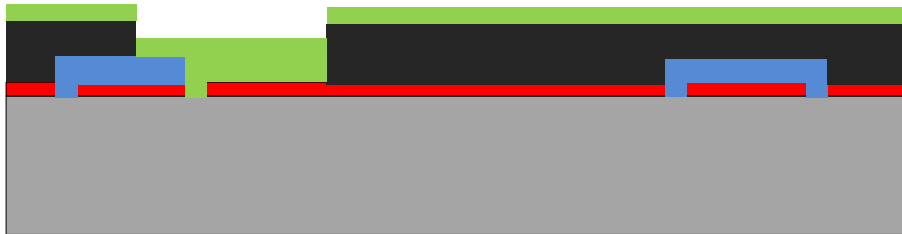
3. Self-adaptive fins acting as vortex generators



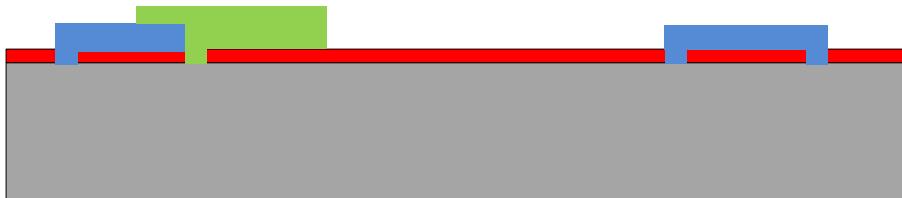
e) Lift-off 1.



f) Photolithography (Mask 3).



g) Material 2 deposition.



h) Lift-off 2.



i) Releasing: sacrificial layer removal.

Figure 3.24. Microfabrication process flow for the fabrication of bimetallic self-adaptive fins (left side of the Si wafer, blue and green colors) and self-adaptive microvalve (right side of the Si wafer, in blue).

3.3.4.2. Microfabrication feasibility study

A microfabrication test was done before the fabrication of the bimetallic fins to validate the process flow using one material (steps a-e + i in the process flow). A 2 μm silicon dioxide (SiO_2) film deposited by PECVD was used as sacrificial layer. The material used to fabricate the fins was a 3,50 μm thick film of silver, deposited by evaporation method. The sacrificial layer was completely removed by immersing the samples in buffered oxide etch (BOE) for 400 min. In this test, the fins were fully released and showed no signs of residual stress (Figure 3.25).

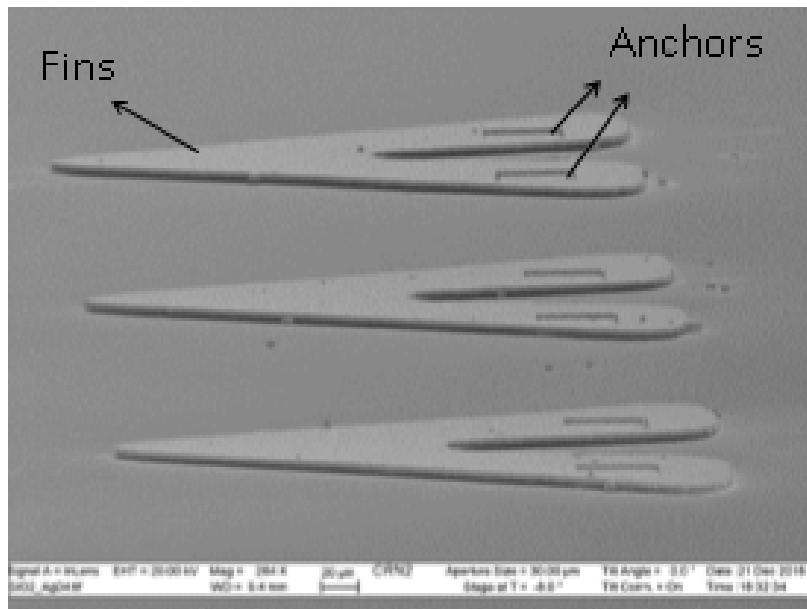


Figure 3.25. Scanning electron microscope (SEM) image of Ag fins fabricated for feasibility study.

3.3.4.3. Microfabrication of bimetallic self-adaptive fins

For the fabrication of the self-adaptive bimetallic fins, a first assessment using Aluminum as high CTE material and Chromium as low CTE material was done, however, the result wasn't successful as aluminum was etched. In order to find a suitable combination of suitable metallic materials, different material combinations are proposed (Table 3.6). An explanation of the succeeded case (Case 8) is given in detail below while the results obtained with other cases are detailed in

3. Self-adaptive fins acting as vortex generators

Annex I. For each material combination, all the models detailed in Table 3.5 are done as they are all printed in the same photomasks.

Case	Sacrificial layer material	High CTE material (CTE ·10 ⁻⁶ K ⁻¹)	Low CTE material (CTE ·10 ⁻⁶ K ⁻¹)	Achieving
1	SiO ₂	Ag (20)	Nb (7)	Not succeed
2	Au	Ni (13)	Nb (7)	Not succeed
3	Au	Ni (13)	Cr (5)	Not succeed
4	Ti	Ag (20)	Mo (5)	Not succeed
5	Al	Au (14)	Cr (5)	Not succeed
6	Al	Ti (8,50)	Cr (5)	Not succeed
7	SiO ₂	Au (14)	Mo (5)	Not succeed
8	SiO ₂	Ag (20)	Au (14)	Succeed
9	W	Al (22)	SiN (3,50)	Not succeed
10	W	Ag (20)	SiN (3,50)	Not succeed
11	Al	Au (14)	SiN (3,50)	Not succeed
12	Al	Nb (7)	SiN (3,50)	Not succeed

Table 3.6. Material combinations tried within the microfabrication of the bimetallic fins.

- **Case 8**

The material of the sacrificial layer was in this case silicon dioxide (SiO₂), the high CTE material was silver (Ag) and the low CTE material was gold (Au). The thicknesses of each material film are listed below:

- SiO₂ = 200 nm
- Ag = 500 nm
- Au = 750 nm

This combination was fabricated successfully, following all the microfabrication steps of the process flow. A scanning electron image (SEM) of the Model 3 described in Table 3.5 is given in Figure 3.26.

3. Self-adaptive fins acting as vortex generators

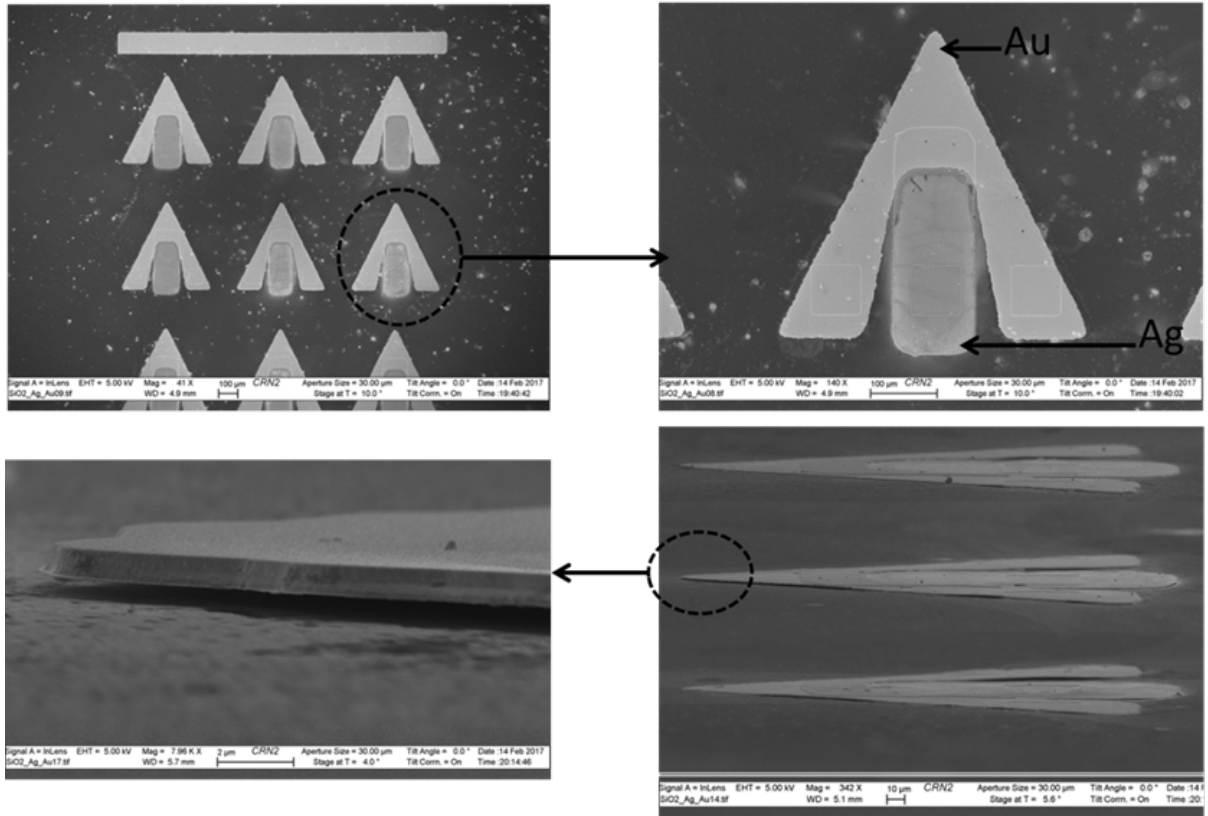


Figure 3.26. SEM images of fabricated Ag-Au bimetallic fins (Model 3) after releasing step.

Once this material combination was successfully fabricated, a simple experimental test bench was designed to test and visualize the behavior of the self-adaptive fins when submitted to a temperature increment (Figure 3.27). Note that within this test bench, the temperature of the fin would be quite lower than the temperature of the hot plate due to the big support of aluminum.

3. Self-adaptive fins acting as vortex generators

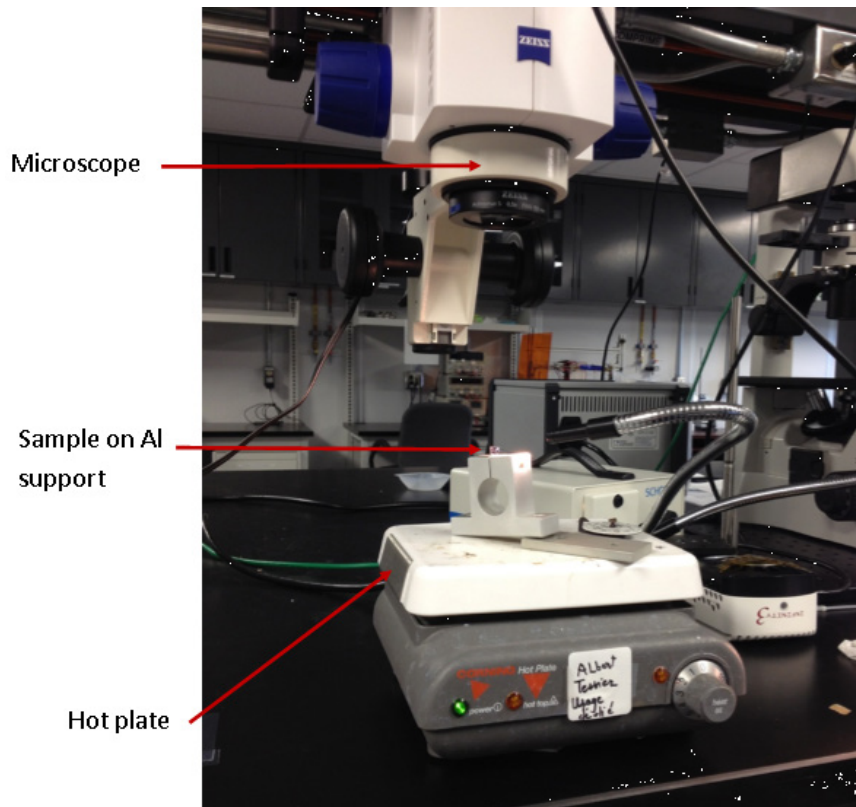
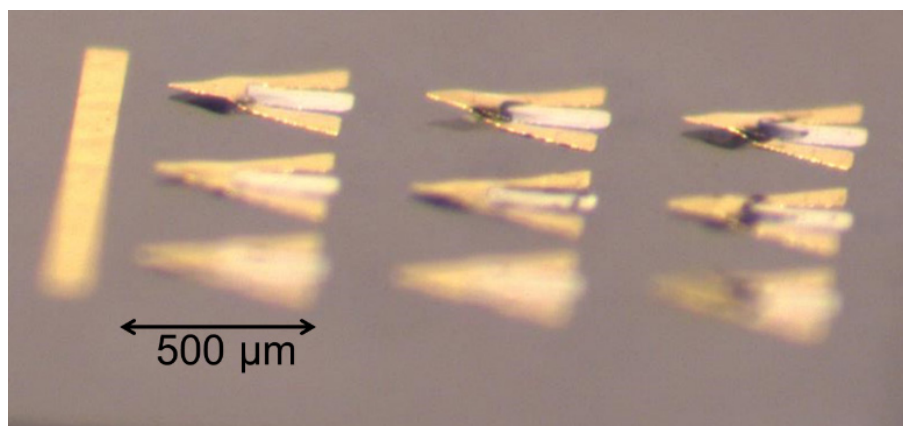
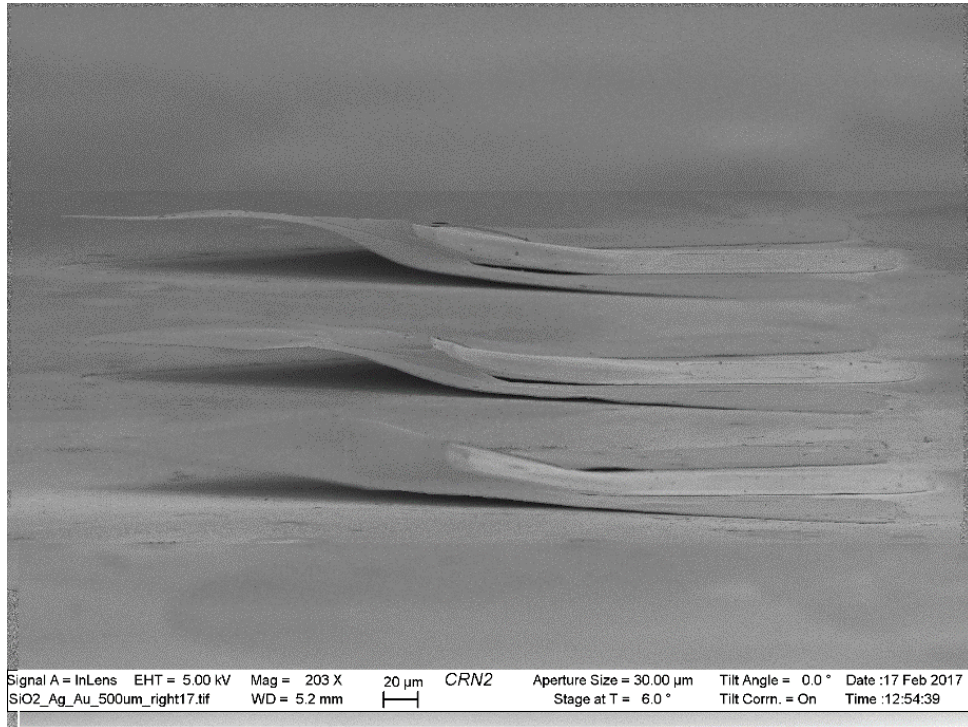


Figure 3.27. Experimental setup for deflection visualization of the self-adaptive fins.

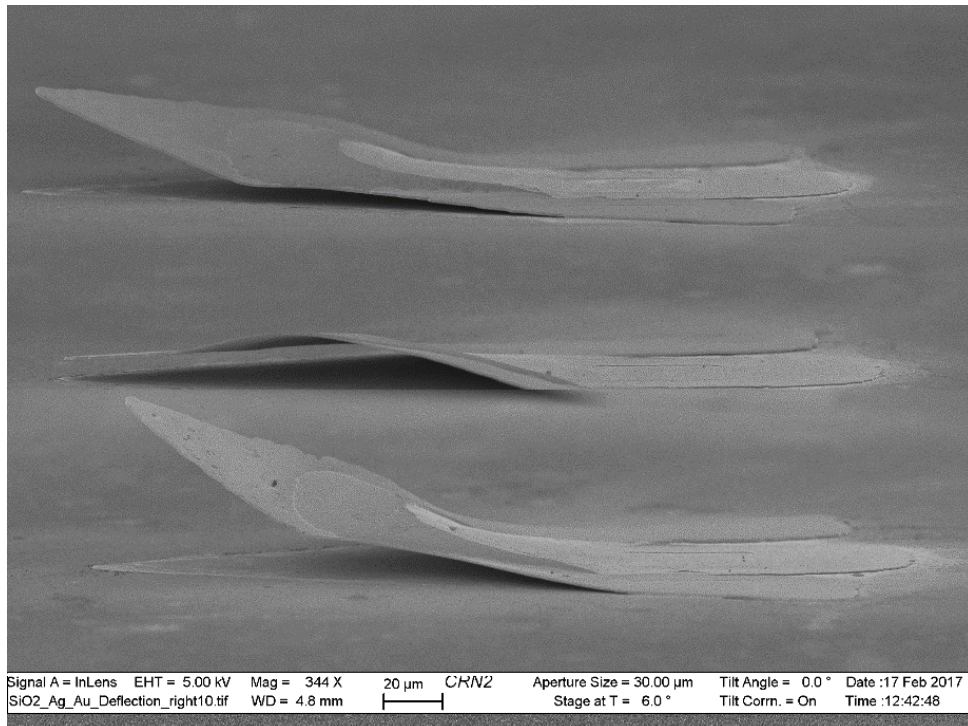
At low temperatures, small deflections were found probably due to the low CTE ratio between the two metals used for the fabrication of these fins. However, at high temperatures ($T_{\text{hot plate}} = 200 \text{ }^{\circ}\text{C}$) plastic deformations were reached (Figure 3.28).



(a)



(b)



(c)

Figure 3.28. (a) Microscopic image of the plastic deformation of the Ag-Au fins when submitted to high temperatures. (b), (c) SEM image of plastic deformations at the Ag-Au fins.

3. Self-adaptive fins acting as vortex generators

Some fins presented no deflection at the tip, what could be related to static friction at the releasing step (Figure 3.29).

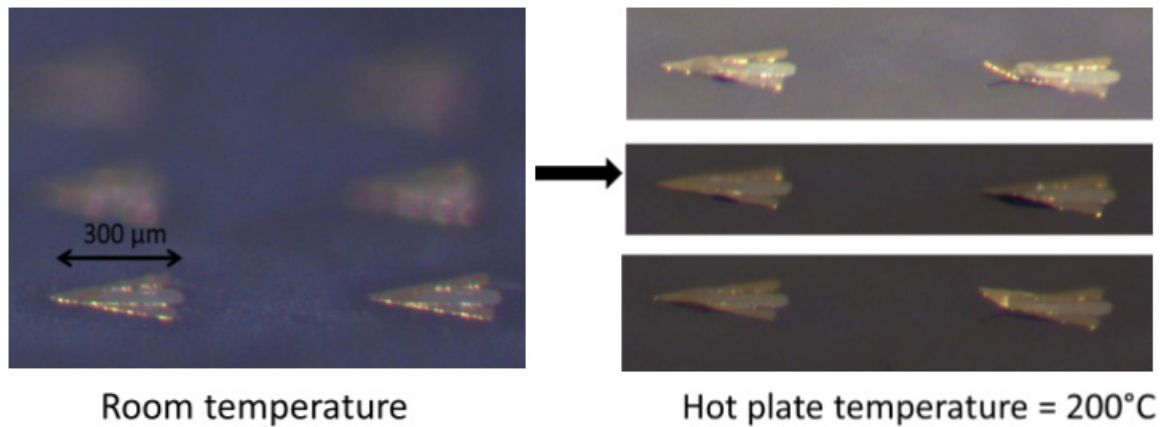


Figure 3.29. Completely released bimetallic fins at room temperature and at high temperature.

3.3.5. Conclusions and perspectives on bimetallic self-adaptive fins

Bimetallic fins seemed a quite promising technology for self-adaptive movements in microelectromechanical systems (MEMS). Nevertheless, after numerical and experimental tests performed within this work, some difficulties have been seen on achieving the goal of heat transfer enhancement within microchannel through this type of fins

Firstly, according to previous simulation results, it was found that the optimum relative height of the fins to maximize the heat transfer enhancement was $z/H = 0,60$ (Figure 3.10). With the numerical studies of the proposed geometries of bimetallic fins, the maximum relative height achieved was $z/H = 0,24$ for model 5, that reached a vertical displacement of $24,27 \mu\text{m}$ with a fin length of $350 \mu\text{m}$. Within this case, the expected heat transfer enhancement ($Nu/Nu_0 = 1,15$ according to Figure 3.10) achieves the initially defined goal of 10 % enhancement.

Nevertheless, the microfabrication process of the self-adaptive fins presented large difficulties to find a suitable combination of high and low CTE materials to create the bimetallic structure. From all the studied material combinations, one was successfully fabricated (Ag as high CTE material and Au as low CTE material), however, due to the small difference between the CTE of

both materials, the achieved deflection of the fin was pretty small. Furthermore, plastic deformations were seen when the fins were submitted to high temperatures. Figure 3.16 demonstrated that small thicknesses of the bimetallic structure lead to higher stresses, so thicker films of material could avoid the plastic deformations.

Another approach to find feasible solution for self-adaptive bimetallic fins within microscale, could be to try different material combinations such as a bi-layer fin made of a polymer and a metal. An experimental test was done in this way, with a structure made of Kapton, chromium and nickel. 30 nm of Cr and 60 nm of Ni were deposited by evaporation on a 25 μm Kapton film, with 1 cm length and 5 mm width. The observed results when the fin was submitted to a temperature increase were quite interesting. When the temperature increase was around 60 K, the displacement of the fin was 2 mm, a 20 % of its length, higher than the results obtained with bimetallic structures. Additionally, no plastic deformations were seen when the fin was submitted to high external stresses. The use of a polyamide film to fabricate the self-adaptive fins present the advantages of having large CTE (from $35 \cdot 10^{-6} \text{K}^{-1}$ to $55 \cdot 10^{-6} \text{K}^{-1}$), high flexibility and thicker layers. Nevertheless, compatibility problems between metal and polymer layers when fabrication on microscale could be expected, as well as a decrease of the resistance to flow pressure.

Clearly, further research needs to be performed within this subject, both in material combination and fabrication and also within fin distribution to see if it is possible to achieve a roughness pattern able to perform higher heat transfer enhancement. However, an alternative solution to the bimetallic self-adaptive fins, with a more robust structure and easier microfabrication, seems to be found and is explained in detail in the next section.

3.4. Doubly clamped structures

3.4.1. Motivation

The difficulties seen within the fabrication and performance of the bimetallic fins turned into the search of new systems able to provide the same or better results of heat transfer

performance within easier ways of fabrication. For this reason, a different working principle for the self-adaptive fins acting as vortex generators within a liquid cooling device is proposed in this section.

This new proposed self-adaptive fins are based on the microfluidic valves presented previously (section 1.3.1.2) and have the same working principle. The main advantage that the use of valves as fins presents over the bimetallic ones is the easier microfabrication process, as it has already been designed within STREAMS project for the fabrication of the valves inside the microfluidic cells. With this working principle, the fins and valves can be fabricated at the same steps of the microfabrication process, using the same photomasks and materials, which simplifies the whole process. Additionally, the use of this new kind of fins will present both more robustness and thermal conduction, as they are doubly clamped to the silicon base instead of being simple clamped like the bimetallic fins. However, due to its geometric structure, the generation of vortices in the flow can be more difficult than using rectangular fins and its impact on the thermo-hydraulic performance of the cooling device must be assessed.

3.4.2. Working principle

3.4.2.1. *Thermoregulated non-linear microvalves*

McCarthy et al. [38]–[40] studied the mechanism of nonlinear thermal buckling of doubly clamped beams with small eccentricities. In these studies, the relation between the beam thickness (t) and its eccentricity (e) was nearly zero ($\epsilon = e/t \rightarrow 0$) (Figure 3.30).

As detailed by McCarthy et al. [38], [39], when the temperature of the beam increases, the difference in the coefficient of thermal expansion between the beam and the restraining material ($\Delta\alpha$) leads to an internal axial force. As the thermal expansion coefficient of the beam is higher than its restraint, the beam is subjected to compression. Due to this effect, the deflection of the beam is negligible at small loads and then buckles at a critical load, achieving high lateral deflections. The critical load for buckling can be geometrically tailored to a specific temperature by modifying some geometric parameters, such as eccentricity, length (L) or thickness.

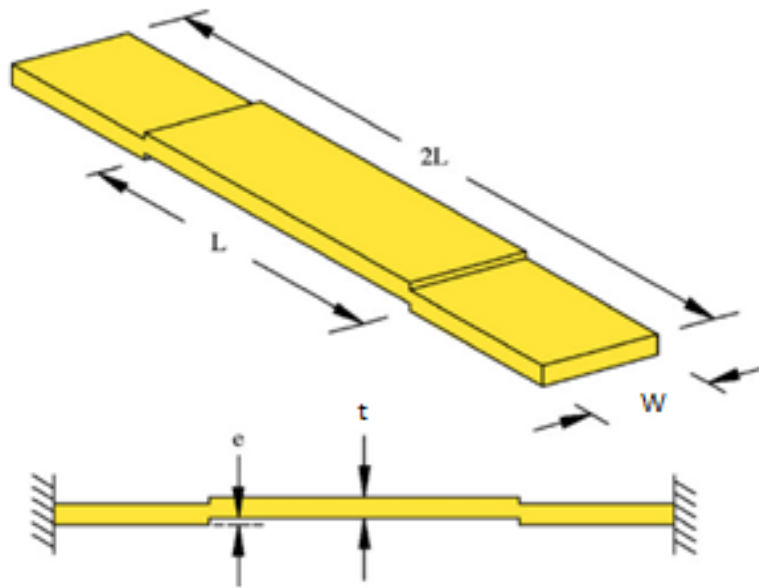


Figure 3.30. Clamped-clamped beams with small eccentricities [39].

The critical load of the fin P_{cr} , that is the force at which a beam without eccentricity will buckle, is defined as (37):

$$P_{cr} = \frac{\pi^2 EI}{L^2} = \frac{\pi^2 EWt^3}{12L^2} \quad (37)$$

The critical temperature, T_{cr} , that is the temperature at which a beam without eccentricity will buckle, is defined as (38):

$$T_{cr} = \frac{P_{cr}}{\Delta\alpha EWt} = \frac{1}{12\Delta\alpha} \left(\frac{\pi t}{L}\right)^2 \quad (38)$$

Non-dimensional and nonlinear curves of the central deflection of the beam are shown for different relations of eccentricity and thickness of the beam (ϵ) (Figure 3.31).

3. Self-adaptive fins acting as vortex generators

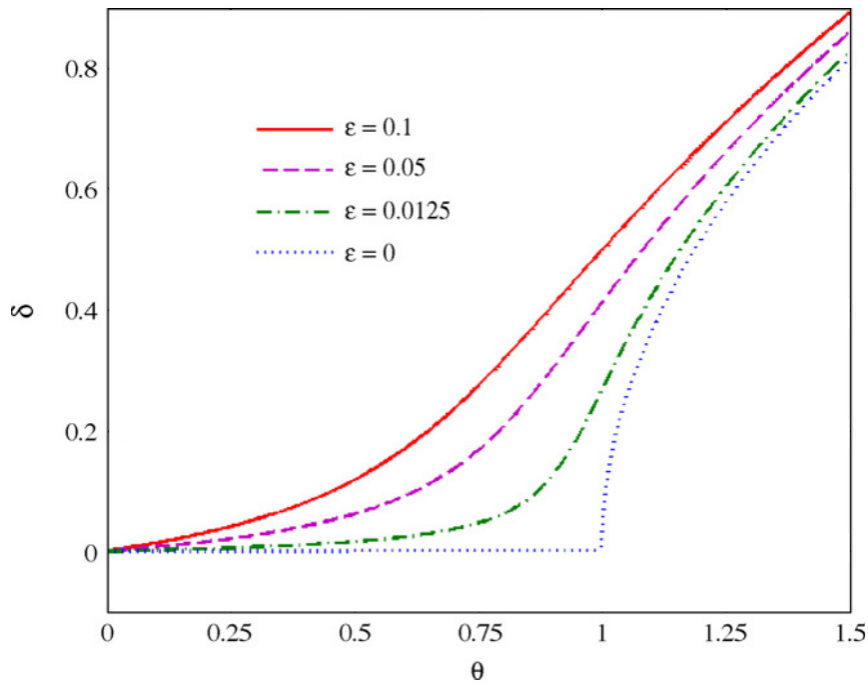


Figure 3.31. Non-dimensional design curves for central deflection at various eccentricities as a function of the temperature rise (θ) [39].

The non-dimensional X axis (θ) represents the temperature rise (39).

$$\theta = \frac{\Delta T}{\Delta T_{cr}} = \frac{12\Delta\alpha\Delta T}{\pi^2} \cdot \left(\frac{L}{t}\right)^2 \quad (39)$$

The non-dimensional Y axis (δ) represents the maximum central deflection of the beam (40).

$$\delta = \frac{z_{max}}{t} = \frac{e}{t} \cdot \left[\sec\left(\frac{L}{2} \sqrt{\frac{F_c}{EI}}\right) - 1 \right] \quad (40)$$

Even though the high interest of the thermoregulated valves presented in [38]–[40], they were studied using air as working fluid. Later, Amnache et al. [106] assessed the adaptation of such microvalves to process it as a chip-cooling component to adapt it to liquid flows. Two Ag valves, of 2000 μm and 1733 μm long respectively, were designed, microfabricated and experimentally

tested to validate their performance in liquid cooling. The 1733 μm valve opening shifted from 2,00 μm to 24,70 μm when exposed to a hot plate at room temperature and at 80 $^{\circ}\text{C}$ respectively and stayed in its elastic deformation range up to 160 $^{\circ}\text{C}$ (Figure 3.32). Moreover, this valve demonstrated that it was possible to regulate water flow rate from < 0,50 ml/min to 3 ml/min at a constant pressure drop of 5 kPa. These results made the microvalve suitable for the thermoregulation of the cooling for the microfluidic cell matrix.

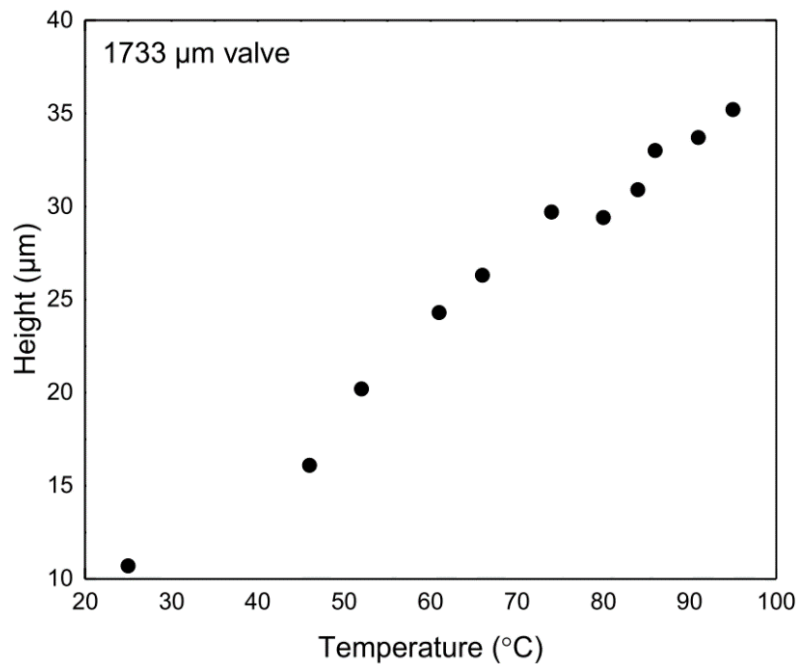


Figure 3.32. Vertical displacement of the 1733 μm valve in function of the hot plate temperature [106].

3.4.2.2. Doubly clamped self-adaptive fins

Based on the thermoregulated non-linear microvalves presented above, the self-adaptive fins are clamped-clamped beams made with a material of high CTE (Ag in this case) and axially restrained to a material of lower thermal expansion coefficient, what leads to a buckling of the beam when its temperature increase.

The thermal buckling of the beam is used as a passive thermal actuator mechanism inside microchannels, creating a self-adaptive device able to tailor its behavior to non-uniform and time dependent heat load scenarios. Hence, when the cooling requirements are high and

3. Self-adaptive fins acting as vortex generators

constant high power densities have to be dissipated from the channel, the fins rise up to generate vortices within the microchannel flow and enhance the heat transfer (Figure 3.33a). When the heat flux applied to the channel is constant and medium, the temperature of the flow will increase along the channel and so, the wall temperature. In this case, only the fins placed at the end of the channel will reach the buckling temperature, while the ones at the beginning will remain in flat position. This effect will enhance the heat transfer at the hottest place of the channel improving the temperature uniformity along it (Figure 3.33b). Another existing case is when non-uniform high heat fluxes are applied to the chip and only affects a small part of the channel. Under these circumstances, only the fins placed above the high heat flux will rise up, enhancing in this zone the heat transfer and maintaining the temperature uniformity along the channel (Figure 3.33c), similarly to the previous case. Finally, when the cooling demands are low, the fins remain in a flat position, reducing the pressure drop in the channel and thus the needed pumping power (Figure 3.33d).

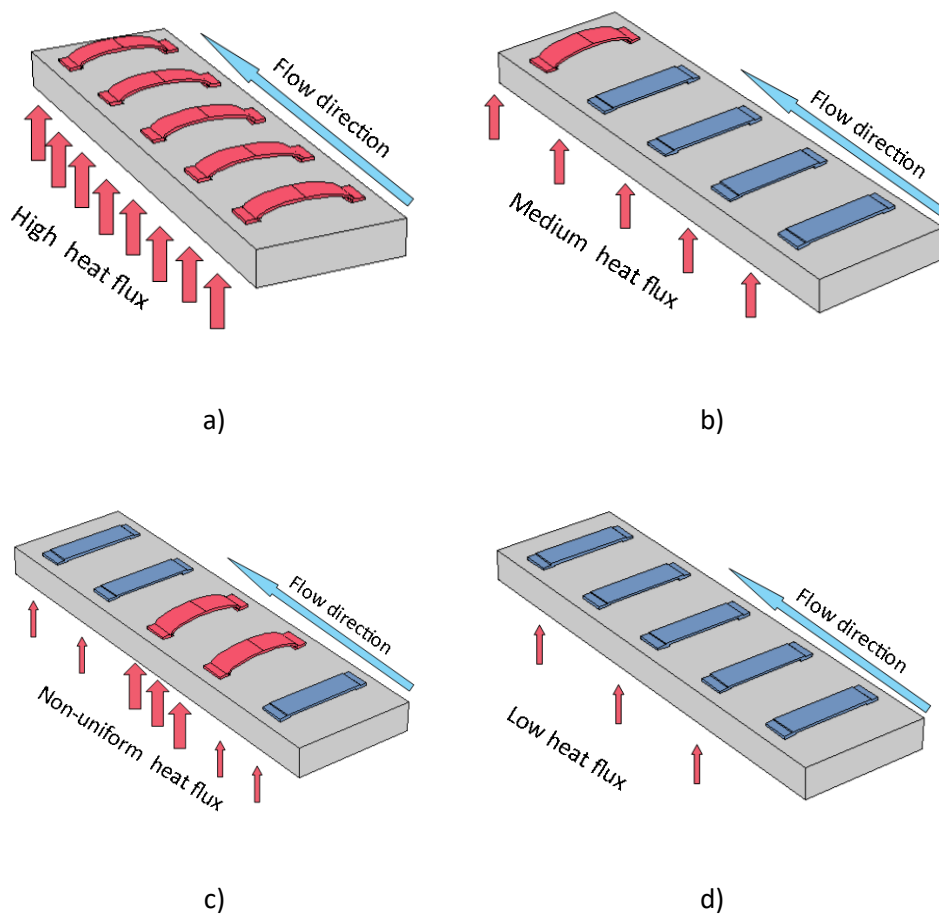


Figure 3.33. Behavior of the self-adaptive fins for different heat flux distributions: a) Uniform high heat flux. b) Uniform medium heat flux. c) Non-uniform heat flux. d) Constant low heat flux.

3.4.3. Geometric study and numerical analysis of the doubly clamped fins

The self-adaptive fins are based on a clamped-clamped beam with small eccentricity (Figure 3.34), and the equations used to study its deflection are explained in detail in [39]. The material used to fabricate the fins will be Ag. The geometric parameters and material characteristics are detailed below (Table 3.7).

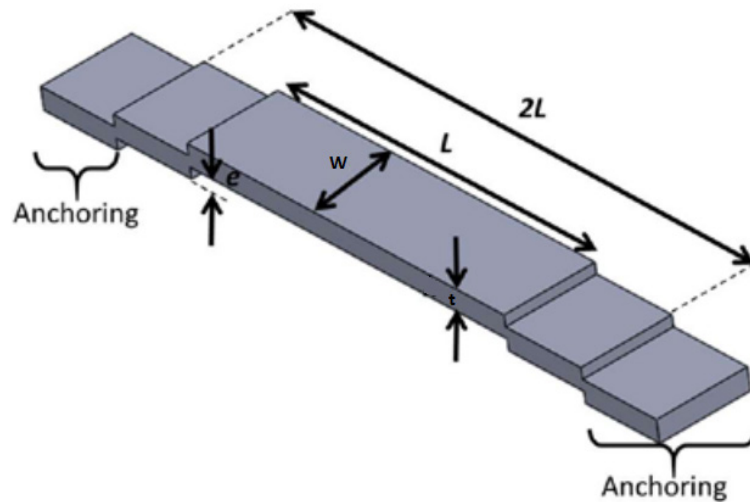


Figure 3.34. Schematic of the microvalve geometry with the main design parameters [106].

Parameter	Value	Description
W	100 μm	Width of the fin
t	10 μm	Thickness of the fin
e	1,50 μm	Eccentricity
E	83 GPa	Young Modulus of the material
$\Delta\alpha$	$17,40 \cdot 10^{-6} \text{ } ^\circ\text{C}^{-1}$	Difference on CTE between the fin and the restraint.

Table 3.7. Geometric dimensions and material values of the doubly clamped fin.

3. Self-adaptive fins acting as vortex generators

For the given dimensions in Table 3.7 and two different lengths of the fin, the critical load (37) and critical temperature (38) have been assessed (Table 3.8).

L (μm)	P_{cr} (N)	T_{cr} ($^{\circ}\text{C}$)
500	0,041	18,91
900	0,013	5,84

Table 3.8. Critical load and temperature for both studied lengths of the fin.

The relation between the maximum central deflection and the temperature rise is not linear, as shown below (Figure 3.35).

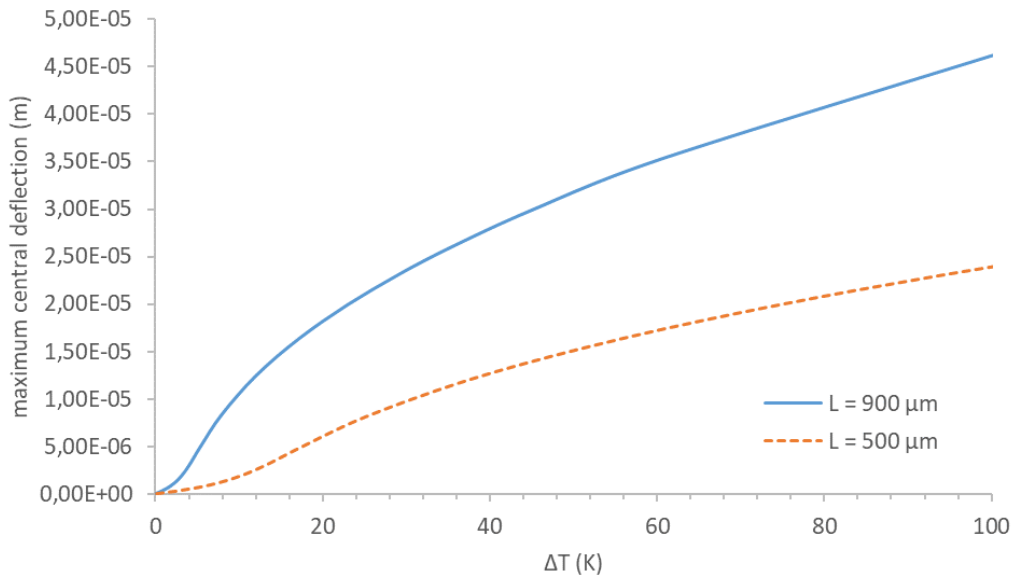


Figure 3.35. Relation between maximum deflection and temperature rise of doubly clamped fins of different lengths.

According to Figure 3.35, for a temperature increase of 50°C and a length of $L = 900 \mu\text{m}$, the deflection achieved by the fin is going to be around $30 \mu\text{m}$, 3,30 % of the fin length.

Additionally, a novel version of the doubly clamped fins is proposed, which is believed to increase more the maximum central deflection and generate more vortices within the flow. This

novel fin consists on a doubly clamped fin with a triangle cut in the middle, that will rise with the beam buckle (Figure 3.36). CFD simulations shown an increase of around 4 % in the central deflection (Table 3.9).

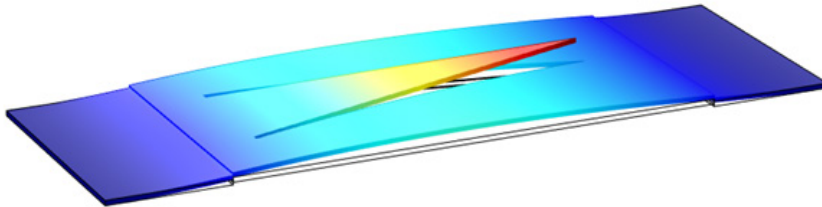


Figure 3.36. Doubly clamped fin with triangle cut in the middle.

	Valve without cut	Valve with triangle cut
z/L (%)	3,30	7,00

Table 3.9. Vertical displacement of the central part of doubly clamped fins (as % of its length).

Figure 3.37 shows the vertical displacement of doubly clamped fins compared with the achieved by some bimetallic fins. Although, in percentage, the vertical rise is not much higher than for the bimetallic fins, the robustness of this model, makes feasible the fabrication of self-adaptive fins with significantly larger dimensions, making possible larger deflections inside the microchannel. Also, the use of a unique material for its microfabrication turns the microfabrication into a simpler process.

Considering the advantages that this kind of fins present over the bimetallic ones, doubly clamped beams are selected to be used as self-adaptive fins inside a microchannel to enhance the heat transfer.

3. Self-adaptive fins acting as vortex generators

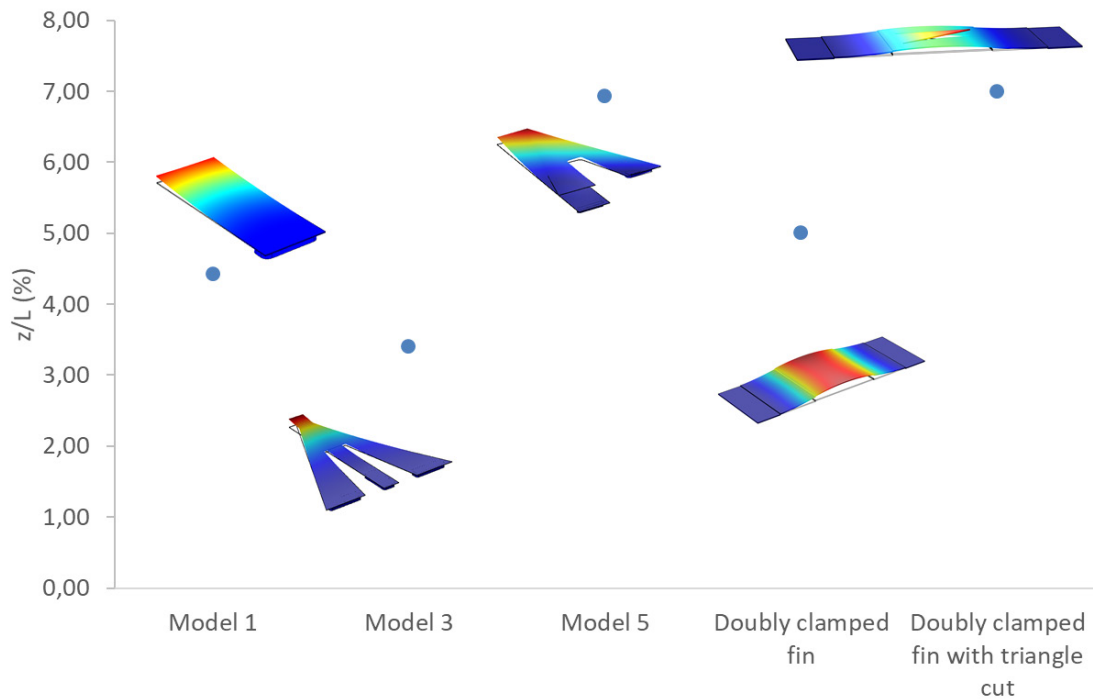


Figure 3.37. Comparison of the rise of some bimetallic fins with the doubly clamped fins.

3.4.4. Possible thresholds of this technology

Doubly clamped fin models seem to have solved the main thresholds of bimetallic fins (section 3.3.5). Due to the use of a unique material and the similitude with the microfluidic valves the microfabrication process has been significantly simplified. Additionally, the valves are more robust and present large deformations.

Nevertheless, the generation of vortices within this kind of fin is not so obvious. Due to its rounded geometry at the top and the space below, the flow can pass around the fins without breaking its boundary layer nor generating vortices with enough strength to enhance the heat transfer. For this reason, a deep study about the impact of self-adaptive doubly clamped fins on the performance of a microchannel and a microfluidic cell will be done in the following chapters.

Additionally, the number of useful cycles of the fins, as well as its fatigue, needs to be analyzed in great detail as can be one important weaknesses of this kind of self-adaptive fins.

IMPACT ASSESSMENT OF THE SELF-ADAPTIVE FINS INSIDE A
MICROCHANNEL

4. IMPACT ASSESSMENT OF THE SELF-ADAPTIVE FINS INSIDE A MICROCHANNEL

Since Tuckerman and Peace proposed microchannel structures for liquid cooling of microelectronics in 1981 [13], this technology has been widely studied within the literature and became the most commonly used liquid cooling technology. Several attempts are found in the literature to overcome the drawbacks that this cooling structure presents, such as large pressure drops and temperature gradients. Some of these studies, focused on improving the thermal performance of the microchannels, are described in detail in section 2.3.1.

In this chapter, a cooling device based on microchannels will be used as the base structure to assess numerically and experimentally the impact of doubly clamped self-adaptive fins on its thermo-hydraulic performance.

4.1. Model definition

The defined cooling device is a $2 \times 2 \text{ cm}^2$ array of microchannels, made of silicon. The size of the cooling device corresponds to the size of the STREAMS test vehicle, described in section 1.3.1. It contains 7 microchannels of 1,95 mm width, 19,50 mm length and 80 μm height (Figure 4.1a). The channel height is designed low in order to improve the heat transfer enhancement generated by the fins. The wall thickness between two microchannels is 0,98 mm. Inside the microchannel, 10 pairs of self-adaptive fins are placed, with a separation of 2 mm between them and an angle of attack (β) of 45° (Figure 4.1b). The dimensions of the fins are 0,9 mm length, 0,18 mm width and 9 μm thickness (Figure 4.1c). For the numerical simulations, to reduce computational resources, the assessment of the impact of the fins within the microchannel has been done considering the geometry of the fins fixed. At the elevated position, 30 μm of elevation are considered for the fins (relative height $z/H = 0,375$).

4. Impact assessment of the self-adaptive fins inside a microchannel

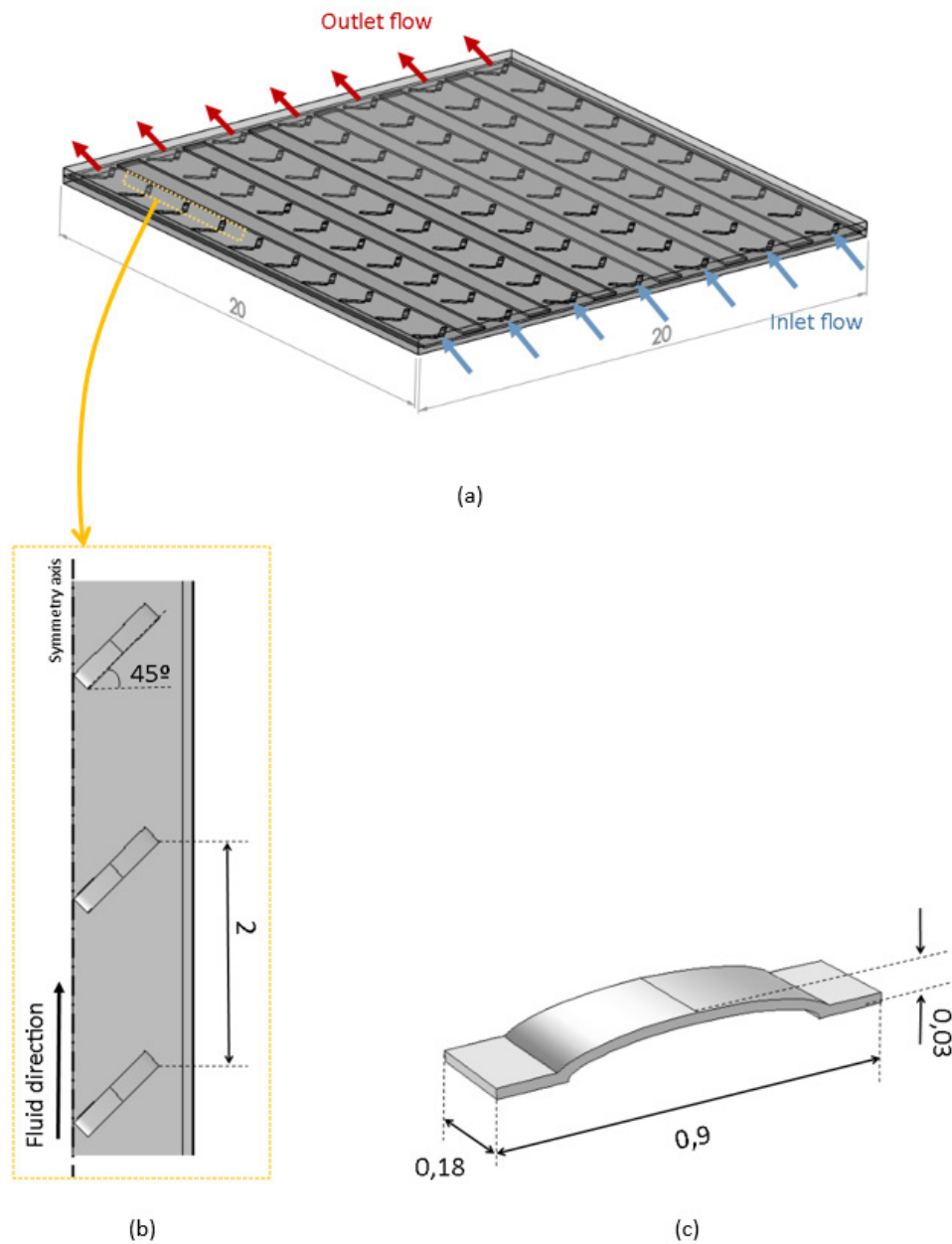


Figure 4.1. (a) Cooling device based on an array of microchannels with the self-adaptive fins inside. (b) Zoom on the fin distribution inside one microchannel. (c) Geometry of one self-adaptive fin. (All units in mm).

Additionally, in order to simplify the meshing procedure of the CFD analysis, the geometry of the self-adaptive fins have been simplified into a semielliptical object (Figure 4.2). The induced error in the simplification, when the fins are placed inside a microfluidic cell, with shorter channel length than a microchannel, has been assessed. To compute the error, the results obtained through a CFD simulation when using solid fins are compared to the ones obtained

when using fine fins (Figure 4.3). The boundary conditions are the same in both cases. It is assumed that the induced error within a microchannel would be smaller as the density of fins is lower.

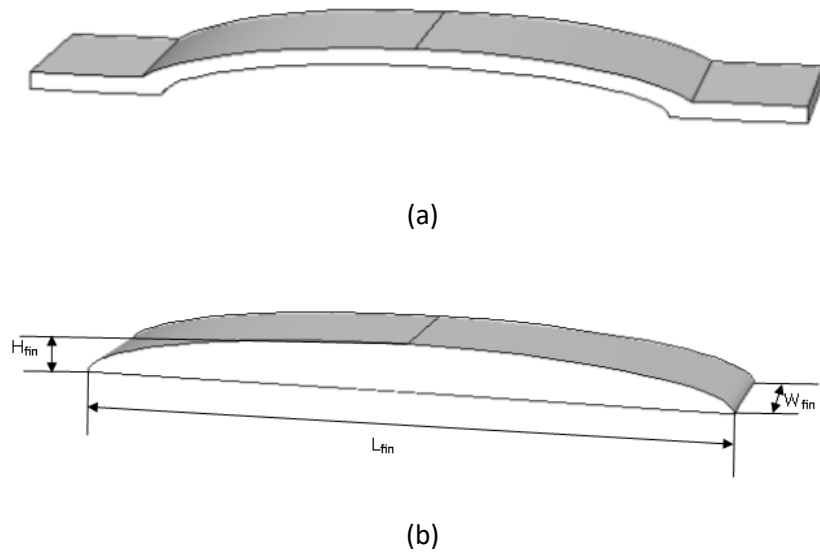
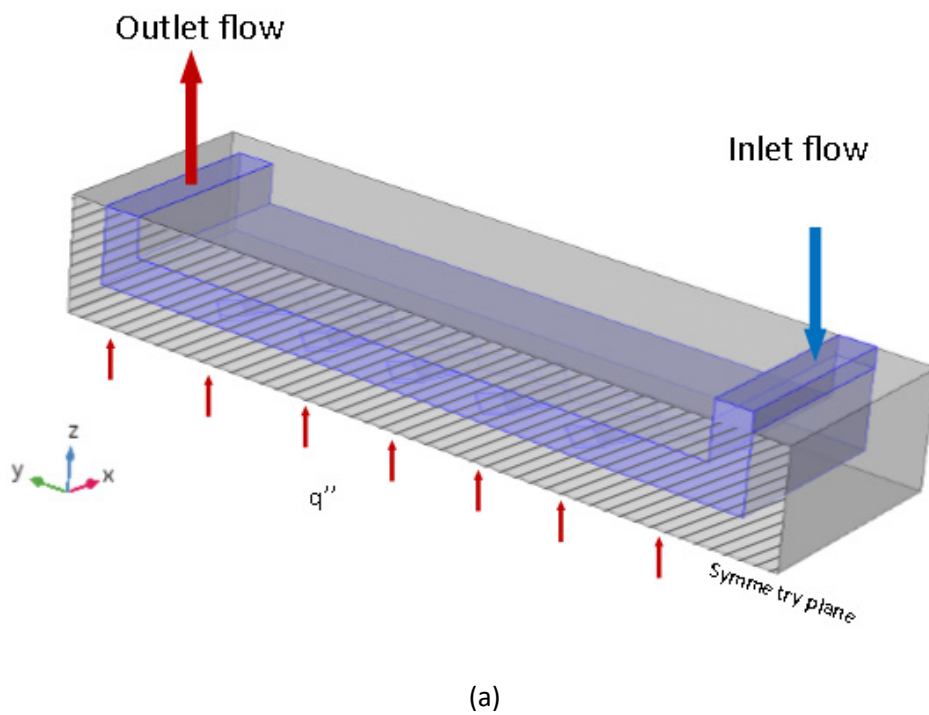


Figure 4.2. a) Schematic of the self-adaptive doubly clamped fin. (b) Simplification of the self-adaptive fins into a semielliptical object.



4. Impact assessment of the self-adaptive fins inside a microchannel

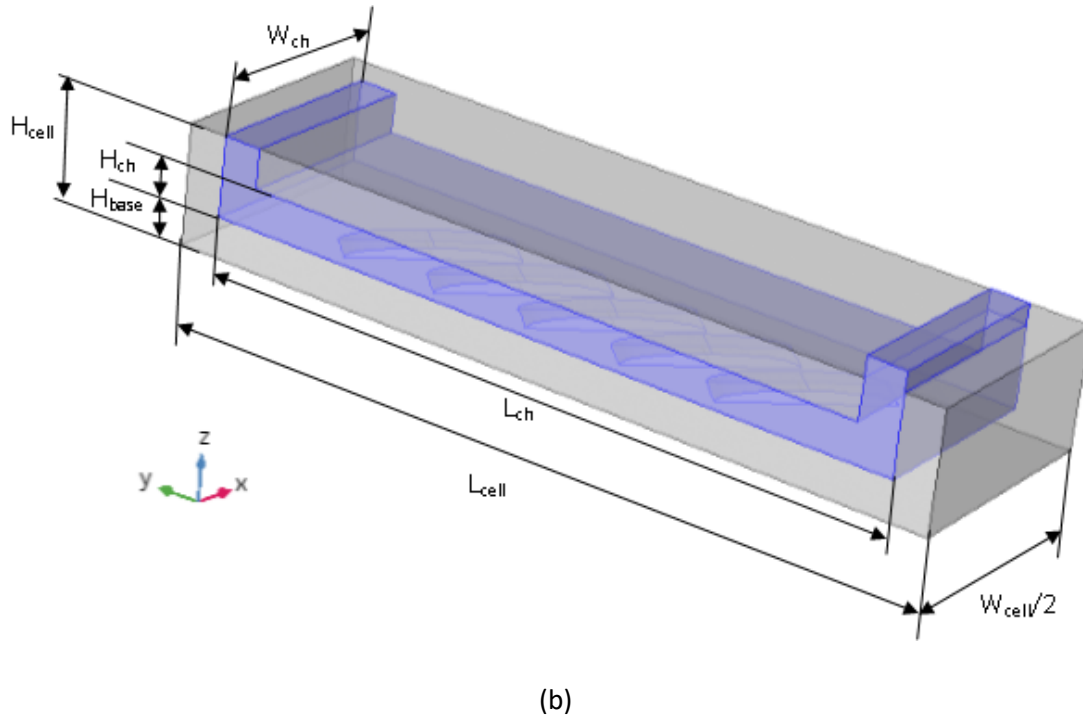


Figure 4.3. Microfluidic cell with (a) fine fins inside and (b) solid fins inside.

The main dimensions of the microfluidic cell where the error is assessed are listed in Table 4.1.

Parameter	Value	Description
L_{cell}	2000 μm	Length of the cell
W_{cell}	1200 μm	Width of the cell
H_{cell}	300 μm	Total height of the cell
L_{ch}	1800 μm	Length of the channel
W_{ch}	1000 μm	Width of the channel
H_{ch}	100 μm	Height of the channel
L_{fin}	440 μm	Length of the fin
W_{fin}	100 μm	Width of the fin
H_{fin}	30 μm	Height of the fin
H_{base}	100 μm	Wall thickness from the chip to the fluid
Δy	250 μm	Distance between fins in y axis

Table 4.1. Geometrical parameters of the microfluidic cell.

4. Impact assessment of the self-adaptive fins inside a microchannel

A constant heat flux of 300 W/cm^2 is applied at the bottom wall of the channel and the inlet temperature of the fluid is $20 \text{ }^\circ\text{C}$. The error is assessed for two flow rates: $Q_1 = 1,10 \cdot 10^{-7} \text{ m}^3/\text{s}$ ($\text{Re} = 200$, calculated at a region of the channel without the fins) and $Q_2 = 2,20 \cdot 10^{-7} \text{ m}^3/\text{s}$ ($\text{Re} = 400$). The flow is assumed to be laminar. Table 4.2 shows the obtained results with both CFD simulations, for the two assessed flow rates. As it is seen in the table, the maximum induced error is in the pressure drop, where it is around 4 %, so it is considered acceptable to simulate the self-adaptive fins as solid semi ellipses. No significant changes within the error are seen when varying the flow rate.

	$T_{f,\text{out}} \text{ (K)}$	$T_{f,\text{av}} \text{ (K)}$	$\Delta P \text{ (Pa)}$	$T_{\text{chip,av}} \text{ (K)}$	$T_{\text{chip,max}} \text{ (K)}$	$T_{\text{chip,min}} \text{ (K)}$	Nu
$\text{Re} = 200$							
Fine fin	311,23	306,47	4355,93	340,49	347,59	331,54	19,87
Solid fin	311,22	306,17	4527,64	340,75	349,65	331,56	19,76
Error (%)	$3,20 \cdot 10^{-3}$	$9,80 \cdot 10^{-2}$	3,94	$7,60 \cdot 10^{-2}$	$5,90 \cdot 10^{-1}$	$6,00 \cdot 10^{-3}$	$5,40 \cdot 10^{-1}$
$\text{Re} = 400$							
Fine fin	301,96	299,98	14698,28	325,13	329,44	318,88	29,41
Solid fin	301,95	299,85	15292,49	325,35	331,95	318,65	29,21
Error (%)	$3,00 \cdot 10^{-3}$	$4,30 \cdot 10^{-2}$	4,04	$6,80 \cdot 10^{-2}$	$7,60 \cdot 10^{-1}$	$7,20 \cdot 10^{-2}$	$6,80 \cdot 10^{-1}$

Table 4.2. Computed relative error on the CFD results between solid valve and fine valve simulation.

4.2. Numerical assessment of self-adaptive fins impact

The impact of self-adaptive fins within the performance of a single microchannel is numerically assessed in this section. Firstly, the heat transfer enhancement that perform the self-adaptive fins within a microchannel, under different conditions, is compared with a plain microchannel.

Then, the pumping power savings due to the use of the self-adaptive system instead of a fixed geometry as flow disturbing elements is assessed.

4.2.1. Boundary conditions

The main dimensions and boundary conditions of the simulated microchannel are shown in Figure 4.4. The flow is assumed to be laminar, steady, incompressible and Newtonian, with gravitational effects neglected. The water properties of density (ρ_f), dynamic viscosity (μ_f), specific heat ($C_{p,f}$) and thermal conductivity (κ_f) are calculated for temperature dependence, while the properties of silicon and silver are assumed constant ($\kappa_{Si} = 130 \text{ W/m}\cdot\text{K}$, $\kappa_{Ag} = 429 \text{ W/m}\cdot\text{K}$). The governing equations for the flow are the continuity equation for conservation of mass and the Navier-Stokes equations for conservation of momentum (19), (20). The energy equations for liquid (21) and solid (22) are also defined in function of the absolute temperature. No slip boundary condition, adiabatic condition at walls and symmetry boundary condition (symmetry plane defined in Figure 4.4) are assumed.

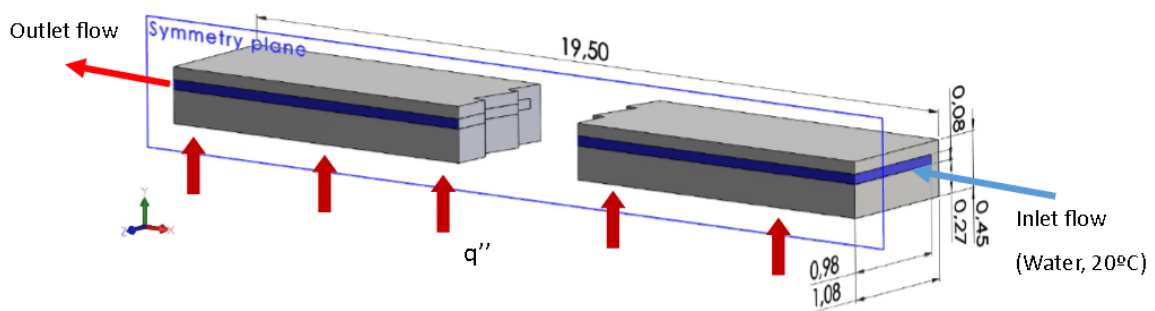


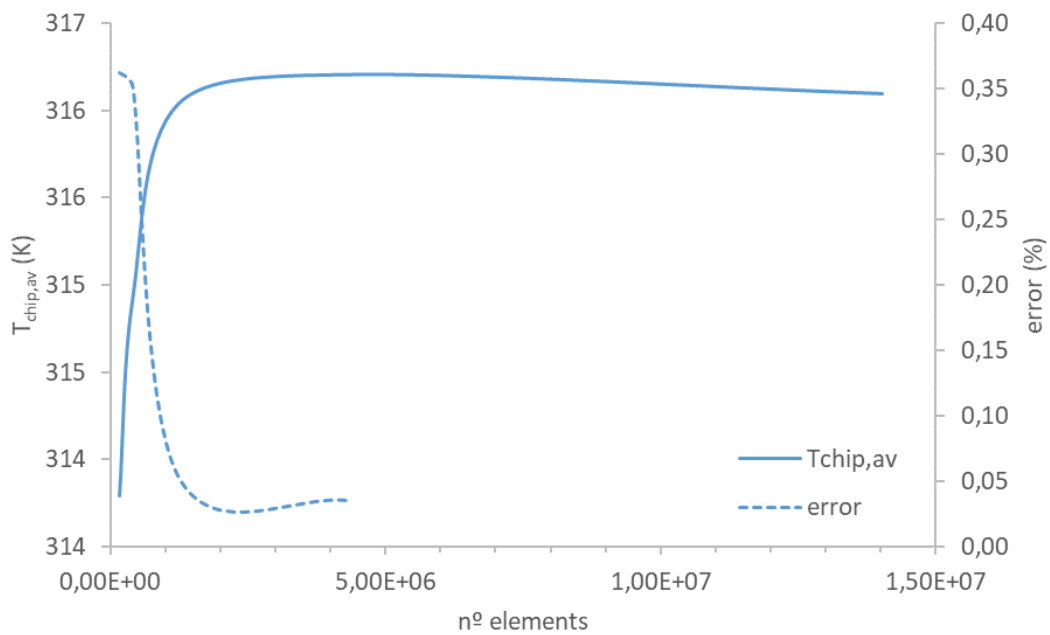
Figure 4.4. Microchannel geometry (units in mm).

At the entrance of the microchannel, the flow is considered fully developed, with an entrance length $L_{entr} = L/10$ (23). The coolant fluid considered is water, with an inlet temperature (24) of 293,15 K. A constant heat flux of 51 W/cm^2 is applied at the microchannel bottom surface (25).

4.2.2. Grid independence test

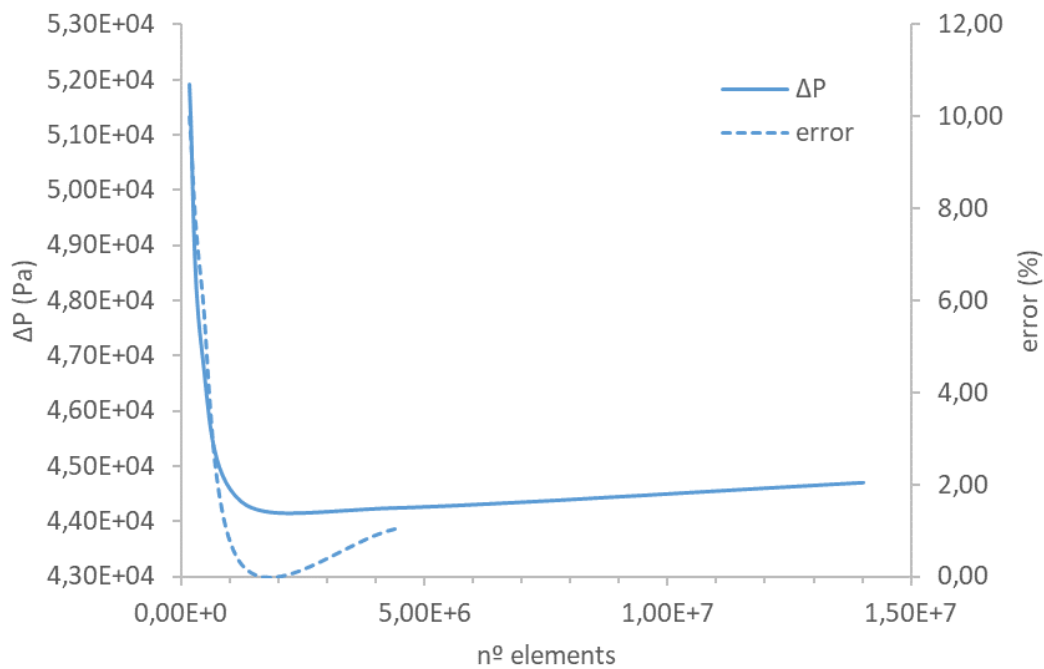
The mesh built on this model is based on tetrahedral elements and 4 boundary layers on the fluid. To ensure that the computational results are independent of the grid size, the number of elements is varied from $172 \cdot 10^3$ to $14 \cdot 10^6$ elements, and the relative error on chip temperature and pressure drop within one microchannel is computed according to (26). A flow rate of $2,03 \cdot 10^{-7} \text{ m}^3/\text{s}$ ($\text{Re} = 200$) is chose to compute the error.

Observing the results of the simulations (Figure 4.5), when the number of elements is bigger than $1 \cdot 10^6$, both relative errors in average chip temperature and pressure drop are less than 1 %, which is considered acceptable. The chosen grid system has 1.234.104 elements and the relative errors with the finest grid are 0,05 % for the chip temperature (Figure 4.5a) and 0,26 % for the pressure drop (Figure 4.5b).



(a)

4. Impact assessment of the self-adaptive fins inside a microchannel



(b)

Figure 4.5. Grid independence test assessed on a) the average chip temperature and b) the pressure drop within the channel.

4.2.3. Numerical results

4.2.3.1. Impact assessment of the self-adaptive fins for different Reynolds number

The impact of the self-adaptive fins inside the microchannel is assessed for different Reynolds numbers and the results are compared with a plain microchannel, without fins inside. The heat transfer enhancement and the pressure drop increment are computed as defined in (8) and (9). The Nusselt number and the apparent friction factor are calculated according to equations (7) and (3) respectively.

A constant heat flux of 51 W/cm^2 is applied at the base of the microchannel and the Reynolds number is varied from 100 to 800. According to previous publications [83], [87], both the heat transfer enhancement and the apparent friction factor relation are expected to increase with

the Reynolds number (Figure 4.6). For $Re = 800$, the calculated heat transfer enhancement is 1,40 and the apparent friction factor increment is equal to 1,49.

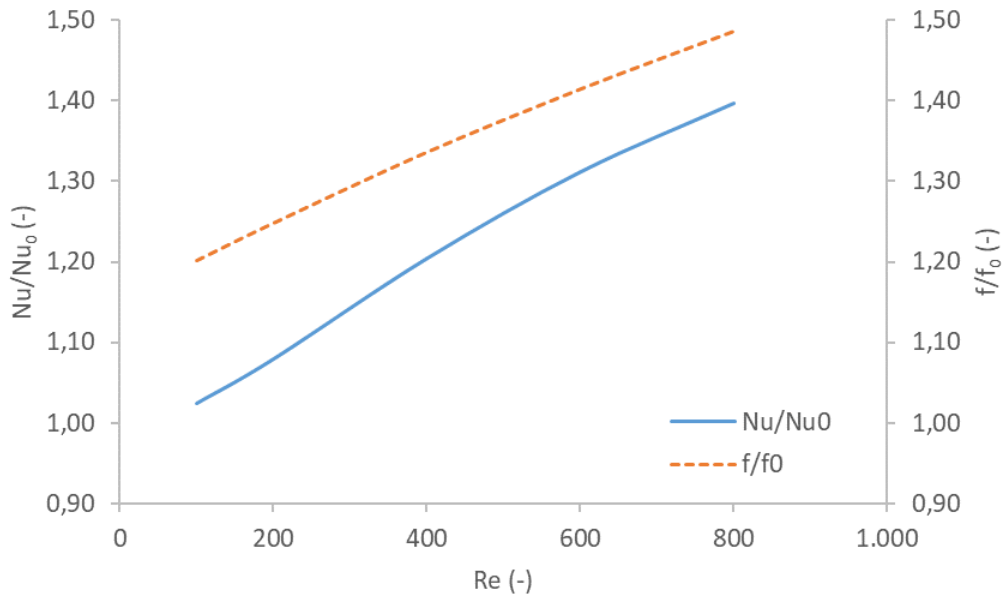
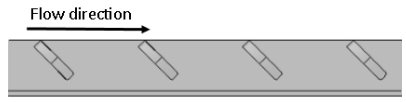



Figure 4.6. Heat transfer enhancement and pressure drop increment in a microchannel due to self-adaptive fins for different Re numbers.

4.2.3.2. Impact assessment of the self-adaptive fins for different fin configurations

For constant heat flux (51 W/cm^2) and constant Reynolds number ($Re = 200$), different configurations of the fins are defined in order to find which one offers the best thermal improvement inside the microchannel. The different configurations are detailed in Table 4.3.

Name	Angle of attack (β)	Number of fins	
Conf. 01	45°	10	
Conf. 02	-45°	10	

4. Impact assessment of the self-adaptive fins inside a microchannel

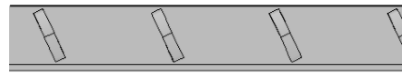
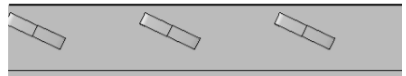

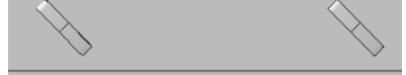
Conf. 03	25 °	10	
Conf. 04	65 °	10	
Conf. 05	45 °	20	
Conf. 06	45 °	5	

Table 4.3. Description of the different configurations of self-adaptive fins inside a microchannel.

The heat transfer enhancement and the pressure drop increment, compared with a plain microchannel, without fins, are assessed for the different configurations of fins (Figure 4.7). The biggest heat transfer enhancement is achieved with conf. 05, where the density of fins is doubled. In this case, Nu/Nu_0 is equal to 1,13, but also the highest pressure drop increment is achieved within this case ($f/f_0 = 1,45$).

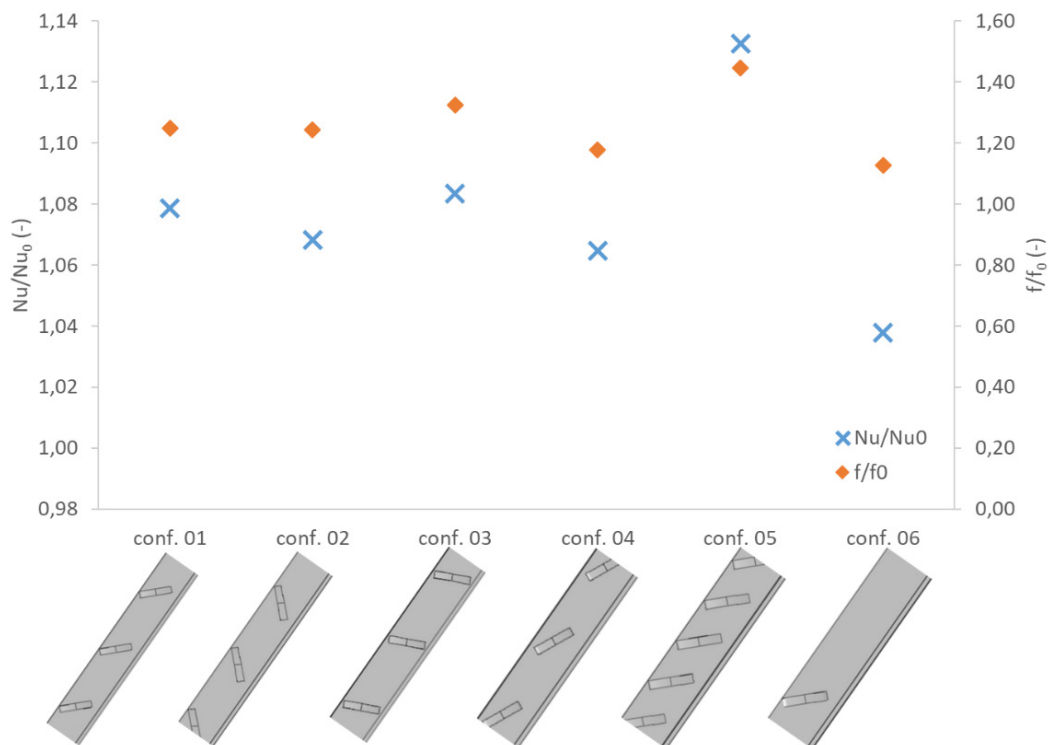


Figure 4.7. Nusselt number enhancement and apparent friction factor increment inside the microchannel for the different configurations of fins, compared with a plain microchannel.

4.2.3.3. Impact assessment of the self-adaptive fins within the cold wall of the microchannel

Additionally, a different configuration, based on the fins placed at the cold wall of the channel is going to be tested. The cold wall of the channel is referred as the channel wall opposite to the heat flux (Figure 4.8). The geometry of the microchannel and the fin distribution within it is the same as in section 4.2.3, the only change is the position of the self-adaptive fins at the opposite wall. The self-adaptive fins placed in the cold surface would probably present a lower vertical raise than the fins in the hot surface due to the temperature difference between both walls, however, the vertical displacement is considered the same in both surfaces for simplification.

The assessment of this new configuration is done because, due to microfabrication limitations, is the one that will be fabricated. For this reason, its results will be useful for comparison with the experimental ones.

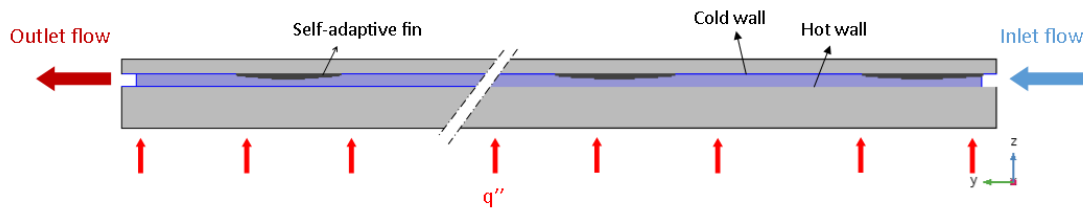


Figure 4.8. Schematic of the fin placement at the cold wall within a single microchannel.

For different Reynolds numbers (varying from 100 to 800), a constant heat flux of 51 W/cm^2 is applied at the bottom wall of the microchannel. The heat transfer enhancement and pressure drop increment compared with a plain microchannel are assessed (Figure 4.9).

As expected, both heat transfer enhancement and pressure drop increment enlarge with Reynolds number. Nevertheless, compared with results from Figure 4.6, where the fins are placed at the hot wall of the microchannel, the increase in heat transfer enhancement is lower, whereas the apparent friction factor increment is similar (Figure 4.10). The difference in heat transfer enhancement increases proportionally with flow rate as, while for $Re = 100$ the figure of merit Nu/Nu_0 is almost the same for both assessed configurations, when $Re = 800$, a difference of 20 %.

4. Impact assessment of the self-adaptive fins inside a microchannel

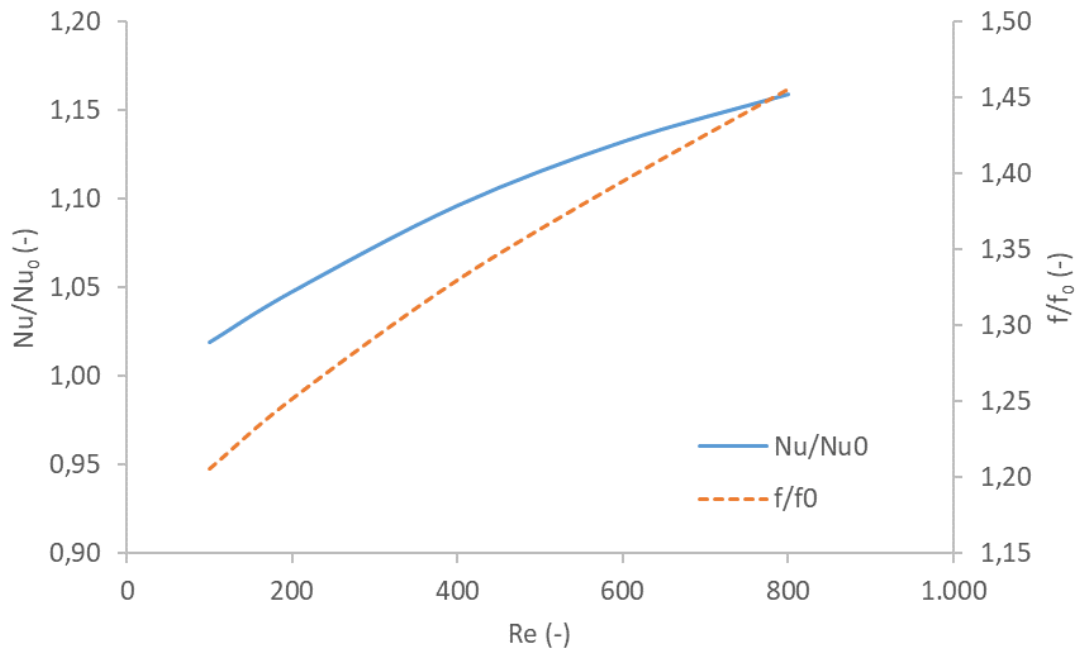


Figure 4.9. Heat transfer enhancement and apparent friction factor increment for different Reynolds numbers when the fins are placed at the cold side of the microchannel.

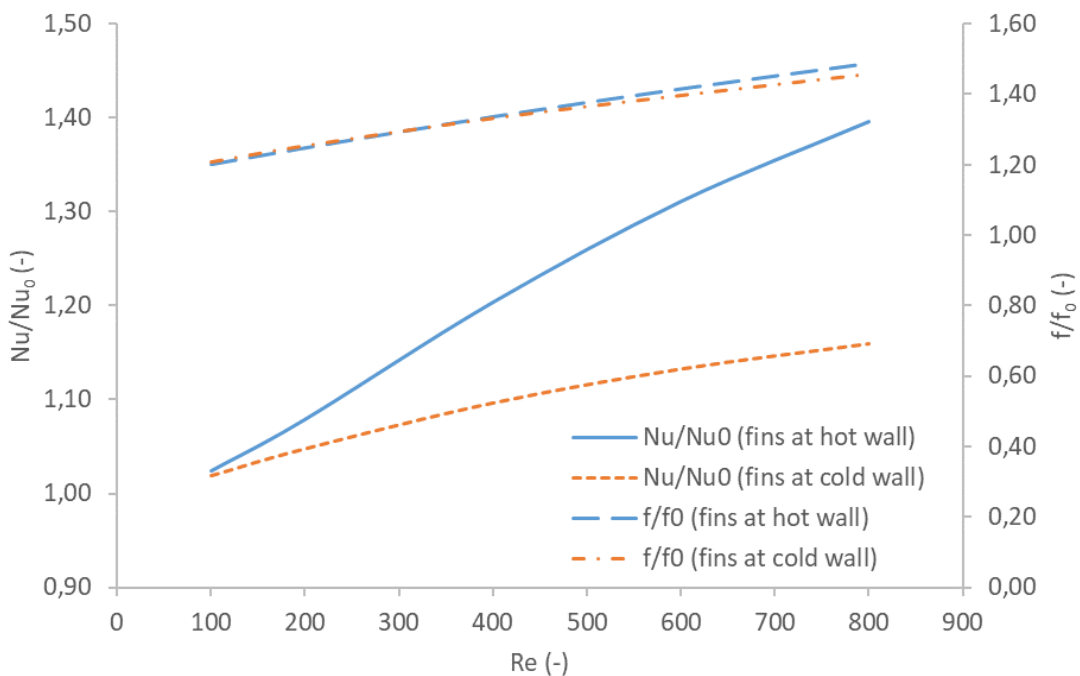


Figure 4.10. Comparison of the heat transfer enhancement and apparent friction factor increment between fins placed at hot or cold wall of the microchannel.

The obtained difference within these results can be attributed to two main reasons. First, when the fins are placed at the cold side wall, the surface of the microchannel closer to the hot source (chip) is reduced, due to the absence of fins. This turns in less surface for heat transfer, what reduces the thermal resistance coefficient and leads to higher temperatures at the chip (Figure 4.11). Additionally, the vortices generated by the fins are seen at the back of the fins, but they are not strong enough to affect the opposite wall, where the flow rate is clearly laminar (Figure 4.12). This leads to a local heat transfer enhancement at the wall near the fin but not at the opposite wall.

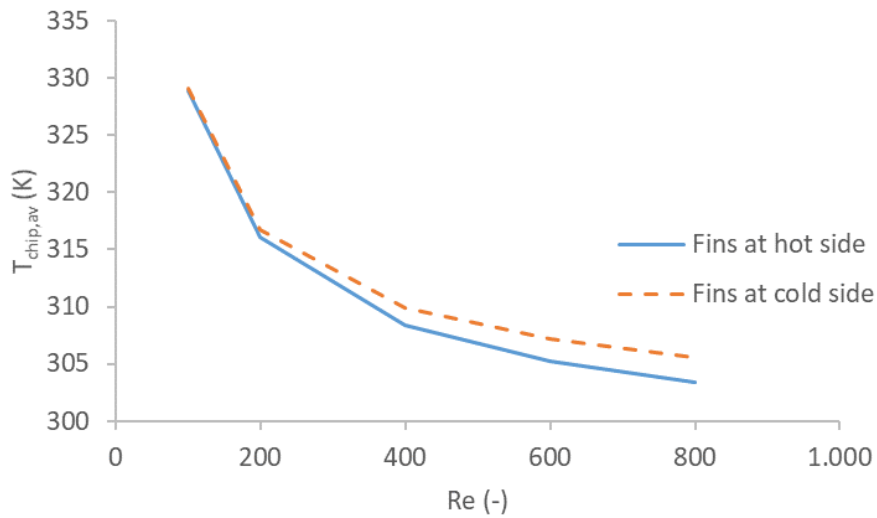


Figure 4.11. Average temperature at the chip surface, cooled down by the microchannels.

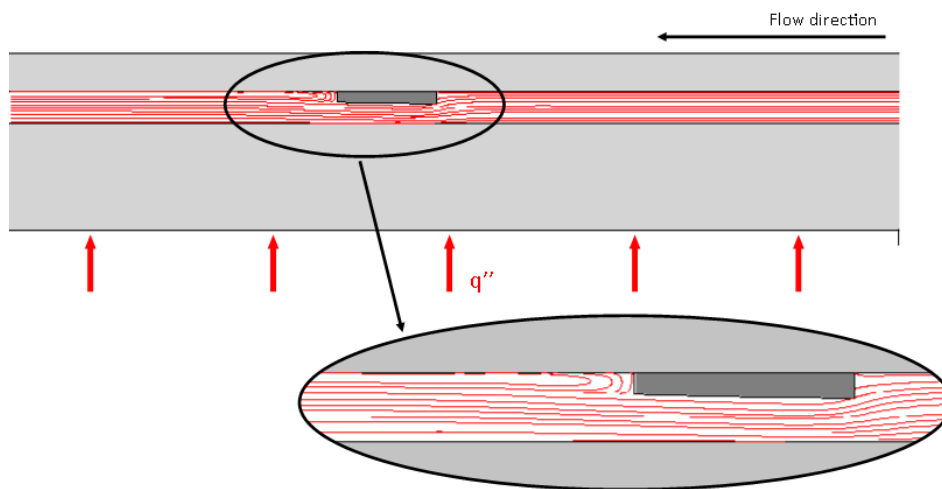


Figure 4.12. Streamline representation of the flow velocity inside the microchannel for $Re=600$ and the fins placed at the cold side wall.

4.2.3.4. Pumping power savings

The addition of fins inside a microchannel tends to increase the pressure drop within it and consequently, the required pumping power. The main goal of the self-adaptive fins concept is to reduce this enlarged pumping power while enhancing the heat transfer within a cooling device. This goal is achieved by using the thermal buckling of doubly clamped silver beams, implemented as a passive actuator to act as a self-adaptive vortex generator.

In this section, the impact on pumping power savings of the self-adaptive fins within a microchannel is assessed for a given unsteady and temporal heat load scenario and a constant flow rate, settled to ensure a maximum junction temperature of 85 °C. The obtained results are compared with a microchannel with fixed fins inside, acting as traditional vortex generators.

The geometry of the fins is the same in both cases, equal as described in previous sections (conf.01 of Table 4.3). Also, the microchannel geometry is the same assessed previously (Figure 4.4). The inlet temperature of the water is 20 °C and the constant flow rate applied is $9,12 \cdot 10^{-8} \text{ m}^3/\text{s}$.

A non-uniform and time dependent heat load scenario is applied to both numerical models, with a background heat flux of 21 W/cm² and high peaks of heat flux of 51 W/cm² (Figure 4.13). This heat load scenario is defined as a periodic pulse function with a period of 30 s and a duty cycle of 1/3. The total time period considered is 240 s.

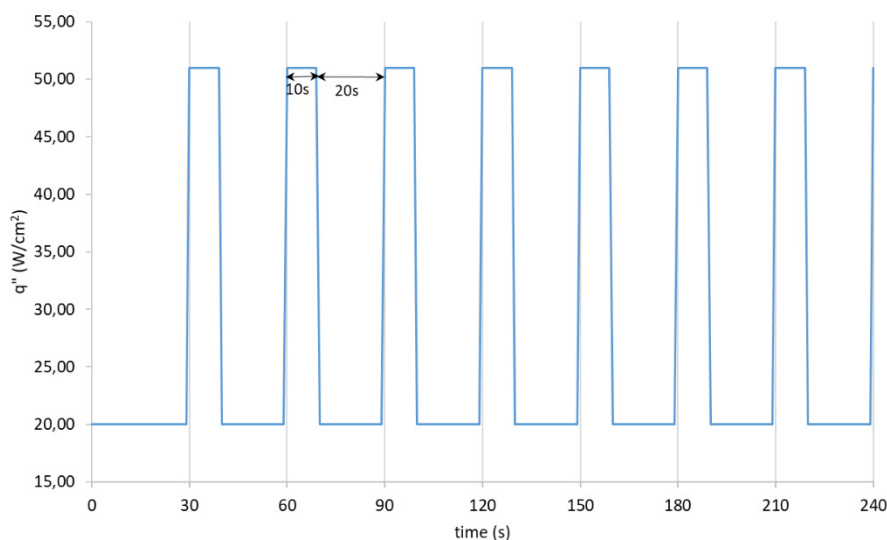


Figure 4.13. Non-uniform and time dependent heat load scenario applied.

The pressure drop within the channel is assessed for both studied geometries, when submitted to the defined heat load scenario (Figure 4.14). When the heat flux is high, the pressure drop decreases due to the reduction of fluid viscosity when the temperature increases. At low heat fluxes, the pressure drop is clearly lower on the self-adaptive system, as the fins are in flat position, whereas in the fixed system the fins create an increase on the pressure drop inside the microchannel. When the heat flux demand increases, the pressure drop in both systems is the same, as the self-adaptive fins rise up to enhance the heat transfer and adopt the same position as the fixed fins.

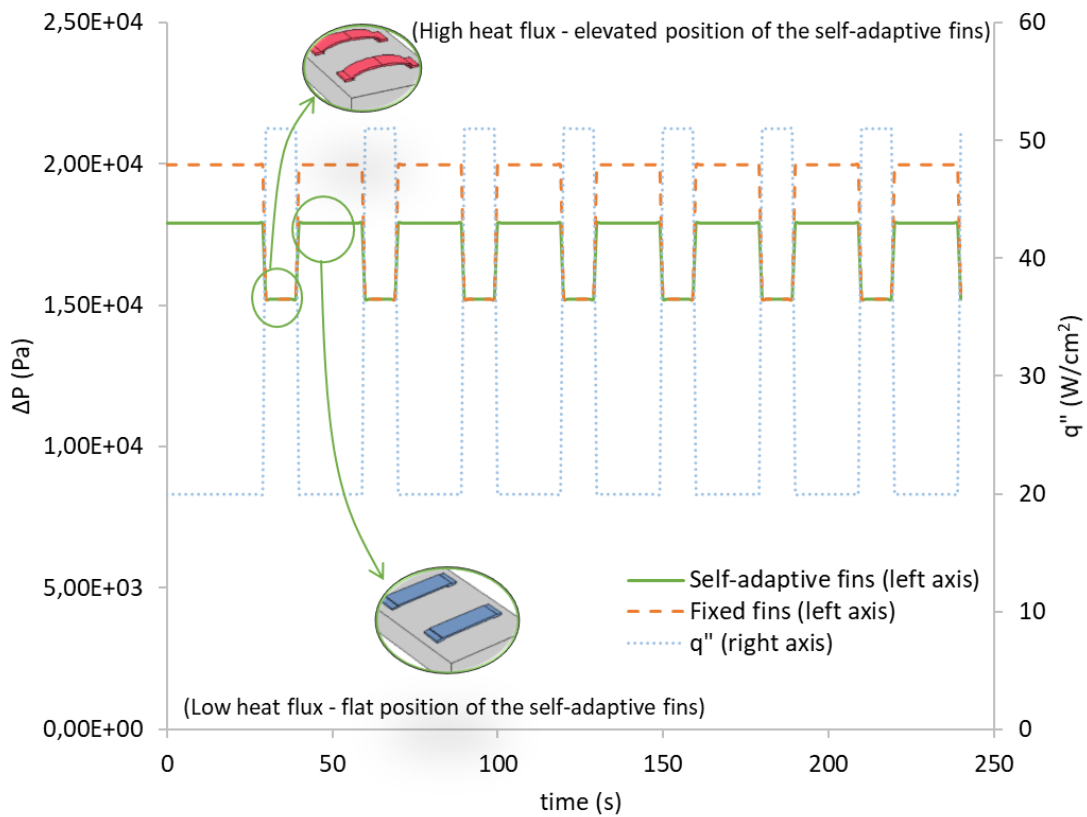


Figure 4.14. Comparison of the pressure drop within the microchannel for the assessed systems.

Due to the reduction on pressure drop while maintaining constant flow rate, the average pumping power, defined in equation (4), is reduced 7,9 % on the self-adaptive system compared with the system with fixed fins (Figure 4.15), for the given heat load configuration. Further

4. Impact assessment of the self-adaptive fins inside a microchannel

reduction of the pumping power is expected to be achieved when combining the self-adaptive fins solution with tailored flow rate within microchannels[41].

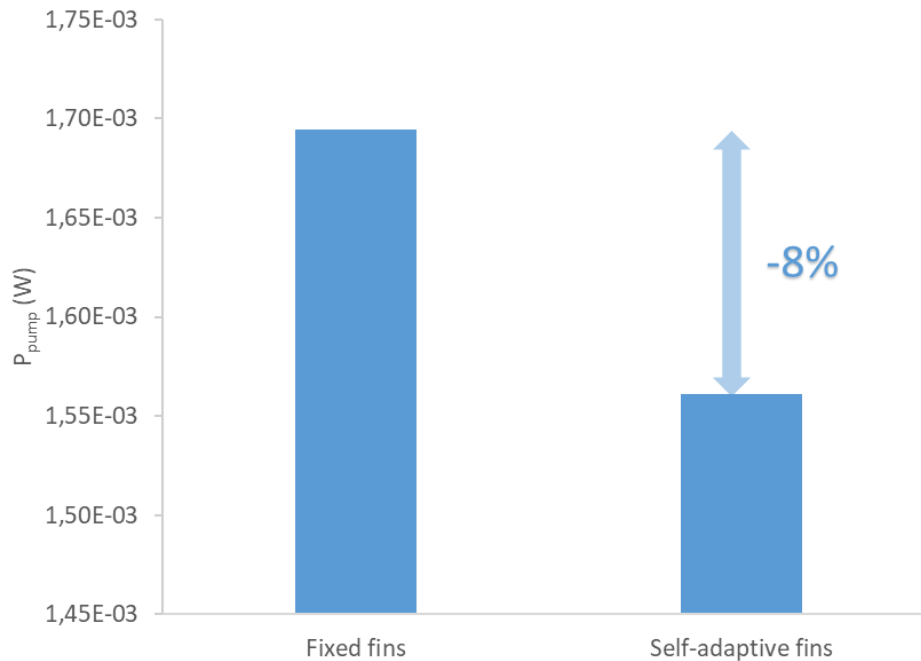


Figure 4.15. Average pumping power of both studied systems.

4.2.3.5. Temperature uniformity

The chip temperature increase along the microchannel base is assessed for a microchannel with self-adaptive fins, a microchannel with fixed fins inside and a plain microchannel. The microchannel dimensions are 19,50 mm length, 0,30 mm width and 80 μm of channel height.

For a fixed flow rate ($Q = 9,12 \cdot 10^{-8} \text{ m}^3/\text{s}$), which ensures a maximum junction temperature of 85 $^\circ\text{C}$ at the plain microchannel, and inlet fluid temperature of 20 $^\circ\text{C}$, a constant high heat flux is applied at the bottom surface (51 W/cm^2).

For the plain microchannel, the temperature increase at its bottom wall is around 60 $^\circ\text{C}$ (Figure 4.16). This increase is not significantly reduced due to the addition of fins. However, assuming that the self-adaptive fins will not buckle until a temperature of around 50 $^\circ\text{C}$ is reached, it can be seen from Figure 4.16 that this temperature is achieved at the position of 6 mm, so the fins

between the positions along the microchannel of 6 mm and 19,50 mm will rise up, while the fins at the beginning of the channel will remain in a flat position for the applied heat flux and flow rate.

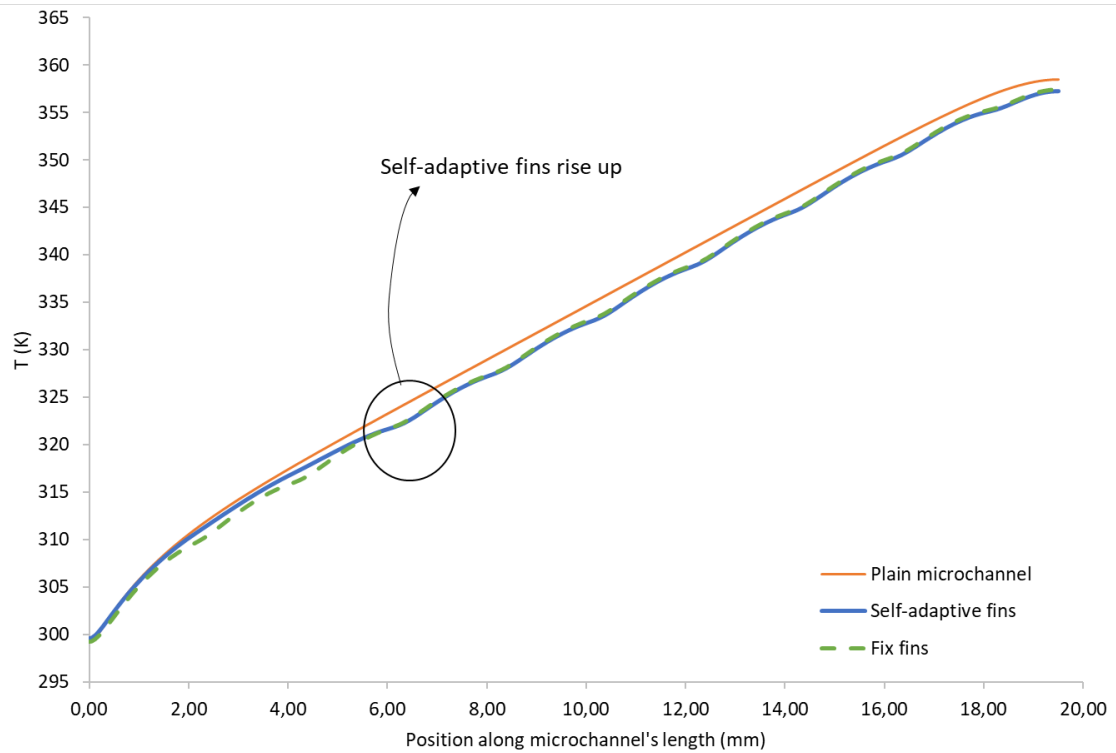


Figure 4.16. Comparison of chip temperature between a plain microchannel, a microchannel with fixed fins and a microchannel with self-adaptive fins.

Analyzing the temperature difference between the plain microchannel and the microchannel with fins inside it is observed that the temperature difference between a plain microchannel and one with fins is increased below the fins, as they enhance the heat transfer and generate vortex on the fluid boundary layer (Figure 4.17). Although the temperature difference is not very significant (around 2 K), a more uniform temperature profile could be achieved increasing the density of fins inside the microchannel. Nevertheless, this implies an increase of the pressure drop and so, the pumping power that must be assessed.

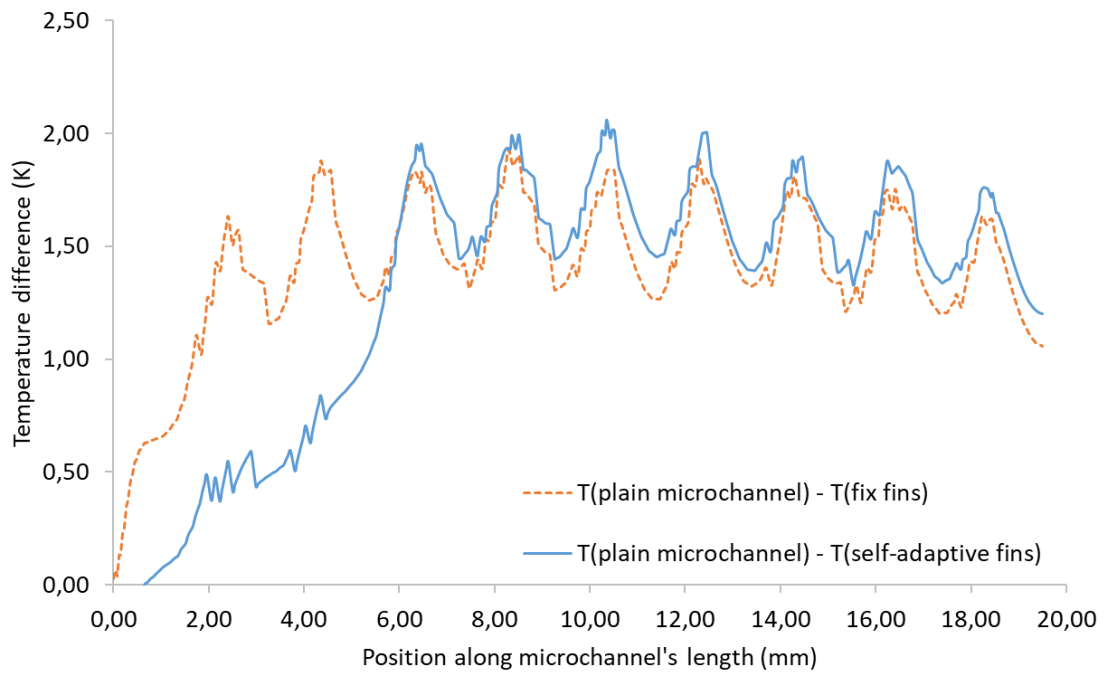


Figure 4.17. Chip temperature difference between the plain microchannel and the microchannels with fixed fins and self-adaptive fins respectively.

4.3. Experimental validation of the impact of the self-adaptive fins inside a microchannel

4.3.1. Experimental test bench and experimental device

The impact of doubly clamped self-adaptive fins on the thermo-hydraulic performance of a cooling device based on microchannels is experimentally assessed in this section. The schematic design of the experimental setup used for this study is shown in Figure 4.18.

The experimental setup is based on two separated hydraulic circuits. In the first one, the water is stored in a thermostatic bath (PolyScience PD07R20-20-A12E) which is connected to the heat exchanger responsible for heating or cooling the water of the second circuit. This second circuit is composed of a 1 μm filter (Shelco MPX) connected to a flowmeter (Bronkhorst mini cori-flow M15) and then to a micro-diaphragm liquid pump (KNF NF5). A diaphragm pulsation damper

(KNF FPD06/1.06-Z), placed after the pump, is responsible for flow stabilization before it enters the heat exchanger. Then, the test module (Figure 4.19) is hydraulically connected to the heat exchanger and finally the water returns to the filter. Type T thermocouples are used to measure inlet and outlet water temperatures and two pressure sensors measure the pressure drop along the device.

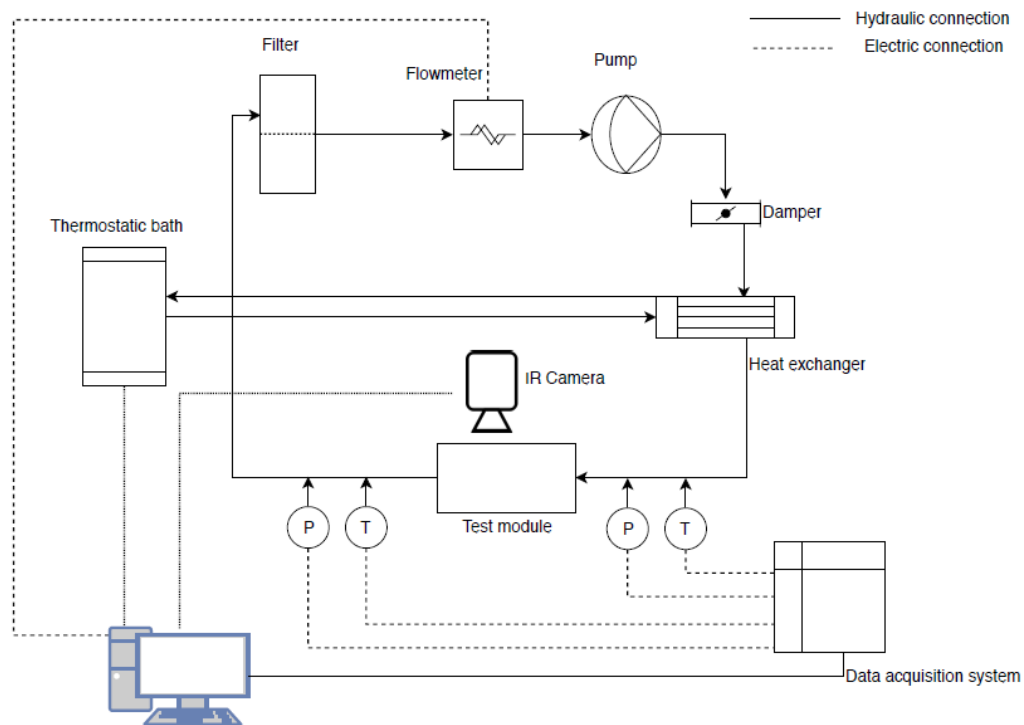


Figure 4.18. Fluidic test module setup.

The test module is heated with an external Kapton flexible heater (Birk BK3561) that can give up to 20 W/cm^2 and is electrically connected to a programmable power source (PSI9200-04T), which can be controlled with LabVIEW software.

Finally, an infrared camera (Flir A655sc) is used for measuring the surface temperatures of the test module.

A data acquisition system (Agilent 34970A) collects the information from the test bench and send them to the computer, where Labview software is used to process it.

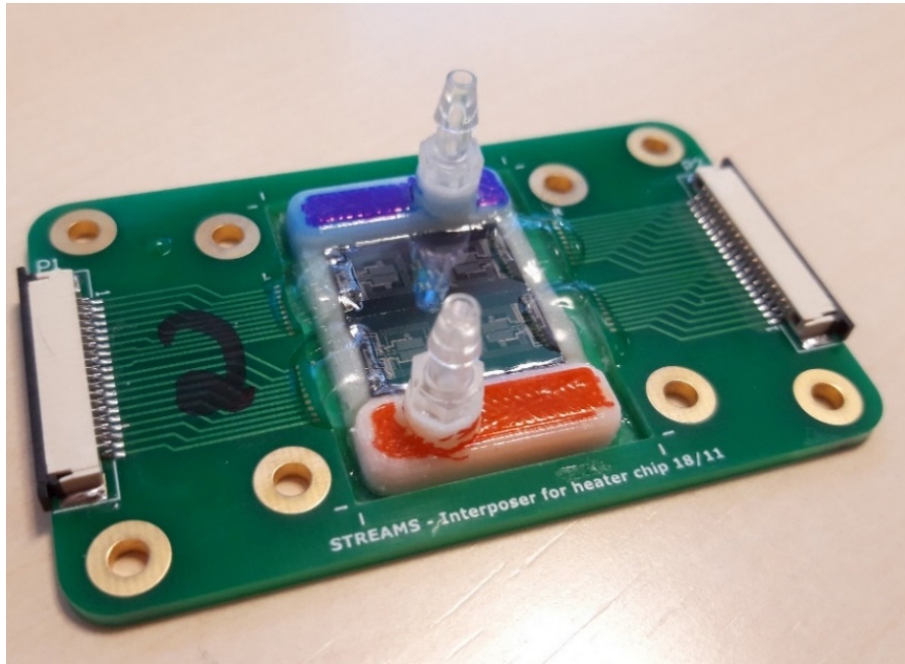


Figure 4.19. Initial microfluidic device based on microchannels to evaluate the impact of self-adaptive fins on its thermo-hydraulic performance.

4.3.2. Error analysis

In order to evaluate the propagation of the experimental errors in the different calculations, expression (41) is used, where the relative error is assessed. x_i is any experimental parameter with an associated error (δx_i).

$$\frac{\delta Er}{|Er|} = \sum_{i=1}^n \frac{\delta x_i}{|x_i|} \quad (41)$$

4.3.2.1. *Temperature*

The error of a Type T thermocouple is $\pm 0,50$ °C, as specified by the manufacturer. To this error it is necessary to add the lecture error of the data acquisition system, which is $\pm 1,00$ °C for this type of thermocouples so, the total error performed within thermocouple measurement is $\pm 1,50$ °C.

4.3.2.2. Pressure drop

According to the manufacturer, the full-scale (FS) of the pressure sensor used is 250 mbar and, its accuracy is $\pm 0,25$ % FS, so $\pm 0,63$ mbar. Also, the sensor has an offset error of $\pm 0,50$ % FS, which is equal to $\pm 1,25$ mbar. Finally, the influence effects of the supply are $\pm 0,005$ % FS/1V. As the given supply to the pressure sensors is 15 V, the induced error for these effects is $\pm 0,19$ mbar. The sum of these errors is equal to $\pm 2,01$ mbar (± 210 Pa).

Additionally, the lecture error of the DAQ system is $\pm 0,0035$ % of lecture + $\pm 0,0005$ % of range. As the lecture is 6 V and the range is 10 V, the error is ± 260 μ V ($\pm 0,0043$ % of the measure). Within the measured interval, this inaccuracy represents a maximum relative error of 0,01 mbar.

When measuring the pressure difference across the device, the total error of the two pressure sensors will be ± 420 Pa.

4.3.2.3. Flow rate

As specified by the manufacturer, the error of the flow rate sensor is $\pm 0,20$ % of the measure plus ± 50 g/h due to zero stability. For the measured interval, this represents a maximum relative error of 1,87 %.

4.3.2.4. Dissipated power by the heater

The resolution of the used power source is, according to the manufacturer, $\pm 0,10$ % of rated value, which represents a maximum relative error of 0,03 W.

4.3.2.5. Convective heat transfer coefficient and Nusselt number

The convective heat transfer coefficient is related with the temperature and the dissipated power as detailed in equation (5). The relative error of this coefficient would be the sum of the

4. Impact assessment of the self-adaptive fins inside a microchannel

relative errors in temperature and dissipated power, as detailed in equation (41). For the measured interval, the maximum error in the heat transfer coefficient is $\pm 10\%$.

The Nusselt number is related with the convective heat transfer coefficient as detailed in equation (7). In this case, the error in this calculation is also $\pm 10\%$.

4.3.3. Results and discussion

4.3.3.1. *Experimental validation of the numerical model for plain microchannels*

The test module used for validation of the numerical model is based on 7 plain microchannels of $195\ \mu\text{m}$ width, $1950\ \mu\text{m}$ length and $80\ \mu\text{m}$ height (Figure 4.20).

The main goal of this test is the validation of the numerical model used for the simulations. In order to do this assessment, a flexible heater of dimensions $1,27\ \text{cm} \times 1,27\ \text{cm}$ is placed above the cooling device (Figure 4.21a). Four thermocouples are placed between the heater and the cooling device to measure the temperature evolution along one microchannel (Figure 4.21b).

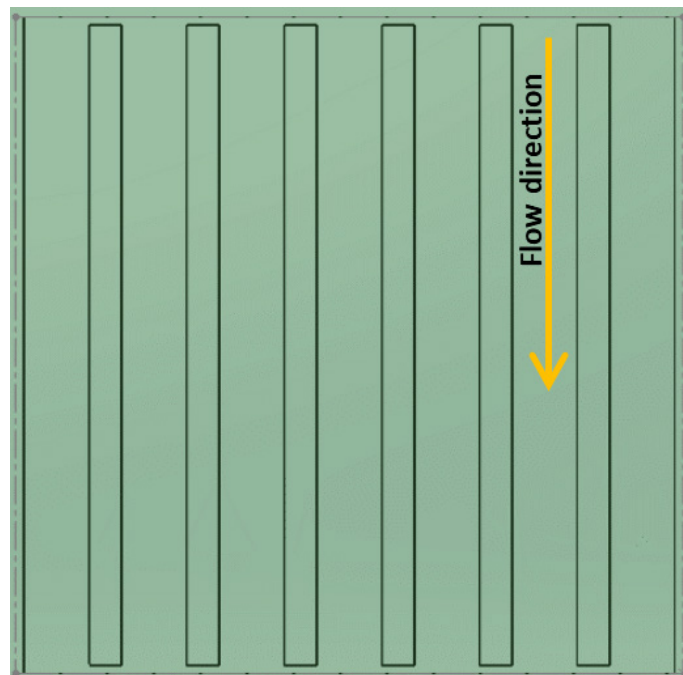


Figure 4.20. Schematic of the assessed device based on a configuration of plain microchannels.

For fixed boundary conditions of fluid inlet temperature ($T_{in} = 30\text{ }^{\circ}\text{C}$) and heat flux ($q'' = 15\text{ W/cm}^2$), the experimental results of average surface temperature, determined through the average value of the four thermocouple measurements along one channel (Figure 4.21b), and pressure drop, are compared with the numerical results found for the same conditions (Figure 4.22). The procedure is repeated three times to ensure the validity of the results.

After evaluating the average surface temperature (Figure 4.22a), a maximum error of 12,60 % is found between numerical and experimental results. Regarding to the pressure drop assessment, although the behavior of the pressure drop in function of the flow rate is the same for both numerical and experimental results, the las ones showed lower pressure drops along the device than the numerical simulations, with a maximum difference of 19 %. This difference can be due to the simulation of solid fins instead of fine fins.

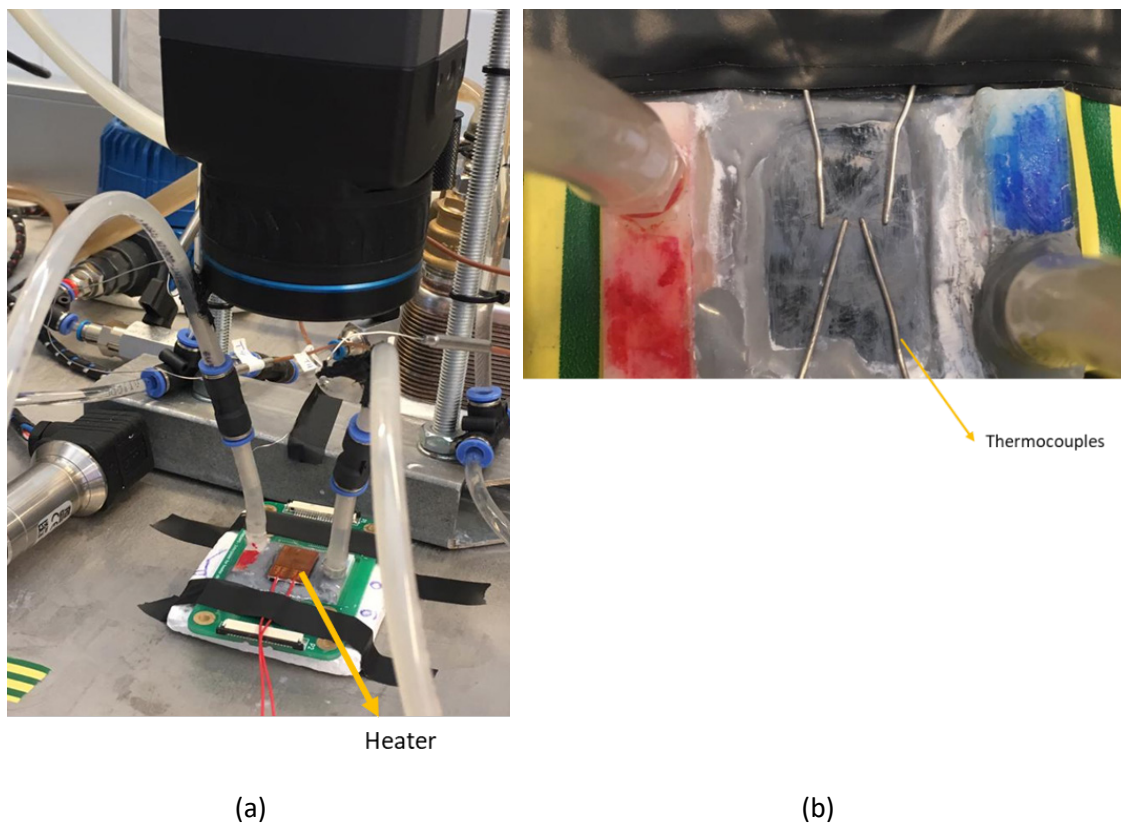
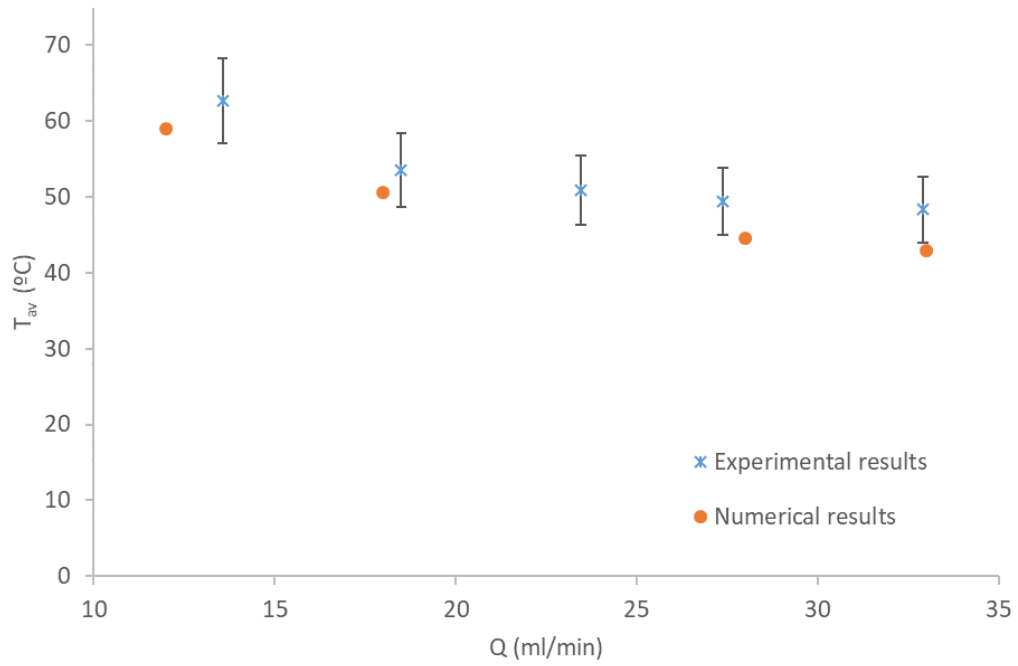
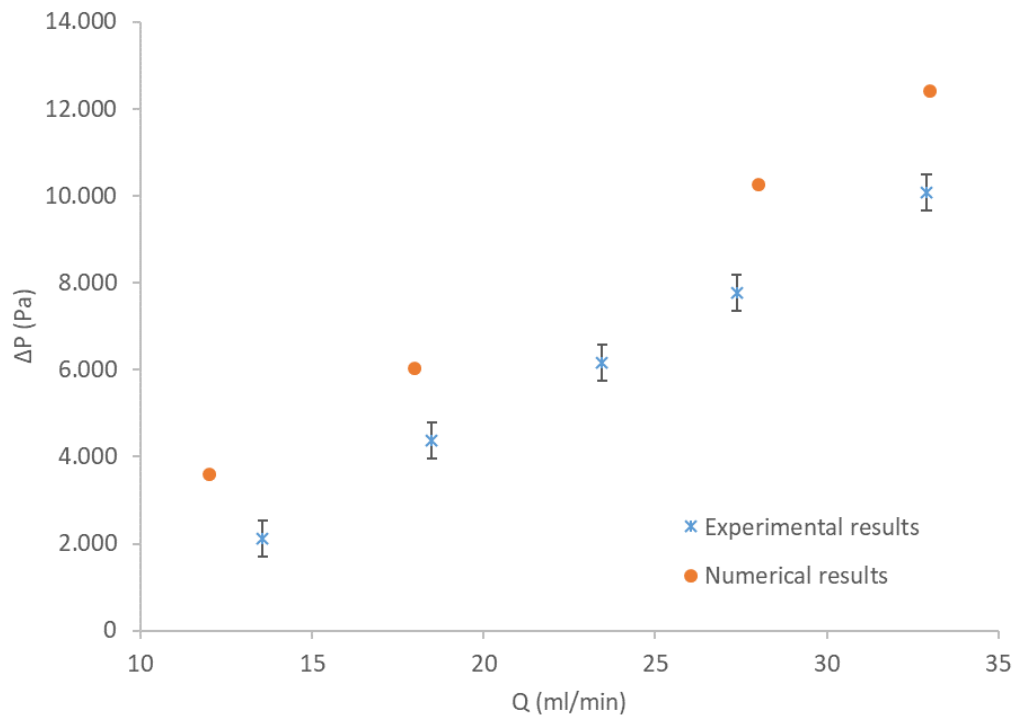


Figure 4.21. (a) Experimental setup with the heater placed above the cooling device. (b) Thermocouples located between the heater and the cooling device following a channel path.

4. Impact assessment of the self-adaptive fins inside a microchannel



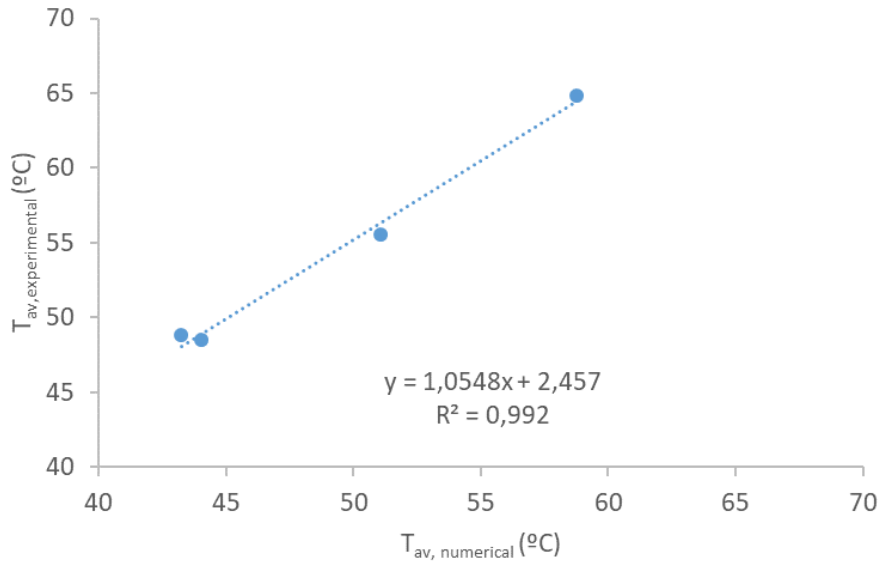
(a)



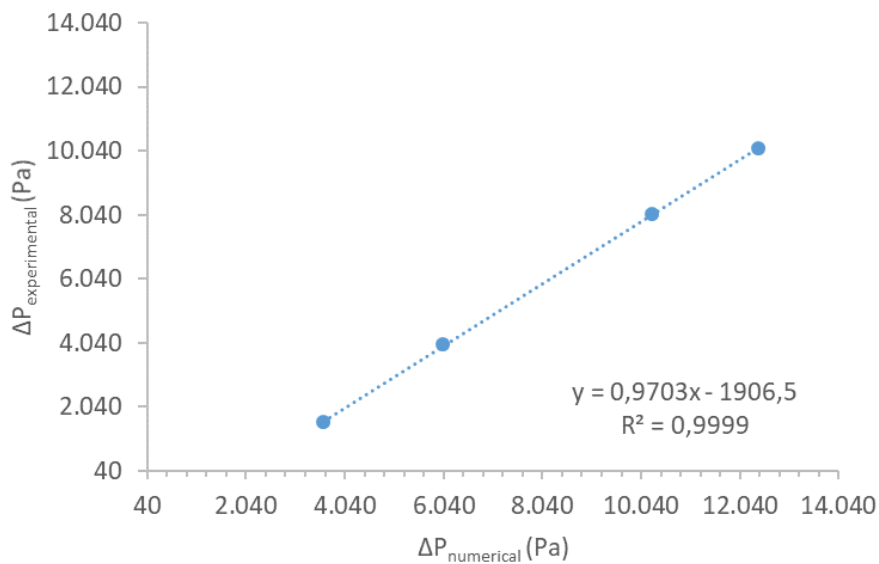
(b)

Figure 4.22. Comparison between numerical and experimental values for (a) average surface temperature and (b) pressure drop along the device.

A correlation between experimental and numerical data is done through the analysis of the slope of the linear regression (Figure 4.23). It is seen that both correlations of temperature (Figure 4.23a) and pressure drop (Figure 4.23b) follow a linear trend, with both the slope (a) and the coefficient of determination (R^2) very close to 1 ($a = 1,0548$ and $R^2 = 0,992$ for the temperature and $a = 0,9703$ and $R^2 = 0,999$ for the pressure drop). These results indicate the strong similarity between the behavior of both assessed models.



(a)



(b)

Figure 4.23. Correlation between experimental and numerical data for (a) Average temperature surface and (b) Pressure drop.

4. Impact assessment of the self-adaptive fins inside a microchannel

Additionally, a t-Test is performed to adjust the model and validate the similarity of both results. Assuming a normal distribution of the measurements and the linear behavior of the regression line (42), it is intended to demonstrate the null hypothesis that the slope a is equal to a specified value a_0 , which will be 1 in this case (43). SE is the standard error of the slope.

$$y = ax + b \quad (42)$$

$$t_{value} = \frac{a - a_0}{SE_a} \quad (43)$$

For a two-tailed normal distribution of t values, 2 degrees of freedom and a significance level of 0,05, the critical value to discard the null hypothesis would be 4,30 (Table 4.4). Within this statement, it can be seen that both t values of average surface temperature and pressure drop are lower than the critical t values ($|t_{value}| < t_{critical}$), what confirms the null hypothesis that the slope a is equal to 1.

With the good agreement that both numerical and simulation results show between them, the numerical results obtained in the previous section can be validated.

	SE_a	Df	Confidence	t_{value}	$t_{critical}$	$ t_{value} < t_{critical}$
T_{av} (°C)	0,07	2	0,95	0,82	4,30	Yes
ΔP (Pa)	0,007	2	0,95	-3,98	4,30	Yes

Table 4.4. T-test evaluation of the results.

4.3.3.2. Infrared camera assessment of the device with self-adaptive fins

The objective of this test is to experimentally assess the impact of the self-adaptive fins on the thermo-hydraulic performance of a microchannel cooling device, compared with a system based on plain microchannels. The initial configuration of this device is the same as the microchannels presented in previous section but with 10 pairs of self-adaptive fins in each channel (Figure 4.24).

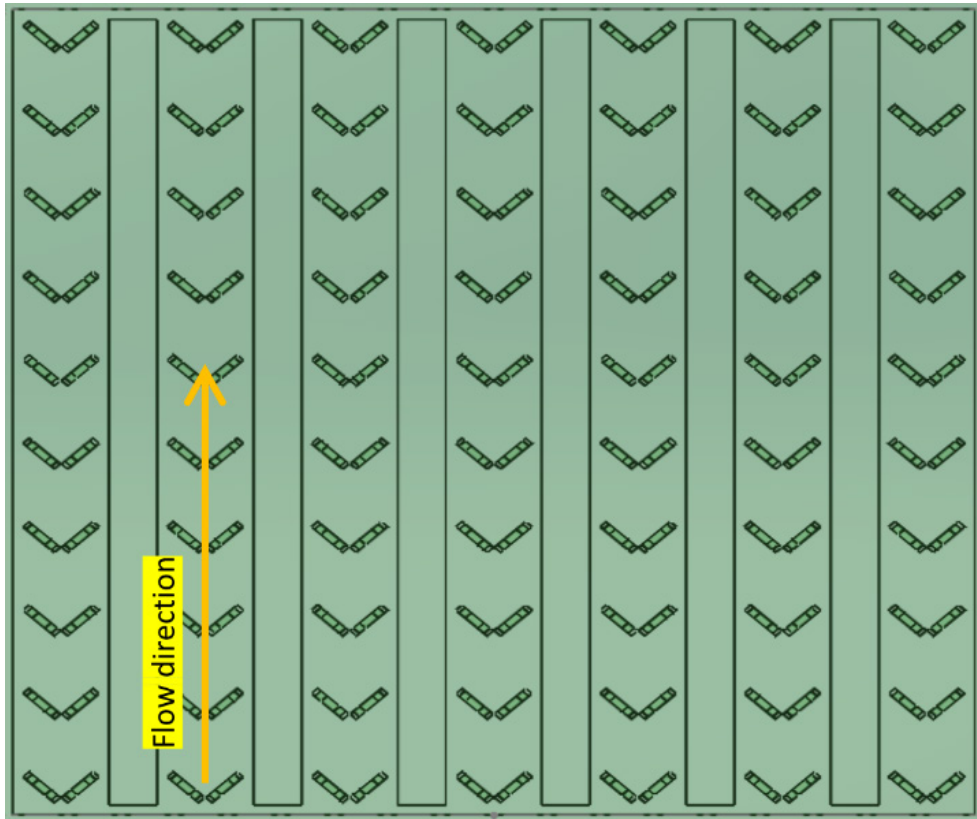
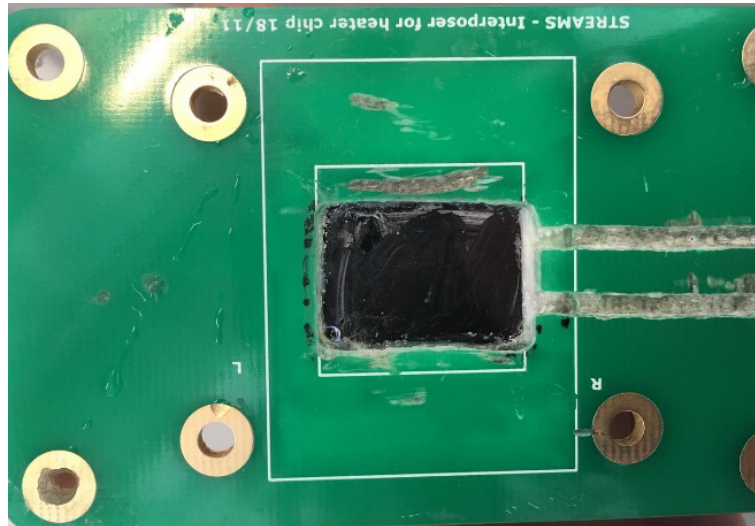


Figure 4.24. Schematic of experimental cooling device based on microchannels with self-adaptive fins inside.

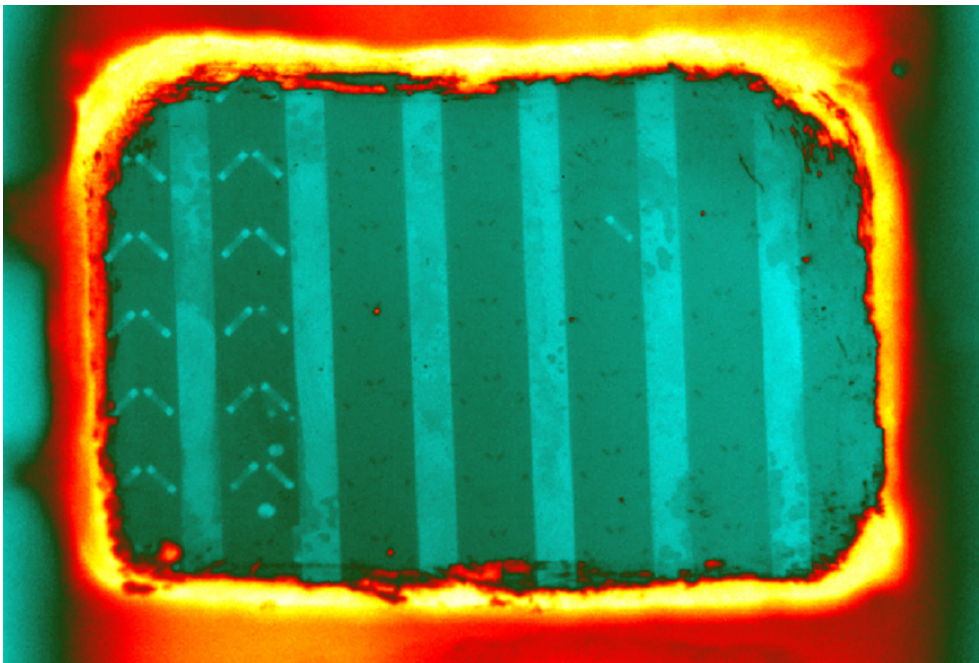
This configuration is verified with the infrared (IR) camera. As silicon is a semitransparent material for low energy levels in the infrared portion of the spectrum, the self-adaptive fins can be seen with the IR camera when looking directly to the wall where they have been etched. To do so, the device is partly disassembled to have direct access with the camera to the wall that have the fins located (Figure 4.25).

What is found with this test is that only two lateral microchannels have fins inside while in the rest of them, the traces of the anchors of the fins are seen but not the fins itself. This lack of the fins can be attributed to microfabrication defects or to an overpressure given to the fins in previous tests.

4. Impact assessment of the self-adaptive fins inside a microchannel



(a)



(b)

Figure 4.25. (a) Reverse part of the microfluidic device with microchannels and self-adaptive fins, partly disassembled to have direct access to the wall where the fins are etched. (b) Infrared camera vision of the Si microchannels with self-adaptive fins (seen through the Si wall where the fins are etched).

Although these results are not the expected, an adaptation of the planned tests has been done to be able to assess the impact of the self-adaptive fins on the performance of a cooling device.

4.3.3.3. Experimental validation of the numerical model for microchannels with self-adaptive fins.

The aim of this test is to compare the experimental and the numerical results obtained when evaluating the impact of the self-adaptive fins in the thermal performance of a microchannel. Previously, the experimental validation of the results for a plain microchannel has been done and now, the same procedure will be done when self-adaptive fins are placed inside a microchannel.

First of all, in order to ensure that the same flow rate passes through all the channels of the device with self-adaptive fins, the five channels where no fins are placed are sealed. In this case, only two channels of the cooling device remain active. Then, the temperature evolution along the surface of one microchannel is evaluated through the measurements of the infrared camera when steady state is reached after applying a heat flux below. As explained before, Silicon is semitransparent to infrared signal, what induces on a bad temperature reading of the surface. To avoid this issue, the surface of one microchannel is painted in black and then, the temperature is assessed above this surface ("Line 1" in Figure 4.26).

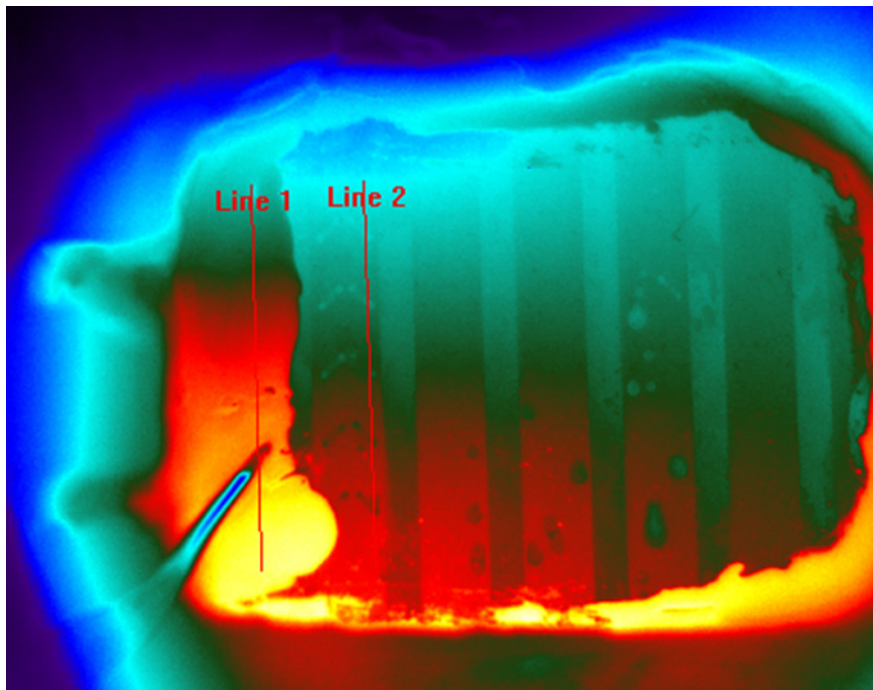


Figure 4.26. IR camera assessment of the temperature along one microchannel when only two of them are active. The Si surface of one channel is painted in black for a correct reading of the temperature ("Line 1").

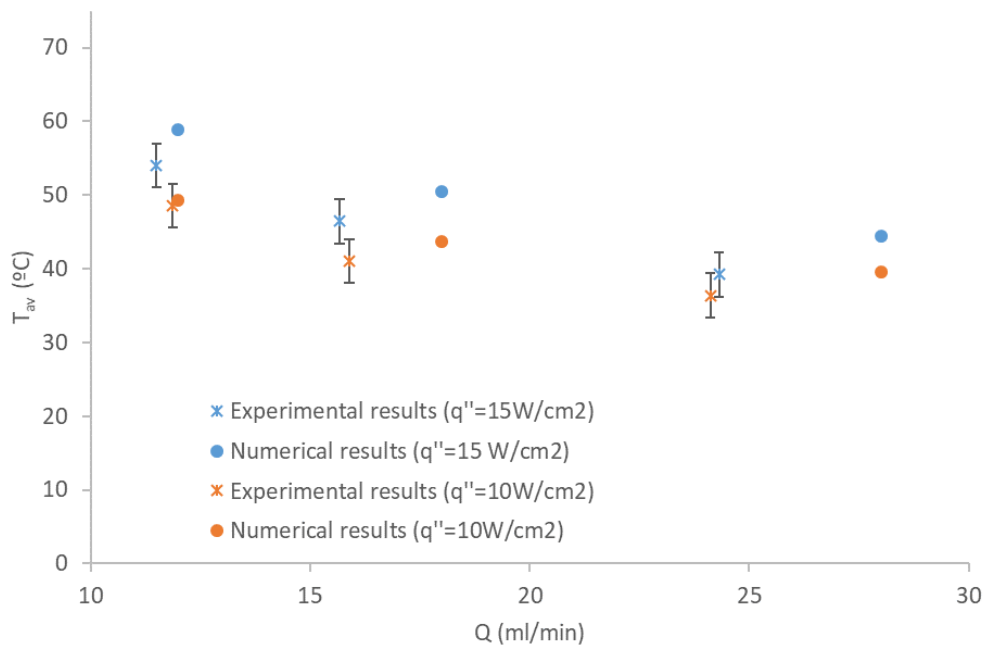
4. Impact assessment of the self-adaptive fins inside a microchannel

For fixed boundary conditions of fluid inlet temperature ($T_{in} = 30 \text{ }^\circ\text{C}$) and two different heat fluxes ($q''_1 = 15 \text{ W/cm}^2$; $q''_2 = 10 \text{ W/cm}^2$), the experimental results of average surface temperature and pressure drop, are compared with the numerical results found for the same conditions.

After evaluating the average surface temperature (Figure 4.27a), a maximum error of 19 % is found between numerical and experimental results. However, when assessing the pressure drop a difference of more than 50 % is found for some data. This difference can be due to the sealed channels in the experimental test, as some water can flow through them, for this reason, little confidence is given to these results.

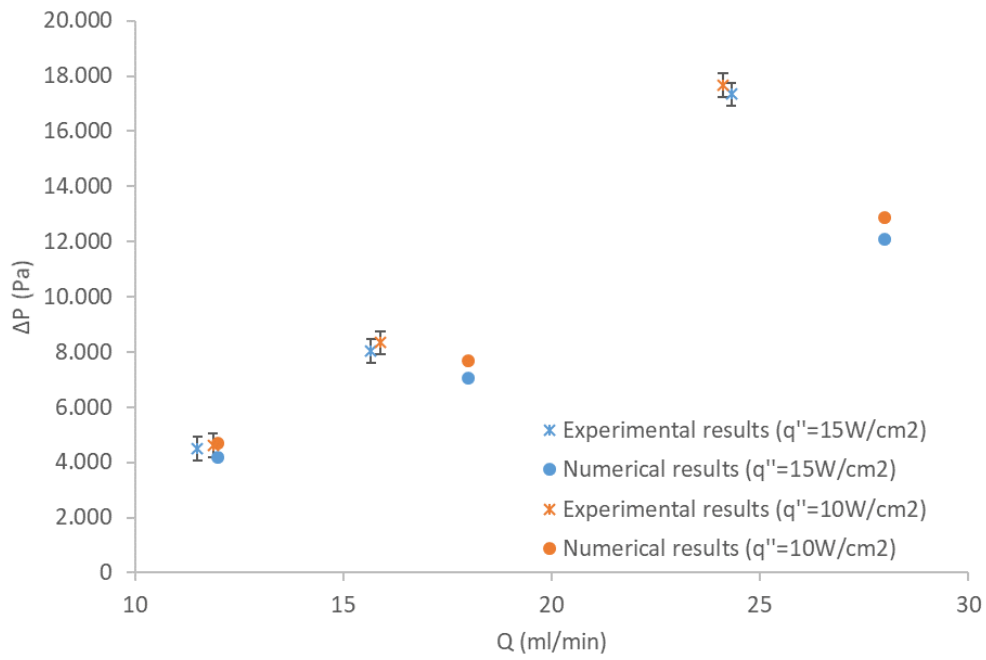
Additionally, a t-Test is performed to adjust the model and validate the similarity of both results. As in previous section, a normal distribution of the measurements and a linear behavior of the regression line (42) are assumed.

For a two-tailed normal distribution of t values, 1 degree of freedom and a confidence level of 0,95, the critical value to discard the null hypothesis would be 4,30 (Table 4.5). Within this statement, it can be seen that both t values of average surface temperature and pressure drop are lower than the critical t values ($|t_{value}| < t_{critical}$), what confirms the null hypothesis that the slope α is equal to 1.



(a)

4. Impact assessment of the self-adaptive fins inside a microchannel



(b)

Figure 4.27. Comparison between numerical and experimental values for (a) average surface temperature and (b) pressure drop along the device.

	q'' (W/cm ²)	a	R ²	SE _a	Df	Confidence	t _{value}	t _{critical}	t _{value} < t _{critical}
T _{av} (°C)	15	0,75	0,97	0,11	1	0,95	-2,08	12,70	Yes
	10	0,98	0,77	0,53	1	0,95	-0,02	12,70	Yes
ΔP (Pa)	15	2,02	0,99	0,10	1	0,95	10,03	12,70	Yes
	10	2,22	0,99	0,12	1	0,95	10,56	12,70	Yes

Table 4.5. T-test evaluation of the results.

Within these results, it is seen the good correlation between numerical and experimental data even the differences obtained in pressure drop and so, the numerical models of microchannels with self-adaptive fins inside can be validated.

4. Impact assessment of the self-adaptive fins inside a microchannel

4.3.3.4. Impact of the self-adaptive fins inside a microchannel when submitted to non-uniform heat flux

In this test, the performance of two microchannels with self-adaptive fins is compared with the performance of the device based on 7 plain microchannels when both submitted to non-uniform heat flux. It is not considered to seal 5 over the 7 plain microchannels due to limitations to seal it temporary. In order to do an equal comparison, the two microchannels with self-adaptive fins are heated with an external flexible heater with a heating area of $0,64 \times 0,64 \text{ cm}^2$ (Figure 4.28a), that gives a heat flux to the channels of $7,50 \text{ W/cm}^2$. Meanwhile, the 7 plain microchannels are heated with a bigger heater, that covers all the channels, and gives a proportional heat flux to them (Figure 4.28b).

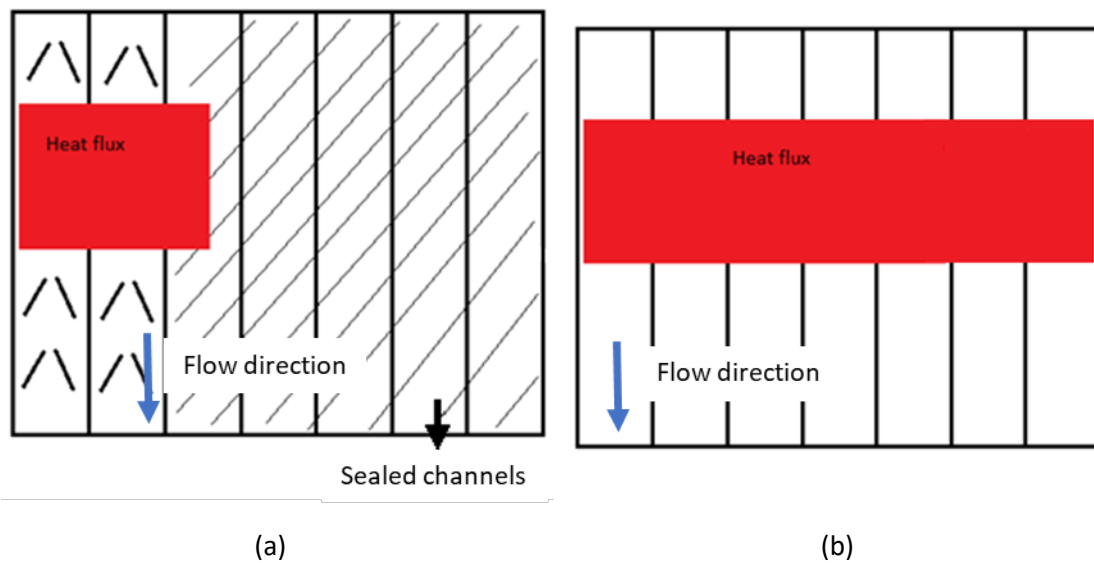


Figure 4.28. Schematic of the non-uniform configuration applied at (a) 2 microchannels with self-adaptive fins; and (b) 7 microchannels without fins.

	Plain microchannels (7 microchannels)	Self-adaptive fins (2 microchannels)
$Q1_{total}$ (ml/min)	38,50	11,00
$Q1_{channel}$ (ml/min·ch)	5,50	5,50
$Q2_{total}$ (ml/min)	52,50	15,00

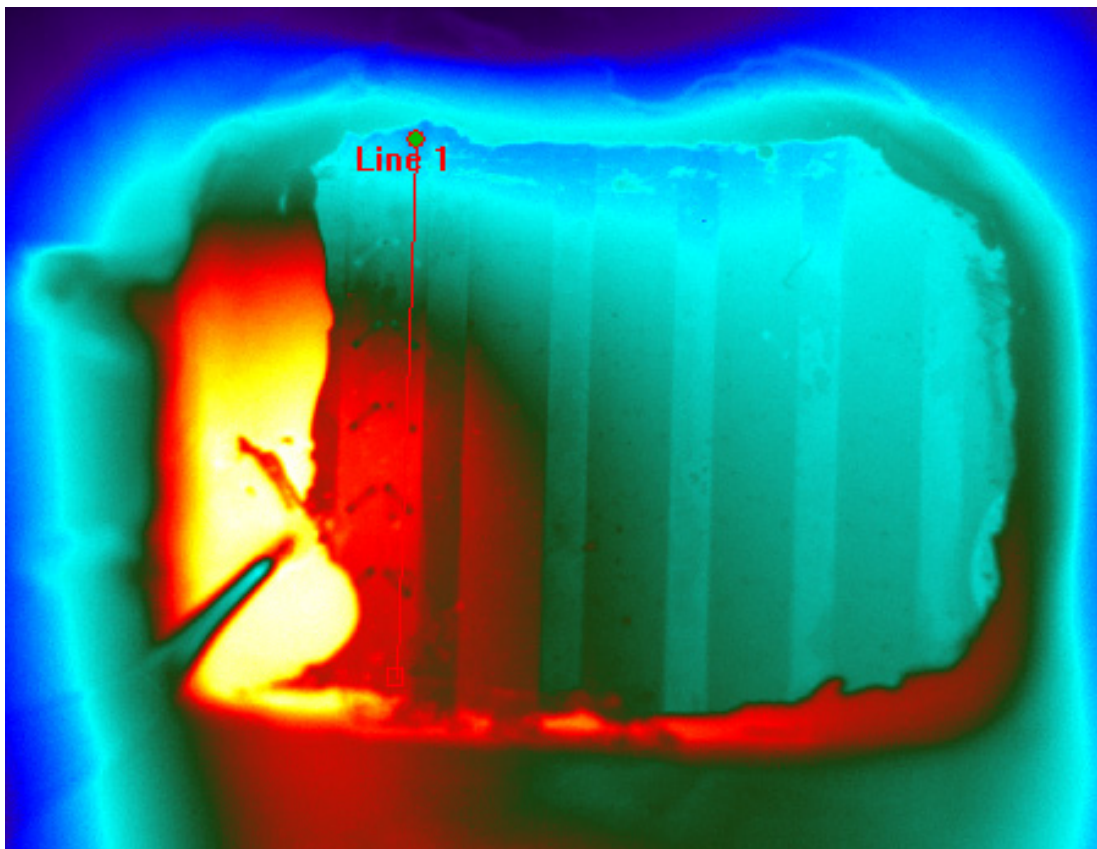
4. Impact assessment of the self-adaptive fins inside a microchannel

$Q_{2\text{channel}}$ (ml/min·ch)	7,50	7,50
q' (W)	10,75	3,07

Table 4.6. Proportional flow rate and heat flux applies to both assessed devices.

A proportional non-uniform heat flux and 2 different flow rates are applied to both devices to ensure the same behavior per each channel (Table 4.6). Then, infrared thermal image is used to assess the temperature along one microchannel in both devices once steady state is reached. “Line 1” in Figure 4.29 indicates where the temperature evolution has been evaluated, which corresponds to the central place of the heater used. Also, the energetic balance has been checked to ensure the validity of the results.

Figure 4.30 shows that, for the same flow rate, the microchannels with self-adaptive fins present a lower thermal gradient, what can be an indicative parameter of the impact of the fins (Table 4.7).



(a)

4. Impact assessment of the self-adaptive fins inside a microchannel

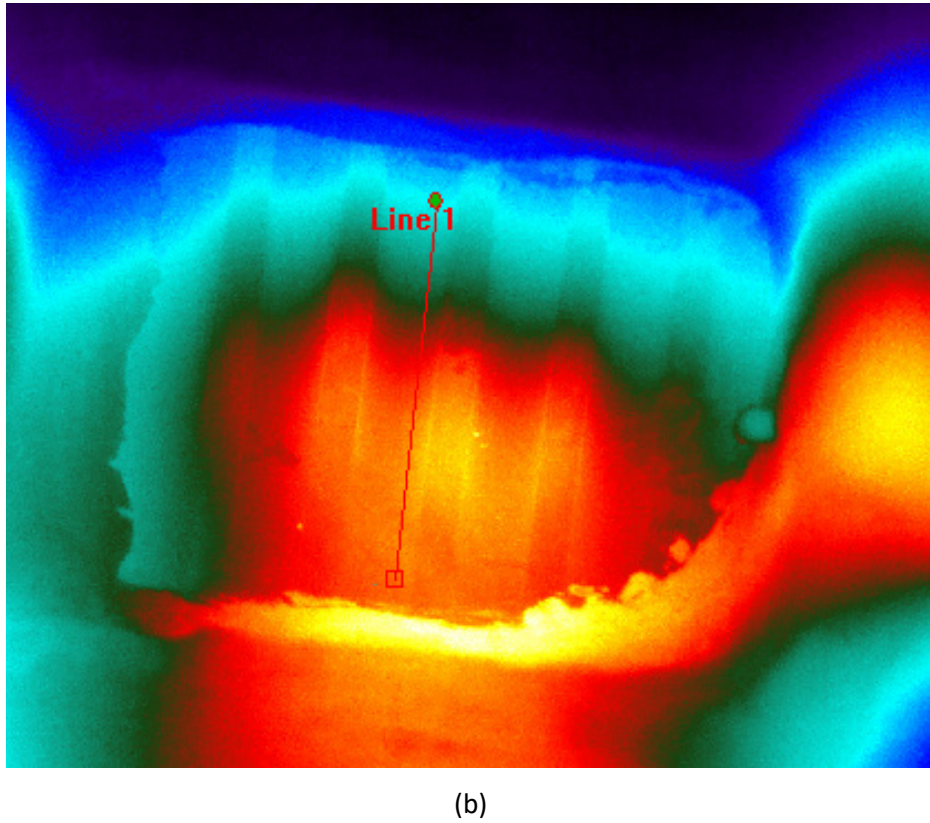


Figure 4.29. Non-uniform heating of (a) Self-adaptive fins: $q'=3,07$ W and (b) Plain microchannels: $q'=10,75$ W.

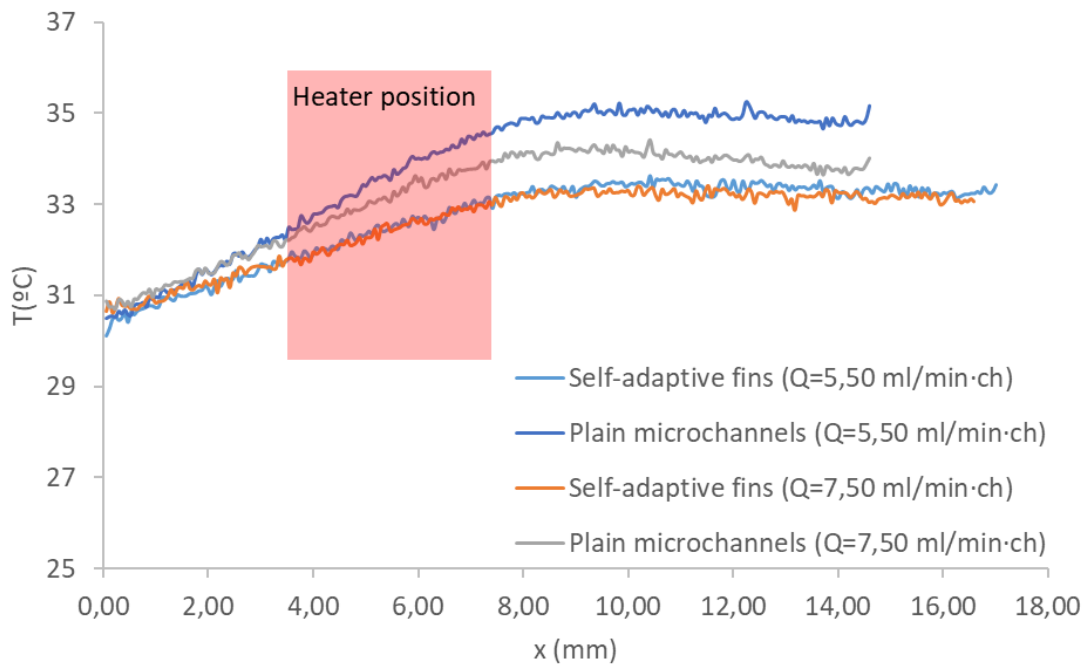


Figure 4.30. Comparison of the temperature evolution along one microchannel in both assessed devices for different flow rates.

4. Impact assessment of the self-adaptive fins inside a microchannel

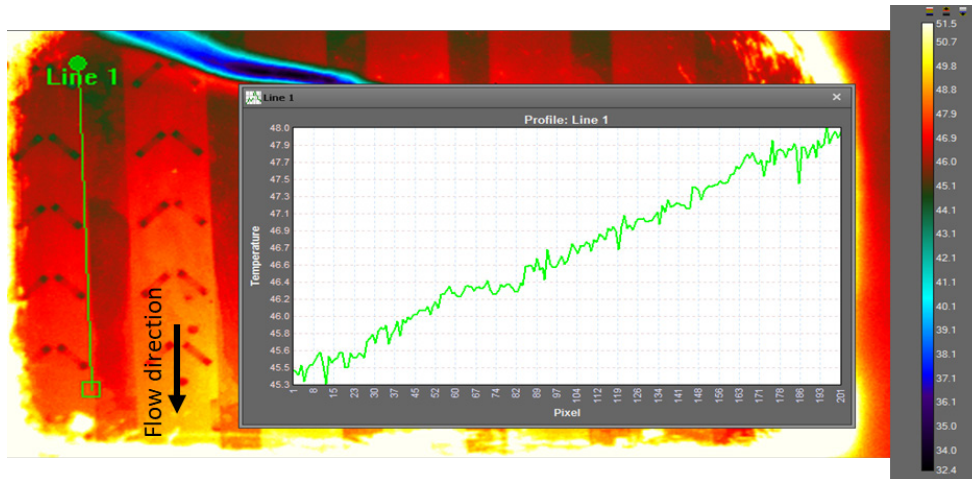
		T_{in} (°C)	$T_{chip,av}$ (°C)	ΔT (°C)
Q = 5,50 ml/min·ch	Plain channel	27,28	37,23	4,76
	Self-adaptive fins	26,27	32,68	3,54
Q = 7,50 ml/min·ch	Plain channel	29,95	36,18	3,72
	Self-adaptive fins	26,91	33,60	2,79

Table 4.7. Assessment of the results for heat transfer enhancement and power efficiency of both devices for two different flow rates.

4.3.3.5. Visualization of the self-adaptive fins deformation through thermal IR camera

Additionally, the deformation of the self-adaptive fins inside a microchannel has been observed through the thermal analysis of the infrared camera when the device is submitted to a uniform heat flux (Figure 4.31). In this case, when the temperature is assessed outside the position of the fins, a linear evolution of the temperature along the microchannel is seen (Figure 4.31a). Moreover, when the temperature is plotted along a line that goes through the anchors of the fins, a clear dip in the measurement at the anchors is noticed, which follows the trend of the wall temperature (Figure 4.31b). This is to be expected since the anchors are in direct contact with the wall and should therefore follow the same temperature distribution. The measurement difference between the wall and the anchor (the dip itself) does not necessarily represent a difference in temperature, since the emissivity of the wall and beam are different. Finally, when the measurement is plotted along a line that crosses the middle of the fins, an interesting profile is obtained (Figure 4.31c). At the entrance of the channel, where the temperature is lower, the fins remain in flat position and so they remain at a temperature near that of the anchors because no water flows below them. However, as the temperature increases along the channel, the self-adaptive fins rise up, allowing the water to pass below them and cooling them. Then, what is seen through the IR camera is that the temperature at the position of the fin becomes more uniform with the surroundings and the temperature peaks gets much smaller because it is showing the water temperature. Although this is a very qualitative assessment, it gives an idea of the self-adaptive behavior of the fins inside a microchannel.

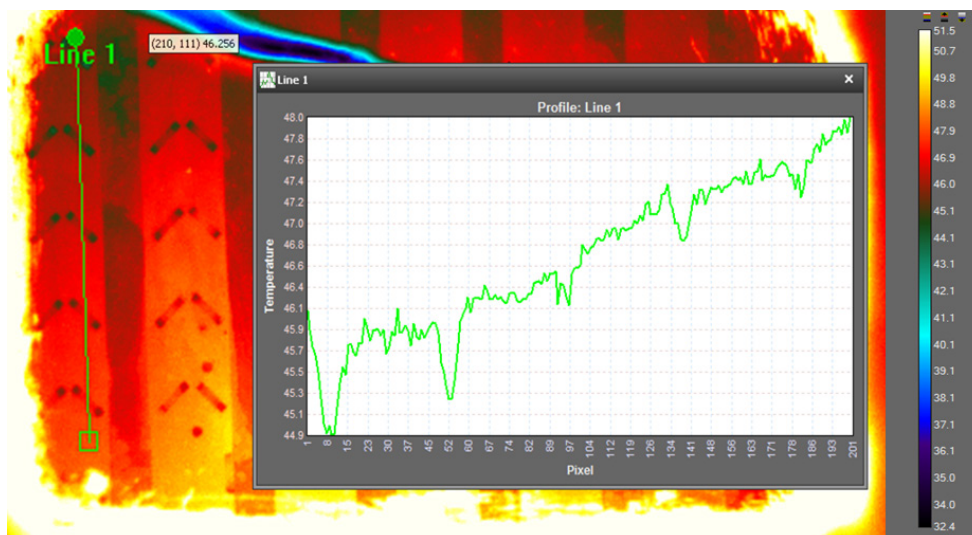
4. Impact assessment of the self-adaptive fins inside a microchannel



(a)



(b)



(c)

Figure 4.31. Temperature evolution along the microchannel for different positions of "Line 1": (a) Outside the self-adaptive fins, (b) Above the anchors and (c) Above the self-adaptive fins.

4.4. General overview of the impact of self-adaptive fins inside a microchannel cooling device

In this chapter, the impact that the doubly clamped self-adaptive fins perform into a microchannel cooling device has been numerically and experimentally assessed.

According to numerical simulations, the heat transfer enhancement due to the presence of fins inside a microchannel cooling device increases with the flow rate, achieving a maximum Nu/Nu_0 of 1,40 when $Re = 800$. As detailed in previous chapters, these results go in line with the literature findings. Additionally, it has been found that the density of fins has an important impact on heat transfer enhancement as, for the same flow rate, it is increased by 5% when the density of fins is doubled. Also, a higher density of fins inside a microchannel performs more impact on the heat transfer enhancement than changing the angle of attack of the fins.

It has also been seen that the use of self-adaptive fins instead of fixed fins inside a microchannel supposed a reduction of 8 % on pumping power, according to numerical simulations, for a determined time dependent heat flux. This result indicates the usefulness of the self-adaptive concept on pumping power reduction and so, the achievement of a more energy efficient cooling device.

A numerical assessment of the temperature uniformity shows a local heat transfer enhancement just after the fin placement; however, it is not a general trend along the whole microchannel due to the small vortex generated. This statement can have a higher impact when the fins are placed inside a microfluidic cell, as the fin density inside them is higher and this local effect of heat transfer enhancement can be translated into a more global effect.

The placement of the fins at the opposite side of the heat flux has also been numerically assessed, as it is the same initial configuration of the experimental devices. In this case, it has been seen that, whereas the pressure drop increment due to the addition of the fins is the same independently of the position of the fins, the heat transfer enhancement difference depends on the flow rate but, in general, is lower when the fins are placed at the opposite wall of the heat flux. For $Re \leq 100$ the heat transfer enhancement is almost the same for both configurations evaluated; however, as flow rate increases, it is clearly seen that the thermal enhancement of the fins placed at the cold wall is worse, achieving a 20 % less heat transfer enhancement than

the fins placed at the same wall as the heat flux when $Re = 800$. This statement shows that, except for $Re \leq 100$, the thermo-hydraulic performance of a device with the fins placed at the opposite wall of the heat flux is worse, as the vortex generated by the self-adaptive fins is not enough to have an important impact at the opposite wall.

Also, the numerical results have been validated through comparison with experimental results, finding good agreement between them when assessing the average surface temperature along a microchannel and the pressure drop along it. Within this statement, the numerical results showed in this chapter are validated, as the same boundary conditions are applied.

Additionally, the effect of the self-adaptive fins on temperature uniformity of the cooling device has been evaluated for non-uniform heat load scenarios. Although the comparison is difficult because the assessed devices do not have the same geometry due to microfabrication problems, the impact of the self-adaptive fins on the thermal performance is noticed, as the thermal gradient in the silicon surface is lower. Also, the behavior of the self-adaptive fins inside a microchannel has been seen through the evaluation of the temperature profile given by the infrared camera. Nevertheless, more tests must be done in this way, with two equal cooling devices and ensuring the good performance of all the self-adaptive fins inside the devices.

IMPACT ASSESSMENT OF THE SELF-ADAPTIVE FINS INSIDE A
MICROFLUIDIC CELL SYSTEM

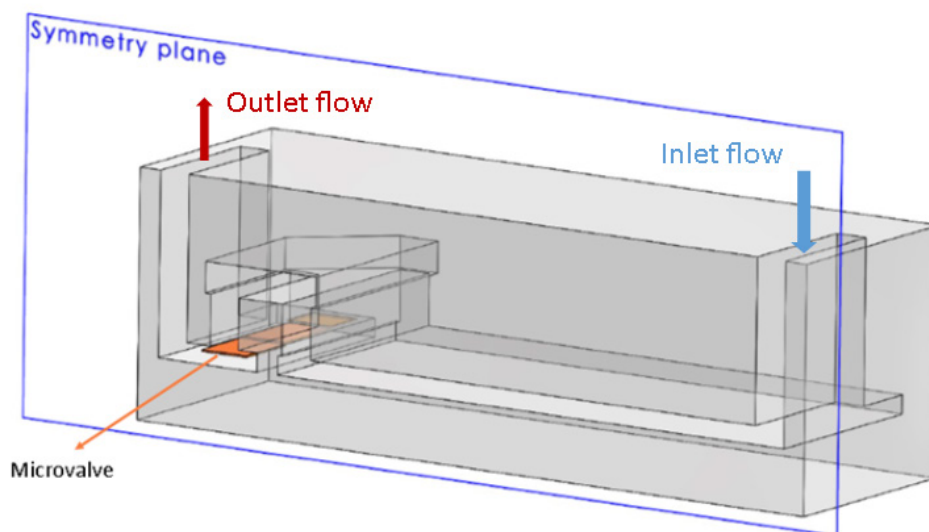
5. IMPACT ASSESSMENT OF THE SELF-ADAPTIVE FINS INSIDE A MICROFLUIDIC CELL SYSTEM

In this chapter the impact of the self-adaptive fins inside a cooling device based on a matrix of microfluidic cells, defined previously in section 1.3.1.1, is going to be numerically assessed.

5.1. Geometry of the microfluidic cell

The cell geometry that has been used in this work to assess the impact of the self-adaptive fins is divided in two parts. First, there is the main channel where the self-adaptive fins will be placed. At the end of the main chamber, there is an elbow (reverse chamber) where the microvalve is placed in order to be opened in the flow direction, otherwise the flow pressure will tend to close it. Finally, after passing through the microvalve gap, the flow exits by the cell outlet (Figure 5.1).

The dimensions of the main channel of the cell are 2,47 mm length, 1,75 mm width and 80 μm height, the rest of the dimensions are listed in Table 5.1. The channel height considered is the same as in the microchannels assessed in previous chapter, for easier comparison.



(a)

5. Impact assessment of the self-adaptive fins inside a microfluidic cell system

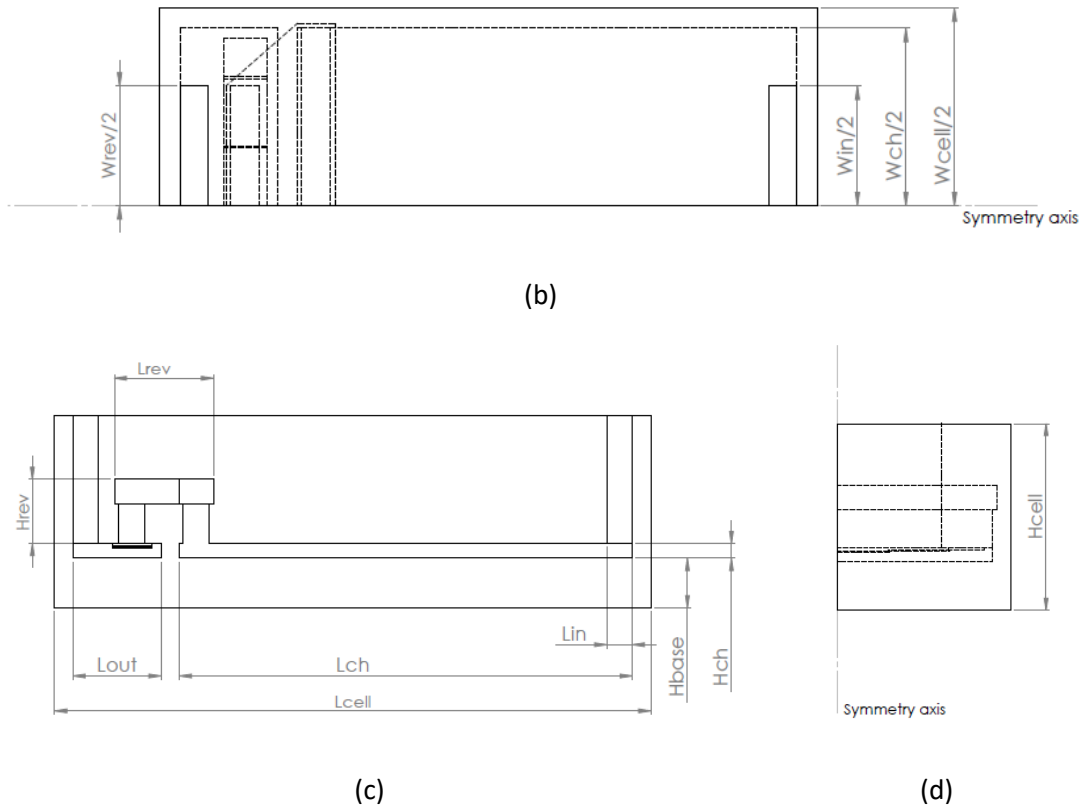


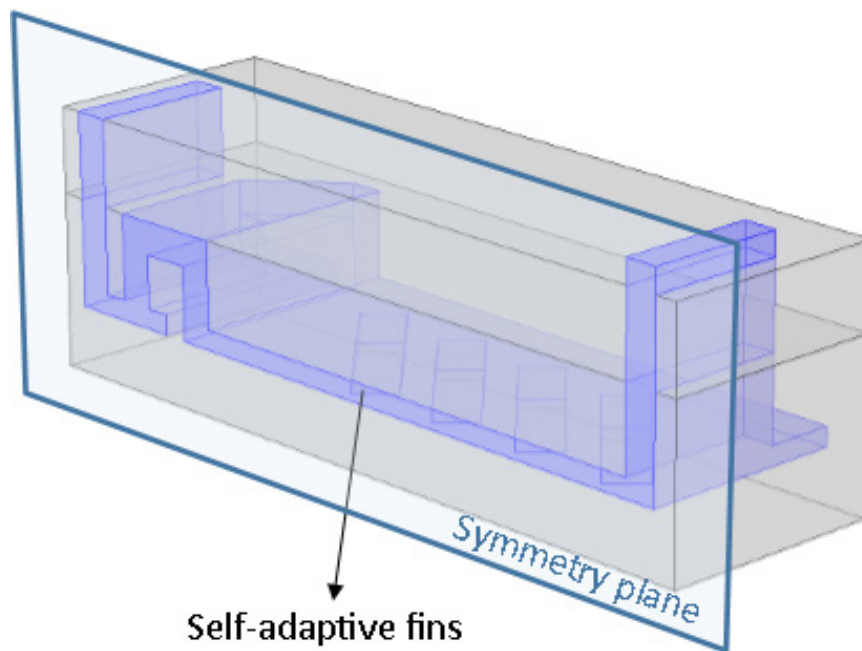
Figure 5.1. (a) 3D view of half empty microfluidic cell with the outlet microvalve. (b) Top view, (c) front view and (d) side view of half microfluidic cell.

Parameter	Value (mm)	Description
L_{cell}	3,25	Total length of the cell
W_{cell}	1,95	Total width of the cell
H_{cell}	0,70	Total height of the cell
L_{ch}	2,47	Channel length (before outlet)
L_{out}	0,48	Length outlet chamber
W_{ch}	1,75	Channel width
W_w	0,10	Wall width
H_{base}	0,27	Base height (From chip to channel)
H_{ch}	0,08	Channel height
L_{rev}	0,34	Length reverse chamber

h_{rev}	0,35	Height reverse chamber
W_{rev}	1,18	Width posterior part reverse chamber
L_{in}	0,16	Inlet and outlet lengths

Table 5.1. Main dimensions of the microfluidic cell.

Inside the microfluidic cell, 4 pairs of self-adaptive fins are placed, with a separation of $430\ \mu\text{m}$ between them and an angle of attack of 45° (Figure 5.2). The self-adaptive fins are made of silver and their geometry is the same defined in Figure 4.1c: $0,90\ \text{mm}$ length, $0,18\ \text{mm}$ width and $9,00\ \mu\text{m}$ thickness. For the numerical simulations, with the aim of reducing computational resources, the assessment of the impact of the fins within the microchannel has been done considering the geometry of the fins fixed. At the elevated position, $30\ \mu\text{m}$ of elevation are considered for the fins (relative height $z/H = 0,375$).



a)

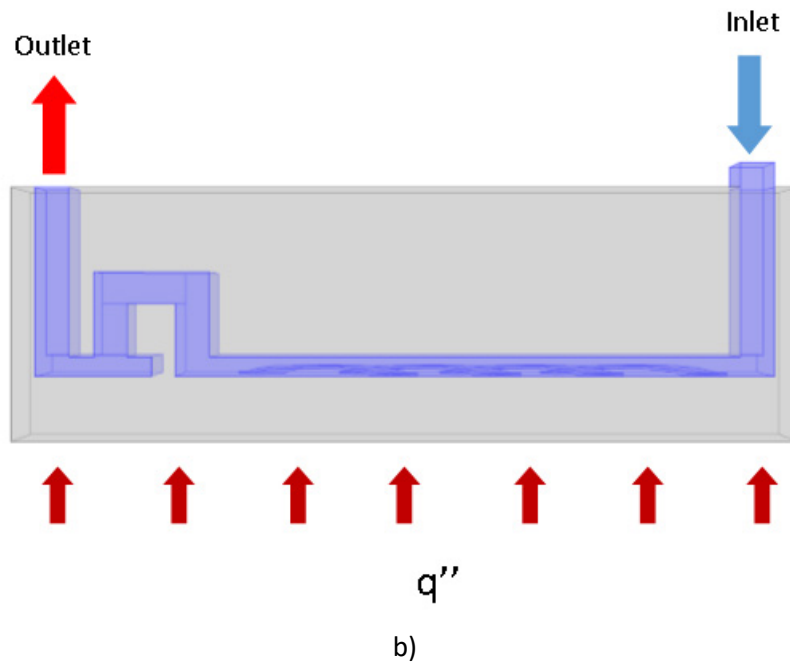


Figure 5.2. 3D view (a) and lateral view (b) of half microfluidic cell with fins inside

5.2. Numerical assessment of self-adaptive fins performance

5.2.1. Boundary conditions

The impact of the self-adaptive fins on the performance of a single microfluidic cell is numerically assessed in this section. Firstly, the heat transfer enhancement that the self-adaptive fins provide within a cell is compared with a plain microfluidic cell, without fins. Then, the pumping power savings due to the use of the self-adaptive system instead of a fixed geometry for vortex generation is computed.

With the aim of reducing computational resources, the CFD simulations of the microfluidic cell are done without considering the outlet microvalve. The influence of the microvalve on the performance of the microfluidic cell will be studied later.

The coolant fluid considered within the cell is water, with an inlet temperature of 20 °C (24). Also, a constant heat flux of 300 W/cm² is applied at the cell bottom surface (25).

The flow is assumed to be laminar, steady, incompressible and Newtonian, with gravitational effects neglected. At the entrance of the cell, the flow is considered fully developed, with an entrance length $L_{entr} = L/10$ (23). The water properties of density (ρ_f), dynamic viscosity (μ_f), specific heat ($C_{p,f}$) and thermal conductivity (κ_f) are calculated for temperature dependence, while the properties of silicon and silver are assumed constant ($\kappa_{Si} = 130 \text{ W/m}\cdot\text{K}$, $\kappa_{Ag} = 429 \text{ W/m}\cdot\text{K}$) due to low changes with temperature. The governing equations for the flow are the continuity equation for conservation of mass and the Navier-Stokes equations for conservation of momentum (19), (20). The energy equations for liquid (21) and solid (22) are also defined in function of the absolute temperature. No slip boundary condition and adiabatic condition at walls and symmetry boundary condition (symmetry plane defined in Figure 5.1) are assumed.

5.2.2. Induced error on the simulation of solid fins

As done in the previous chapter, to simplify the meshing procedure and computation time of the CFD analysis, the geometry of the self-adaptive fins has been simplified into a semielliptical object (Figure 4.2) and the induced error has been calculated. Although in the previous section the error has been calculated inside a microfluidic cell, in this case the fin density is higher and channel height is lower, so the error has been calculated again. For the error calculation, the obtained results through CFD simulation when using solid fins within a microfluidic cell are compared with the results when using fine fins inside a cell.

Assuming the distribution of fins detailed in Figure 5.2a, and for a laminar flow rate of $1,83 \cdot 10^{-7} \text{ m}^3/\text{s}$ ($Re = 200$, calculated at the beginning of the main channel, in a region without the fins), a constant heat flux of 300 W/cm^2 applied at the bottom wall of the cell and an inlet temperature of the fluid of $20 \text{ }^\circ\text{C}$, the results are evaluated.

As shows Table 5.2, the induced errors on chip temperature are quite high, what leads to a maximum error on Nusselt number calculation of more than 7 %. In this case, the induced error is considered too high and not acceptable, so the fins will be simulated with its original geometry instead of a solid semielliptical object.

5. Impact assessment of the self-adaptive fins inside a microfluidic cell system

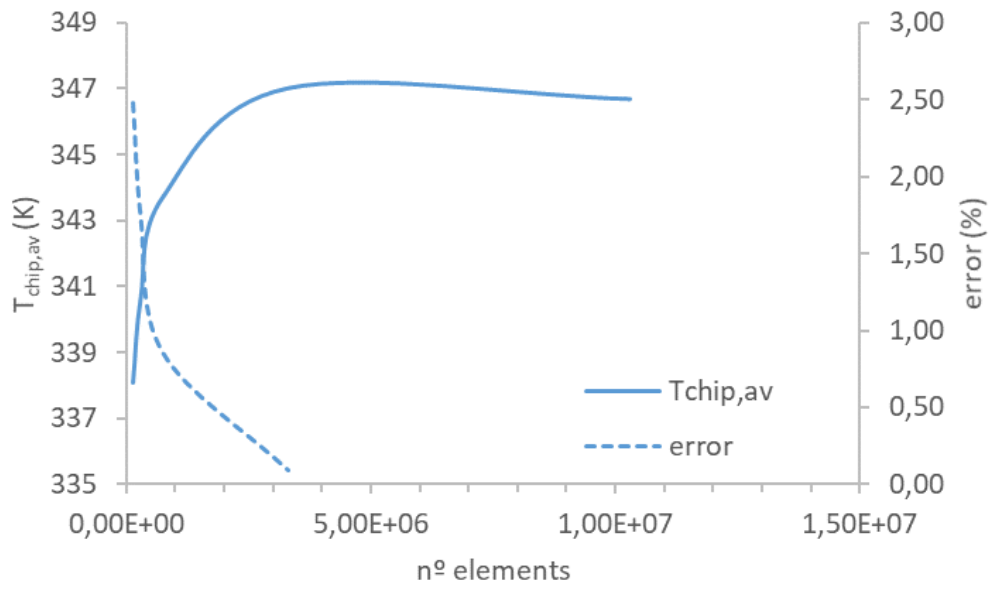
	$T_{f,out}$ (K)	$T_{f,av}$ (K)	ΔP (Pa)	$T_{chip,av}$ (K)	$T_{chip,max}$ (K)	$T_{chip,min}$ (K)	Nu
Re = 200							
Fine fin	319,82	312,12	14115,26	347,01	354,21	335,68	14,69
Solid fin	319,66	311,67	14537,24	343,31	349,35	332,99	15,78
Error (%)	0,05	0,14	2,99	1,07	1,37	0,80	7,38

Table 5.2. Relative error on the CFD simulation results between solid valve and fine valve simulation.

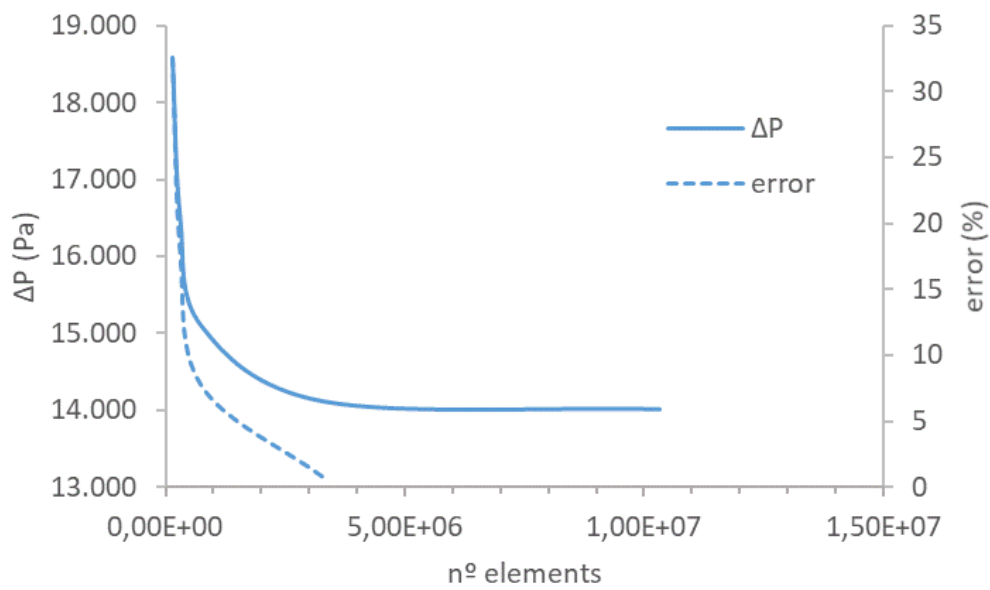
5.2.3. Grid independence test

A grid independence test is performed to ensure that the computational results are independent of the grid size. The built mesh is based on tetrahedral elements and 4 boundary layers on the fluid. The grid density is varied from $83 \cdot 10^3$ elements to $6,30 \cdot 10^6$ elements, and the relative error within the results is computed as defined in to (26). A flow rate of $1,83 \cdot 10^{-7} \text{ m}^3/\text{s}$ is assumed, which corresponds to a Reynolds number of 200, calculated at the beginning of the main channel.

According to the computational results (Figure 5.3), when the grid density is bigger than $3,30 \cdot 10^6$ elements, both relative errors on average chip temperature and pressure drop are lower than 1 %, which is considered acceptable. The selected grid has 3.307.300 elements and the relative errors with the finest grid selected is 0,10 % for the average chip temperature (Figure 5.3a) and 0,71 % for the pressure drop within the cell (Figure 5.3b).



(a)



(b)

Figure 5.3. Grid independence test performed on a) the average chip temperature of the microfluidic cell and b) the pressure drop within the cell.

5.2.4. Numerical results

5.2.4.1. Impact assessment of the self-adaptive fins for different Reynolds number

The impact that the self-adaptive fins have on the thermo-hydraulic performance of a microfluidic cell is assessed in this section for various Reynolds numbers. The obtained results are compared with a plain cell, without fins inside.

The geometry of the microfluidic cell with self-adaptive fins inside is defined in Figure 5.2. Also, the applied boundary conditions are the same defined in section 5.2.1, changing the flow rate from $Q = 4,58 \cdot 10^{-8} \text{ m}^3/\text{s}$ ($Re = 50$) to $Q = 7,32 \cdot 10^{-7} \text{ m}^3/\text{s}$ ($Re = 800$).

First, the Nusselt number and apparent friction factor, computed as defined in equations (7) and (3) respectively, are evaluated when the fins inside the cell are elevated. As expected, both Nusselt number and friction factor increase with Reynolds number (Figure 5.4).

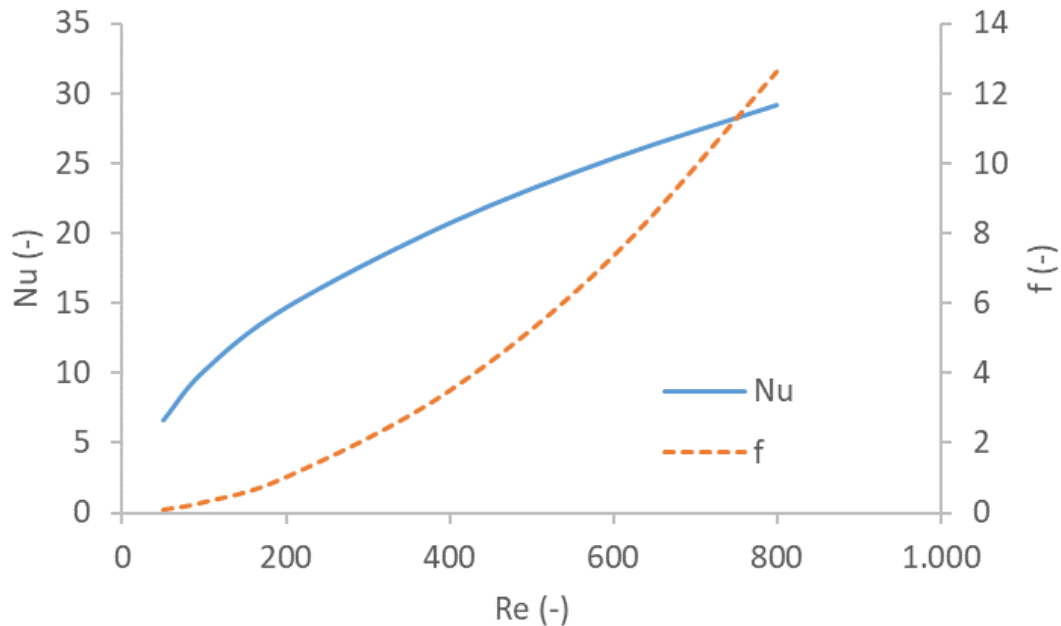


Figure 5.4. Nusselt number and Fanning friction factor of the microfluidic cell with self-adaptive fins.

The results showed in Figure 5.4 are compared with the Nusselt number and apparent friction factor of a plain microfluidic cell, without fins inside. The heat transfer enhancement and pressure drop increment obtained due to the addition of fins are assessed according to equations (8) and (9) (Figure 5.5). The Nusselt relation (Nu/Nu_0) is bigger than one for all the studied cases, so it is seen that the fins perform a heat transfer enhancement within the cell even at low flow rates. This enhancement increases with the Re number, achieving a maximum of $Nu/Nu_0 = 1,20$ for $Re = 800$. Contrarily, the pressure drop difference compared with a plain cell is lower at higher Re, reaching a minimum of $f/f_0 = 1,20$ for $Re = 800$. Higher Reynolds numbers are not considered in this thesis as it is focused in laminar flow rates.

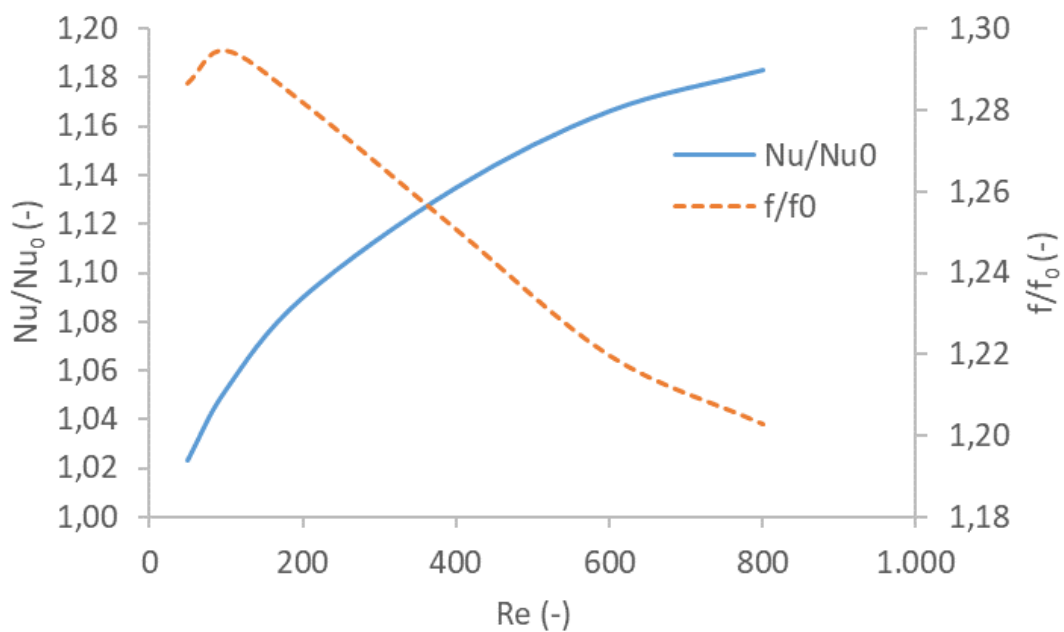


Figure 5.5. Heat transfer enhancement and pressure drop increment in a microfluidic cell with fins inside compared with a plain cell for different Reynolds.

5.2.4.2. Impact assessment of the self-adaptive fins for different fin configurations

The impact of the fins on the thermo-hydraulic performance of a microfluidic cell is assessed for two different configurations with the aim of finding the one that offers highest heat transfer enhancement. The first configuration is the same evaluated in previous section, with 4 pairs of

fins with an angle of attack of 45° . The dimensions of the fins are defined in Figure 4.1c and the configuration of one cell with fins this configuration of fins is illustrated in Figure 5.6a. The second configuration is based in long diagonal fins inside the microfluidic cell. In this case, 6 fins are transversal to the cell with an inclination angle of 20° . The length of the central fins is $1660\ \mu\text{m}$ and the length of the fins placed at the extremes is $900\ \mu\text{m}$. The rest of the dimensions are the same as in the first configuration (Figure 5.6b).

The boundary conditions applied are defined in section 5.2.1, without considering symmetry plane for the second configuration. The Reynolds number has been changed for both configurations from $Re = 50$ up to $Re = 800$ and the heat transfer enhancement achieved when comparing these configurations with a plain cell is assessed (Figure 5.7).

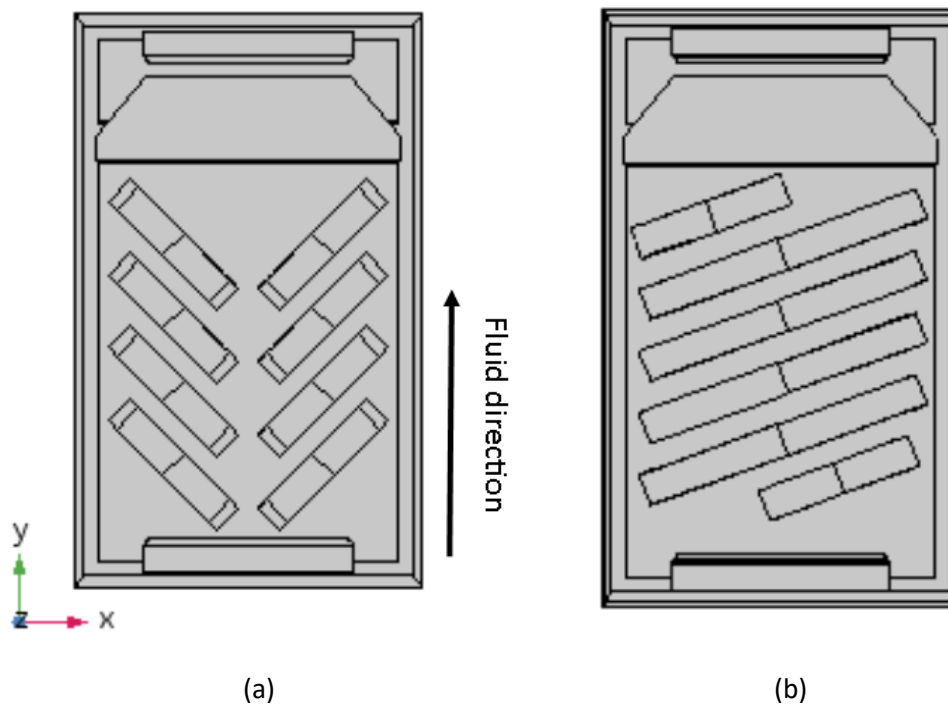


Figure 5.6. (a) Configuration based in 4 pairs of fins. (b) Configuration based in long transversal fins inside the microfluidic cell.

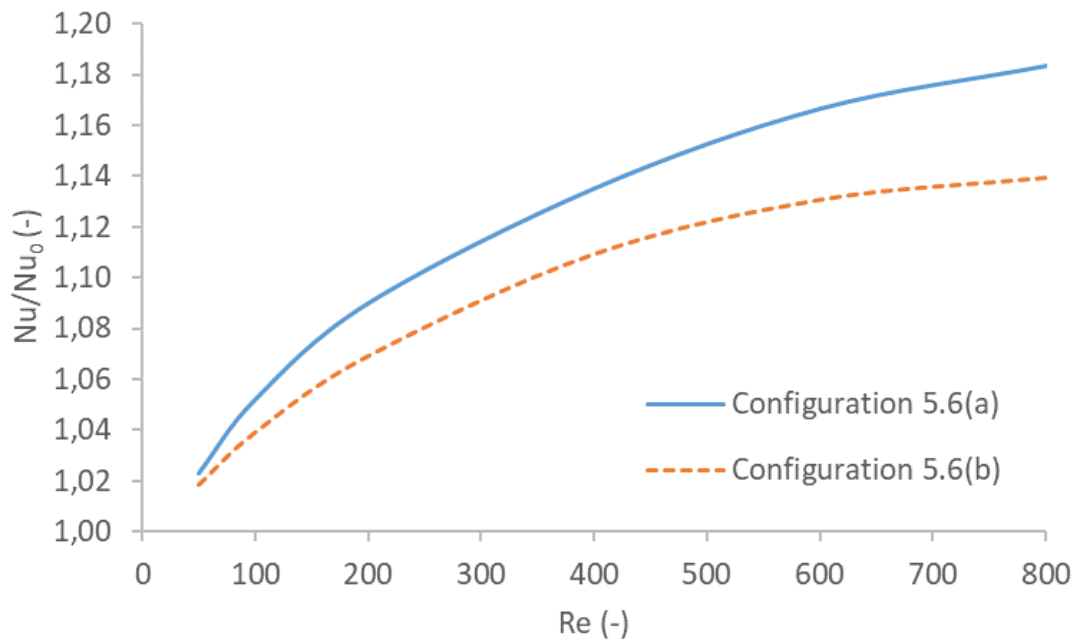


Figure 5.7. Heat transfer enhancement inside a microfluidic cell performed by both configurations of fins.

It can be seen that the heat transfer enhancement is higher for the first configuration (5.7a), which is based in short fins, and the difference between both configurations becomes greater as the Reynolds number increase. Additionally, the pressure drop increment in both configurations is assessed through the apparent friction factor difference (9) between the enhanced microfluidic cell and an smooth one (Figure 5.8). The variation of pressure drop due to the addition of fins within the cell is lower for the configuration 5.6(a).

After evaluating both figures of merit, heat transfer enhancement and pressure drop increment, it is seen that the configuration 5.7(a), which consists of 4 pairs of fins with an angle of attack of 45° performs a higher impact within the microfluidic cell than the configuration based on long transversal fins.

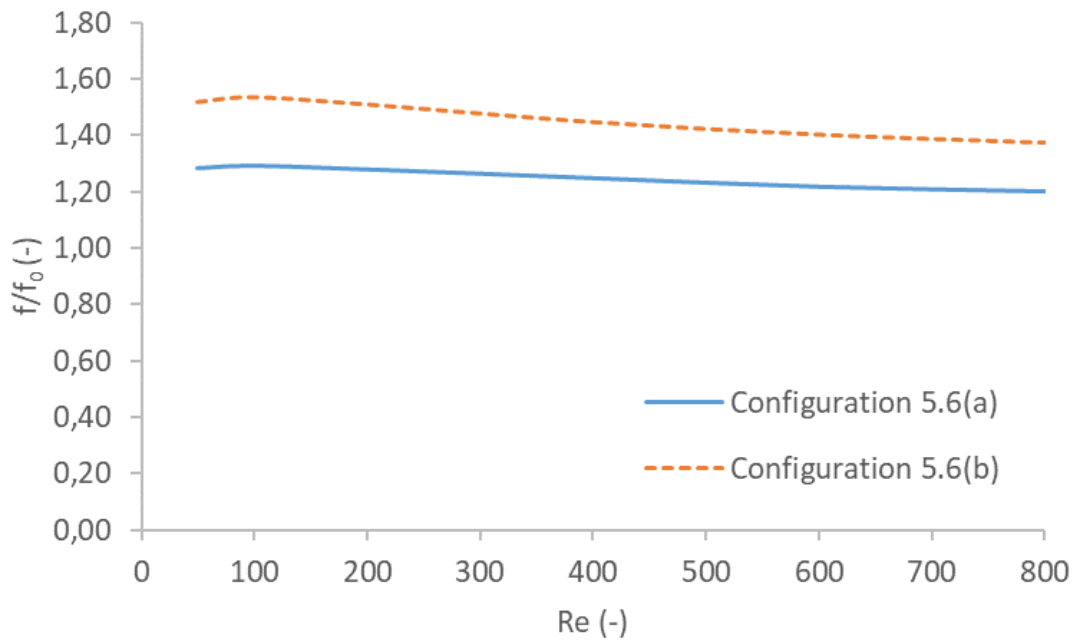


Figure 5.8. Apparent friction factor for both configurations within a microfluidic cell.

5.2.4.3. Impact assessment of the self-adaptive fins placed at the cold wall of the cell

Additionally, a different configuration, based on the fins placed at the cold wall of the microfluidic cell is going to be tested, as done within microchannels in previous chapter. The cold wall of the microfluidic cell is referred as the cell wall opposite to the heat flux (Figure 5.9).

The microfluidic cell geometry, fin geometry and fin distribution is the same as in section 5.2.1, or configuration 1 in previous section, the only change is the position of the self-adaptive fins at the opposite wall. The assessment of this new configuration is done for the same reason as done in previous chapter, due to microfabrication limitations, as is the one that is going to be fabricated. For this reason, its results will be useful for comparison with the experimental ones and for the validation of the numerical models.

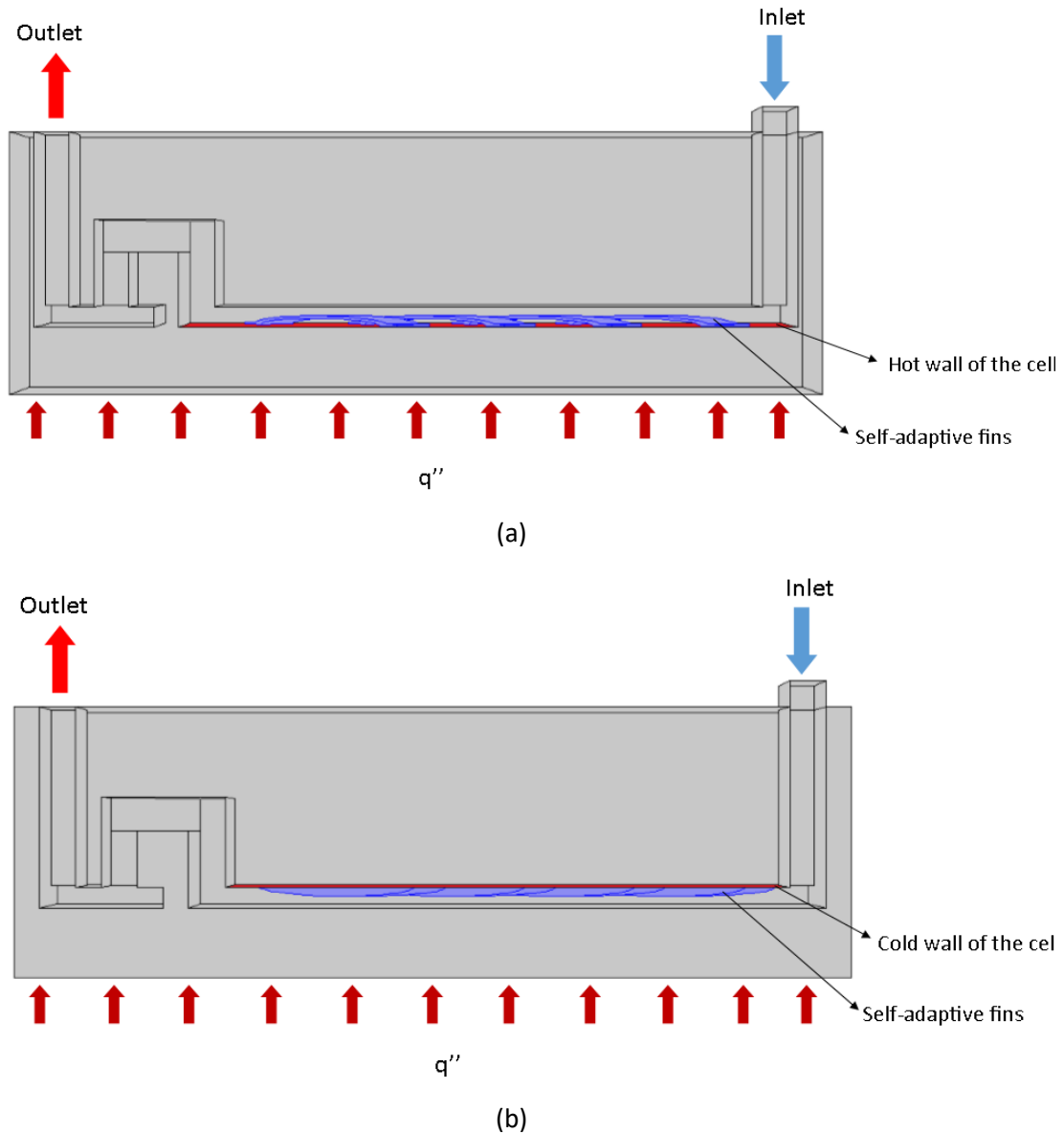


Figure 5.9. Schematic vision of half microfluidic cell with (a) fins placed at the hot wall of the cell, and (b) fins placed at the cold wall of the cell.

The flow rate has been changed from $Q = 4,58 \cdot 10^{-8} \text{ m}^3/\text{s}$ ($Re = 50$) to $Q = 7,32 \cdot 10^{-7} \text{ m}^3/\text{s}$ ($Re = 800$), and a constant heat flux of $300 \text{ W}/\text{cm}^2$ has been applied at the bottom wall of the cell. The heat transfer enhancement and pressure drop increment within this configuration are compared with the results obtained in section 5.2.4.1, for the same configuration of fins but placed at the hot wall (Figure 5.10).

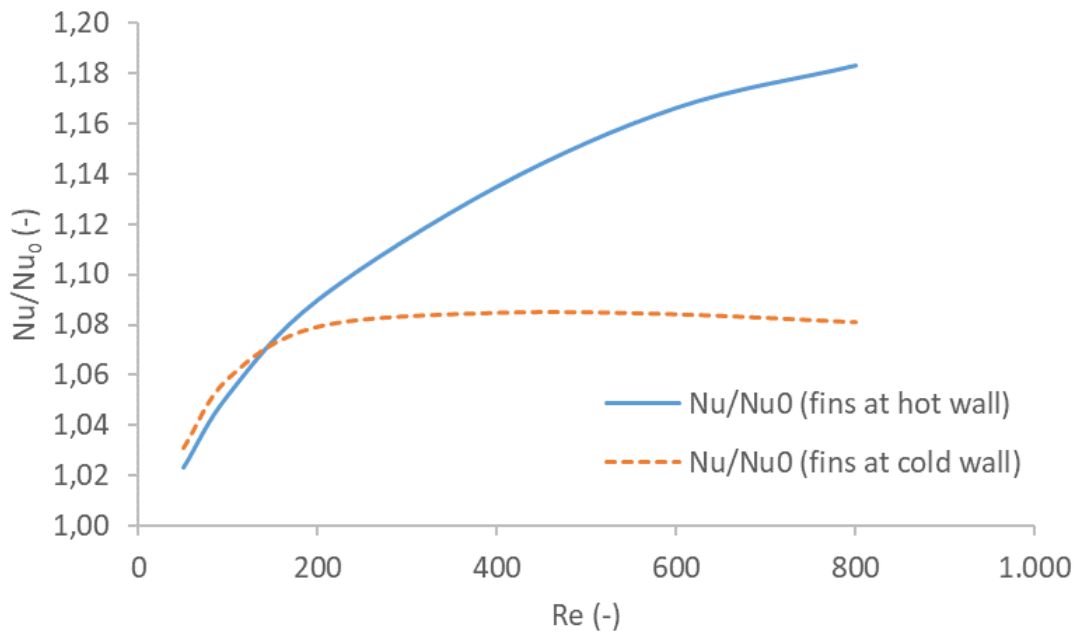


Figure 5.10. Heat transfer enhancement within a microfluidic cell when the fins are placed in its hot or cold wall.

For Reynolds numbers lower than 200, the heat transfer enhancement is pretty similar in both configurations. However, for higher Reynolds, the heat transfer enhancement is significantly higher when the fins are placed at the hot wall of the cell. In the case of the fins placed at the cold wall of the microfluidic cell, the heat transfer enhancement remains almost constant for $Re > 200$, with a value of $Nu/Nu_0 = 1,08$ (Figure 5.10).

5.2.4.4. Impact assessment of the self-adaptive microvalve within the microfluidic cell

The influence of the outlet microvalve, detailed in section 1.3.1.2 of this thesis, over the thermo-hydraulic performance of the cell is assessed in this section. The dimensions of the valve are listed in Table 5.3 (Figure 5.11).

Parameter	Value (mm)	Description
L_{valve}	1,30	Valve length

5. Impact assessment of the self-adaptive fins inside a microfluidic cell system

W_{valve}	0,217	Valve width
L_{anch}	0,21	Valve anchor length
t_{valve}	0,009	Valve thickness
H_{valve}	0,04	Valve opening

Table 5.3. Dimensions of the microfluidic valve placed at the outlet of the cell.

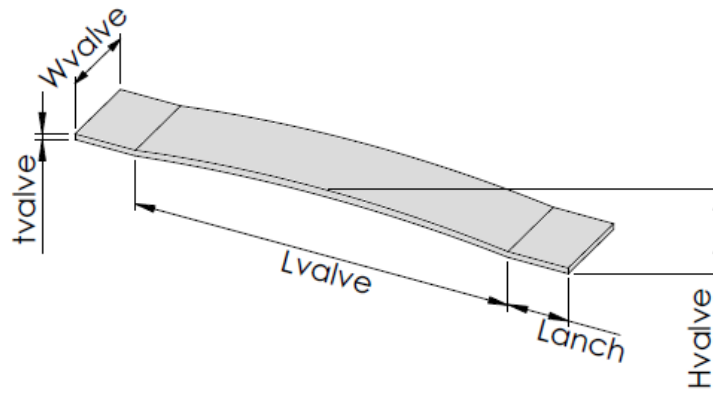


Figure 5.11. Outlet microvalve placed in the microfluidic cell.

A pressure drop increment is expected in the cell due to the addition of the microfluidic valve at the outlet (Figure 5.12). This increment is evaluated for a cell with a channel height $H_{\text{ch}} = 400 \mu\text{m}$ and a base thickness (from the chip to the channel) $H_{\text{base}} = 125 \mu\text{m}$. The rest of the dimensions are the same defined in Table 5.1.

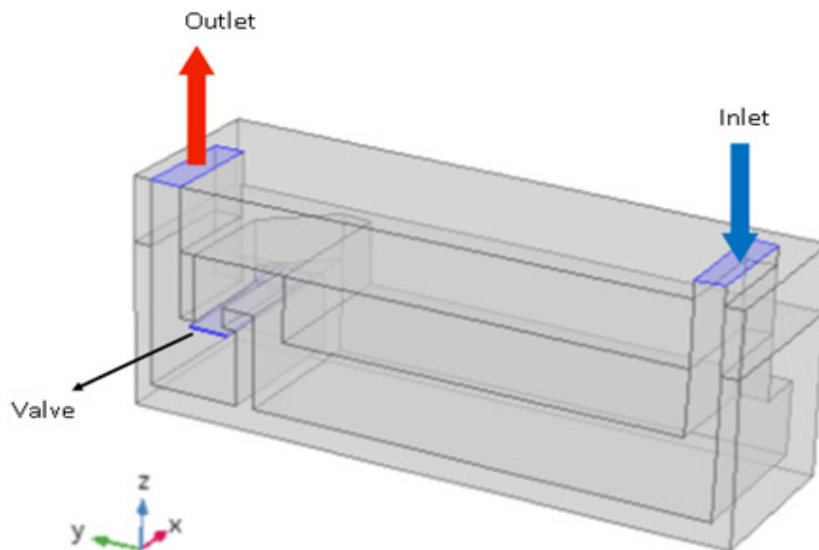


Figure 5.12. Schematic of the microfluidic cell where the effect of the microvalve is assessed.

5. Impact assessment of the self-adaptive fins inside a microfluidic cell system

The pressure drop in the valve is numerically assessed as the pressure drop difference between a cell with outlet valve and a cell without the valve (44).

$$\Delta P_{valve} = \Delta P_{cell\ with\ valve} - \Delta P_{cell\ without\ valve} \quad (44)$$

The pressure drop at the microfluidic valve follows a 2nd degree polynomial trend in function of the flow rate that passes through it, with a coefficient of determination $R^2 = 1$ when the regression line is drawn (Figure 5.13). This relation can also be expressed in function of the flow rate and the pressure drop within a cell without valve (45), $\Delta P'$, achieving an error lower than 3 % compared with the value obtained from simulations (Table 5.4).

$$\Delta P'_{valve} = \Delta P_{cell\ without\ valve} + 0,28 \cdot Re^2 \quad (45)$$

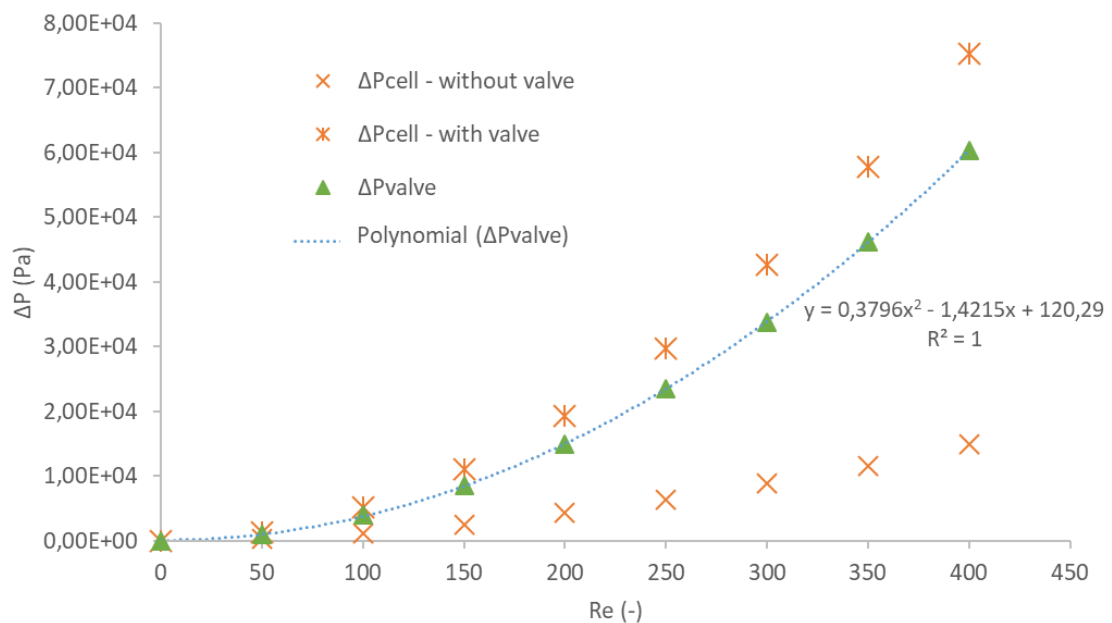


Figure 5.13. Pressure drop at the cell with and without outlet valve and pressure drop at the valve with its regression line represented.

Re	ΔP_{valve}	$\Delta P'_{\text{valve}}$	Error (%)
0	0,00	0,00	2,02
50	1037,24	1016,31	0,81
100	3921,53	3953,25	2,36
150	8555,43	8757,70	2,91
200	14967,43	15403,55	1,62
250	23413,47	23793,27	0,69
300	33713,28	33947,29	0,99
350	46161,92	45703,24	1,35
400	60374,79	59556,96	2,02

Table 5.4. Relative error on the numerical calculation of pressure drop compared with the values obtained from simulations.

For a microfluidic cell with a channel height of 400 μm , a considerable pressure drop is induced within the cell due to the addition of the microvalve at the outlet and this, becomes higher when the flow rate increases.

Nonetheless, the microfluidic cell used in this chapter to assess the impact of the self-adaptive fins has a lower channel height, of 80 μm . For a fixed flow rate of $Q = 2,15 \cdot 10^{-7} \text{ m}^3/\text{s}$, the pressure drop induced by the outlet microvalve is compared for both cell heights (Figure 5.14). Although the pressure drop in the lower cell is higher due to the channel reduction, the pressure drop at the outlet valve is quite similar between both microfluidic cells.

Additionally, the thermal resistance (6) of the cell with and without outlet valve is assessed for both channel heights (Figure 5.15). In general, the thermal resistance of the cell is decreased with the channel height, however, the effect of the microvalve on the thermal resistance of the cell is more significant for the cell with a channel height of 400 μm . In this case, the reduction of the thermal resistance due to the addition of the outlet microvalve is of 2,20 % whereas for the cell with a channel height of 80 μm , this reduction is of 0,20 %. Although the outlet microvalve has an impact on the thermal resistance of the cell, this is very low and considered negligible in this case.

5. Impact assessment of the self-adaptive fins inside a microfluidic cell system

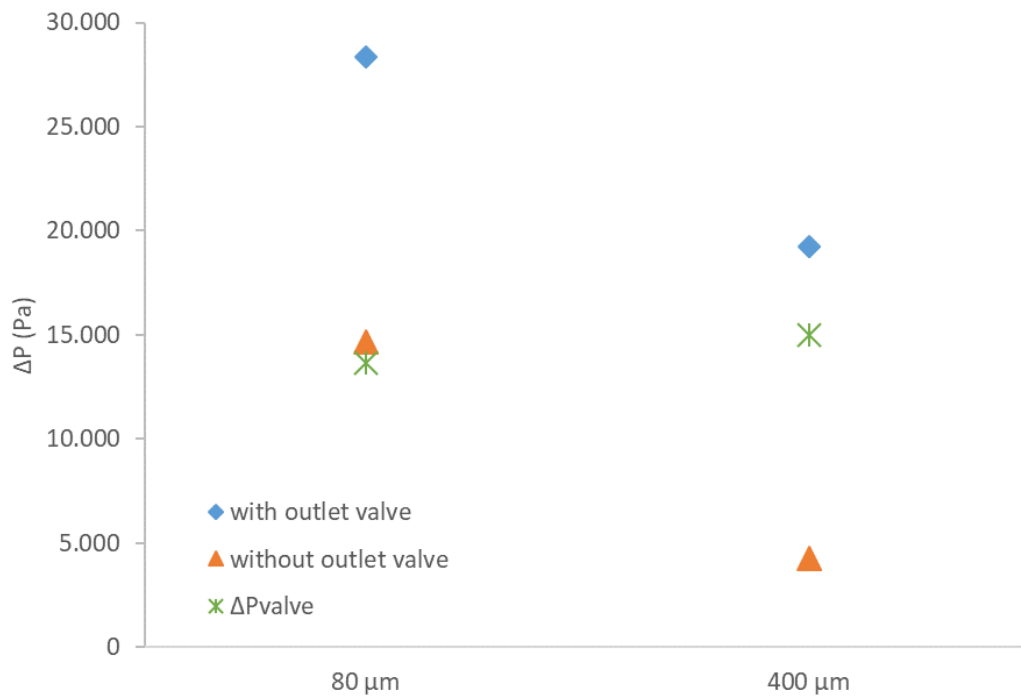


Figure 5.14. Pressure drop within a microfluidic cell of different channel height with and without outlet microvalve and pressure drop induced by the microvalve in each case.

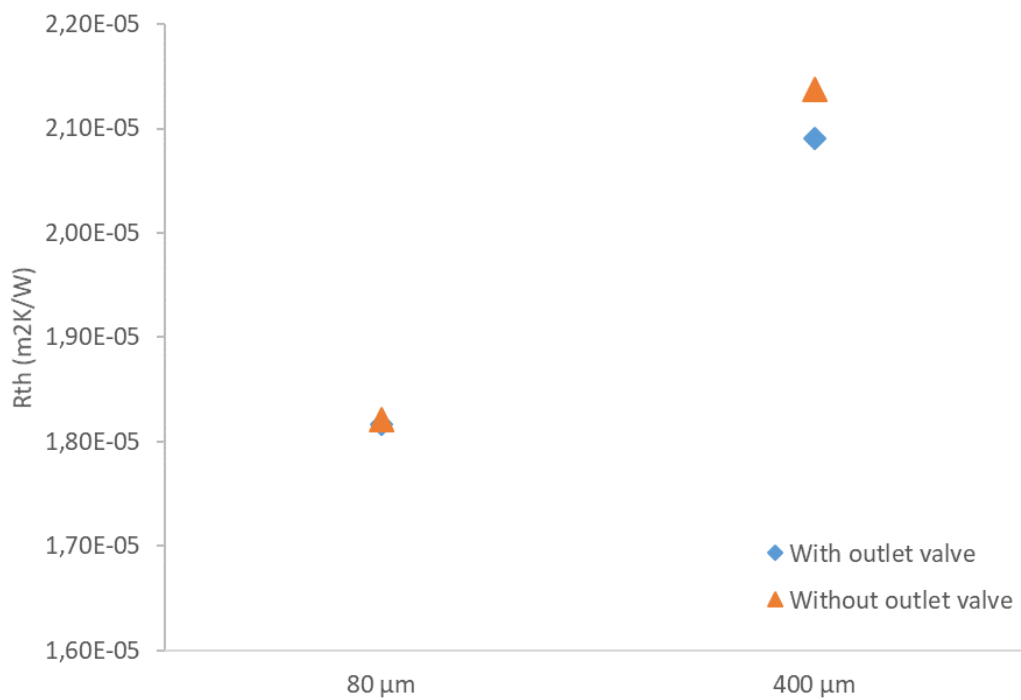


Figure 5.15. Thermal resistance of the microfluidic cell with and without outlet valve assessed for two different channel heights.

5.2.4.5. Pumping power savings

The savings on pumping power when using self-adaptive fins instead of fixed fins inside a microfluidic cell are computed for a given heat load scenario which consists on a train of pulses with a period of 30 s and a duty cycle of 1/3 (Figure 5.16). The high heat flux, that defines the hotspot is 300 W/cm^2 , and the low heat flux, which defines the background region, is 20 W/cm^2 .

For the given heat load scenario, the pressure drop is assessed within the cell comparing two configurations: a cell with fixed fins inside, having the same geometry as the self-adaptive fins described previously, and a cell with self-adaptive fins inside (Figure 5.17). The inlet temperature of the fluid is $20 \text{ }^\circ\text{C}$ and the Reynolds number is fixed at 200 ($Q = 1,83 \cdot 10^{-7} \text{ m}^3/\text{s}$), which ensures a maximum chip temperature of $85 \text{ }^\circ\text{C}$ for the plain cell.

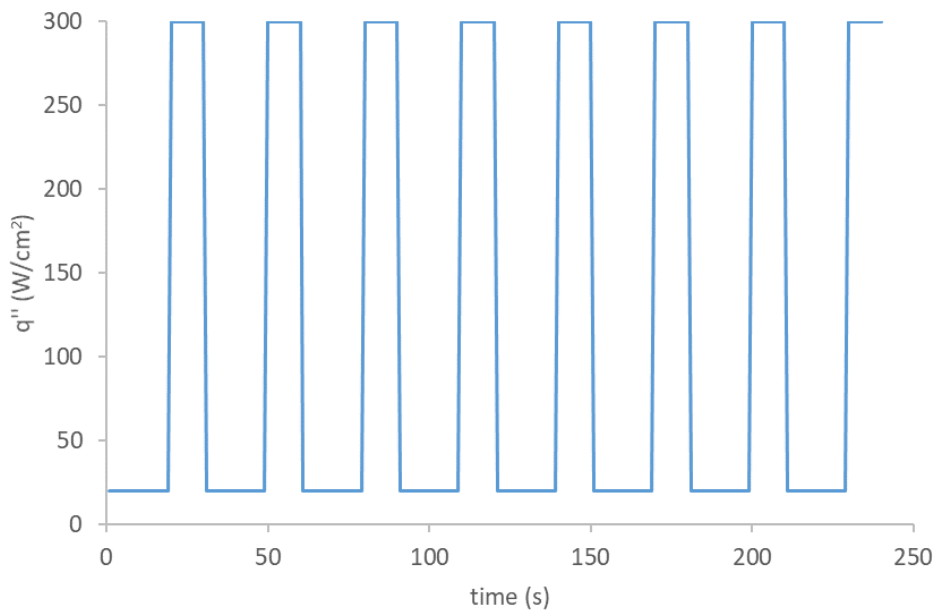


Figure 5.16. Heat load scenario defined.

The behavior of the self-adaptive fins within the cell is detailed in Figure 5.17. Maintaining constant the flow rate, for low heat flux demands ($q'' = 20 \text{ W/cm}^2$ in this case), the pressure drop inside the cell with self-adaptive fins is lower than in a cell with fixed fins, as they remain in flat position compared to the ones that are raised. On the other hand, for high heat demand

5. Impact assessment of the self-adaptive fins inside a microfluidic cell system

($q'' = 300 \text{ W/cm}^2$ here), the pressure drop decreases in both cases due to reduction on fluid viscosity when the temperature rise. In this case, both systems achieve the same pressure drop as the self-adaptive fins adopt the same position as the fixed fins.

The difference in pressure drop between both systems when the heat flux is low affects the overall pumping power of the self-adaptive system, which is significantly reduced compared with the system with fixed fins (4). For the given heat load scenario, the pumping power savings obtained with the self-adaptive system in comparison with the fixed one are around 10,50 % (Figure 5.18).

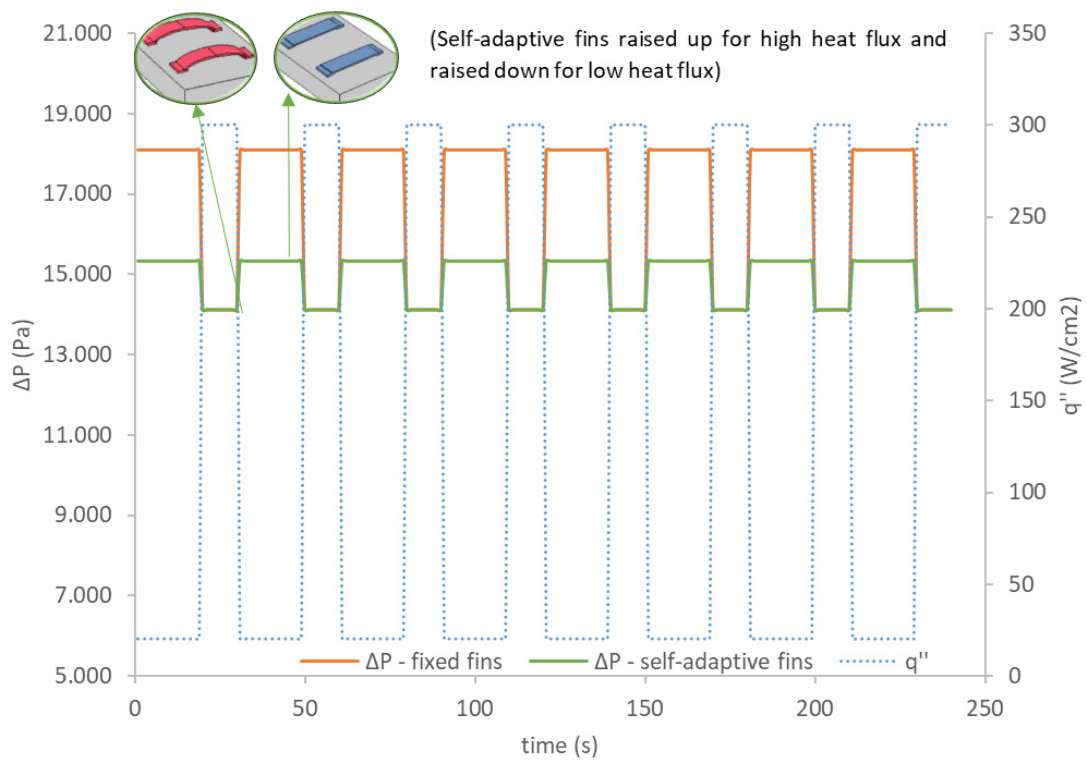


Figure 5.17. Pressure drop assessed within the microfluidic cell for the different configurations for the given heat load scenario.

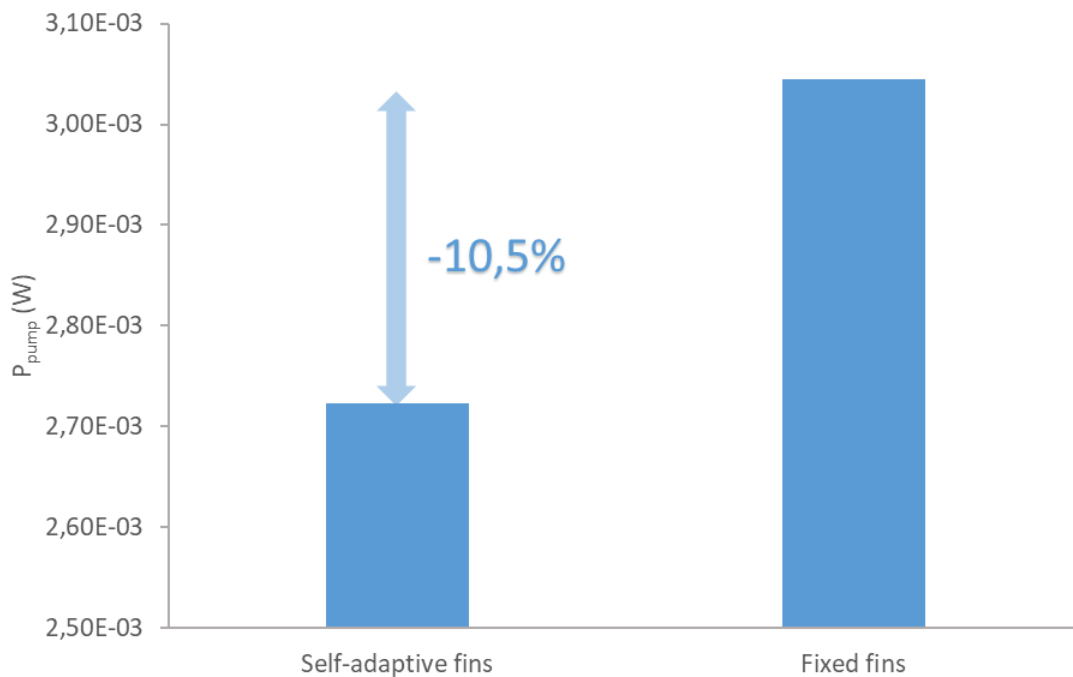


Figure 5.18. Average pumping power required for the fix system and the system with self-adaptive fins.

5.2.4.6. Temperature uniformity

One of the main advantages that microfluidic cells present over conventional microchannels is the highest temperature uniformity on the surface due to its shortest length. The fins within the cell are expected to even reduce more the chip temperature gradient along the coolant flow path. For a fixed Reynolds number ($Re = 200$), which ensures a maximum chip temperature of $85\text{ }^{\circ}\text{C}$ at the plain cell, the central base temperature of the microfluidic cell is assessed along its length for both an empty cell and one with fins inside (Figure 5.19). The temperature evolution along the cell has a similar trend in both cases, but with lower temperature when the fins are placed inside the cell. For the empty cell, the temperature increment at the base is of 19 K , whereas for the cell with fins, this increment is of 16 K , what represents a reduction of $15,80\%$ on the chip temperature gradient.

Additionally, the temperature uniformity at the chip surface is assessed for different Reynolds numbers (Figure 5.20). For both the empty cell and the cell with fins, the thermal gradient gets smaller as the Reynolds number increases. Furthermore, the difference between the surface thermal gradient of the empty cell and the one of the cell with fins gets bigger as Reynolds

5. Impact assessment of the self-adaptive fins inside a microfluidic cell system

number increases. This means that, at high Re numbers the effect of the fins on achieving an isothermal chip conditions becomes more significant.

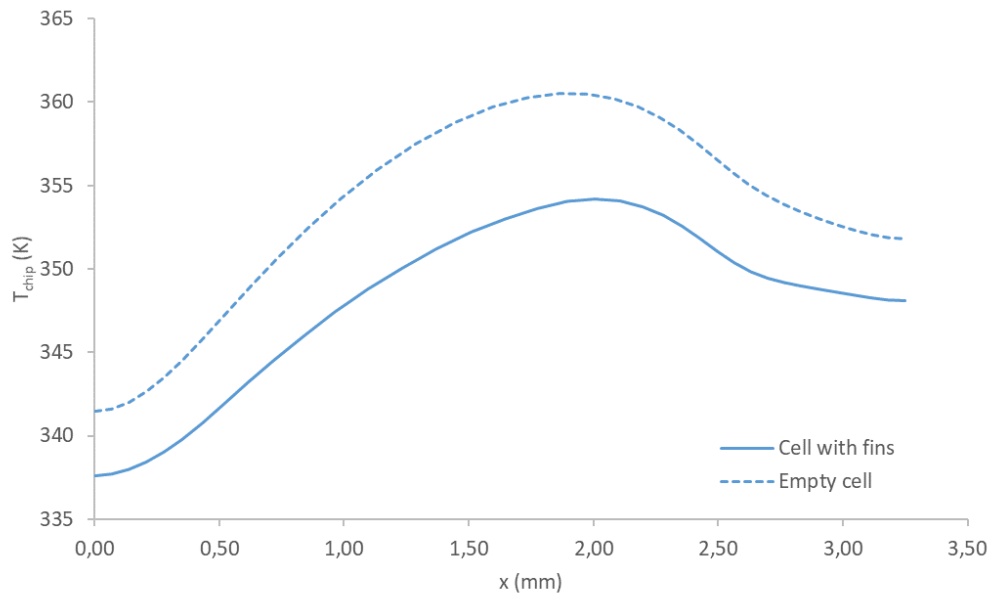


Figure 5.19. Chip temperature along the cell length for an empty cell and a cell with fins ($Re = 200$).

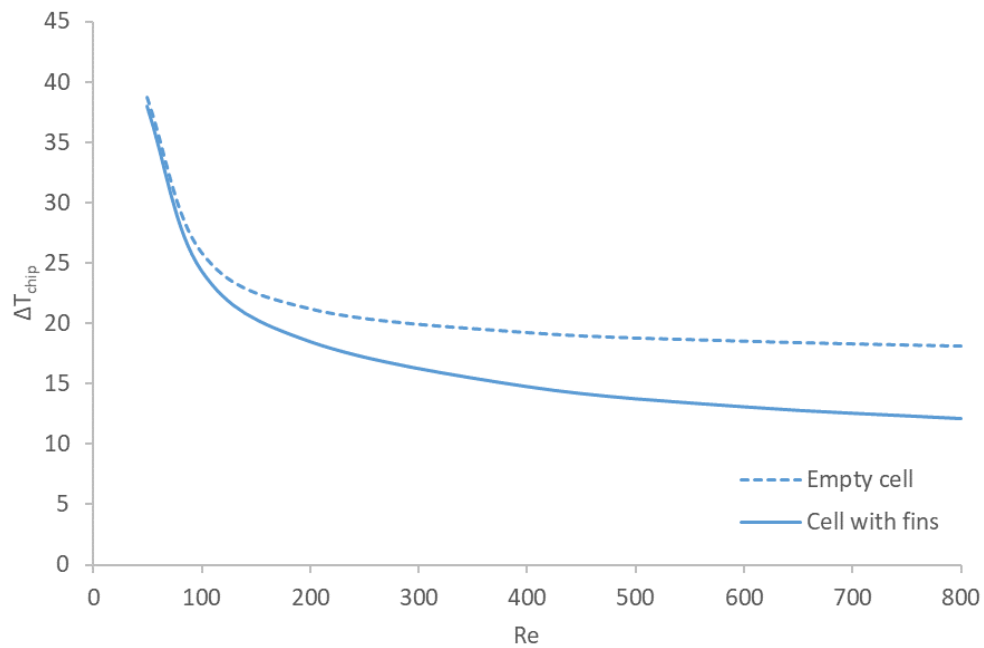


Figure 5.20. Temperature gradient at the base of the cell for different Re .

5.3. General overview of the impact of self-adaptive fins inside a microfluidic cooling cell.

In this chapter, the impact of the self-adaptive fins on the thermo-hydraulic performance of a microfluidic cooling cell has been numerically assessed. Microfluidic cooling cells have been designed to achieve lower pumping powers and more temperature uniformity in the cooling device, as described previously [37].

First of all, the heat transfer enhancement that the fins provide within a micro-cooling cell has been demonstrated, achieving a maximum Nu/Nu_0 of 1,20 for Reynolds number of 800. This heat transfer enhancement increases with Reynolds numbers, in line with the conclusions of the previous chapter and previous studies in literature. In general, the enhancement in heat transfer is lower than the obtained when using the self-adaptive fins inside microchannels; however, for low Reynolds number ($Re = 200$), which is the range where the cooling device will be working, the thermal enhancement is similar to the obtained numerically in the previous chapter.

In order to find an optimum configuration of the self-adaptive fins distribution inside the microfluidic cell cooling device at Reynolds number of 200, different configurations of the fins inside the microcells have been tested. The results showed that a pair of fins with an angle of attack against the flow have a higher impact on the better thermal performance of the cooling device than long transversal fins through all the cell.

Also, the impact of the fins on the thermo-hydraulic performance of the cooling device when placed at the opposite wall of the heat flux has been assessed. In this case it has been found that the heat transfer enhancement is lower than in microchannels and remains practically constant at Reynolds numbers higher than 200. Nevertheless, around this Reynolds number, the value of heat transfer enhancement is not very different from the obtained with the fins placed at the same wall as the heat flux ($Nu/Nu_0 = 1,08$).

As defined previously (section 1.3.1.2), the microfluidic cells include a microvalve responsible for flow rate regulation in each cell. Although this functionality is not object of study in this thesis, the additional pressure drop that will induced in the microfluidic cell is evaluated. A correlation between flow rate and additional pressure drop due to the presence of the valve has been defined through a 2nd degree polynomial expression (45).

Finally, for a determined time dependent heat flux, the pumping power savings are assessed due to the effect of the self-adaptive fins. In this case, the pumping power is reduced more than 10 % when using self-adaptive fins compared with a system of fixed vortex generators. This reduction of pumping power is also higher than the achieved with the use of self-adaptive fins inside a microchannel cooling device, as detailed in previous chapter.

GENERAL CONCLUSIONS

6. GENERAL CONCLUSIONS

After an exhaustive review of the existing literature on 3D-IC liquid cooling and the proposed solutions to enhance the heat transfer while overcoming large temperature gradients and pressure drops, it has been seen the lack of these systems to adapt their behavior to changing boundary conditions in time and space. This fact leads to overcooling when the refrigerating demands are low and so, additional pressure drops are induced in the fluid channel and oversized pumping powers are obtained for changing conditions. Also, in the existing works, the surface temperature uniformity of the chip is only optimized for a given heat load distribution and cannot be adapted to variable heat load scenarios in time and space.

To overcome these problems, this thesis proposes a system based on self-adaptive fins acting as passive thermal actuators. The principle of thermal expansion of the materials is the responsible for the smart behavior of these fins, which will be activated, without any external excitation, in function of their own temperature. The demonstrated capabilities of flow disturbing elements inside microchannels are used only for high cooling demands; otherwise, the fins will remain in flat position, reducing the pressure drop inside the cooling device. With this solution, the system will be able to tailor its internal geometry to time dependent and non-uniform heat flux distributions, optimizing the local heat transfer enhancement and the pressure drop to the instantaneous cooling need and thus, reducing the needed pumping power for a more energy efficient cooling system.

A previous work done with shape memory alloys acting as self-adaptive fins inside a fluid channel demonstrated the capabilities of these smart fins to provide enhanced temperature uniformities and, within these results, new perspectives for developing universal cooling devices, able to adapt their behavior to different time-dependent and non-uniform heat load scenarios, without the need of sensors nor active control, were opened. Nevertheless, this validation was done in a miniscale, as SMA materials are not feasible for microscale fabrication. For this reason, other alternatives of self-adaptive fins, feasible for microscale applications, were searched within this thesis.

The first objective to overcome in this work was the design, fabrication and validation of the self-adaptive fins to reach the desired behavior of self-adaptation by using the thermal expansion of the materials.

Initially, the requirements that the fins must fit in order to perform an optimum performance inside a microchannel have been defined. It has been determined that, for a Reynolds number around 200, which ensures a maximum chip temperature of 85 °C, the maximum heat transfer enhancement is achieved for a relative height of the fin, compared to the channel height, of 0,57. However, for a lower relative height, of 0,24, the thermal enhancement is superior to 10 %, which is the objective of the thesis and lower pumping powers are obtained in this case due to lower pressure drops for same flow rate. Additionally, the Von Mises yield criterion has been used to determine the minimum thickness of the self-adaptive fins to both avoid plastic deformations and backward bending due to the flow pressure. Considering a flow rate of 7 ml/min (Reynolds number around 200), 2 µm fin thickness has been founded suitable for the fabrication of the fins.

Within the defined requirements, the first proposal of self-adaptive fins was based on bimetallic structures made with two metals of significantly different thermal expansion coefficients (aluminum and chromium). Different geometries have been proposed to achieve the maximum rising, which was a 7 % of its length for a determined structure. This rise represents a relative height of 0,24 for a channel height of 100 µm what, according to previous findings, could indicate a heat transfer increase of 10 % in the cooling device. Additionally, the channel height could be reduced to 80 µm to have higher relative height. Nevertheless, different problems appeared for the reliability of these type of fins. First of all, the Von Mises stress for the fins was quite closer to the elastic limit of the aluminum in all the cases, what could lead to plastic deformations. Also, the microfabrication process flow presented large difficulties on finding a suitable combination of high and low CTE materials to create the bimetallic structure. Different material combinations were tested and only one was successfully fabricated, using silver as high CTE material and gold as low CTE material. However, due to the small difference between CTE of both materials, the achieved deflections were pretty small. Also, plastic deformations were seen when the fins were submitted to high temperatures. Due to the difficulties presented for the fabrication and reliability of bimetallic fins, an alternative was searched. However, further research can be done in this topic in the future to find suitable material combinations for example, using a bilayer of a metal and a polymer.

As said before, an alternative solution of self-adaptive fins was defined, being them more robust and easier for microfabrication. These fins are based on doubly clamped structures that buckles at a determined temperature and their working principle has already been assessed in the

literature. The vertical displacement of these fins is not much different than the achieved by some bimetallic fins however, the use of a unique material for the fabrication of the model and its robustness, makes them more reliable than bimetallic fins. Within this new structure, the objective of design, fabrication and validation of the self-adaptive fins has been accomplished as their behavior with temperature rise have been demonstrated experimentally.

The second specific objective of the thesis was the increment of the convective heat transfer by more than 10 % compared with a cooling system without flow disturbing elements inside. In this line, the impact of doubly clamped fins on the thermal performance of two different cooling devices has been assessed, the first one based on microchannels and the second one based on microfluidic cells, presented by Laguna et al. [37].

When the fins were placed inside a microchannel cooling device, it has been numerically demonstrated that the heat transfer enhancement increases with Reynolds number, achieving an enhancement of 40 % for $Re = 800$. However, for $Re = 200$, which is the range of flow rate that ensures a maximum junction temperature of $85\text{ }^{\circ}\text{C}$, the thermal enhancement is lower than 10 %, so the objective is not reached. To improve this result, it has been seen that the density of fins inside the cooling device has an important impact on the thermal enhancement and, when the density of fins doubled the initial configuration, an enhancement of 13 % is reached. The validity of the numerical results has been assessed through experimental tests for determined testing conditions.

When assessing the impact that the self-adaptive fins have on the thermo-hydraulic performance of a microfluidic cooling cell, it has been seen that the heat transfer enhancement is worse than with the fins inside a microchannel, achieving a maximum of 20 % enhancement for $Re = 800$. Nevertheless, for Reynolds numbers around 200, the value of heat transfer enhancement is similar to the obtained with the microchannels, around 8 % of enhancement.

The third specific objective to accomplish in this work was the achievement of more temperature uniformity when non-uniform heat loads were applied. Within this way, when the fins were placed inside a microchannel, even the temperature uniformity is not significantly enhanced, a local enhancement just beyond the fins is observed. This result could indicate that the vortices generated by the doubly clamped fins are not strong enough to have a significant

impact on the thermal performance of the hole device and their effect is only seen locally where the fins are placed. This conclusion would go in line with the second specific objective as, due to the weakness of the generated vortices, not enough heat transfer enhancement is achieved

Experimentally, it has been seen a more uniform thermal gradient inside the microchannels with self-adaptive fins than in plain microchannels when applying non-uniform heat fluxes. However, further work has to be done in this way to validate the obtained results.

When numerically assessing the temperature uniformity in a microfluidic cell, the obtained results are slightly different, as more temperature uniformity is obtained when self-adaptive fins are placed within the channel path. Also, it is seen an increase in the temperature gradient magnitude with the Reynolds numbers as more uniform temperatures are achieved with self-adaptive fins and higher flow rates. This result can be attributed to the fact that the density of fins in a microfluidic cell is higher than in a microchannel and thus implies that the local effect seen in the microchannels becomes greater in the microfluidic cells.

Finally, the last specific objective to assess in this thesis was the reduction of the pumping power by 25 % compared with a system of fixed vortex generators inside. For a determined time-dependent heat flux, when the fins are placed inside a microchannel cooling device, an 8 % reduction in pumping power is achieved due to the self-adaptation concept of the fins. Within a microfluidic cooling cell, for the same time-dependent heat flux, a 10 % reduction in the pumping power is achieved. Although this result does not meet the targeted objective, it has been seen that the pressure drop of the microelectronics cooling devices is very sensitive to the fin position and placement and so, little changes on the placement of the structure could induce high reductions of pressure drop. Additionally, to further reduce the pumping power, the self-adaptive cooling system can be combined with a tailoring of the flow rate through a smart control of the pump, able to give the minimum pumping power necessary any time. It has been demonstrated that a reduction of 20 % of the pumping power can be achieved within this system [41] which, combined with the self-adaptive fins, would reach the objective of 25 % reduction of pumping power, creating a more energy efficient and smart active cooling system.

FUTURE WORK

7. FUTURE WORK

This thesis has done an initial validation of the possibilities that the self-adaptive fins can have to obtain smart and energy efficient active cooling. However, more work has to be done to further demonstrate the capabilities of this system and also to assess the reliability of this system in different environments and scales.

First of all, the experimental assessment of the impact of self-adaptive fins on the thermo-hydraulic performance of a cooling device has to be done in different conditions. The impact within microchannels has been validated with a system of only two microchannels with fins and would be highly interested to have a full device based on microchannels with self-adaptive fins. Additionally, the impact of the fins inside a microfluidic cell could not have been assessed due to the lack of well-fabricated samples to perform it. This assessment is planned to be done in the near future.

The reliability of the doubly clamped fins, its fatigue and the number of useful cycles have not been assessed in this work; however, these parameters must be evaluated to determine the reliability of this technology in a commercial environment. Within this line, and to continue the work of this thesis, the project *Experimental Validation and Commercial Viability of an Energy Efficient Universal Cooling Scheme*, financed by the *Generalitat de Catalunya* through the grants *Indústria del Coneixement 2018– modalitat Producte*, where the author is the scientific entrepreneur, will assess the technical and commercial viability of an energy efficient and smart cooling device based on the use of doubly clamped self-adaptive fins, with the aim of achieving a TRL6 (technology demonstrated in relevant environment) for this technology.

Finally, more effects can be done in the future with the bimetallic self-adaptive fins in order to find a suitable combination of metals that makes their microfabrication feasible and also a good structure which ensures to avoid plastic deformations. If it is possible to validate its behavior, these fins can have a very promising future as they are able to generate stronger vortices than the doubly clamped fins and thus can improve the thermo-hydraulic performance of the cooling system.

PUBLICATIONS

8. PUBLICATIONS

During the realization of the PHD thesis, several publications in scientific journals and conferences have been done. Also, a patent about the concept of self-adaptive fins due to thermal displacement has been submitted, coauthored with other members of the team.

8.1. Journals

- **Vilarrubí, M.**; Morell, G.; Rosell, J.; Fréchette, L.-G.; Barrau, J.; “Experimental characterization of a self-adaptive shape memory alloy cooling approach to regulate temperature under varying heat loads”; *International Journal of Heat and Mass Transfer*; vol. 139, pp. 632-640, Aug. 2019.
- Laguna, G.; **Vilarrubí, M.**; Ibáñez, M.; Rosell, J.; Badia, F.; Azarkish, H.; Collin, L.-M.; Fréchette, L.-G.; Barrau, J.; “Impact of the self-adaptive valve behavior on an array of microfluidic cells under unsteady and non-uniform heat load distributions”; *Journal of Applied Fluid Mechanics*; vol. 12 (Special Issue), pp. 29-36, 2019
- Laguna, G.; **Vilarrubí, M.**; Ibáñez, M.; Betancourt, Y.; Illa, J.; Azarkish, H.; Amnache, A.; Collin, L.-M.; Coudrain, P.; Fréchette, L.-G.; Barrau, J.; “Numerical parametric study of a hotspot-targeted microfluidic cooling array for microelectronics”; *Applied Thermal Engineering*; vol. 144, pp. 71-80, Jul. 2018
- **Vilarrubí, M.**; Riera, S.; Ibáñez, M.; Omri, M.; Laguna, G.; Fréchette, L.G.; Barrau, J.; “Experimental and numerical study of micro-pin-fin heat sinks with variable density for increased temperature uniformity”; *International Journal of Thermal Sciences*; vol. 132, pp. 424-434, Oct. 2018.
- Fernández, A.; Laguna, G.; Rosell, J.; **Vilarrubí, M.**; Ibáñez, M.; Sisó, G.; Illa, J.; Barrau, J.; “Assessment of the impact of non-uniform illumination and temperature profiles on a dense array CPV receiver performance”; *Solar Energy*; vol. 171, pp. 863-870, Sept. 2018.

- Riera, S.; Barrau, J.; Rosell, J.; Fréchette, L.-G.; Omri, M.; **Vilarrubí, M.**; Laguna, G.; “Smoothing effect of the thermal interface material on the temperature distribution in a stepwise varying width microchannel cooling device”; *Heat and Mass transfer*; vol. 53, pp. 2987-2997, Sept. 2017.

8.2. Conferences

- Amnache, A.; Collin, L.-M.; Laguna, G.; **Vilarrubí, M.**; Hamel, S.; Barrau, J.; Fréchette, L.-G.; “Thermoregulate microvalve for self-adaptive microfluidic cooling”; in *24th International Workshop on Thermal Investigations of ICs and Systems (THERMINIC 2018)*, Stockholm Sept. 2018.
- **Vilarrubí, M.**; Laguna, G.; Amnache, A.; Collin, L.-M.; Rosell, J.; Ibáñez, M.; Illa, J., Fréchette, L.-G.; Barrau, J.; “Thermostatics fins for spatially and temporally adaptive microfluidic cooling”; in *24th International Workshop on Thermal Investigations of ICs and Systems (THERMINIC 2018)*, Stockholm Sept. 2018.
- Da Luz, S.; Kattinger, G.; Laguna, G.; Azarkish, H.; **Vilarrubí, M.**; Collin, L.-M.; Fréchette, L.-G.; Barrau, J.; Billat, S.; “Variable pumping control for low power microfluidic chip cooling”; in *24th International Workshop on Thermal Investigations of ICs and Systems (THERMINIC 2018)*, Stockholm Sept. 2018.
- Coudrain, P.; Colonna, J.-P.; Collin, L.-M.; Prieto, R.; Fréchette, L.-G.; Barrau, J.; Savelli, G.; Vivet, P.; Struss, Q.; Widiez, J.; Vladimirova, K.; Triantopoulos, K.; Beckrich-Ros, H.; **Vilarrubí, M.**; Laguna, G.; Azarkish, H.; Sirazi, M.; Michailos, J.; “Shaping circuit environment to face the thermal challenge: Innovative technologies from low to high power electronics”; in *38th IEEE Symposium in VLSI Technology*, Honolulu Jun. 2018.
- Laguna, G.; **Vilarrubí, M.**; Fernández, A.; Sisó, G.; Rosell, J.; Ibáñez, M.; Illa, J.; Badia, F.; Fréchette, L.-G.; Darnon, M.; Collin, L.-M.; Dollet, A.; Barrau, J.; “Dense array CPV receivers: impact of the cooling device on the net PV output for different illumination

profiles”; in *14th International Conference on Concentrator Photovoltaic Systems (CPV 2018)*, Puertollano Apr. 2018.

- Laguna, G.; Azarkish, H.; **Vilarrubí, M.**; Ibáñez, M.; Rosell, J.; Betancourt, Y.; Illa, J.; Collin, L.-M.; Barrau, J.; Fréchette, L.-G.; Coudrain, P.; Savelli, G.; “Microfluidic cell cooling system for electronics”; in *23rd International Workshop on Thermal Investigations of ICs and Systems (THERMINIC 2017)*, Amsterdam Sept. 2017
- Laguna, G.; Barrau, J.; Fréchette, L.-G.; Rosell, J.; Ibáñez, M.; **Vilarrubí, M.**; Betancourt, Y.; Azarkish, H.; Collin, L.-M.; Fernández, A.; Sisó, G.; “Distributed and self-adaptive microfluidic cell cooling for CPV dense array receivers”, in *13th International Conference on Concentrator Photovoltaic Systems (CPV 2017)*, Ottawa May 2017.

8.3. Patent

Inventors: Luc Fréchette, Jérôme Barrau, Montse Vilarrubí

Title: Deformable Fin Heat Exchanger

Solicitude nº: PCT/CA2019/050247

Priority country: United States of America

Titular Entity: University of Lleida, University of Sherbrooke.

LITERATURE

Literature

- [1] G. E. Moore, "Cramming more components onto integrated circuits," *Proc. IEEE*, vol. 86, no. 1, pp. 82–85, 1998.
- [2] R. H. Dennard, F. H. Gaensslen, V. L. Rideout, E. Bassous, and A. R. LeBlanc, "Design of ion-implanted MOSFET's with very small physical dimensions," *IEEE J. Solid-State Circuits*, vol. 9, no. 5, pp. 256–268, 1974.
- [3] M. Bohr, "A 30 Year Retrospective on Dennard's MOSFET Scaling Paper," *IEEE Solid-State Circuits Newsl.*, vol. 12, no. 1, pp. 11–13, 2007.
- [4] R. H. Dennard, J. Cai, and A. Kumar, "A perspective on today's scaling challenges and possible future directions," *Solid. State. Electron.*, vol. 51, no. 4 SPEC. IS, pp. 518–525, 2007.
- [5] M. Graef *et al.*, "International technology roadmap for semiconductors 2.0: 2015," 2015.
- [6] K. Ebrahimi, G. F. Jones, and A. S. Fleischer, "A review of data center cooling technology, operating conditions and the corresponding low-grade waste heat recovery opportunities," *Renew. Sustain. Energy Rev.*, vol. 31, pp. 622–638, 2014.
- [7] J. Glanz, "Power, Pollution and the Internet," *New York Times*, pp. 1–10, 2012.
- [8] M. Avgerinou, P. Bertoldi, and L. Castellazzi, "Trends in Data Centre Energy Consumption under the European Code of Conduct for Data Centre Energy Efficiency," *Energies*, vol. 10, no. 10, p. 1470, 2017.
- [9] S. V. Garimella, T. Persoons, J. Weibel, and L. T. Yeh, "Technological drivers in data centers and telecom systems: Multiscale thermal, electrical, and energy management," *Appl. Energy*, vol. 107, pp. 66–80, 2013.
- [10] A. Almoli, A. Thompson, N. Kapur, J. Summers, H. Thompson, and G. Hannah, "Computational fluid dynamic investigation of liquid rack cooling in data centres," *Appl. Energy*, vol. 89, no. 1, pp. 150–155, 2012.
- [11] J. Ni and X. Bai, "A review of air conditioning energy performance in data centers," *Renew. Sustain. Energy Rev.*, vol. 67, pp. 625–640, 2017.

- [12] G. I. Meijer, "Cooling energy-hungry data centers," *Science*, vol. 328, no. 5976, pp. 318–319, 2010.
- [13] D. B. Tuckerman and R. F. W. Pease, "High-performance heat sinking for VLSI," *IEEE Electron Device Lett.*, vol. 2, no. 5, pp. 126–129, 1981.
- [14] P. S. Lee, S. V. Garimella, and D. Liu, "Investigation of heat transfer in rectangular microchannels," *Int. J. Heat Mass Transf.*, vol. 48, no. 9, pp. 1688–1704, 2005.
- [15] C. S. Sharma, M. K. Tiwari, B. Michel, and D. Poulikakos, "Thermofluidics and energetics of a manifold microchannel heat sink for electronics with recovered hot water as working fluid," *Int. J. Heat Mass Transf.*, vol. 58, no. 1–2, pp. 135–151, 2013.
- [16] W. Escher, B. Michel, and D. Poulikakos, "A novel high performance, ultra thin heat sink for electronics," *Int. J. Heat Fluid Flow*, vol. 31, no. 4, pp. 586–598, 2010.
- [17] S. G. Kandlikar and A. V. Bapat, "Evaluation of jet impingement, spray and microchannel chip cooling options for high heat flux removal," *Heat Transf. Eng.*, vol. 28, no. 11, pp. 911–923, 2007.
- [18] C. S. Sharma, S. Zimmermann, M. K. Tiwari, B. Michel, and D. Poulikakos, "Optimal thermal operation of liquid-cooled electronic chips," *Int. J. Heat Mass Transf.*, vol. 55, no. 7–8, pp. 1957–1969, 2012.
- [19] H. Esmailzadeh, E. Blem, R. St. Amant, K. Sankaralingam, and D. Burger, "Power Limitations and Dark Silicon Challenge the Future of Multicore," *ACM Trans. Comput. Syst.*, vol. 30, no. 3, pp. 1–27, 2012.
- [20] B. Sinharoy *et al.*, "IBM POWER7 multicore server processor," *IBM J. Res. Dev.*, vol. 55, no. 3, 2011.
- [21] C. S. Sharma *et al.*, "Energy efficient hotspot-targeted embedded liquid cooling of electronics," *Appl. Energy*, vol. 138, pp. 414–422, 2015.
- [22] C. S. Sharma, G. Schlottig, T. Brunswiler, M. K. Tiwari, B. Michel, and D. Poulikakos, "A novel method of energy efficient hotspot-targeted embedded liquid cooling for electronics: An experimental study," *Int. J. Heat Mass Transf.*, vol. 88, pp. 684–694, 2015.
- [23] D. Kearney, T. Hilt, and P. Pham, "A liquid cooling solution for temperature redistribution in 3D IC architectures," *Microelectronics J.*, vol. 43, no. 9, pp. 602–610, 2012.

-
- [24] S. G. Kandlikar, "Review and Projections of Integrated Cooling Systems for Three-Dimensional Integrated Circuits," *J. Electron. Packag.*, vol. 136, no. 2, p. 24001, 2014.
- [25] B. Dang, M. S. Bakir, and J. D. Meindl, "Integrated thermal-fluidic I/O interconnects for an on-chip microchannel heat sink," *Electron Device Lett. IEEE*, vol. 27, pp. 117–119, 2006.
- [26] S. G. Kandlikar and W. J. Grande, "Evaluation of Single Phase Flow in Microchannels for High Heat Flux Chip Cooling — Thermohydraulic Performance Enhancement and Fabrication Technology," *Heat Transf. Eng.*, vol. 25, no. 8, pp. 5–16, 2004.
- [27] T. Brunschwiler, H. Rothuizen, S. Paredes, B. Michel, E. Colgan, and P. Bezama, "Hotspot-adapted Cold Plates to Maximize System Efficiency," in *15th International Workshop on Thermal Investigations of ICs and Systems, 2009*.
- [28] A. M. Waddell, J. Punch, J. Stafford, and N. Jeffers, "The characterization of a low-profile channel-confined jet for targeted hot-spot cooling in microfluidic applications," *Int. J. Heat Mass Transf.*, vol. 101, pp. 620–628, 2016.
- [29] P.-S. Lee and S. V. Garimella, "Hot-Spot Thermal Management With Flow Modulation in a Microchannel Heat Sink," in *ASME International Mechanical Engineering Congress and Exposition, 2005*.
- [30] Y. J. Lee, P. S. Lee, and S. K. Chou, "Hotspot mitigating with obliquely finned microchannel heat sink-an experimental study," *IEEE Trans. Components, Packag. Manuf. Technol.*, vol. 3, no. 8, pp. 1332–1341, 2013.
- [31] J. Barrau, D. Chemisana, J. I. Rosell, L. Tadrist, and M. Ibañez, "An experimental study of a new hybrid jet impingement/micro-channel cooling scheme," *Appl. Therm. Eng.*, vol. 30, no. 14–15, pp. 2058–2066, 2010.
- [32] S. Riera, J. Barrau, M. Omri, L. G. Frechette, and J. I. Rosell, "Stepwise varying width microchannel cooling device for uniform wall temperature: Experimental and numerical study," *Appl. Therm. Eng.*, vol. 78, pp. 30–38, 2015.
- [33] M. Vilarrubí *et al.*, "Experimental and numerical study of micro-pin-fin heat sinks with variable density for increased temperature uniformity," *Int. J. Therm. Sci.*, vol. 132, pp. 424–434, 2018.

- [34] L.-M. Collin *et al.*, "Hot spot aware microchannel cooling add-on for microelectronic chips in mobile devices," *16th IEEE Intersoc. Conf. Therm. Thermomechanical Phenom. Electron. Syst.*, 2017.
- [35] N. A. C. Sidik, M. N. A. W. Muhamad, W. M. A. A. Japar, and Z. A. Rasid, "An overview of passive techniques for heat transfer augmentation in microchannel heat sink," *Int. Commun. Heat Mass Transf.*, vol. 88, pp. 74–83, 2017.
- [36] M. Héder, "From NASA to EU: The evolution of the TRL scale in Public Sector Innovation," *Innov. J.*, vol. 22, no. 2, pp. 1–23, 2017.
- [37] G. Laguna *et al.*, "Numerical parametric study of a hotspot-targeted microfluidic cooling array for microelectronics," *Appl. Therm. Eng.*, vol. 144, pp. 71–80, 2018.
- [38] M. McCarthy, N. Tiliakos, V. Modi, and L. G. Fréchette, "Characterization and modeling of thermal buckling in eccentrically loaded microfabricated nickel beams for adaptive cooling," in *ASME International Mechanical Engineering Congress and Exposition*, 2005.
- [39] M. McCarthy, N. Tiliakos, V. Modi, and L. G. Fréchette, "Thermal buckling of eccentric microfabricated nickel beams as temperature regulated nonlinear actuators for flow control," *Sensors Actuators, A Phys.*, vol. 134, no. 1, pp. 37–46, 2007.
- [40] M. McCarthy, N. Tiliakos, V. Modi, and L. G. Fréchette, "Temperature-regulated nonlinear microvalves for self-adaptive MEMS cooling," *J. Microelectromechanical Syst.*, vol. 17, no. 4, pp. 998–1009, 2008.
- [41] S. Da Luz *et al.*, "Variable Pumping Control for Low Power Microfluidic Chip Cooling," in *24th International Workshop on Thermal Investigations of ICs and Systems, Proceedings*, 2018.
- [42] G. Savelli and P. Coronel, "Cooling device provided with a thermoelectric sensor," WO/2013/017750, 2013.
- [43] M. E. Steinke and S. G. Kandlikar, "Single-phase liquid friction factors in microchannels," *Int. J. Therm. Sci.*, vol. 45, no. 11, pp. 1073–1083, 2006.
- [44] R. L. Webb, "Performance evaluation criteria for use of enhanced heat transfer surfaces in heat exchanger design," *Int. J. Heat Mass Transf.*, vol. 24, no. 4, pp. 715–726, 1981.
- [45] V. Yadav, K. Baghel, R. Kumar, and S. T. Kadam, "Numerical investigation of heat transfer

- in extended surface microchannels,” *Int. J. Heat Mass Transf.*, vol. 93, pp. 612–622, 2016.
- [46] A. Ebrahimi, E. Roohi, and S. Kheradmand, “Numerical study of liquid flow and heat transfer in rectangular microchannel with longitudinal vortex generators,” *Appl. Therm. Eng.*, vol. 78, pp. 576–583, 2015.
- [47] J. Marschewski, R. Brechbüler, S. Jung, P. Ruch, B. Michel, and D. Poulikakos, “Significant heat transfer enhancement in microchannels with herringbone-inspired microstructures,” *Int. J. Heat Mass Transf.*, vol. 95, pp. 755–764, 2016.
- [48] A. Sabaghan, M. Edalatpour, M. C. Moghadam, E. Roohi, and H. Niazmand, “Nanofluid flow and heat transfer in a microchannel with longitudinal vortex generators: Two-phase numerical simulation,” *Appl. Therm. Eng.*, vol. 100, pp. 179–189, 2016.
- [49] J. F. Li and C. W. Wu, “Is 3D integration an opportunity or just a hype?,” in *Proceedings of the Asia and South Pacific Design Automation Conference, ASP-DAC*, 2010.
- [50] M. S. Bakir *et al.*, “3D heterogeneous integrated systems: Liquid cooling, power delivery, and implementation,” in *Custom Integrated Circuits Conference*, 2008.
- [51] Y. Zhang *et al.*, “Coupled electrical and thermal 3D IC centric microfluidic heat sink design and technology,” in *Electronic Components and Technology Conference*, 2011.
- [52] C. R. King, J. Zaveri, M. S. Bakir, and J. D. Meindl, “Electrical and fluidic C4 interconnections for inter-layer liquid cooling of 3D ICs,” in *60th Electronic Components and Technology Conference (ECTC)*, 2010.
- [53] J.-M. Koo, S. Im, L. Jiang, and K. E. Goodson, “Integrated Microchannel Cooling for Three-Dimensional Electronic Circuit Architectures,” *J. Heat Transfer*, vol. 127, no. 1, p. 49, 2005.
- [54] S. G. Kandlikar, “Fundamental issues related to flow boiling in minichannels and microchannels,” *Exp. Therm. Fluid Sci.*, vol. 26, no. 2–4, pp. 389–407, 2002.
- [55] D. Sekar *et al.*, “A 3D-IC technology with integrated microchannel cooling,” in *2008 IEEE International Interconnect Technology Conference, IITC*, 2008.
- [56] B. Dang *et al.*, “Integrated microfluidic cooling and interconnects for 2D and 3D chips,” *IEEE Trans. Adv. Packag.*, vol. 33, no. 1, pp. 79–87, 2010.

- [57] F. Alfieri, M. K. Tiwari, I. Zinovik, D. Poulidakos, T. Brunswiler, and B. Michel, "3D Integrated Water Cooling of a Composite Multilayer Stack of Chips," *J. Heat Transfer*, vol. 132, no. 12, art. no. 121402, 2010.
- [58] M. S. Bakir and Y. Zhang, "Independent interlayer microfluidic cooling for heterogeneous 3D IC applications," *Electron. Lett.*, vol. 49, no. 6, pp. 404–406, 2013.
- [59] B. Shi, A. Srivastava, and A. Bar-Cohen, "Hybrid 3D-IC Cooling System Using Micro-fluidic Cooling and Thermal TSVs," in *2012 IEEE Computer Society Annual Symposium on VLSI*, 2012.
- [60] N. Khan *et al.*, "3-D packaging with through-silicon via (TSV) for electrical and fluidic interconnections," *IEEE Trans. Components, Packag. Manuf. Technol.*, vol. 3, no. 2, pp. 221–228, 2013.
- [61] L. M. Collin *et al.*, "Microchannel design study for 3D microelectronics cooling using a hybrid analytical and finite element method," in *ASME 2015, 13th International Conference on Nanochannels, Microchannels, and Minichannels*, 2015.
- [62] G. Hetsroni, A. Mosyak, Z. Segal, and G. Ziskind, "A uniform temperature heat sink for cooling of electronic devices," *Int. J. Heat Mass Transf.*, vol. 45, no. 16, pp. 3275–3286, 2002.
- [63] C. A. Rubio-Jimenez, S. G. Kandlikar, and A. Hernandez-Guerrero, "Numerical analysis of novel micro pin fin heat sink with variable fin density," *IEEE Trans. Components, Packag. Manuf. Technol.*, vol. 2, no. 5, pp. 825–833, 2012.
- [64] G. Xie, F. Zhang, B. Sundén, and W. Zhang, "Constructal design and thermal analysis of microchannel heat sinks with multistage bifurcations in single-phase liquid flow," *Appl. Therm. Eng.*, vol. 62, no. 2, pp. 791–802, 2014.
- [65] L. Lin, Y.-Y. Chen, X.-X. Zhang, and X.-D. Wang, "Optimization of geometry and flow rate distribution for double-layer microchannel heat sink," *Int. J. Therm. Sci.*, vol. 78, pp. 158–168, 2014.
- [66] S. Riera *et al.*, "Smoothing effect of the thermal interface material on the temperature distribution in a stepwise varying width microchannel cooling device," *Heat Mass Transf.*, vol. 53, no. 9, pp. 2987–2997, 2017.

-
- [67] C. S. Sharma, M. K. Tiwari, and D. Poulikakos, "A simplified approach to hotspot alleviation in microprocessors," *Appl. Therm. Eng.*, vol. 93, pp. 1314–1323, 2016.
- [68] H. F. Hamann *et al.*, "Hotspot-Limited Microprocessors: Direct Temperature and Power Distribution Measurements," *IEEE J. Solid-State Circuits*, vol. 42, no. 1, pp. 56–65, 2007.
- [69] A. Bar-Cohen, "Thermal management of on-chip hot spots and 3D chip stacks," in *2009 IEEE International Conference on Microwaves, Communications, Antennas and Electronics Systems*, 2009.
- [70] C. Green, A. G. Fedorov, and Y. K. Joshi, "Fluid-to-Fluid Spot-to-Spreader (F2/S2) Hybrid Heat Sink for Integrated Chip-Level and Hot Spot-Level Thermal Management," *J. Electron. Packag.*, vol. 131, no. 2, art. no. 025002, 2009.
- [71] W. Huang, S. Ghosh, S. Velusamy, K. Sankaranarayanan, K. Skadron, and M. R. Stan, "HotSpot: A compact thermal modeling methodology for early-stage VLSI design," *IEEE Trans. Very Large Scale Integr. Syst.*, vol. 14, no. 5, pp. 501–513, 2006.
- [72] C. Torregiani, H. Oprins, B. Vandeveldel, E. Beyne, and I. De Wolf, "Compact thermal modeling of hot spots in advanced 3D-stacked ICs," *Proc. Electron. Packag. Technol. Conf. EPTC*, no. 1, pp. 131–136, 2009.
- [73] A. E. Bergles, M. K. Jensen, and B. Shome, "The literature on enhancement of convective heat and mass transfer," *J. Enhanc. Heat Transf.*, vol. 4, no. 1, pp. 1–6, 1996.
- [74] W. Q. Tao, Y. L. He, Q. W. Wang, Z. G. Qu, and F. Q. Song, "A unified analysis on enhancing single phase convective heat transfer with field synergy principle," *Int. J. Heat Mass Transf.*, vol. 45, no. 24, pp. 4871–4879, 2002.
- [75] M. E. Steinke and S. G. Kandlikar, "Single-Phase Heat Transfer Enhancement Techniques in Microchannel and Minichannel Flows," in *ASME 2nd International Conference on Microchannels and Minichannels*, 2004.
- [76] M. Fiebig, "Vortices and Heat Transfer," *ZAMM - J. Appl. Math. Mech.*, vol. 77, pp. 3–18, 1997.
- [77] M. Fiebig, P. Kallweit, N. Mitra, and S. Tiggelbeck, "Heat transfer enhancement and drag by longitudinal vortex generators in channel flow," *Exp. Therm. Fluid Sci.*, vol. 4, pp. 103–114, 1991.

- [78] M. S. Aris, I. Owen, and C. J. Sutcliffe, "The development of active vortex generators from shape memory alloys for the convective cooling of heated surfaces," *Int. J. Heat Mass Transf.*, vol. 54, no. 15–16, pp. 3566–3574, 2011.
- [79] C. Liu *et al.*, "Experimental investigations on liquid flow and heat transfer in rectangular microchannel with longitudinal vortex generators," *Int. J. Heat Mass Transf.*, vol. 54, no. 13–14, pp. 3069–3080, 2011.
- [80] K. Y. Hsiao, C. Y. Wu, and Y. T. Huang, "Fluid mixing in a microchannel with longitudinal vortex generators," *Chem. Eng. J.*, vol. 235, pp. 27–36, 2014.
- [81] C. Chen *et al.*, "A study on fluid flow and heat transfer in rectangular microchannels with various longitudinal vortex generators," *Int. J. Heat Mass Transf.*, vol. 69, pp. 203–214, 2014.
- [82] G. Wang, D. Niu, F. Xie, Y. Wang, X. Zhao, and G. Ding, "Experimental and numerical investigation of a microchannel heat sink (MCHS) with micro-scale ribs and grooves for chip cooling," *Appl. Therm. Eng.*, vol. 85, pp. 61–70, 2015.
- [83] A. Datta, D. Sanyal, and A. K. Das, "Numerical investigation of heat transfer in microchannel using inclined longitudinal vortex generator," *Appl. Therm. Eng.*, vol. 108, pp. 1008–1019, 2016.
- [84] M. T. Al-Asadi, F. S. Alkasmoul, and M. C. T. Wilson, "Heat transfer enhancement in a micro-channel cooling system using cylindrical vortex generators," *Int. Commun. Heat Mass Transf.*, vol. 74, pp. 40–47, 2016.
- [85] A. Renfer *et al.*, "Microvortex-enhanced heat transfer in 3D-integrated liquid cooling of electronic chip stacks," *Int. J. Heat Mass Transf.*, vol. 65, pp. 33–43, 2013.
- [86] G. D. Xia, D. D. Ma, W. Wang, and Y. L. Zhai, "Effects of different structures and allocations on fluid flow and heat transfer performance in 3D-IC integrated micro-channel interlayer cooling," *Int. J. Heat Mass Transf.*, vol. 91, pp. 1167–1175, 2015.
- [87] Y. F. Li, G. D. Xia, D. D. Ma, Y. T. Jia, and J. Wang, "Characteristics of laminar flow and heat transfer in microchannel heat sink with triangular cavities and rectangular ribs," *Int. J. Heat Mass Transf.*, vol. 98, pp. 17–28, 2016.
- [88] A. D. Stroock, S. Dertinger, A. Ajdari, I. Mezić, H. A. Stone, and G. M. Whitesides, "Chaotic

- Mixer for Microchannels,” *Science*, vol. 295, no. 5555, pp. 647–651, 2002.
- [89] S. Hong, J. L. Thiffeault, L. G. Fréchette, and Modi, “Numerical Study of Mixing in Microchannels With Patterned Zeta Potential Surfaces,” in *ASME International Mechanical Engineering Congress and Exposition*, 2003.
- [90] H. . Wu and P. Cheng, “An experimental study of convective heat transfer in silicon microchannels with different surface conditions,” *Int. J. Heat Mass Transf.*, vol. 46, no. 14, pp. 2547–2556, 2003.
- [91] G. Gamrat, M. Favre-Marinet, S. Le Person, R. Baviere, and F. Ayela, “An experimental study and modelling of roughness effects on laminar flow in microchannels,” *J. Fluid Mech.*, vol. 594, pp. 399–423, 2008.
- [92] G. Gamrat, M. Favre-Marinet, and S. Le Person, “Modelling of roughness effects on heat transfer in thermally fully-developed laminar flows through microchannels,” *Int. J. Therm. Sci.*, vol. 48, no. 12, pp. 2203–2214, 2009.
- [93] T. P. Brackbill and S. G. Kandlikar, “Application of lubrication theory and study of roughness pitch during laminar, transition, and low reynolds number turbulent flow at microscale,” *Heat Transf. Eng.*, vol. 31, no. 8, pp. 635–645, 2010.
- [94] M. Andresen and M. Liserre, “Impact of active thermal management on power electronics design,” *Microelectron. Reliab.*, vol. 54, no. 9–10, pp. 1935–1939, 2014.
- [95] J. S. Go, “Design of a microfin array heat sink using flow-induced vibration to enhance the heat transfer in the laminar flow regime,” *Sensors Actuators, A Phys.*, vol. 105, no. 2, pp. 201–210, 2003.
- [96] P. H. G. Allen and T. G. Karayiannis, “Electrohydrodynamic enhancement of heat transfer and fluid flow,” *Heat Recover. Syst. CHP*, vol. 15, no. 5, pp. 389–423, 1995.
- [97] M.-A. Hessami, A. Berryman, and P. Bandopdhayay, “Heat Transfer Enhancement in an Electrically Heated Horizontal Pipe Due to Flow Pulsation,” in *ASME International Mechanical Engineering Congress and Exposition*, 2003.
- [98] R. Fang and J. A. Khan, “Active Heat Transfer Enhancement in Single-Phase Microchannels by Using Synthetic Jets,” *J. Therm. Sci. Eng. Appl.*, vol. 5, no. 1, art. no. 011006, 2013.
- [99] P. R. Champagne and A. E. Bergles, “Development and testing of a novel, variable-

- roughness technique to enhance, on demand, heat transfer in a single-phase heat exchanger," *J. Enhanc. Heat Transf.*, vol. 8, no. 5, pp. 341–352, 2001.
- [100] M. Vilarrubí, G. Morell, J. Rosell, L. G. Fréchette, and J. Barrau, "Experimental characterization of a self-adaptive shape memory alloy cooling approach to regulate temperature under varying heat loads," *Int. J. Heat Mass Transf.*, vol. 139, pp. 632–640, 2019.
- [101] COMSOL Multiphysics, "CFD Module - User's Guide," in *Comsol Multiphysics Manual, version 5.3a*, 2017, pp. 1–638.
- [102] COMSOL Multiphysics, "Heat Transfer Module - User's Guide," in *Comsol Multiphysics Manual, version 5.3a*, 2017, pp. 1–626.
- [103] S. Timoshenko, "Analysis of bi-metal thermostats," *J. Opt. Soc. Am.*, vol. 11, no. 3, pp. 233–255, 1925.
- [104] S. Cherneva, R. Iankov, and D. Stoychev, "Characterisation of mechanical properties of electrochemically deposited thin silver layers," in *Transactions of the Institute of Metal Finishing*, 2010, vol. 88, no. 4, pp. 209–214.
- [105] COMSOL Multiphysics, "Structural Mechanics Module - User's Guide," in *Comsol Multiphysics Manual, version 5.3a*, 2017, pp. 1–938.
- [106] A. Amnache *et al.*, "Thermoregulated Microvalve for Self-Adaptive Microfluidic Cooling," in *24rd International Workshop on Thermal Investigations of ICs and Systems*, 2018.

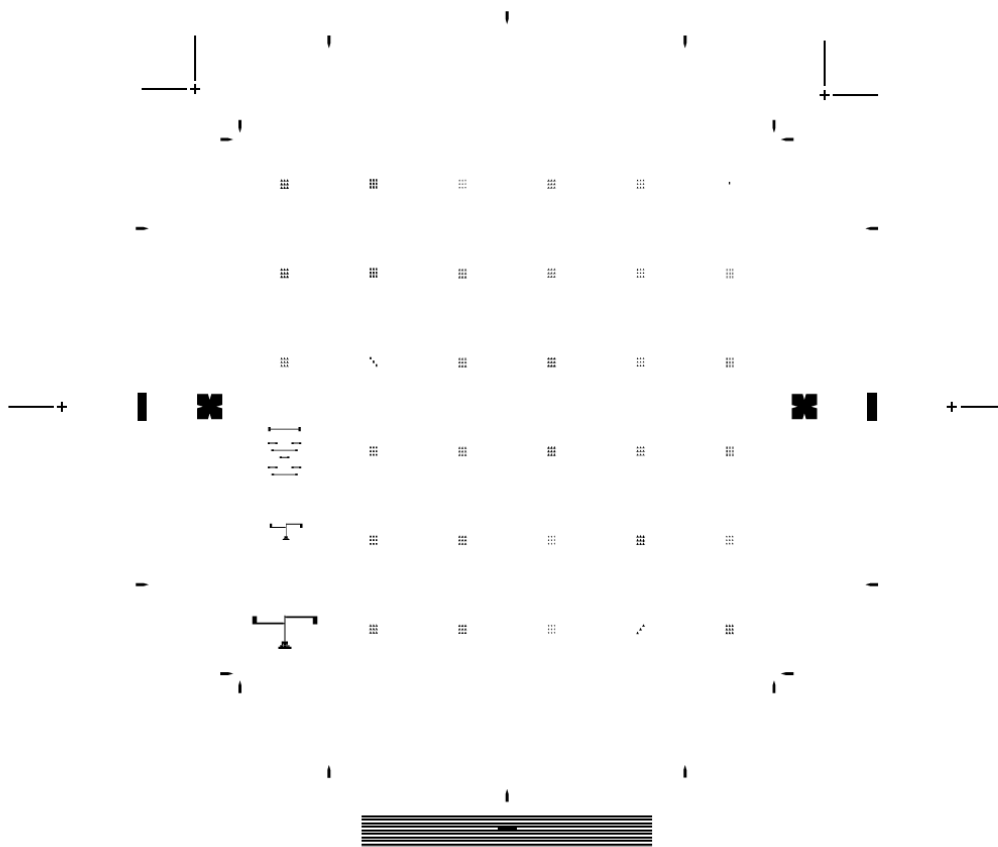
ANNEX I

Annex I

Microfabrication of the self-adaptive bimetallic fins

Photomasks designed for the bimetallic fins

3 photomasks were created for the fabrication of the bimetallic self-adaptive fins: Mask A (anchors), Mask B (low CTE material) and Mask C (high CTE material). The masks include 33 different configurations of the self-adaptive fins inside a microfluidic cell. A general overview of Mask B and a detailed view of Models 3 and 4 (Table 3.5) designed for mask printing are given in Figure A.1. This two detailed models are the one which showed better results after the microfabrication steps.



(a)

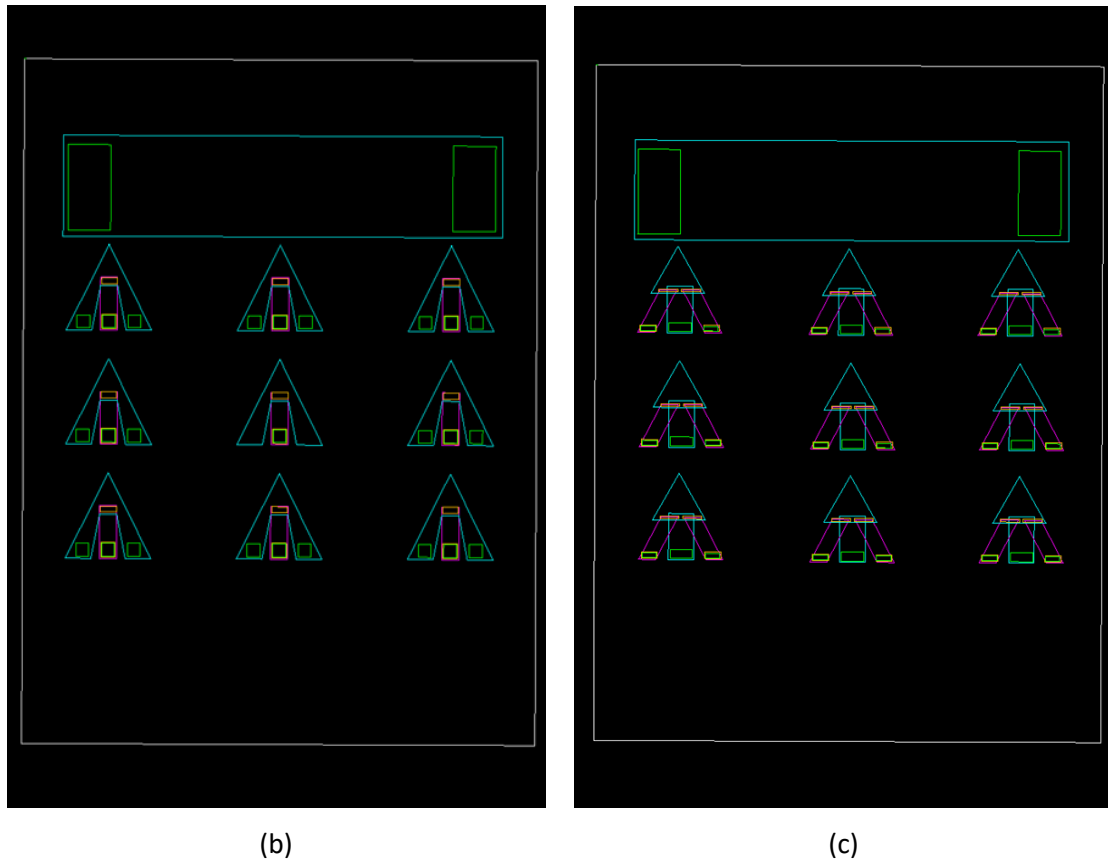


Figure A.1. (a) General overview of Mask B (low CTE material mask). (b) Detail of Model 3 designed for the photomask. Each color corresponds to one mask. (c) Detail of Model 4 designed to print at the photomask.

Evaluation of the material combination for the fabrication of the bimetallic fins

In Table 3.6 the different material combinations tried to successfully fabricate bimetallic self-adaptive fins are listed. Some cases are explained in detail here.

- **Case 1**

In this case, the sacrificial layer was silicon dioxide (SiO_2), the high CTE material was silver and the low CTE material was Niobium (Nb). In this case, the high and low CTE materials were exchanged in comparison with the defined geometries in chapter 3. The thicknesses of each material were:

- $\text{SiO}_2 = 2,00 \mu\text{m}$
- $\text{Ag} = 3,50 \mu\text{m}$

- Nb = 3,50 μm

Steps a-h of the process flow were done successfully (Figure A.2), however the Nb film was etched by the buffered oxide etch (BOE) at the releasing step.

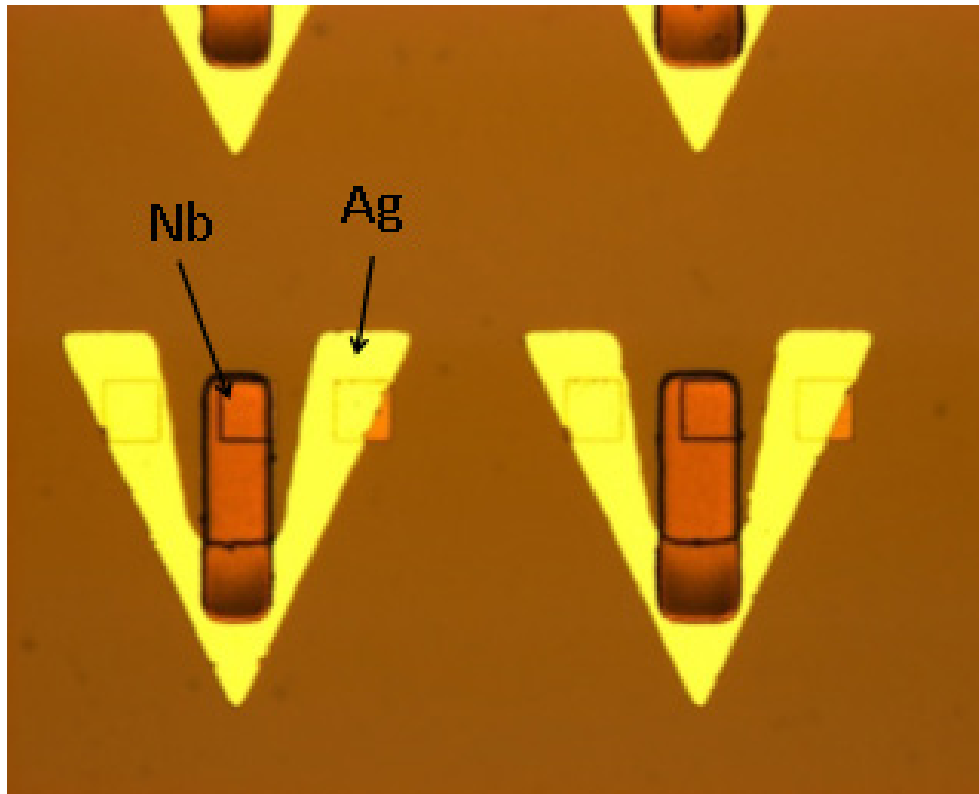


Figure A.2. Microscopic image of the bimetallic Ag-Nb fins (Model 3) after the double lift-off (before releasing).

- **Case 2**

The sacrificial layer of the second case was gold (Au), the high CTE material was nickel (Ni) and the low CTE material was Niobium (Nb). In this case, the high and low CTE materials were exchanged in comparison with the defined geometries in chapter 3. The thicknesses of each material were:

- Au = 250 nm
- Ni = 400 nm
- Nb = 800 μm

The double lift-off of the Ni and Nb films (steps a-h of the process flow) was done successfully, however, the Ni layer showed ripples due to residual stresses after deposition (Figure A.3). Consequently, the releasing step had not been done due to the presence of defects in the nickel film.

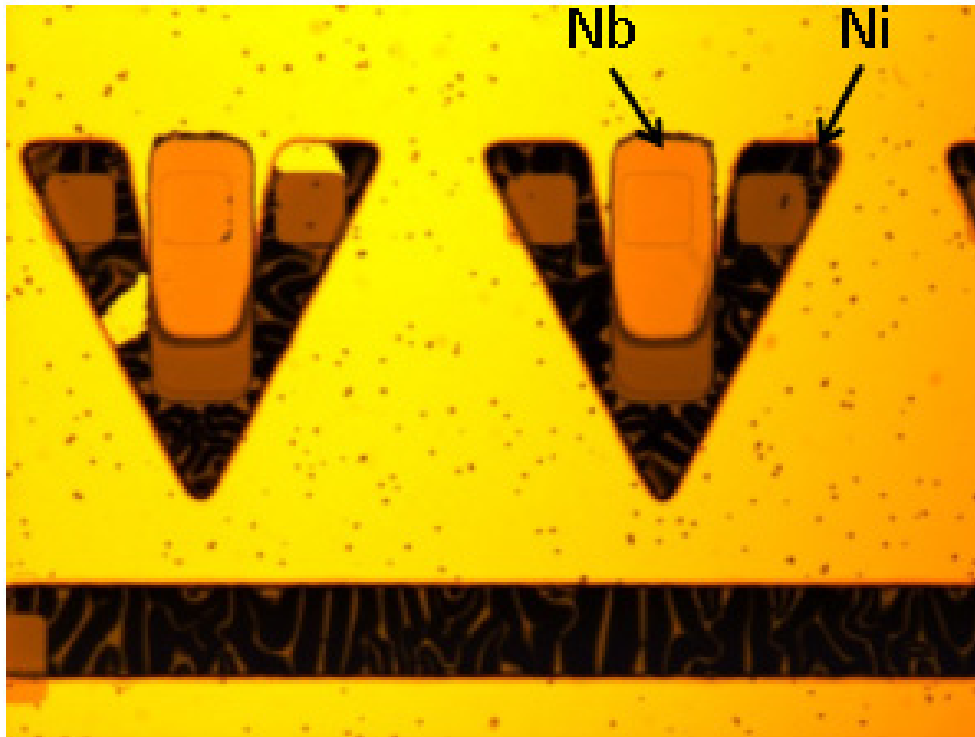


Figure A.3. Microscopic image of the Ni-Nb bimetallic fins (Model 3) after the double lift-off (before releasing).

- **Case 3**

The sacrificial layer in this case was Au, the high CTE material was Ni and the low CTE material was Cr. In this case, the high and low CTE materials were exchanged in comparison with the defined geometries in chapter 3. The thicknesses of each material were:

- Au = 250 nm
- Ni = 400 nm
- Cr = 600 μm

Similarly to the second case, despite the double lift-off of the Ni and Cr fins was done successfully, the nickel layer showed cracks due, probably, to residual stress after deposition (Figure A.4). The releasing step had not been done due to the defects that appeared in the nickel film.

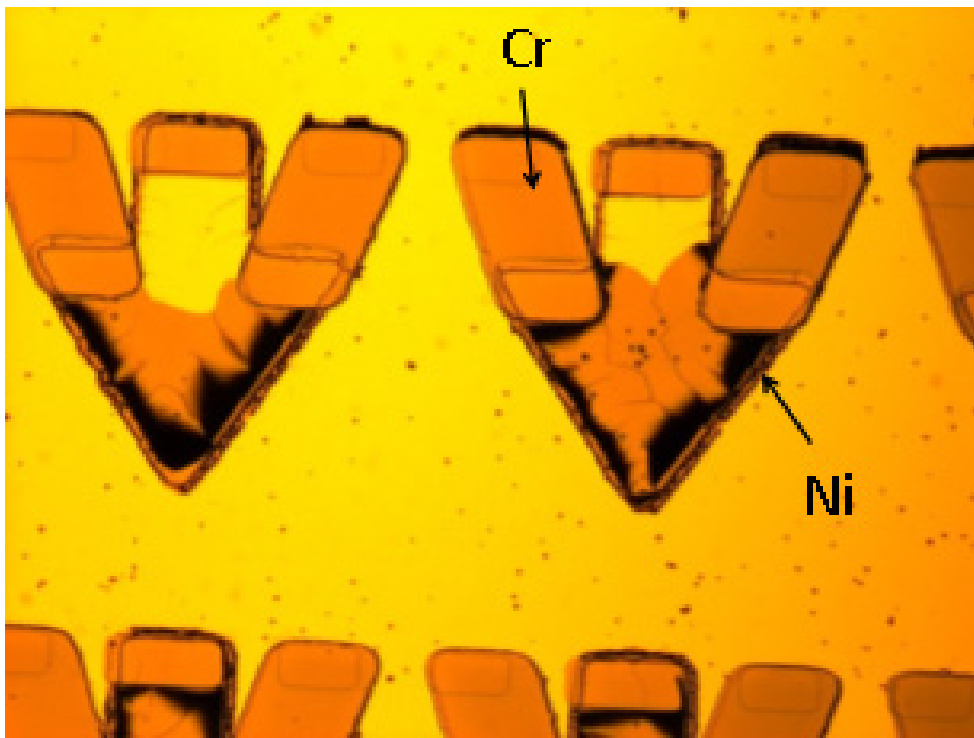


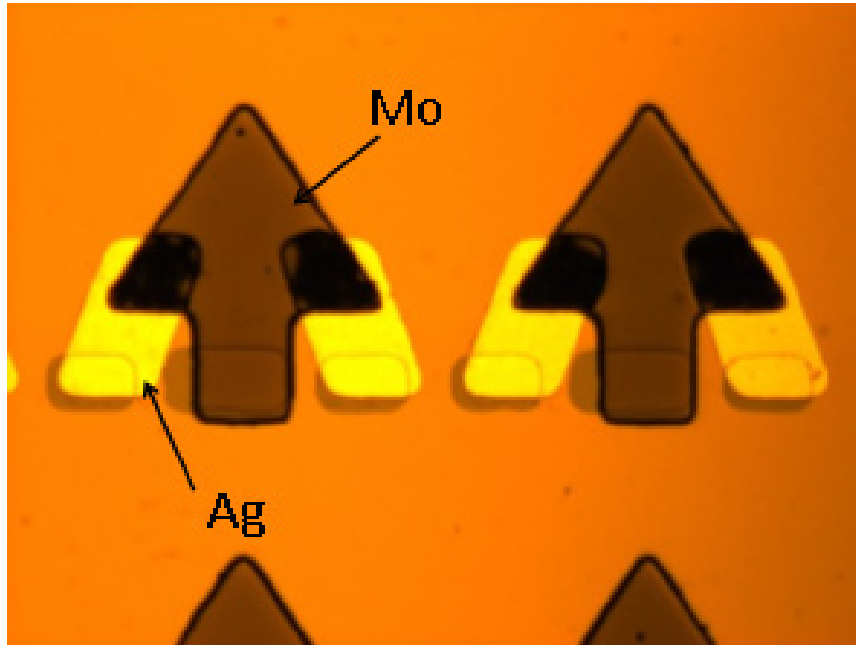
Figure A.4. Microscopic image of the Ni-Cr fabricated bimetallic fins (Model 4) after the double lift-off (before releasing).

- **Case 4**

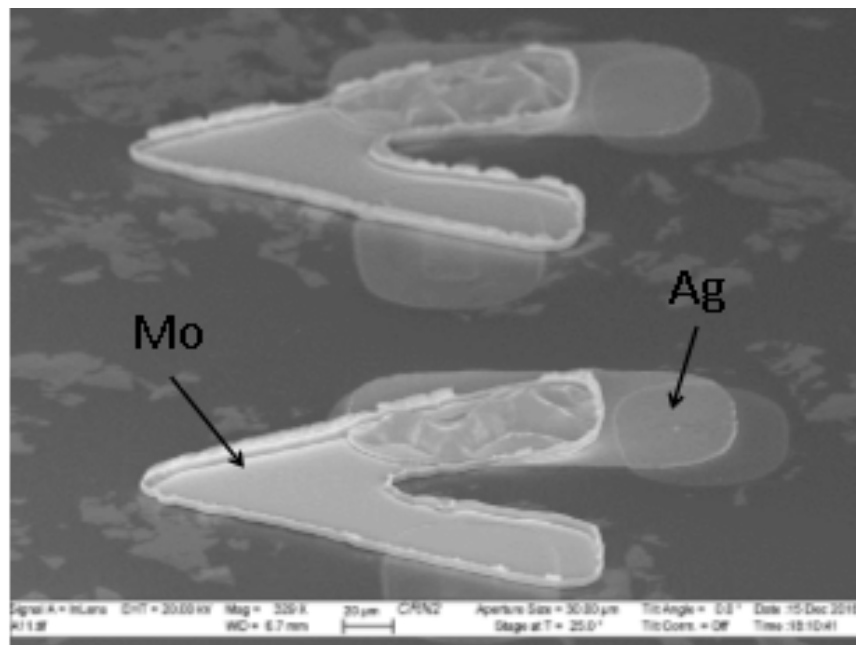
In this case, the sacrificial layer was titanium (Ti), the high CTE material was Ag and the low CTE material was molybdenum (Mo). The thicknesses of each film were:

- Ti = 500 nm
- Ag = 2,00 μm
- Mo = 2,80 μm

Steps a-h of the process flow were done successfully (Figure A.5a). Nonetheless, at the overlap between the two metals, the Mo film showed ripples due, probably, to residual stresses after deposition (Figure A.5b).



(a)



(b)

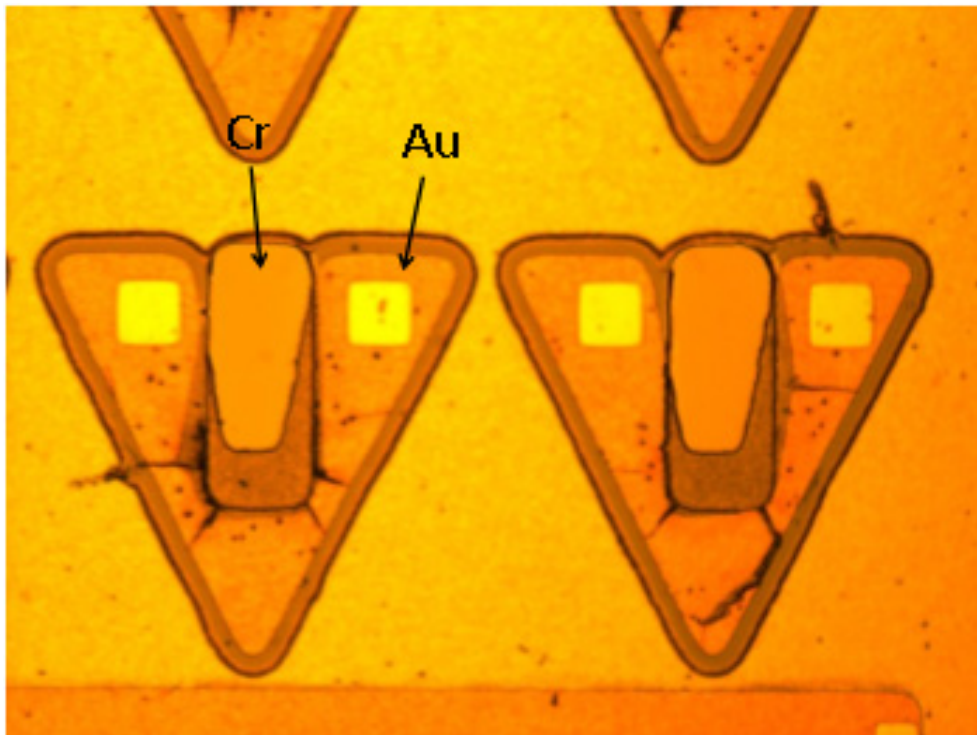
Figure A.5. (a) Microscopic image of the Ag-Mo fins (Model 4) fabricated after the double lift-off, before releasing. (b) SEM image of the same bimetallic fins after releasing.

- **Case 5**

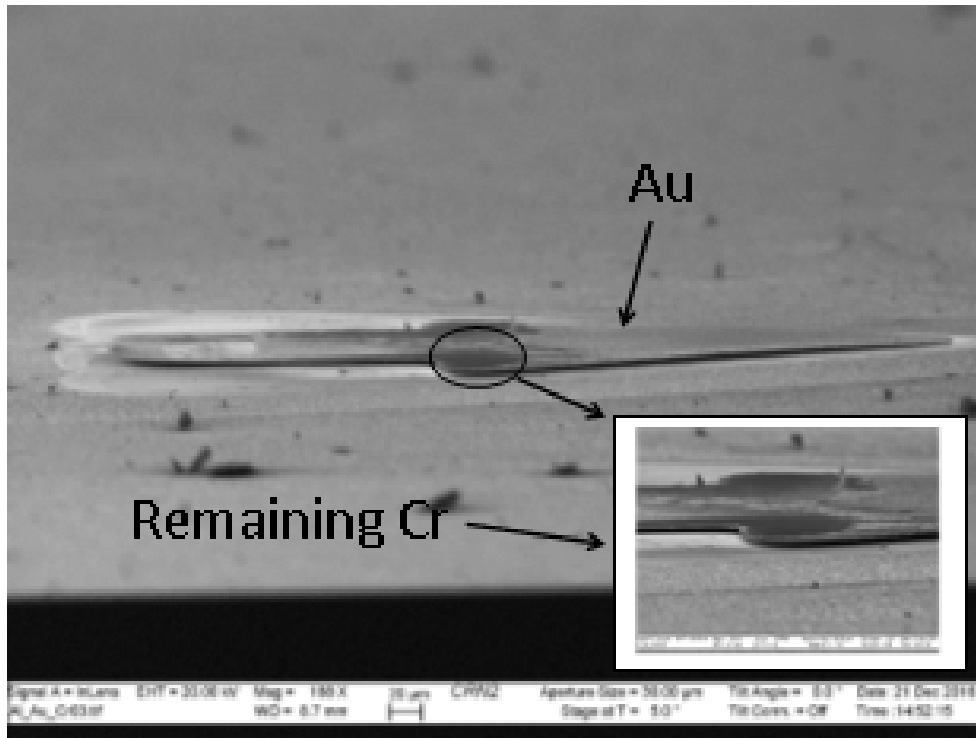
The sacrificial layer of this case was aluminum (Al), the high CTE material was Au and the low CTE material was Cr. The high and low CTE materials were exchanged in comparison with the defined geometries in chapter 3. Their respective thicknesses were:

- Al = 500 nm
- Au = 1,20 μm
- Cr = 600 nm

The double lift-off of the Au and Cr fins was done successfully (steps a-h of the process flow), although some cracks were observed on the gold film (Figure A.6a). After the releasing step (step i of the process flow) the chrome film disappeared due to the use of BOE for the release (Figure A.6b). The gold film showed no defects caused by residual stress after releasing.



(a)



(b)

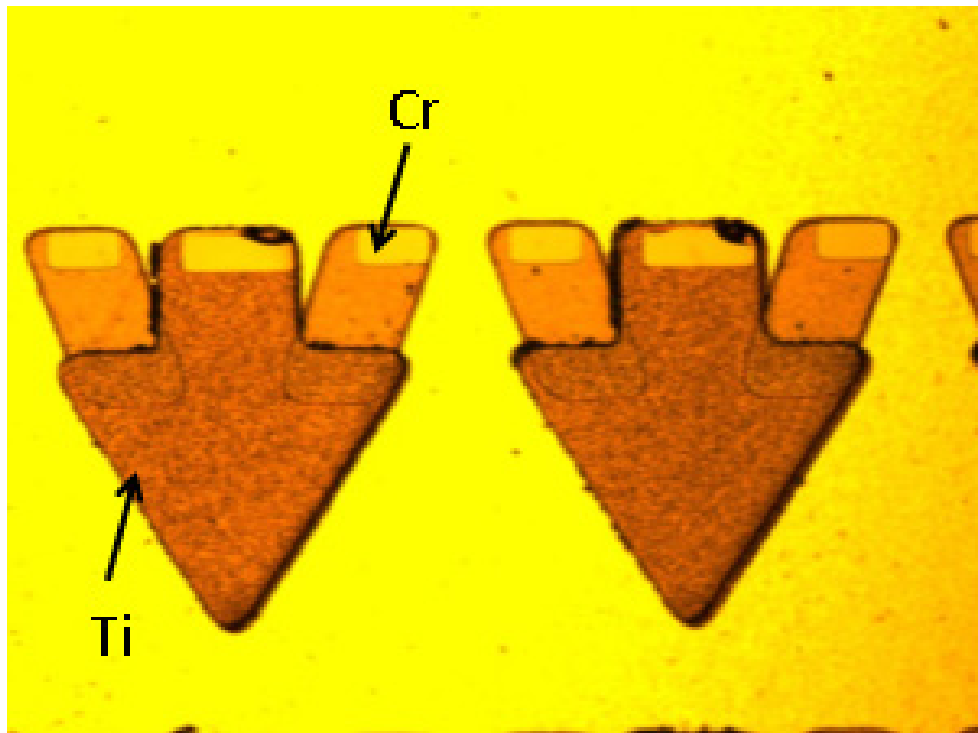
Figure A.6. (a) Microscopic image of the Au-Cr fins (Model 3) before releasing. (b) SEM image of the Au-Cr bimetallic fins (Model 2) after the releasing process.

- **Case 6**

In this case, the sacrificial layer case was Al, the high CTE material was Ti and the low CTE material was Cr. The high and low CTE materials were exchanged in comparison with the defined geometries in chapter 3. Their respective thicknesses were:

- Al = 500 nm
- Ti = 500 nm
- Cr = 600 nm

The double lift-off of the Ti and Cr fins was successfully done (Figure A.7a). Also, the releasing process was done for this bimetallic fins although some detachments were observed between Cr and Ti films. The small difference in thickness between both metals is believed to be the cause of this effect. A deposition of thicker Cr film and a deposition by sputtering instead of evaporation method are suggested to improve the result.



(a)

Figure A.7. Microscopic image of the Ti-Cr fins (Model 4) before releasing.

